Tectonique et hydrologie en mer de Marmara : Histoire de l'ouverture de la mer de Marmara et reconstitution de la réponse hydrologique aux variations climatiques depuis le dernier interglaciaire

Julia Kende

To cite this version:

Julia Kende. Tectonique et hydrologie en mer de Marmara : Histoire de l'ouverture de la mer de Marmara et reconstitution de la réponse hydrologique aux variations climatiques depuis le dernier interglaciaire. Tectonique. Aix Marseille Université, 2018. Français. NNT : . tel-01907260

HAL Id: tel-01907260
https://hal.science/tel-01907260

Submitted on 28 Oct 2018

Thèse de doctorat

Présentée en vue de l’obtention du grade de
Docteur de l’Université d’Aix Marseille

Spécialité : **Géosciences**

par

Julia KENDE

Tectonique et hydrologie en mer de Marmara : Histoire de l’ouverture de la mer de Marmara et reconstitution de la réponse hydrologique aux variations climatiques depuis le dernier interglaciaire

---

Date de soutenance : 12 mars 2018

Devant le jury composé de :

Marina Rabineau	Rapporteur
Yann Klinger	Rapporteur
Cecilia McHugh	Examinateur
Kürşad Kadir Eriş	Examinateur
Nicolas Chamot-Rooke	Examinateur
Edouard Bard	Examinateur
Pierre Henry	Directeur de thèse

Thèse préparée au Centre Européen de Recherche et d’Enseignement des Géosciences de l’Environnement (CEREGE), Aix-Marseille

“We are not to tell nature what she’s gotta be. …
She's always got better imagination than we have.”

Richard Feynman, 1979

TABLE DES MATIERES

LISTE DES FIGURES

INTRODUCTION

CHAPITRE I

CHAPITRE II

CHAPITRE III

ANNEXES

LISTE DES TABLES

CHAPITRE II

CHAPITRE III

REMERCIEMENTS

C'est avec une grande joie que j'ouvre ces remerciements en m'adressant à Pierre Henry. Pierre, merci de m'avoir fait confiance et de m'avoir guidée pendant ces quelques années. Je te remercie surtout pour la manière dont tu as dirigé mon travail. Tu as su te comporter avec moi comme avec une collègue chercheuse et je ne me suis jamais sentie étudiante bien que tu aies, sans aucun doute, très professionnellement dirigé ma thèse. Merci ensuite pour ta versatilité scientifique. La variété de domaines que j'ai abordé est pour beaucoup dans le plaisir que j'ai eu, jour après jour, à découvrir les ressorts de la vie de chercheur. Je te remercie enfin pour ton intégrité scientifique et humaine à toute épreuve et j'espère emporter un peu de cet enseignement avec moi, quel que soit mon avenir professionnel. Je termine cette thèse persuadée que je n'aurais pu trouver meilleur directeur de thèse !

Un très grand merci à Edouard Bard, membre de la communauté des Géoliens qui, le premier, m'a parlé de la mer de Marmara avant de me mettre en contact avec Pierre. Merci, également, pour ta confiance et, pour les cessions de travails au cours desquels tu as toujours su nous proposer de nouvelles perspectives issues de ta connaissance spectaculaire de toutes les dernières publications.

Je remercie ensuite Louis Geli qui a été pour moi comme un co-directeur de thèse pendant la première partie de mes travaux. Merci aussi pour ton accueil chaleureux à Brest dans ton laboratoire et chez toi en compagnie de ta famille.

Merci à Xavier Le Pichon et Celâl Şengör pour cette semaine studieuse dans la bibliothèque de Celâl. Ce fut un honneur de travailler pendant ces quelques jours à vos côtés.

Je garderais un très bon souvenir de mes escapades stambouliotes grâce à mes collègues, guides et amis de l'Université Techniques d'Istanbul. Kadir Eriş, Sinan Özeren, Namık Çağatay, Gulsen Uçarkus, Dursun Acar, j'espère que la Mer de Marmara continuera d'inspirer vos recherches et que nous pourrons nous retrouver un jour pour partager encore un dîner magique au milieu des lumières du Bosphore.

Je remercie maintenant les membres de mon jury : Nicolas Chamot-Rooke, Yann Klinger, Marina Rabineau et Cecilia McHugh qui ont rejoint Edouard Bard et Kadir Eriş. Merci à vous tous d'avoir accepté d'évaluer mon travail et d'avoir été présents le jour-J. J'ajoute un grand merci supplémentaire à Cécilia pour son enthousiasme communicatif et pour le temps passé à ses côtés sur le bateau ainsi qu'à Brême.

De tous les membres du « Club Marmara » des sciences, le plus illustre est sans aucun doute Céline Grall ! Merci à toi pour ton aide et pour avoir disséminé, au cours de ton travail de thèse, les problématiques qui allaient devenir les miennes. Je reste impressionnée et admirative de ta passion pour la géologie parmi milles autre choses !

De nombreuses personnes m'ont apporté un appui scientifique et technique, parfois pour quelques instants, parfois pendant plusieurs mois. Je tiens donc à remercier Nicolas Thouveny, Frauke Rostek, Kazuyo Tachikawa, Daniel Borschneck, Patricia Roeser, Luc Beaufort, Laetitia Licari, Angélique Roubi, Bertrand Devouard, François Demory, Jean-Pierre Margerel, Julien Longerey et François Fournier pour leur aide décisive et leurs enseignements.

Doriane Delanghe, Christine Pailles et Marta Garcia, vous m'avez également soutenue et accompagnée pendant une partie de mon travail. En plus de vous remercier pour votre aide, votre professionnalisme, votre curiosité et votre engouement pour mon sujet, je vous remercie d'être devenues des amies.

J'ai très certainement eu la chance d'être entourée de personnes bienveillantes à mon égard, et il y en a une pour qui je regrette de n'avoir pas fait une thèse en littérature afin de savoir mieux exprimer ma gratitude. Sophie, merci pour tout : pour tes conseils, pour nos discussions, merci surtout de croire en moi et de m'avoir donné les clefs qui m'ont permis d'initier un tournant vers l'autre domaine qui me passionne : l'informatique fondamentale. Alors que j'écris ces lignes je ne sais pas où je serai en septembre mais je te promets que nous organiserons des soirées pour confronter à nouveau ma cervelle discrète à ton cerveau continu sur des bidules mathématiques !

Je poursuis avec l'autre personne grâce à qui j'ai pu développer ma double vie pendant cette dernière année : Jean-Luc Mari. Jean-Luc, merci de m'avoir suggéré la candidature en tant qu'ATER au département d'informatique. Je te dois énormément : en plus d'avoir eu un plaisir fou à pouvoir me plonger dans les cours d'automates ou de théorie des graphes, j'ai découvert un nouveau métier, l'enseignement, que je ne m'attendais pas à apprécier autant.

Un immense merci, enfin, à mes camarades de St Charles :

En premier lieu, merci à Justine et Cécile pour avoir été mes deux comparses, complices et, bien sûr, BFF depuis mon arrivée à Marseille ! Ces trois années ont beau avoir vu passer quelques révolutions sociales, le bonheur dépend encore parfois des copines à qui l'on peut tout confier et je ne peux imaginer ce qu'aurait été le temps passé ici sans vous.

A vous deux s'ajoute la ribambelle de ceux que je considère comme une famille ici à Marseille : Matonti, Baptiste, Anne-Sabine, Vincenzo, Simon, Jouves, Lucie, Irène, Roland, Dawin, Anthony, Quentin, Geoffrey, Gabrielle, Mélody et Sébastien. Merci d'avoir créé cette ambiance que, malgré les hauts et les bas de la vie de thésarde, j'étais chaque jour impatiente de retrouver. Merci pour nos multiples pauses, pour nos débats, nos chamailleries, nos scandaaaaaales, notre joie partagée à chaque repas gastronomique au RU, nos soirées à boire des milliards de maurèkes, nos discussions sur les chats, nos discussions sur les fonctions primitives du corps humain et les sanitaires autrichiens, merci pour Périlithon, pour les aventures spéléologiques, pour les initiations footballistiques, pour votre humour, vos sketch, votre second degré, pour avoir résisté à la guillémisation, merci d'avoir pris soin des copains du tiroir, de m'avoir abreuvé de Paulaner, d'avoir chanté le 12 mars, de m'avoir suivi à l'opéra… Merci, enfin, de m'avoir adoptée dès le premier jour et de ne pas avoir changé depuis ! J'ajoute un merci à vous tous pour Ernesto, Pixel, Décibelle, Jon, Link, Zelda, Treize, Philaé, Ouranos, Ebène, Vachette et Philippe qui sont bien heureux que, entrainée par Cécile, notre génération de thésards ait montré qu'il est possible de révolutionner la science tout en vidant les refuges animaliers.

Pour terminer cette liste St Charlienne, il me reste à remercier quelques personnes de plus. Jean Borgomano, après trois années à travailler face à ton portrait, je fus bien contente de voir la légende se matérialiser. Merci d'être si naturellement attentif à tous les habitants du laboratoire. Tu es parfaitement à la hauteur du mythe qui s'est construit en ton absence ! Juliette Lamarche, je te suis reconnaissante pour les quelques fois où je suis allée te demander de l'aide. Merci d'avoir su, à ces occasions, m'apporter de justes conseils sur les aspects sociaux du monde de la recherche. Enfin, je termine avec Jocelyne Turiello, notre Tata à tous. Joss, merci pour ta présence jour après jour, pour ton accent chantant et pour les surnoms affectueux que tu nous as donnés.

Pour finir, je remercie mes parents parce que ce sont les meilleurs du monde, Mathias et Charlotte, parce que ma fratrie est un des piliers fondamental de mon existence et, bien sûr, Aurélien. Aurélien, merci d'être le meilleur des coéquipiers du tourbillon de la vie et de m'avoir accompagnée à travers chaque journée de ce long travail !

INTRODUCTION GENERALE

1. Contexte scientifique

Pour le géologue, la mer de Marmara constitue un objet fascinant à plus d'un titre. L'origine de la Mer de Marmara est à chercher dans le système de failles complexes qu'elle recouvre. A la frontière entre la plaque Anatolienne et la plaque Eurasienne, la branche nord de la faille décrochante dextre Nord-Anatolienne traverse la Mer de Marmara de bout en bout. Aujourd'hui, des composantes normales, notamment au niveau de « releasing bends » sont également mesurées [*Altınok and Alpar* 2006 ; *Şengör et al.*, 2014]. Mais on soupçonne qu'une phase antérieure, principalement extensive, a créé une première ouverture de la mer de Marmara, et notamment des bassins du Sud, peu actifs aujourd'hui [*Le Pichon et al.*, 2003 ; *Gökaşan et al.*, 2003 ; *Rangin et al.*, 2004].

Par ailleurs, la situation de la Mer de Marmara, entre la Mer Méditerranée qu'elle relie par le détroit des Dardanelles, et la Mer Noire de l'autre côté du détroit du Bosphore en fait la clef de voute d'un système hydrique complexe. Si, pendant les périodes froides, le niveau de la mer a pu baisser en deçà de la profondeur du détroit des Dardanelles, transformant la Mer de Marmara et la Mer Noire en mers intérieures fermées, la Mer de Marmara constitue le reste du temps un relais actif entre la mer Noire et la Mer Méditerranée, responsable par exemple du développement périodique de sapropèles dans l'Est de la Mer Méditerranée [*Aksu et al.*, 2002]. Et les dépôts successifs de sédiments de la mer de Marmara, alternant épisodes lacustres et marins, sont à la fois les témoins de l'évolution de cet environnement si particulier et un enregistrement des variations climatiques dans la région.

Mais ces caractéristiques uniques seraient sans doute restées marginalement étudiées si la prise de conscience graduelle de l'importance du risque humain dû à la proximité de la mégalopole d'Istanbul n'avait pas provoqué la multiplication d'études en vue de l'évaluation et de la prévention des risques sismiques liés à la faille Nord-Anatolienne.

Les premières mentions éparses de tremblements de Terre dans la région de la Mer de Marmara remontent au IIIème siècle av. J.-C. [*Ambraseys*, 2002]. Mais, ce n'est qu'en 1509 qu'a lieu le premier séisme gravé dans l'histoire comme un traumatisme en raison de sa proximité avec la capitale ottomane [*Ambraseys*, 2001]. Cependant, si de nombreux séismes ont causé des dommages à la capitale, peu étaient véritablement situés sur le principal segment de la faille Nord-Anatolienne en Mer de Marmara. Le dernier séisme majeur sur ce segment pourrait être celui de 1894, mais, plus probablement, son épicentre était situé dans le bassin de

Çınarcık [*Parsons et al.,* 2004]. La dernière rupture pourrait donc remonter à 1766 ou même à 989 [*Ambraseys,* 2002]. Aujourd'hui, après le séisme de Ganos en 1912, à l'Ouest de la mer de Marmara, et le séisme de Kocaeli, ou séisme d'İzmit, en 1999 à l'Est, le segment d'Istanbul est devenu une lacune sismique faisant craindre la possibilité d'un tremblement de terre imminent de grande envergure.

En 1999, suite à cette prise de conscience et au choc international au lendemain du séisme de Kocaeli, sont lancées les premières étapes de ce qui deviendra une collaboration scientifiques internationale fructueuse, tout particulièrement entre la France et la Turquie. S'en suivront notamment la campagne Marmara à bord du bateau océanographique le Suroit en 2000, qui permit une première cartographie du système de faille, puis les campagnes Seismarmara (2001), Marmaracore (2001), Marmarascarps (2002), MarmaraVT (2004), Marnaut (2007), Marmesonet (2009) toutes opérées à bord de navires océanographiques de l'Ifremer.

La caractérisation du système de faille en Mer de Marmara est toujours un objectif de ces missions et la profusion de moyens et d'occasions ont permis de mener des études variées allant de la cartographie par relevés sismiques (réflexion, réfraction et profils 3.5 kHz) [e.g. *Laigle et al.*, 2008 ; *Bécel et al*., 2009] à l'étude de carottes de sédiment pour l'identification de turbidites provoquées par les séismes [e.g. *McHugh et al.*, 2006 ; 2014 ; *Beck et al.*, 2007] en passant par l'installation d'un observatoire sous-marin de stations géodésiques de part et d'autre de la faille pour mesurer son évolution au plus près [*Sakic et al.*, 2016]. Les missions ont aussi été l'occasion d'étudier, par exemple, les microfossiles [e.g. *Paillès et al.*, 2014], les concrétions carbonatées et les échappements gazeux [e.g. *Zitter et al.*, 2008 ; *Tryon et al.*, 2010 ; *Crémière et al*., 2013] et, plus généralement, les variations environnementales et climatiques enregistrées dans les sédiments [e.g. *Aloisi et al.*, 2015 ; *Çağatay et al.*, 2015], souvent en relation avec la mer Noire ou la Mer Méditerranée [e.g. *Vidal et al*., 2010].

Dans la continuité de ces missions, le projet de cette thèse était de s'appuyer sur les données nouvelles qui allaient être acquises durant la campagne MARSITE à bord du navire océanographique de l'Ifremer Pourquoi Pas ? en octobre 2014. Les données sismiques acquises précédemment avaient permis de proposer un modèle d'âge des sédiments de la mer de Marmara permettant indirectement de mesurer une vitesse moyenne au long terme de décrochement de la faille de Marmara [*Sorlien et al*., 2012 ; *Grall et al*.,2013]. Mais, ce modèle d'âge reposant sur des extrapolations de taux de sédimentation et des interprétations d'unités sédimentaires laissait de larges barres d'erreurs. La campagne de carottage de la mission MARSITE visait donc à atteindre les sédiments correspondant aux réflecteurs sismiques interprétés et à les dater, soit directement, soit par l'étude de l'alternance des niveaux marins et lacustres.

2. La faille Nord-Anatolienne

La faille Nord-Anatolienne est une faille décrochante continentale, l'une des plus longues du monde, et les séismes qu'elle provoque atteignent régulièrement des magnitudes de 7 sur l'échelle de Richter. De son extrémité Est dans les hauts plateaux Anatoliens à son extrémité Ouest à l'aplomb des côtes grecques, elle s'étend sur plus de 1200 km le long de la limite transformante entre les plaques Anatolienne et Eurasienne. Au niveau de la Mer de Marmara, la branche principale, aussi appelée faille de Marmara, passe à 20 km au Sud d'Istanbul.

La faille Nord-Anatolienne accommode l'échappement vers l'Ouest, en une rotation antihoraire, de la plaque Anatolienne, poussée au Sud-Est par l'indentation de la plaque Arabique et tirée au Sud-Ouest par le recul de la zone de subduction hellénique (voir Figure 1). Au niveau de la péninsule des Balkans, la déformation se transmet sur une large région, distribuant la contrainte décrochante jusqu'à la zone de subduction hellénique [*Şengör,* 1979].

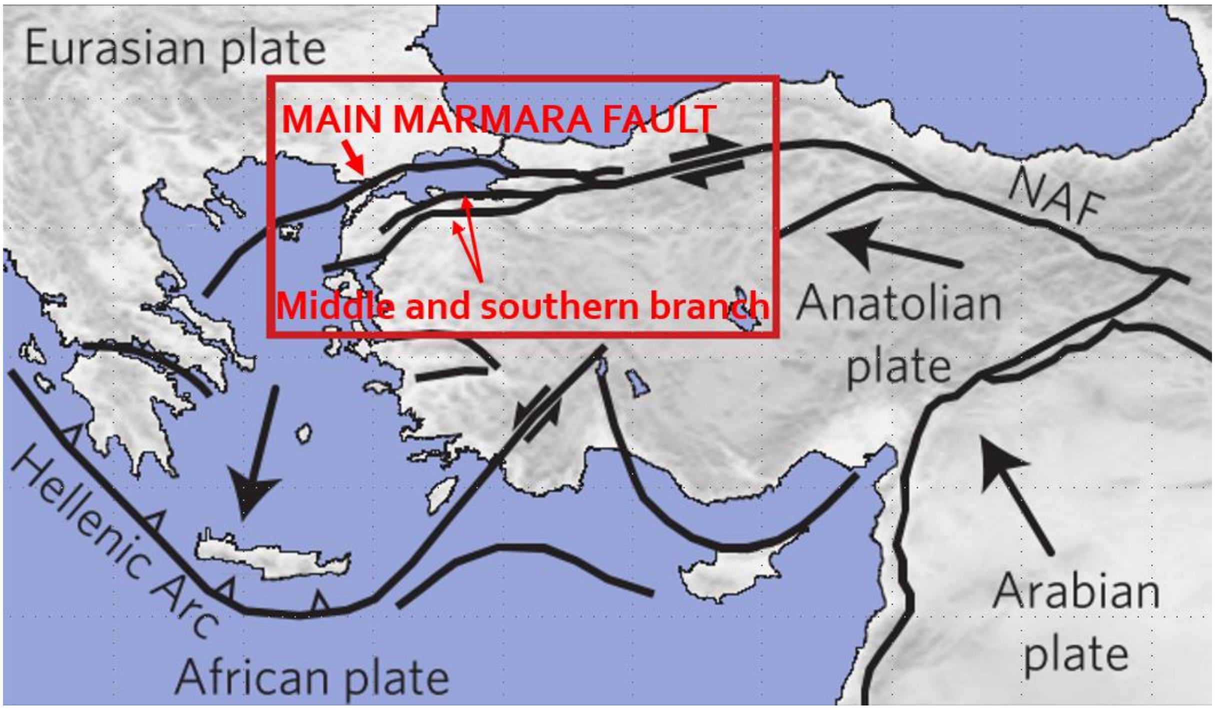

Figure 1. Contexte tectonique actuel de la faille Nord-Anatolienne. Figure modifiée de [Hergert & Heidbach, 2010]

Provoquée par la collision des plaques arabique et africaine avec la plaque eurasienne, la propagation de la faille Nord-Anatolienne à travers l'Anatolie et la mer de Marmara aurait démarré à l'Est à la fin du Miocène [*Şengör*, 1979 ; 2004 ; *Yilmaz et al.*, 1993], et se serait propagée vers l’Ouest en suivant la zone de suture Intra-Pontide [*Şengör et Yılmaz*, 1981 ; *Şengör et al.*, 2004].

Le mouvement relatif dextre de la faille est aujourd’hui bien contraint entre 20 et 27 mm/an par les études GPS [*McClusky et al.*, 2000; *Reilinger et al.*, 2006 ; *Hergert and Heidbach*, 2010]. Cependant, des incertitudes existent toujours quant au mouvement dextre total depuis la formation de la faille avec des estimations allant de 35 à 100 km [*Armijo et al.*, 1999 ; *Hubert-Ferrari et al.*, 2002 ; *Akbayram et al.*, 2016]. Si les décalages mesurés sur les structures géologiques concordent généralement, la source principale d’incertitude réside dans la détermination de l’époque précise depuis laquelle les décalages sont le fait des déplacements le long de la Faille Nord Anatolienne et non le fait de mouvements précoces dans la zone de déformation associée à la faille.

3. La Mer de Marmara – un complexe tectonique ancien et actif

A l’Ouest du Golf d’İzmit, la branche principale de la faille Nord-Anatolienne devient sous-marine et plonge sous la mer de Marmara, une mer de 170 km de long, 70 km de large et dont la profondeur maximale dépasse les 1300 m.

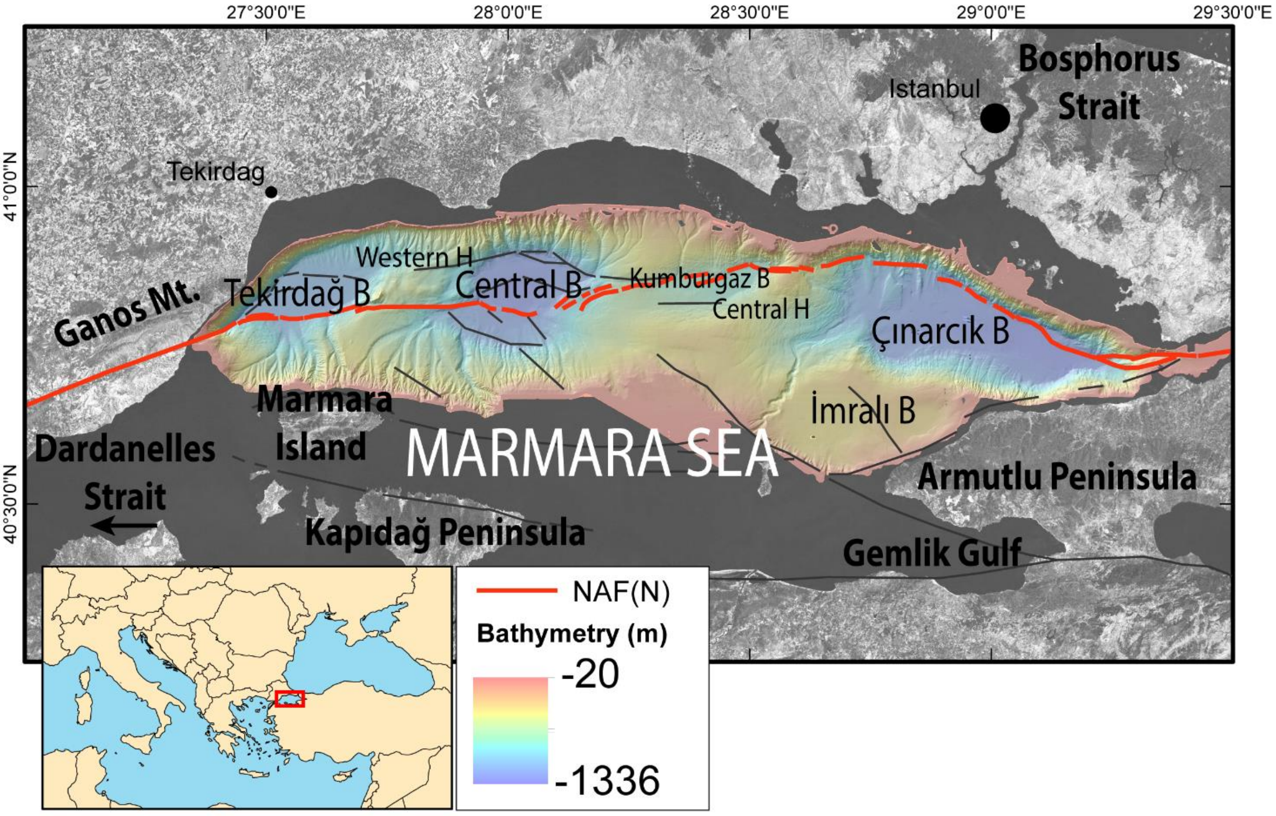

Figure 2. Contexte géographique et contexte géologique simplifié de la Mer de Marmara. B : Bassin, H : High (ou haut topographique). La cartographie simplifiée du système de faille

est modifiée de Şengör et al. [2014] et Hergert et Heidbach [2011]. Les données bathymétriques proviennent du relevé « EM300 multibeam ».

La mer de Marmara est constituée de plusieurs zones de subsidences creusées par l'extension subie par la région depuis plusieurs millions d'années [*Grall et al.*, 2012]. La construction graduelle du bassin global a créé une géométrie asymétrique avec un large plateau au Sud et un mince plateau au Nord. Entre les deux, les trois bassins principaux de Tekirdağ, Central et Çınarcık sont séparés par le Haut Ouest et le Haut Central. Au Sud des bassins profonds, des dépressions correspondent à des bassins sédimentaires actuellement affectés d'une subsidence moins rapide, comme le bassin d'İmralı, marqué par un canyon incisant profondément la bathymétrie.

Si l'ouverture des bassins sud a pu se faire majoritairement sous l'effet de contraintes extensives liées à des détachements [*Bécel et al.*, 2009], la géométrie des trois bassins principaux correspond au jeu de la faille Nord-Anatolienne telle qu'elle fonctionne encore actuellement. Le bassin Central présente une architecture typique de Pull-apart de relais au sens de *Biddle & Christie-Blick* [1983] avec des failles en échelon et une structure « en fleur » à l'est [*Armijo et al.*, 2002]. Le bassin de Çınarcık s'ouvre sous l'effet du jeu du « releasing bend » d'Istanbul [*Kurt et al.*, 2013, *Seeber et al.*, 2004] et le bassin de Tekirdağ est un demi graben bordé par des failles secondaires à l'ouest et au nord [*McHugh et al.*, 2006 *Seeber et al.*, 2004].

En profondeur (voir Figure 3), d'après la distribution de la sismicité, les failles multiples se rejoindraient à environ 10 km pour se propager à la verticale [*Karabulut et al.*, 2002 ; *Données de l'observatoire de Kandilli*] jusqu'à une profondeur de 15 à 20 km, profondeur de la limite entre croûte supérieure et inférieure [*Schmittbuhl et al.*, 2016]. La topographie du manteau, intégrée dans la Figure 3, fait l'objet du premier chapitre de ce manuscrit.

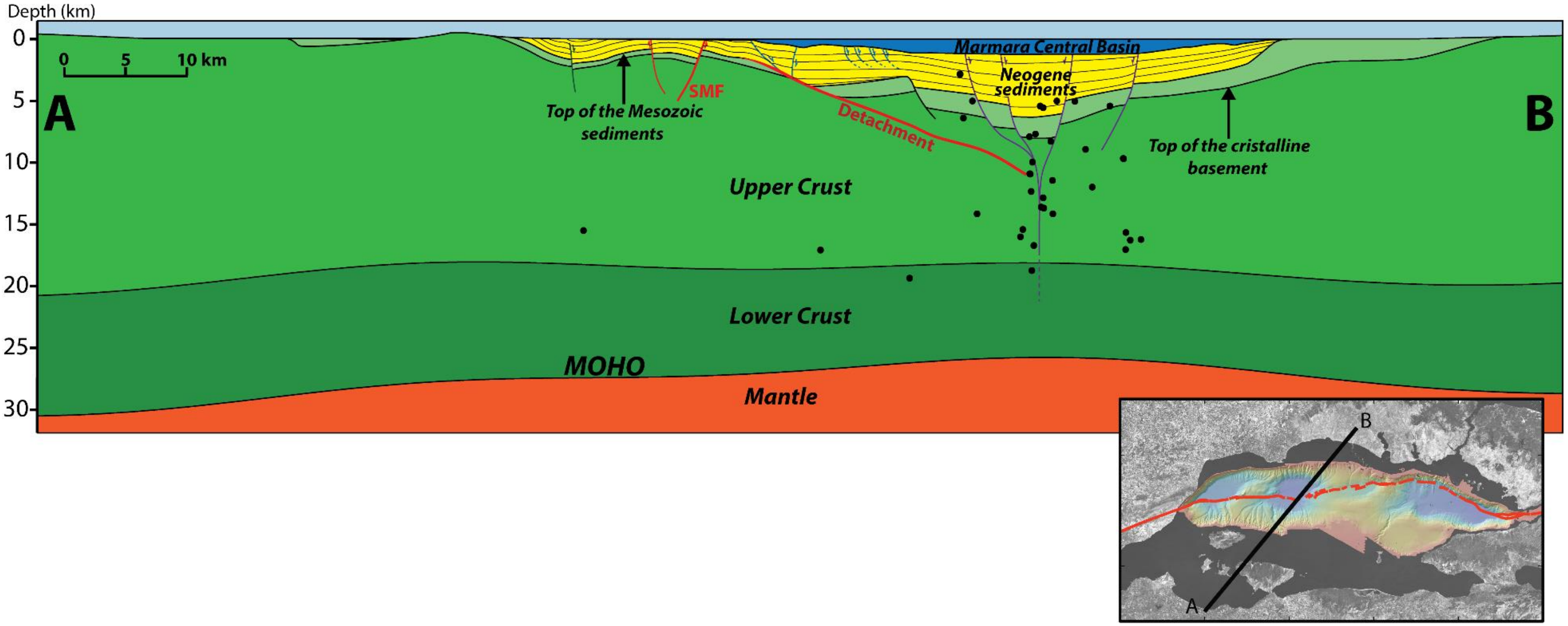

Figure 3 : Coupe de la structure interne de la mer de Marmara. Figure de [Le Pichon et al., 2015]

4. La Mer de Marmara – hydrologie actuelle et variations passées

La Mer de Marmara est une mer intracontinentale connectée à la Mer Méditerranée à l'ouest par le détroit des Dardanelles et à la Mer Noire à l'est par le détroit du Bosphore. Actuellement, le seuil du détroit des Dardanelles se situe à une profondeur de 65 m et celui du Bosphore à 35 m. Les échanges hydriques, à l'Est comme à l'Ouest, se font sur deux niveaux (voir Figure 4) [*Özsoy et al.*, 1996 ; *Aksu et al.*, 2002]. A la surface, une eau froide et peu salée en provenance de la Mer Noire coule vers la Mer Méditerranée et forme la masse d'eau supérieure de la Mer de Marmara ainsi que d'une petite partie de la Mer Égée à proximité des Dardanelles. Sous cette masse superficielle de 20 à 30 m, l'eau fortement salée et plus chaude de la Mer Méditerranée occupe la grande majorité du volume de la Mer de Marmara et est transportée en profondeur jusqu'à la Mer Noire [*Özsoy et al.*, 1996 ; *Aksu et al.*, 2002].

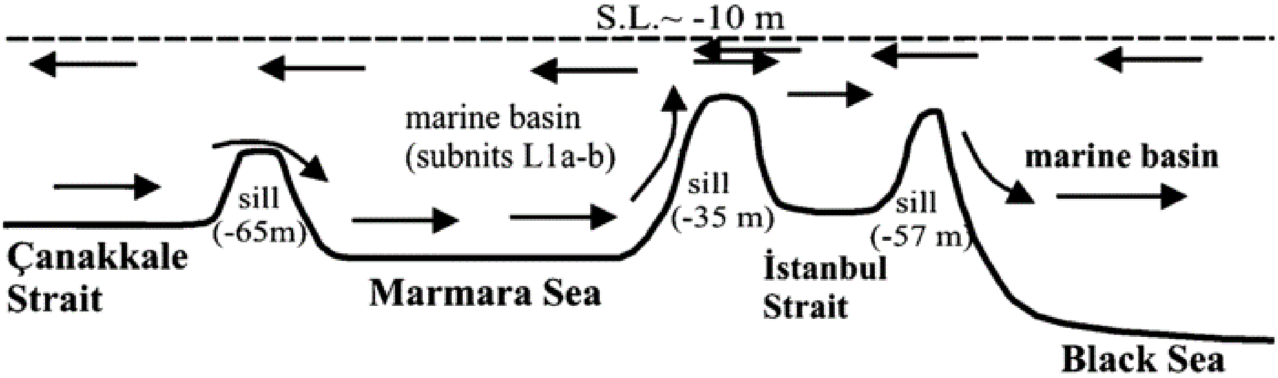

Figure 4. Flux hydrique et bathymétrie approximative des détroits autour de la Mer de Marmara depuis environ 4.5 ka. Figure de Eriş et al. [2010].

Mais cette circulation ne constitue qu'une situation temporaire en Mer de Marmara. En effet, la faible profondeur du détroit des Dardanelles et du détroit du Bosphore induit que, lors des périodes glaciaires, le niveau marin peut baisser sous le Bosphore, isolant la Mer Noire, puis sous le niveau des Dardanelles et provoquer ainsi la déconnection de la mer de Marmara de l'Océan Global [e.g. *Vidal et al.*, 2010 ; *Soulet et al.*, 2011 ; *Çağatay et al.*, 2015]. L'alternance des cycles glaciaux-eustatiques à l'échelle de 100 ka se répercutent donc, en Mer de Marmara, par une alternance de périodes marines et lacustres, visibles à travers des variations de géométries et de natures des dépôts sédimentaires [*Sorlien et al.*, 2012, *Kurt et al.*, 2013; *Grall et al.*, 2013, *Grall et al.*, 2014].

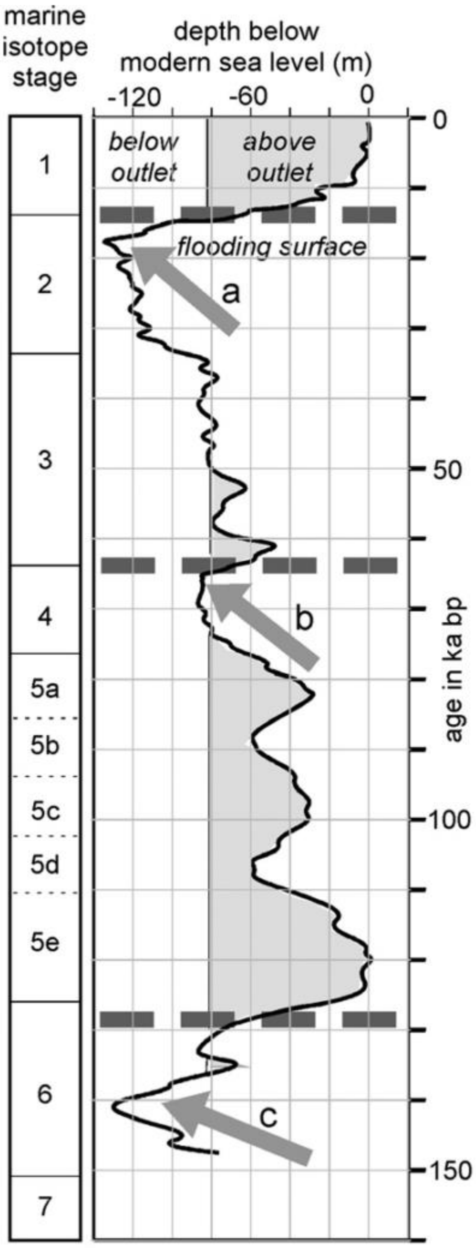

Figure 5. Illustration de l'alternance des périodes lacustres et marines au cours des derniers 150 ka. Figure de Çağatay et al. [2009]

Cependant, parce que la fermeture de la Mer de Marmara dépend à la fois des variations du niveau marin et des variations de la profondeur du seuil des Dardanelles, il est peu probable que chaque cycle de 100 ka ait été associé à une période lacustre [*Çağatay et al.,* 2009 ; *Badertscher et al.,* 2011]. Des périodes intermédiaires ont régulièrement existé. Lorsque la connexion avec la Mer Méditerranée était moins importante que celle d'aujourd'hui, un système hydrique profondément différent, limitant davantage la circulation en provenance de la mer Méditerranée, a pu s'établir.

5. Motivations

L'élaboration de scénarios possibles pour les futurs séismes affectant la région d'Istanbul s'appuie sur l'étude de la sismicité historique [e.g. *Ambraseys & Jackson*, 2000 ; *Ambraseys* 2002], sur la localisation et les mécanismes au foyer de la sismicité enregistrée [e.g. *Karabulut et al.*, 2002 ; *Schmittbuhl et al*., 2016], sur la cartographie des failles actives et l'estimation des taux de déplacement géologiques [e.g. *Armijo et al.,* 1999 ; *Hubert-Ferrari et al.,* 2002 ; *Şengör et al., 2014* ; *Akbayram et al.,* 2016], sur la géodésie, basée principalement sur les données terrestres (GPS, SAR) [e.g. *Provost et al.,* 2003 ; *Reilinger et al.,* 2006 ; *Özeren & Holt,* 2010 ; *Ergintav et al.,* 2014] et, depuis peu, sur des expériences de géodésie sous-marine [*Sakic et al.,* 2016].

Cependant, de nombreuses questions restent en suspens. Celle faisant peser le plus de pression sur la communauté scientifique est de savoir si les segments de la faille de Marmara sont actuellement bloqués ou bien si un glissement lent des deux blocs relâche une partie de la contrainte accumulée. L'installation du réseau d'observatoire géodésique sous-marin vise précisément à répondre à cette question [*Sakic et al.,* 2016]. Mais des éclaircissements sur les relations des structures géologiques à plusieurs échelles dans la région et sur leur évolution dans le temps apporteraient également des données complémentaires utiles pour l'amélioration des modèles.

Parmi les questions de sismotectonique en suspens, on peut citer :

- Quel est le lien entre l'étendue des ruptures sismiques, la géométrie des failles et la structure crustale ? La structure crustale intervient-elle dans la segmentation de la faille de Marmara ? La profondeur du point de Curie [*Aydin et al.,* 2005] ainsi que des données sismiques [*Bécel et al.,* 2009 ; *Karabulut et al.,* 2013] suggèrent un amincissement de la croute sous la mer de Marmara, mais les détails de la relation entre cette structure et le système de faille restent à déterminer.
- Quelles sont les échelles de temps à considérer pour l'évolution géologique du système de faille actuel en Mer de Marmara ? A ce jour, des modèles de régime permanant depuis l'ouverture de la mer de Marmara jusqu'à aujourd'hui ont été proposés [*Armijo et al.,* 2002 ; *Seeber et al.,* 2004] aussi bien que des modèles suggérant une incursion de la faille Nord-Anatolienne dans un système extensif préexistant [*Le Pichon et al.,* 2003 ; *Gökaşan et al.,* 2003 ; *Rangin et al.,* 2004].
- Quelle est la quantité d'extension et quelle est sa distribution ? Comment influe-t-elle sur la structure crustale et la segmentation ? Plusieurs études suggèrent l'existence d'un

système extensif antérieur à l'accommodation de l'échappement Anatolien par l'incursion de la faille Nord-Anatolienne en mer de Marmara [*Le Pichon et al.*, 2003 ; *Gökaşan et al.*, 2003 ; *Rangin et al.*, 2004]. Or, si la croûte était déjà déformée et amincie par un système extensif préexistant avant l'incursion de la faille de Marmara, cela a pu déterminer les modalités de la propagation de la faille et de la construction de ses différents segments.

- Comment réconcilier les estimations de vitesses de glissement effectuées à diverses échelles de temps ? Les estimations proposées se basent sur des mesures GPS, des études de tranchées de failles, des décalages post-glaciaux et sur des décalages de structures datés par interprétation stratigraphique. Or, cette dernière méthode, la seule à permettre des estimations de vitesse sur le long terme, repose sur des estimations d'âges d'horizons sismiques faites par extrapolation du taux de sédimentation moyen des 40 000 dernières années [*Vidal et al.*, 2010 ; *Grall et al.*, 2013 ; *Sorlien et al.*, 2012].

Concernant ce dernier point, la paléo-océanographie pourrait permettre une avancée. En effet, la succession des dépôts lacustres et marins est utilisée pour les interprétations stratigraphiques en considérant les alternances observées corrélées avec les cycles glacio-eustatiques de 100 ka [*Grall et al.*, 2013]. Cependant, l'application de cette hypothèse demande une connaissance poussée des évolutions paléo-océanographiques en mer de Marmara. Par exemple, si des preuves de variations de la profondeur des Dardanelles et du Bosphore ont été exposées [*Yaltirak et al.*, 2002 ; *Gökaşan et al.*, 2008 ; *Çağatay et al.*, 2009 ; *Soulet et al.*, 2011], les connaissances restent incertaines et se limitent à la dernière période glaciaire. Or, des variations majeures pendant les cycles précédents pourraient impliquer un système hydrique complètement différent de ce qui est observé depuis le dernier interglaciaire et, donc, des dépôts sédimentaires également différents. Sans possibilité de dater directement les sédiments, la validation de l'interprétation des séquences sédimentaires en relation avec les cycles glacio-eustatiques nécessite donc des progrès dans la connaissance de l'évolution paléo-océanographique de la mer de Marmara. A l'inverse, la connaissance des variations des conditions paléo-environnementales en Mer de Marmara et la datation des transitions pourraient nous aider à contraindre les variations glacio-eustatiques globales.

Enfin, certaines questions sont directement à la croisée de la tectonique et de la paléo-océanographie. L'activité sismique en Mer de Marmara est à l'origine de glissements de terrains sous-marins, de tsunamis, et de dépôts de coulées de débris et de turbidites-homogénites [*Gasperini et al.*, 2011 ; *McHugh et al.*, 2014]. Or, certaines périodes semblent avoir été plus propices aux instabilités de pente [*Grall et al.*, 2014] ce qui pourrait être lié au cycle glacioeustatique. De plus, la variabilité de la profondeur des seuils des détroits de part et d'autre de la mer de Marmara pourrait être, au moins partiellement, liée aux mouvements tectoniques.

Le travail présenté dans cette thèse aborde plusieurs de ces questions sous divers angles.

Tout d'abord, nous présentons une étude visant à préciser la géométrie 3D du Moho par modélisation gravimétrique afin de déterminer la distribution de l'extension crustale et de la quantifier. Ceci dans le but de montrer les relations possibles entre l'extension géologique, les variations spatiales d'épaisseur crustale et les caractéristiques actuelles du réseau de failles.

Dans un deuxième temps, nous avons cherché à caractériser et dater précisément le réflecteur H1 « rouge » corrélé en sismique HR sur l'ensemble de la Mer de Marmara et atteint par carottage lors de la campagne MARSITE. Ce réflecteur, attribué au début du stade MIS 5 [*Sorlien et al.*, 2012 ; *Grall et al.*, 2013], est le plus récent sur lequel s'appuient les modèles d'âges. Les méthodes employées pour le caractériser et le dater vont de la sédimentologie à la géophysique avec un large rôle de la paléo- océanographie pour l'interprétation des variations stratigraphiques et permettent de proposer une évaluation critique des interprétations des séquences sédimentaires et des modèles d'âge proposés en Mer de Marmara.

6. Organisation du manuscrit

Le premier chapitre présente une étude visant à établir comment, dans un système actuellement majoritairement cisaillant, des bassins extensifs ont pu se former et si les taux d'extension ont beaucoup varié au cours du temps. L'extension depuis le début de la formation de la Mer de Marmara est quantifiée par comparaison de la géométrie du volume de croûte terrestre avant et après la déformation. Pour établir le volume de croûte dans la région de la mer de Marmara, nous présentons une méthode basée sur l'équation de Parker et contrainte par des études géophysiques variées afin d'inverser le champ d'anomalie de gravité corrigé de l'influence des bassins sédimentaires. La comparaison des taux de déformation extensive depuis l'ouverture de la Mer de Marmara et des vitesses actuellement mesurées suggère que l'extension dans la région a pu être stable ou seulement légèrement décroître depuis 5 Ma. L'incursion de la faille Nord-Anatolienne aurait redistribué la déformation extensive en superposant un système cisaillant dominant à un régime de contrainte extensif préexistant. L'étude de la géométrie du volume défini par le bas des bassins sédimentaires et le Moho permet aussi d'établir l'existence de mouvements ductiles modérés dans la croûte inférieure qui exercent un rôle dans la répartition de la déformation et la distribution de l'amincissement de la croûte sous les bassins.

Le deuxième chapitre porte sur la problématique de l'estimation de la vitesse de mouvement de la faille Nord-Anatolienne à l'échelle d'environ 500 ka. Prouver une continuité entre les mesures GPS actuelles et les taux passés permettrait de soutenir la possibilité d'extrapoler les uns et les autres. Cependant, les seules estimations actuelles de la vitesse de décrochement moyenne sur la faille de Marmara sur le long terme (environ 500 ka) reposent sur l'étude de la migration du dépocentre du bassin de Cinarcik [*Kurt et al.*, 2013] et sur l'observation d'un complexe de glissements de terrain déposé de part et d'autre de la faille et donc divisé en deux blocs s'écartant graduellement l'un de l'autre [*Grall et al.*, 2013]. Les vitesses sont données par les décalages mesurés et par les âges de l'horizon sismique marquant le plus vieux dépocentre observé, dans le premier cas, et de l'horizon sismique sous-jacent au glissement de terrain, dans le deuxième cas. Or, ces âges sont des estimations reposant principalement sur l'extrapolation de taux de sédimentation sur les derniers 40.000 ans. Ce chapitre présente en détail les bases des modèles d'âges estimatifs des sédiments en Mer de Marmara et précise comment la campagne en mer MARSITE visait à atteindre des horizons sismiques anciens afin de vérifier directement la validité des extrapolations des modèles. Nous montrons également comment la compréhension et l'interprétation de la stratigraphie nécessite la combinaison d'une approche géophysique et paléo-environnementale. Enfin, nous présentons les premiers résultats de cette mission ainsi que les conclusions apportées par l'identification et la datation du premier réflecteur principal utilisé dans les différents modèles d'âge : le « rouge » H1.

Le troisième Chapitre détaille l'étude paléo-environnementale menée sur la carotte MRS-CS-22 prélevée lors de la mission MARSITE à bord du « Pourquoi Pas ? ». Cette étude s'appuie sur l'observation de variations chimiques et faunistiques elles-mêmes expliquées par l'alternance des périodes marines et lacustres en mer de Marmara. A ces proxys paléo-environnementaux s'ajoutent l'étude des enregistrements d'événements globaux, tels que des excursions magnétiques, ou régionaux, tels que des éruptions volcaniques. La somme de ces différents indices permet de définir un modèle d'âge qui date les réflecteurs sismiques traversés par la carotte. Le plus important d'entre eux est le réflecteur « rouge » H1 qui définit la première limite de séquence stratigraphique en mer de Marmara [*Sorlien et al.*, 2012]. Cette étude, combinant géophysique et indicateurs paléo environnementaux, permet une détermination directe de l'âge des séquences sédimentaires en mer de Marmara.

En Annexe, sont présentés les scripts MATLAB écrits pour le premier et le troisième chapitre, ainsi qu'un article auquel j'ai participé. Cet article intègre le modèle crustal développé dans le Chapitre I parmi les preuves de l'existence passée d'un stade extensif pur en Mer de Marmara, avant l'incursion de la faille Nord-Anatolienne.

Références

Akbayram, K., Sorlien, C. C., & Okay, A. I. (2016). Evidence for a minimum 52 ± 1 km of total offset along the northern branch of the North Anatolian Fault in northwest Turkey. *Tectonophysics, 668–669*, 35–41. http://doi.org/10.1016/j.tecto.2015.11.026

Aksu, A. E., Hiscott, R. N., Kaminski, M. A., Mudie, P. J., Gillespie, H., Abrajano, T., & Dogan, Y. (2002). Last glacial-Holocene paleoceanography of the Black Sea and Marmara Sea : stable isotopic , foraminiferal and coccolith evidence. *International Journal of Marine Geology, Geochemistry and Geophysics*, 190, 119–149.

Aloisi, G., Soulet, G., Henry, P., Wallmann, K., Sauvestre, R., Vallet-Coulomb, C., … Bard, E. (2015). Freshening of the Marmara Sea prior to its post-glacial reconnection to the Mediterranean Sea. *Earth and Planetary Science Letters*, 413, 176–185. http://doi.org/10.1016/j.epsl.2014.12.052

Altınok, Y., & Alpar, B. (2006). Marmara Island earthquakes , of 1265 and 1935 ; Turkey. *Natural Hazards and Earth System Science*, 6, 999–1006.

Ambraseys, N. N., & Jackson, J. a. (2000). Seismicity of the Sea of Marmara (Turkey) since 1500. *Geophysical Journal International*, *141*(3), F1–F6. http://doi.org/10.1046/j.1365-246x.2000.00137.x

Ambraseys, N. N. (2001). The earthquake of 1509 in the sea of Marmara, Turkey, revisited. *Bulletin of the Seismological Society of America*, 91(6), 1397–1416. http://doi.org/10.1785/0120000305

Ambraseys, N. (2002). The Seismic Activity of the Marmara Sea Region over the Last 2000 Years. *Bulletin of the Seismological Society of America*, *92*(1), 1–18.

Armijo, R., Meyer, B., Hubert, A., & Barka, A. (1999). Westward propagation of the North Anatolian fault into the northern Aegean: Timing and kinematics. *Geology*. http://doi.org/10.1130/0091-7613(1999)027<0267:WPOTNA>2.3.CO;2

Armijo, R., Meyer, B., Navarro, S., King, G., & Barka, A. (2002). Asymmetric slip partitioning in the Sea of Marmara pull-apart: a clue to propagation processes of the North Anatolian Fault? *Terra Nova*, *14*(2), 80–86. http://doi.org/10.1046/j.1365-3121.2002.00397.x

Aydin, I., Karat, H. I., & Koçak, A. (2005). Curie-point depth map of Turkey. *Geophysical Journal International*, *162*, 633–640. http://doi.org/10.1111/j.1365-246X.2005.02617.x

Badertscher, S., Fleitmann, D., Cheng, H., Edwards, R. L., Göktürk, O. M., Zumbühl, a., … Tüysüz, O. (2011). Pleistocene water intrusions from the Mediterranean and Caspian seas into the Black Sea. *Nature Geoscience*, *4*(4), 236–239. http://doi.org/10.1038/ngeo1106

Bécel, A., Laigle, M., de Voogd, B., Hirn, A., Taymaz, T., Galvé, A., … Özalaybey, S. (2009). Moho, crustal architecture and deep deformation under the North Marmara Trough, from the

SEISMARMARA Leg 1 offshore–onshore reflection–refraction survey. *Tectonophysics*, 467(1–4), 1–21. http://doi.org/10.1016/j.tecto.2008.10.022

Beck, C., Mercier de Lépinay, B., Schneider, J.-L., Cremer, M., Çağatay, M. N., Wendenbaum, E., … Jaouen, A. (2007). Late Quaternary co-seismic sedimentation in the Sea of Marmara's deep basins. *Sedimentary Geology*, 199(1–2), 65–89. http://doi.org/10.1016/j.sedgeo.2005.12.031

Biddle, K. T., & Christie-Blick, N. (1985). Glossary - Strike-slip deformation, basin formation, and sedimentation. Special Publication of the Society of Economic Paleontologists and Mineralogists, 375–386.

Çağatay, M. N., Eriş, K., Ryan, W. B. F., Sancar, Ü., Polonia, A., Akçer, S., … Bard, E. (2009). Late Pleistocene–Holocene evolution of the northern shelf of the Sea of Marmara. *Marine Geology*, *265*(3–4), 87–100. http://doi.org/10.1016/j.margeo.2009.06.011

Çağatay, M. N., Wulf, S., Sancar, Ü., Vidal, L., Henry, P., Appelt, O., & Gasperini, L. (2015). The tephra record from the Sea of Marmara for the last ca . 70 ka and its palaeoceanographic implications. *Marine Geology*, 361, 96–110. http://doi.org/10.1016/j.margeo.2015.01.005

Crémière, A., Bayon, G., Ponzevera, E., & Pierre, C. (2013). Paleo-environmental controls on cold seep carbonate authigenesis in the Sea of Marmara. *Earth and Planetary Science Letters*, *376*, 200–211. http://doi.org/10.1016/j.epsl.2013.06.029

Ergintav, S., Reilinger, R. E., Çakmak, R., Floyd, M., Çakir, Z., Doğan, U., … Özener, H. (2014). Istanbul's earthquake hot spots:Geodetic constraints on strain accumulation along faults in the Marmara seismic gap. *Geophysical Research Letters*, 1–5. http://doi.org/10.1002/2014GL060985.Received

Eriş, K. K., Çağatay, M. N., Akçer, S., Gasperini, L., & Mart, Y. (2010). Late glacial to Holocene sea-level changes in the Sea of Marmara: new evidence from high-resolution seismics and core studies. *Geo-Marine Letters*, *31*(1), 1–18. http://doi.org/10.1007/s00367-010-0211-1

Gasperini, L., Polonia, A., Çağatay, M. N., Bortoluzzi, G., & Ferrante, V. (2011). Geological slip rates along the North Anatolian Fault in the Marmara region. *Tectonics*, *30*(6). http://doi.org/10.1029/2011TC002906

Gökaşan, E., Ustaömer, T., Gazioglu, C., Yucel, Z. Y., Öztürk, K., Tur, H., … Tok, B. (2003). Morpho-tectonic evolution of the Marmara Sea inferred from multi-beam bathymetric and seismic data. *Geo-Marine Letters*, *23*(1), 19–33. http://doi.org/10.1007/s00367-003-0120-7

Gökaşan, E., Ergin, M., Özyalvaç, M., Sur, H. I., Tur, H., Görüm, T., … Özturan, M. (2008). Factors controlling the morphological evolution of the Çanakkale Strait (Dardanelles, Turkey). *Geo-Marine Letters*, *28*(2), 107–129. http://doi.org/10.1007/s00367-007-0094-y

Grall, C., Henry, P., Thomas, Y., Westbrook, G. ., Çağatay, M. N., Marsset, B., … Géli, L. (2013). Slip rate estimation along the western segment of the Main Marmara 1 Fault over the last 405-490 ka by correlating Mass Transport Deposits. *Tectonics, 32*(6), 1587–1601. http://doi.org/10.1002/2012TC003255

Grall, C., Henry, P., Westbrook, G. K., Thomas, Y., Marsset, B., Borschneck, D., … Cifc, G. (2014). Submarine Mass Movements and Their Consequences. Advances in Natural and Technological Hazards Research, 37, 595–603. http://doi.org/10.1007/978-3-319-00972-8

Hergert, T., Heidbach, O., Bécel, A., & Laigle, M. (2011). Geomechanical model of the Marmara Sea region-I. 3-D contemporary kinematics. *Geophysical Journal International*, *185*(3), 1073–1089. http://doi.org/10.1111/j.1365-246X.2011.04991.x

Hubert-Ferrari, A., Armijo, R., Geoffrey, K., Meyer, B., & Barka, A. (2002). Morphology, displacement, and slip rates along the North Anatolian Fault, Turkey. *Journal of Geophysical Research, 107*(B10), 2235. http://doi.org/10.1029/2001JB000393

Laigle, M., Bécel, A., de Voogd, B., Hirn, A., Taymaz, T., & Ozalaybey, S. (2008). A first deep seismic survey in the Sea of Marmara: Deep basins and whole crust architecture and evolution. *Earth and Planetary Science Letters*, 270(3–4), 168–179. http://doi.org/10.1016/j.epsl.2008.02.031

Karabulut, H., Bouin, M., Bouchon, M., & Dietrich, M. (2002). The Seismicity in the Eastern Marmara Sea after the 17 August 1999 Izmit Earthquake. *Bulletin of the Seismological Society of America*, *92*(1), 387–393. http://doi.org/10.1785/0120000820

Karabulut, H., Paul, A., Afacan Ergun, T., Hatzfeld, D., Childs, D. M., & Aktar, M. (2013). Long-wavelength undulations of the seismic Moho beneath the strongly stretched Western Anatolia. *Geophysical Journal International*, *194*(1), 450–464. http://doi.org/10.1093/gji/ggt100

Kurt, H., Sorlien, C. C., Seeber, L., Steckler, M. S., Shillington, D. J., Cifci, G., … Carton, H. (2013). Steady late quaternary slip rate on the Cinarcik section of the North Anatolian fault near Istanbul, Turkey. *Geophysical Research Letters, 40,* 4555–4559. http://doi.org/10.1002/grl.50882

Le Pichon, X., Chamot-Rooke, N., Rangin, C., & Şengör, A. M. C. (2003). The North Anatolian fault in the Sea of Marmara. *Journal of Geophysical Research, 108*(B4), 1–20. http://doi.org/10.1029/2002JB001862

Le Pichon, X., Şengör, A. M. C., Kende, J., İmren, C., Henry, P., Grall, C., & Karabulut, H. (2015). Propagation of a strike-slip plate boundary within an extensional environment : the westward propagation of the North Anatolian Fault . *Canadian Journal of Earth Sciences, 53*. http://doi.org/10.1139/cjes-2015-0129

Mcclusky, S., Balassanian, S., Barka, A., Demir, C., Ergintav, S., Georgiev, I., … Tealeb, A. (2000). Global Positioning System constraints on plate kinematics and dynamics in the eastern Mediterranean and Caucasus. *Journal of Geophysical Research, 105*(B3), 5695–5719.

McHugh, C. M. G., Seeber, L., Cormier, M., Dutton, J., Çağatay, M. N., Polonia, A., … Gorur, N. (2006). Submarine earthquake geology along the North Anatolia Fault in the Marmara Sea, Turkey: A model for transform basin sedimentation. *Earth and Planetary Science Letters*, 248(3–4), 661–684. http://doi.org/10.1016/j.epsl.2006.05.038

McHugh, C. M. G., Braudy, N., Çağatay, M. N., Sorlien, C., Cormier, M. H., Seeber, L., & Henry, P. (2014). Seafloor fault ruptures along the North Anatolia Fault in the Marmara Sea, Turkey: Link with the adjacent basin turbidite record. *Marine Geology*, 353, 65–83. http://doi.org/10.1016/j.margeo.2014.03.005

Özeren, M. S., & Holt, W. E. (2010). The dynamics of the eastern Mediterranean and eastern Turkey. *Geophysical Journal International*, *183*(3), 1165–1184. http://doi.org/10.1111/j.1365-246X.2010.04819.x

Özsoy, E., Latif, M. A., Sur, H. I., & Goryachkin, Y. (1996). A review of the exchange flow regime and mixing in the Bosphorus Strait. *Bulletin de l'Institut Océanographique*, *17*(1996), 187–204. Retrieved from http://cat.inist.fr/?aModele=afficheN&cpsidt=3101944

Paillès, C., Poulin, M., Boudouma, O., Pierre, C., Paddock, M., & Cleve, T. (2014). Entomoneis calixasini sp . nov ., a new fossil diatom from the Turkish Marmara Sea sediments. *Diatom Research*, 29(4), 411–422. http://doi.org/10.1080/0269249X.2014.921645

Parsons, T. (2004). Recalculated probability of M ≥ 7 earthquakes beneath the Sea of Marmara, Turkey. *Journal of Geophysical Research*, *109*(B5), B05304. http://doi.org/10.1029/2003JB002667

Provost, A.-S., Chéry, J., & Hassani, R. (2003). 3D mechanical modeling of the GPS velocity field along the North Anatolian fault. *Earth and Planetary Science Letters*, *209*(3–4), 361–377. http://doi.org/10.1016/S0012-821X(03)00099-2

Rangin, C., Le Pichon, X., Demirbag, E., & Imren, C. (2004). Strain localization in the Sea of Marmara: Propagation of the North Anatolian Fault in a now inactive pull-apart. *Tectonics*, *23*(2), n/a-n/a. http://doi.org/10.1029/2002TC001437

Reilinger, R., McClusky, S., Vernant, P., Lawrence, S., Ergintav, S., Cakmak, R., … Karam, G. (2006). GPS constraints on continental deformation in the Africa-Arabia-Eurasia continental collision zone and implications for the dynamics of plate interactions. *Journal of Geophysical Research*, *111*(B5), B05411. http://doi.org/10.1029/2005JB004051

Sakic, P., Piété, H., Ballu, V., Royer, J. Y., Kopp, H., Lange, D., … Deschamps, A. (2016). No significant steady state surface creep along the North Anatolian Fault offshore Istanbul: Results of 6 months of seafloor acoustic ranging. *Geophysical Research Letters*, 43(13), 6817–6825. http://doi.org/10.1002/2016GL069600

Schmittbuhl, J., Karabulut, H., Lengliné, O., & Bouchon, M. (2016). Seismicity distribution and locking depth along the Main Marmara Fault, Turkey. *Geochemistry, Geophysics, Geosystems*, *17*(3), 954–965. http://doi.org/10.1002/2015GC006120

Seeber, L., Emre, O., Cormier, M.-H., Sorlien, C. C., McHugh, C. M. G., Polonia, A., … Çağatay, M. N. (2004). Uplift and subsidence from oblique slip: the Ganos–Marmara bend of the North Anatolian Transform, western Turkey. *Tectonophysics, 391*(1–4), 239–258. http://doi.org/10.1016/j.tecto.2004.07.015

Şengör, A. M. . (1979). The North Anatolian transform fault: its age, offset and tectonic significance. *Journal of the Geological Society, 366*(November 1939), 269–282. http://doi.org/10.1144/gsjgs.136.3.0269

Şengör, A. M. C., & Yılmaz, Y. (1981). Tethyan evolution of Turkey: A plate tectonic approach. *Tectonophysics*, *75*(3–4), 181–241. http://doi.org/10.1016/0040-1951(81)90275-4

Şengör, A. M. ., Tüysüz, O., Imren, C., Sakınç, M., Eyidoğan, H., Görür, N., … Rangin, C. (2004). The North Anatolian Fault: A new look. *Annual Review of Earth and Planetary Sciences, 33*, 37–112. http://doi.org/10.1146/annurev.earth.32.101802.120415

Şengör, A. M. C., Grall, C., Imren, C., Pichon, X. Le, Görür, N., Henry, P., … Siyako, M. (2014). The geometry of the North Anatolian transform fault in the Sea of Marmara and its temporal evolution : implications for the development of intracontinental transform faults. *Canadian Journal of Earth Sciences*, 51(February), 222–242. http://doi.org/10.1139/cjes-2013-0160

Sorlien, C. C., Akhun, S. D., Seeber, L., Steckler, M. S., Shillington, D. J., Kurt, H., … Diebold, J. B. (2012). Uniform basin growth over the last 500ka, North Anatolian Fault, Marmara Sea, Turkey. *Tectonophysics, 518–521*, 1–16. http://doi.org/10.1016/j.tecto.2011.10.006

Soulet, G., Ménot, G., Lericolais, G., & Bard, E. (2011). A revised calendar age for the last reconnection of the Black Sea to the global ocean. *Quaternary Science Reviews, 30*(9–10), 1019–1026. http://doi.org/10.1016/j.quascirev.2011.03.001

Tryon, M. D., Henry, P., Çağatay, M. N., Zitter, T. a C., Géli, L., Gasperini, L., … Grall, C. (2010). Pore fluid chemistry of the North Anatolian Fault zone in the Sea of Marmara: A diversity of sources and processes. *Geochemistry, Geophysics, Geosystems*, 11(10), 1–22. http://doi.org/10.1029/2010GC003177

Vidal, L., Ménot, G., Joly, C., Bruneton, H., Rostek, F., Çağatay, M. N., … Bard, E. (2010). Hydrology in the Sea of Marmara during the last 23 ka: Implications for timing of Black Sea connections and sapropel deposition. *Paleoceanography*, *25*(1), PA1205. http://doi.org/10.1029/2009PA001735

Yaltirak, C., Sakinç, M., Aksu, A. E., Hiscott, R. N., Galleb, B., & Ulgen, U. B. (2002). Late Pleistocene uplift history along the southwestern Marmara Sea determined from raised coastal deposits and global sea-level variations. *Marine Geology, 190*(1–2), 283–305. http://doi.org/10.1016/S0025-3227(02)00351-1

Yilmaz, Y. (1993). New evidence and model on the evolution of the southeast Anatolian orogen New evidence and model on the evolution of the southeast Anatolian orogen.

Geological Society of America Bulletin, (2), 251–271. http://doi.org/10.1130/0016-7606(1993)105<0251

Zitter, T. a. C., Henry, P., Aloisi, G., Delaygue, G., Çağatay, M. N., Mercier de Lépinay, B., … Lericolais, G. (2008). Cold seeps along the main Marmara Fault in the Sea of Marmara (Turkey). Deep Sea Research Part I: *Oceanographic Research Papers*, 55(4), 552–570. http://doi.org/10.1016/j.dsr.2008.01.002

CHAPITRE I
Profondeur du Moho et épaisseur crustale dans la région de la Mer de Marmara par inversion du champ d'anomalie de gravité

This chapter has been published as:

Moho depth and crustal thinning in the Marmara Sea region from gravity data inversion
Kende J., Henry P., Bayrakci G., Özeren M. S., and Grall C.

Journal of Geophysical Research: Solid Earth, 122(2), 1381–1401.
doi: 10.1002/2015JB012735

Résumé étendu

A l’aplomb de failles transformantes, la formation de bassins est généralement liée à une extension crustale. La quantité d’extension et la géométrie du relais extensif où se forme le bassin sont alors déterminantes dans le contrôle de la forme des bassins et de l’accommodation de la déformation dans la croûte par remontée du Moho.

En mer de Marmara, l’existence d’un amincissement de la croûte a été observée sur des données sismiques [*Bécel et al,.* 2009, *Karabulut et al.*, 2013]. Cependant, la résolution de ces études et l’impossibilité d’effectuer des relevés sur un réseau à mailles denses en dehors des bassins en eau limitent la connaissance de la géométrie du Moho au-delà des limites de la mer. Grâce à l’étude du champ de gravité, ce travail présente une modélisation de la géométrie 3D de la croûte dans toute la région de la mer de Marmara.

Dans un premier temps, nous avons construit un modèle géologique 3D des couches sédimentaires des bassins. La base de ce modèle a été proposée par *Bayrakci et al.* [2013] sur la base d’une tomographie de temps de trajet des ondes P. Nous l’avons enrichi d’informations sur le bassin de Thrace et la mer Noire issue de *Robinson et al* [1996] et *Siyako et Huvaz* [2007]. Ainsi, nous avons obtenu, sur toute notre surface d’étude, la topographie/bathymétrie, la profondeur de la base des sédiments plio-quaternaires, considérées comme synchrones de l’ouverture de la mer de Marmara, et la profondeur de la base des sédiments plus anciens et plus denses. Par ailleurs, nous avons fusionné des données satellites du champ de gravité de la région [téléchargeable sur *http://topex.ucsd.edu]* avec les données issues du gravimètre du navire océanographique Pourquoi Pas ? lors de la campagne MARSITE. Cette opération nous a permi d’éliminer des artefacts présents dans les données satellite, notamment au niveau de la sortie des eaux du Bosphore.

Nous avons ensuite utilisé le modèle géologique pour corriger le champ de gravité de l’influence des bassins. Une fois le champ de gravité débarrassé de l’effet de la présence de la couche d’eau et des couches de sédiment, les variations restantes doivent correspondre à des anomalies révélant des variations de densité en profondeur. Pour corriger le champ de gravité, nous avons utilisé la méthode de *Parker* [1972] qui intègre successivement l’effet de chaque couche en considérant la profondeur et la variation de densité aux interfaces.

En considérant ensuite que le champ d’anomalie ainsi obtenu représente uniquement les variations de la profondeur du Moho, nous proposons une méthode d’inversion des données pour estimer la profondeur du Moho en intégrant des contraintes issues des études sismiques. La profondeur du Moho obtenue ainsi que la topographie du haut de la croûte définissent finalement un modèle 3D de la croûte sous la mer de Marmara. Une première conclusion est que l'amincissement s'étale au-delà de la limite des bassins et est notamment importante sous les bassins sud, même au niveau de l'île de Marmara.

Nous utilisons ensuite ce modèle pour quantifier l'extension totale dans la région depuis l'ouverture de la mer de Marmara. En considérant une épaisseur de référence, correspondant à l'épaisseur moyenne de la croûte dans la région au-delà des zones affectées par l'extension, nous calculons quelle surface peut être accommodée par le volume de croûte présent dans le modèle avec cette épaisseur de référence. La différence entre cette surface théorique et la surface réelle de notre zone d'étude nous donne l'extension dans la région depuis le début de l'ouverture de la mer de Marmara. Il est à noter que l'extension ainsi obtenu, 2050 km^2, rapportée à l'âge maximal estimé des premiers bassins, 5 Ma, donne un taux d'extension proche de ceux mesurés actuellement par GPS. Cela suggère que la composante extensive de la déformation a peu varié dans l'histoire de la Mer de Marmara. Si le système a connu une première phase purement extensive avant l'incursion de la faille Nord-Anatolienne, alors l'extension a pu se maintenir à un taux comparable tout en passant d'un large système de détachements crustaux [*Bécel et al.*, 2009, *Le Pichon et al.*, 2015] à un système où l'extension est maintenant surtout concentrée le long de la faille décrochante.

Pour finir, nous présentons un calcul de bilan de volume à l'intérieur de 4 blocs définis par la limite entre la croûte ductile et la croûte cassante et par la limite Sud des principaux bassins. La comparaison de la proportion d'amincissement profond par rapport à l'amincissement superficiel dans les blocs Nord et Sud permet d'estimer le ratio d'amincissement profond accommodé par les flux ductiles du Sud vers le Nord dans la croûte inférieure. Bien que notre modèle donne en réalité la valeur maximum possible du flux de croûte inférieur vers les bassins, nos calculs aboutissent à un ratio relativement modéré indiquant que 15 à 30 % de l'extension a pu être accommodée par des flux ductiles.

Cette étude permet aussi de placer la mer de Marmara comme un cas intermédiaire en termes de température de croûte et de ductilité entre la mer Morte (cas relativement froid et rigide) et la Vallée de la Mort (cas relativement chaud et ductile), deux bassins en pull-apart sous lesquels aucune remontée du Moho n'est observée. La ductilité intermédiaire du manteau et de la croûte inférieure sous la mer de Marmara permet une remontée du Moho, qui semble ne pas pouvoir se produire sous la Mer Morte [*Ten Brink et al.*, 1993; *Petrunin and Sobolev*, 2006], mais ne permet pas un aplatissement par fluage à l'échelle régionale comme ce qui est observé en Californie [*De Voogd et al.*, 1988; *Fliedner et al.*, 1996].

Abstract

The free air gravity in the Marmara Sea reveals that the low density of sedimentary basins is partly compensated in the lower crust. We compiled geophysical upper crust studies to determine the sediment basin geometries in and around the Marmara Sea and corrected the gravity signal from this upper crust geology with the Parker method. Then, assuming long wavelength anomalies in the residual gravity signal are caused by variations in the Moho topography, we inverted the residual to build the Moho topography. The result shows that the Moho is uplifted on an area greater than the Marmara Sea with a maximum crust thinning beneath the basins where the Moho is at about 25 km, 5 km above the reference depth. We then evaluated the Neogene extension by comparing the surface covered by our 3D thinned model with the surface covered by an un-thinned model with same crustal volume. Comparing this surface with areal extension rate from GPS data, we found a good compatibility indicating that the extension rate averaged over the Sea of Marmara area probably remained close to its present day value during major changes of tectonic regime, as the incursion of the North Anatolian Fault system during the Pliocene lead to the establishment of the dominantly strike-slip present day system. We also show that crustal extension is distributed over a wider domain in the lower crust than in the upper crust, and that this may be accounted for by a relatively minor component of lower crustal ductile flow.

1. Introduction

Basin formation along strike-slip fault zones generally results from crustal extension at a releasing bend or releasing overstep [e.g. *Christie-Blick and Biddle*, 1985; *Biddle and Christie-Blick*, 1985]. The rheology of the lower crust and the ratio of step-over width to brittle crust thickness thus appear as essential parameters controlling the distribution of extension, basin geometry and sediment thickness [*Petrunin and Sobolev.*, 2006; *Smit et al.*, 2008]. With this respect, the Dead Sea and the Death Valley have been considered as end member cases. The Dead Sea pull-apart corresponds to a small 10 km step-over in a mostly brittle 35 km crust, in which case the extension occurs along the basin axis and remains confined in the narrow corridor defined by the bounding strike-slip faults [*Katzman et al.*, 1995; *Petrunin and Sobolev*, 2006; *Ten Brink et al.*, 1993]. The Death Valley fault corresponds to a more than 50 km step-over in a relatively thin brittle crust, in which case the basin developed as an oblique structure bounded by normal faults [*Burchfiel and Stewart*, 1966].

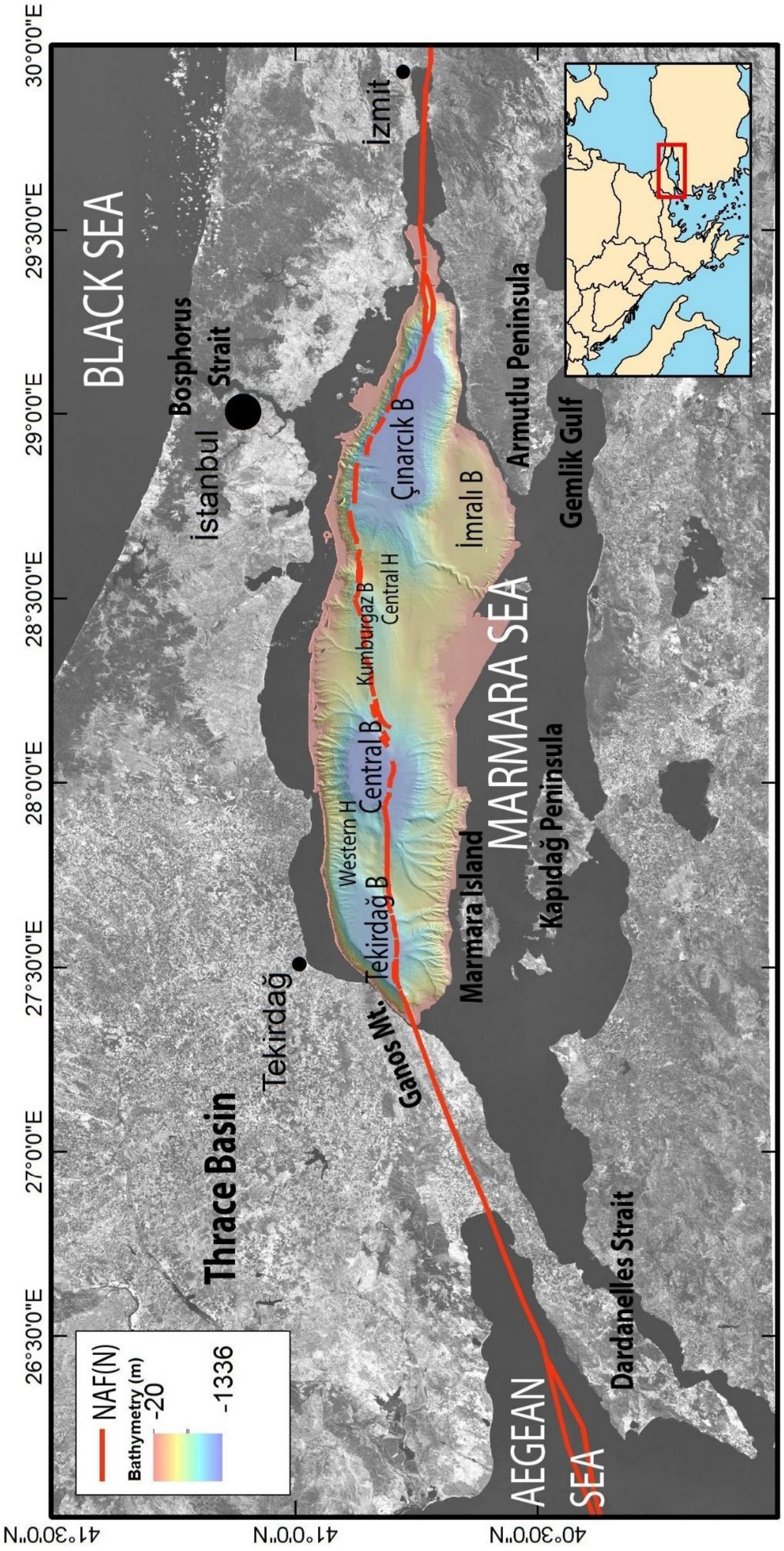

Figure 1. Geographic and simplified tectonic setting of the Marmara Sea. B stands for Basins, H for Highs and NAF(N) for the Northern branch of the North Anatolian Fault. The Fault location is modified from Şengör et al. [2014]. Bathymetry data are from the EM300 multibean survey.

Remarkably, in both cases, the Moho is not uplifted beneath the basins for contrasted reasons. The Dead Sea basin is essentially uncompensated, with little involvement of the mantle in the formation of the basin [*Ten Brink et al.*, 1993; *Petrunin and Sobolev*, 2006]. Below the Death Valley, the crust is hot and highly ductile, affected by the regional Basin and Range extension, resulting in compensation within the crust and a flat Moho [*De Voogd et al.*, 1988; *Fliedner et al.*, 1996]. The Marmara Sea corresponds to an intermediate case where the step width is comparable to the width of the brittle crust (15-20 km), as may be estimated from the depth distribution of earthquakes [*Schmittbuhl et al.*, 2016], and wide-angle refraction studies indicate a Moho at 26 km depth below sea level beneath the Marmara Sea troughs, implying at least 5 km of uplift [*Bécel et al.*, 2009]. Compared to the Dead Sea low heat flow, estimated less than 50 mW.m^{-2} [*Ben-Avraham et al.*, 1978; *Garfunkel et al.*, 1996], and the heat flow above 100 mW.m^{-2} of the Death valley [*Sass et al.*, 1994], the Marmara Sea, with a crustal heat flow ranging between 55 and 85 mW.m^{-2} [*Grall et al.*, 2012; *Pfister et al.*, 1998] appears as intermediate, and representative of average continental crust heat flow [*Pollack et al.*, 1993]. The Marmara Sea case may thus provide some insight on the influence of crustal heat flow and rheology on strike-slip basin development and associated crustal thinning, hence motivating the present study.

The Marmara Sea is situated along a segment of the North Anatolian Fault (NAF), a vast fault system carrying 20 to 27 mm/yr of dextral strike-slip motion, according to GPS, between the Anatolian and the Eurasian plates [*Reilinger et al.*, 2006; *Hergert and Heidbach*, 2010]. In its western part, the NAF splits into several branches. The Marmara Sea overlies the NAF northern branch, the Main Marmara Fault (MMF) [*Le Pichon et al.*, 2001, *Şengör et al.*, 2005] (see Figure 1). While the MMF is interpreted as a pure, or dominantly, strike-slip fault [e.g. *Rangin et al.*, 2004; *Seeber et al.*, 2004], there are remaining uncertainties about the amount of extension taken up in the Marmara Sea region and about the extensional mechanisms that led to the present basin geometries. *Bécel et al.* [2009] interpreted a northward dipping seismic reflector as a detachment oriented N40°E south of the Central Basin and suggested an asymmetric crustal thinning towards the SW. In the same study, *Bécel et al.* [2009] identified Pn wave, refracted on top of the upper mantle, in wide-angle seismic data and showed that the crustal thinning spreads southward over a broader domain than the deep basins composing the North Marmara Trough (NMT). This result has been confirmed by a north to south onshore seismic survey [*Karabulut et al.*, 2013], cutting the Marmara Sea at about the Marmara Island longitude and showing a smooth 5 km thinning over a zone wider than the Marmara Sea.

We conducted a gravity data analysis, using seismic study results as constraints [*Bécel et al.*, 2009; *Karabulut et al.*, 2013; *Bayrakci et al.*, 2013], to produce a Moho depth map, draw a budget of crustal extension, and evaluate the lower crustal ductile flow contribution to the extension processes.

2. Data

2.1. Gravity and topographic data

The gravity anomaly map used in our study was obtained by merging a global gravity model and marine ship data acquired in the Marmara Sea. First, we retrieved a gravity grid from the Scripps Institution of Oceanography website. Available on http://topex.ucsd.edu/WWW_html/mar_grav.html, the data grid is based, for the marine domain, on past 3×10^{-5} to 4×10^{-5} $m.s^{-2}$ (3 to 4 mGal) accurate Geosat and ERS-1 satellites data and new altimeter data from Jason-1 and CryoSat-2 satellites , with the later providing the dense coverage of a 2.5 km track spacing [*Sandwell and Smith*, 1997; *Sandwell et al.*, 2014]. The estimated accuracy at the Marmara Sea Latitude is about 1.7×10^{-5} $m.s^{-2}$ [*Sandwell et al.*, 2013]. The land part of this global model is based on the Earth Gravitational Model 2008 [*Pavlis et al.*, 2008]. A linear interpolation was used to refine the map in order to obtain a 256 x 512 cell grid covering the considered area and appropriate for Fast Fourier Transform, which is optimized for grid sizes that are powers of 2. The area of our study covers latitudes between 40° and 41.5° and longitudes between 26° and 30°.

The second data source is the gravity data collected during the Marsite Cruise in October and November 2014 on board the survey vessel N/O Pourquoi Pas?. The ship is equipped with a Bodenseewerk KSS 31 gravimeter working with a spring on a stabilized platform. The device is installed at the ship steadiest spot and records data at a high time resolution giving a space resolution of about 1 m. As the data we accessed are not calibrated at port station, the mean value of the ship data was moved to match the satellite data mean value in the Marmara Sea. Then, a 256 x 512 cell grid covering our area of study was created from the ship data with linear interpolation and extrapolation from the closest value.

Figure 2. shows a comparison of the two data sources on a transect, as well as the satellite data grid with the transect location. The inconsistency visible in the east probably corresponds to a location where the spline interpolation of the satellite data creates short wavelet oscillations. Another feature that will be removed when integrating the ship gravity data is the negative

anomaly near the Bosphorus Strait. The high speed of the jet current at the Bosphorus outlet (about 2 m.s^{-1}) results in negative sea topography. This local lowering of the sea surface results in an apparent gravity low in the satellite gravity map.

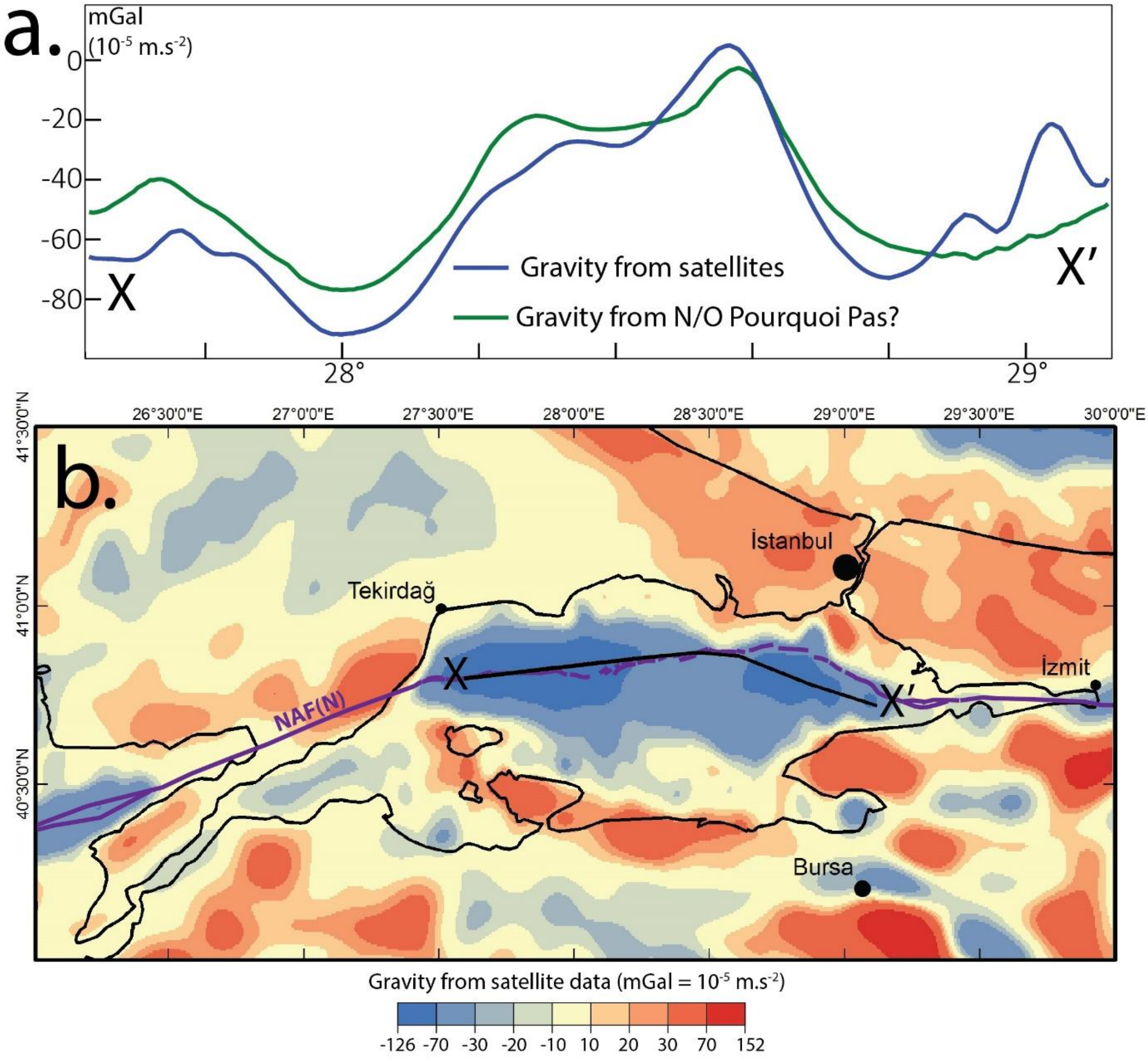

Figure 2. Gravity field. a. Comparison of free air gravity data from satellite altimetry [Sandwell et al., 2014] and from N/O Pourquoi Pas? shipboard gravimeter on a transect. b. Free air anomaly field interpolated from satellite data only and location of the transect shown in a.

The data were combined by using the grid created from ship data within 1700 m of the ship track and the grid from satellite data further than 4200 m. The corridors in between were filled by a biharmonic spline interpolation available in MATLAB and based on *Sandwell* [1987]. Figure 3 shows our final free air gravity map.

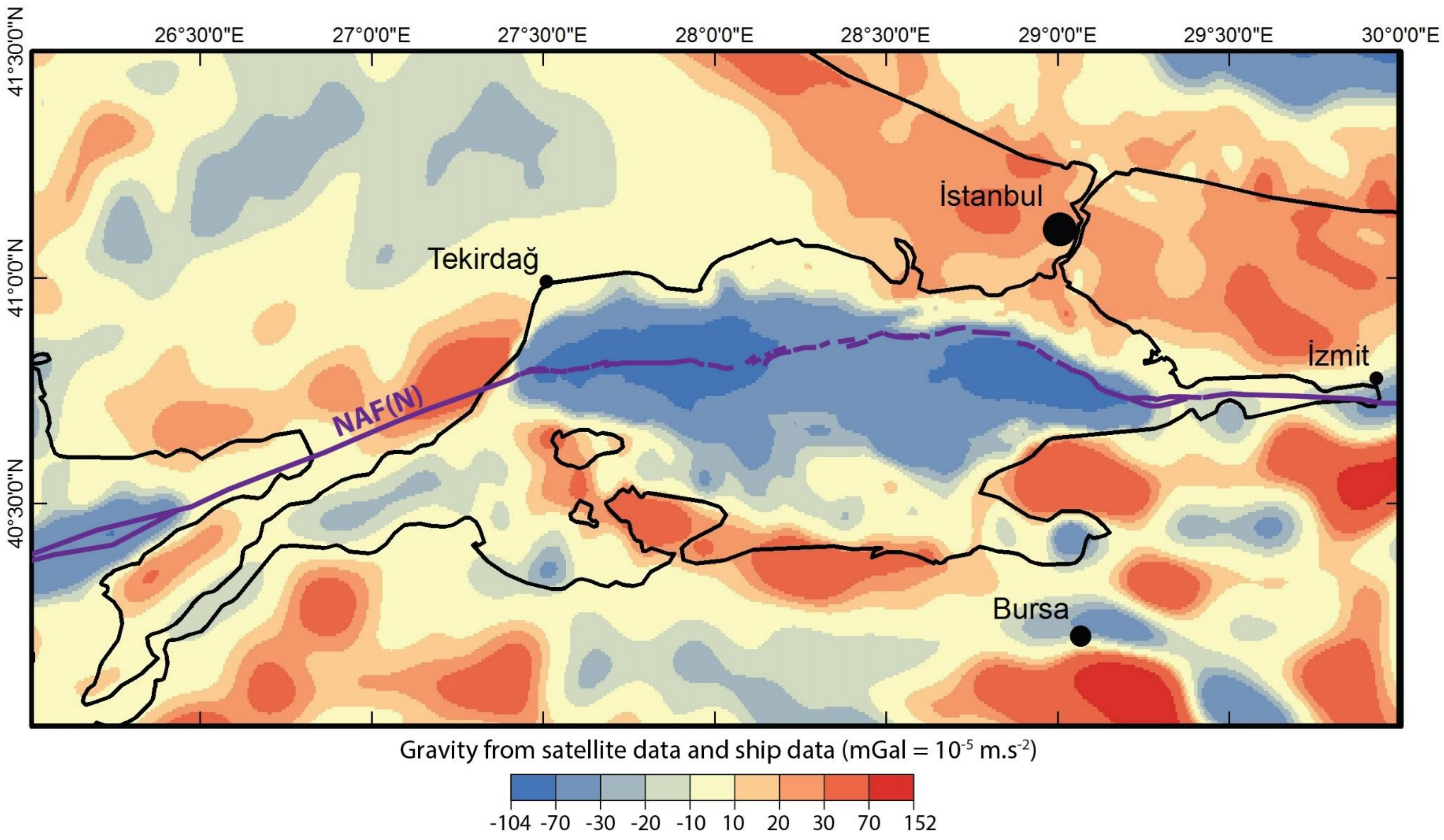

Figure 3. Final Free air anomaly map combining the satellite data and the MARSITE cruise gravity measurements.The merging delivered finer data in the Marmara Sea and eliminated small artifacts in the Eastern part of the Marmara Sea (see Figure 2).However, as the ship tracks were not evenly spaced over the entire study area, artifacts may remain in the final grid.

The bathymetric data used for the Marmara deep basins, presented in Figure 1, is based on the EM300 multibeam survey of the Marmara Sea basins [*Le Pichon et al.*, 2001]. On the shelves and on land, we used the global topographic grid available from the Scripps Institution of Oceanography website.

2.2. Sediment thickness Data

The basin model used in this study is mostly based on the sediment thicknesses derived from the tomographic study presented in *Bayrakci et al.* [2013]. We adopted the distinction of a syn-kinematic layer and a pre-kinematic layer first introduced by *Laigle et al.* [2008] and corresponding respectively to the sediments deposited during and before the opening of the Marmara basins. *Laigle et al.* [2008] identified the boundary between the two layers while *Bayrakci et al.* [2013] estimated that the 4.2 km.s^{-1} and 5.2 km.s^{-1} P-wave velocity isocontours delimit them.

The velocity/density model is probably more complex and heterogeneous in details. The presence of a damaged zone with low seismic velocities and negative density anomalies has been observed around the North Anatolian Fault east of the Marmara Sea [Ben-Zion et al., 2003] and in the San Andreas fault zone area [eg: Feng et al., 1983; Wang et al., 1986]. It is very likely that a damage zone associated with density contrasts also occurs in the Marmara Sea, for instance between the NMT and its surrounding. However, the seismic surveys on which the basin model is based do not show clear evidence for this, and the resolution of the gravity data is also too low to account for such contrasts.

The sediment thickness model was extended over the southern shelf based on interpretation of TPAO multichannel seismic profiles [*Le Pichon et al.*, 2013]. In this interpretation, Plio-Quaternary sediments are distinguished from pre-kinematic Miocene to early Pliocene sediments, which are deposited on basement or cretaceous carbonates. P-wave velocity, as described in *Bayrakci et al.* [2013] was also considered when known.

In order to limit edge effects in the gravity inversion, the area of interest is not limited to the Marmara Sea. Nearby structures had to be modeled as well: the Black Sea and the Thrace Basin.

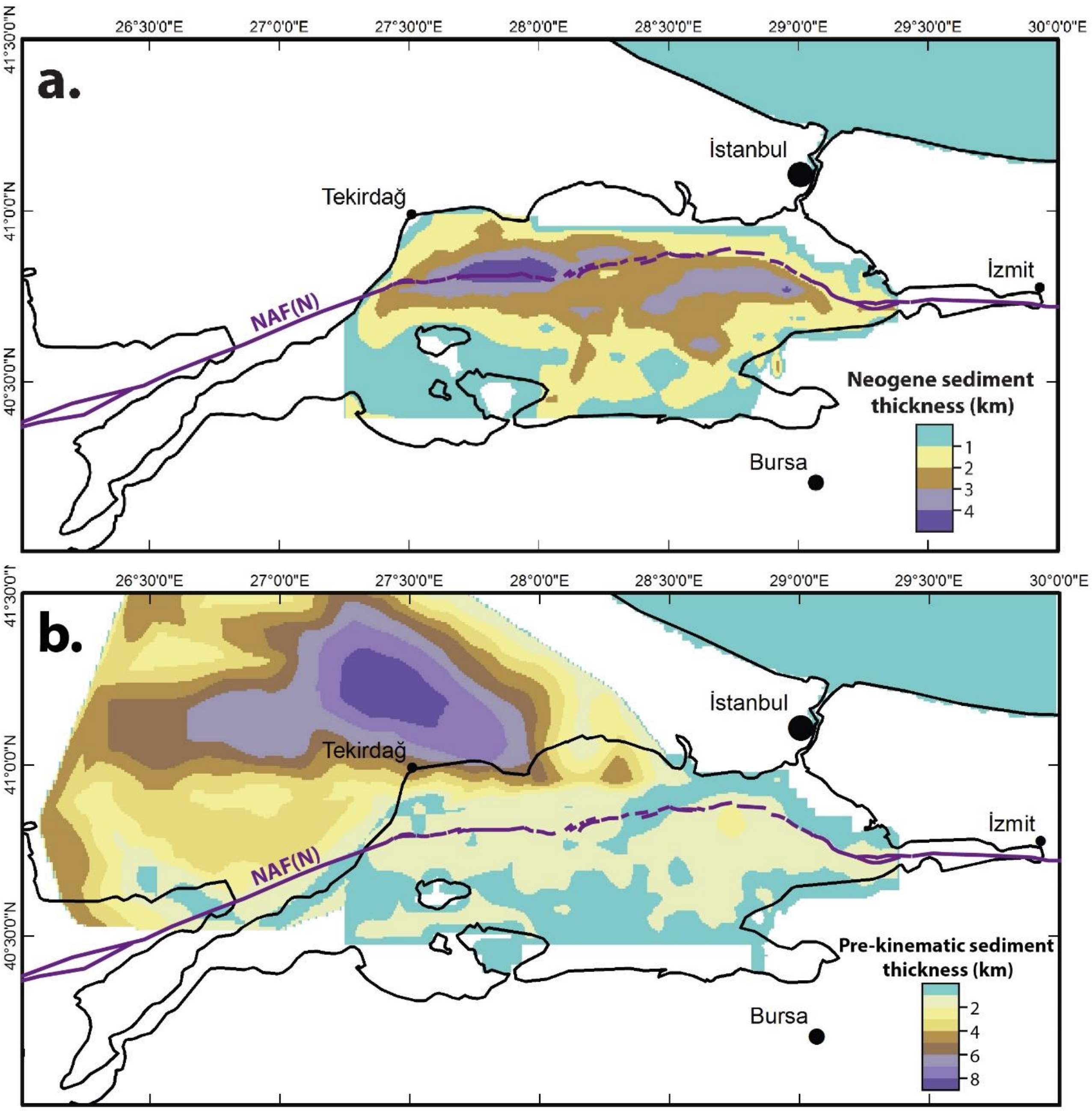

Figure 4. Thickness of the two sediment layers expended from Bayrakci et al. [2013] model defined between 27.25° - 29.4° E and 40.5° - 41.1° N. The layers initial definition is based on P-wave velocity. The syn-kinematic sediment layer corresponds to velocities lower than 4.2 km.s^{-1} and the pre-kinematic sediment layer have P-wave velocities comprised between 4.2 km.s^{-1} and 5.2 km.s^{-1}. Bayrakci et al. [2013] model was expanded interpreting the bottom of the Plio-Quaternary sediments as the interface between the two layers when P-wave velocities were not available. Plio-Quaternary sediment thickness is neglected in the Thrace Basin and a simple model with constant thickness is applied to the Black Sea.

Only the southwestern part of the Black Sea was included in the domain of study. The sediment layers were extrapolated from the profile presented on Plate 14 in *Robinson et al.* [1996] by adopting a constant thickness of 600 m for the first as well as for the second layer of sediment. Thus, we obtain sediment depths directly related to the bathymetry. Although this is a rough approximation of the Black Sea sedimentary structure, this approximation does not strongly affect our model in the Marmara Sea area.

The Oligocene-Eocene Thrace Basin geometry is well constrained from seismic surveys and industry boreholes. We used the sediment depth model presented in *Siyako and Huvaz* [2007] and mainly based on well data [*Huvaz et al*., 2000]. We ignored the Plio-Quaternary sediment layer as its thickness is always less than 500 m [*Siyako and Huvaz*, 2007].

Finally, the two sediment depth maps were refined using a linear interpolation in order to obtain a 256 x 512 cell grid matching the gravity data grid. Figure 4 shows the final thickness map for the two sediment layers.

2.3. Crustal structure

The existence of a reflective lower crust has been shown by both multi-channel seismic [*Laigle et al.*, 2008] and ocean bottom seismometer [*Bécel et al.*, 2009] data. However the deep reflections could only be identified on few multi-channel seismic profiles due to the multiples or lateral echoes. The top of the lower crust, as well as the Moho, are therefore constrained by wide-angle refraction-reflection data recorded by far offset stations and few OBSs that provide enough depth penetration. *Bécel et al.* [2009] imaged the top of the lower crust on three 2D profiles and proposed a 2D model where the lower crust and the Moho have a similar geometry, with the upper/lower crust interface lying at 2/3 of the Moho depth. We assume that the continental crust retains these proportions in the modeled domain in 3D, as we don’t have any other independent data to constrain the 3D model. The geometry of the interface between the upper and the lower crust will thus be calculated together with the geometry of the Moho using the inversion method detailed below. The calculated Moho and the upper/lower crust interface depths will then be compared to available constraints from seismic studies.

3. Method

Modelling the Moho depth variations from gravity data is a two-step process. First, the impact of the known geology and topography on the gravity must be accounted for and removed from the free air gravity. The resulting gravity anomaly represents the effect of density variations in the deeper part of the crust and in the mantle. We assumed that the remaining anomalies are related to Moho depth variations and can be inverted to determine the geometry of the Moho.

For the first step, we computed the effect of our upper-crust model on gravity in the onshore and offshore domains:

3.1. Gravity correction over the onshore domain

For the onshore domain, we first applied a Bouguer correction to remove the effect of the topography. In the Thrace basin, we used a sediment density for the Bouguer calculation equal to the density of the pre-kinematic sediment layer and then corrected for the Thrace basin sediment thickness using the same procedure as for the offshore domain.

Prior to computing the Bouguer correction, a Gaussian filter with a 20 km window was applied on the topography. This filtering was needed because wavelengths shorter than 20 km are absent from the satellite gravity grid. This filtering does create a risk of interfering with crustal effect on gravity and losing part of the signal [*Aitken et al.*, 2013].

3.2. Gravity correction in the Marmara Sea, in the Black Sea and in the Thrace Basin

The Bouguer correction is a fast and effective approximation of the gravity anomaly caused by topography on land. But, as we need to account for the effect of the Marmara Sea basins, the gravity must be corrected from the influence of the bathymetry variations and from the effect of water and sediment layers:

$$g_{corrected} = g_{measured} - \delta g_w - \delta g_{S_1} - \delta g_{S_2}$$

Where δg_w, δg_{S_1}, and δg_{S_2} are the effect on gravity of, respectively, the layer of water, the syn-kinematic sediments and the pre-kinematic sediments.

The basin correction was performed through the application of the Parker method [*Parker*, 1972], which is based on a Fourier transform of the gravity equation:

$$F[g(x)] = -2\pi G \Delta\rho e^{-|k|z_0} \sum_{n=1}^{\infty} \frac{|k|^{n-1}}{n!} F[h^n(x)] \qquad (1)\ Parker\ equation$$

Where $\Delta\rho$ is the density difference at the considered interface, k is the wavenumber of the transform function and z_0 is the mean depth of the considered interface. $F[g(x)]$ and $F[h^n(x)]$ are, respectively, the Fourier transform of the gravity field and of the interface depth.

We used the Parker equation to calculate the gravity correction based on our three interfaces: the water/syn-kinematic sediment interface, the syn-kinematic/ pre-kinematic sediment interface and the pre-kinematic sediment/Crust interface. We obtain the gravity correction to be applied on the observed gravity field to account for differences between our model and an ideal model with a flat topography and no sedimentary basins.

In the Thrace Basin, we have the special case of a sedimentary basin with a positive topography. The Bouguer correction accounted for the positive topography and the Parker method accounted for the sedimentary basin below sea level.

3.3. Residual anomaly inversion and Moho depth variation determination

Methods for determining the Moho variations and crustal thickness from gravity data have been used for more than a century [e.g. *Vening Meinesz*, 1931]. Approaches include inversion, forward-modeling, process-oriented modeling and spectral analysis (see *Aitken et al.* [2013] for a review).

Here, we developed a fast inversion method, close to the Parker-Oldenburg algorithm [*Oldenburg*, 1974]. First, the Parker equation was linearized, retaining only the first term of the Taylor development:

$$F[g(x)] = -2\pi G\Delta\rho e^{-|k|z_0} F[h(x)] \qquad (2)$$

This equation direct inversion is:

$$F[h(x)] = -\frac{e^{|k|z_0}}{2\pi G\Delta\rho} F[g(x)] \qquad (3)$$

This equation would not yield satisfactory results for the Moho because the high wave number terms are amplified while in fact they are unconstrained by data at wavelengths shorter than the crustal thickness. The method we propose is preconditioning to 0 the amplitude of Moho variations. A Least Square misfit function is thus defined, in the Fourrier domain as:

$$S[h] = \frac{1}{2\pi G\Delta\rho} \|F[g](k) - F[g_{obs}](k)\|^2 + \left\|\frac{F[h](k)}{\sqrt{C(k)}}\right\|^2 (4)$$

Where the covariance diagonal matrix C(k) scales the model deviation from the *a priori* model (flat Moho) with the error on data projected in the model space [*Tarantola*, 2005]. We will assume C(k) constant, independent of wavenumber. At short wavelengths, the first term is nearly independent of the model, and, at the minimum of S, h(k) ≈ 0. For long wavelengths, the first term becomes dominant, and the preconditioning has little effect on inversion results. The solution of this linear Least Square Problem is [*Tarantola*, 2005]:

$$F[h(x)] = \frac{1}{2\pi G\Delta\rho}\left(e^{-|k|z_0} \times e^{-|k|z_0} + \frac{1}{C}\right)^{-1} \times e^{-|k|z_0} \times F[g_{obs}(x)] \qquad (5)$$

This is equivalent to applying a low pass filter to the linearly inverted Moho, where C controls the cut-off wavelength. One theoretical advantage of this method is that the shape of the filter is consistent with a preconditioning approach [*Tarantola*, 2005].

The lowpass filter corresponds to:

$$filter = \left(e^{-|k|z_0} \times e^{-|k|z_0} + \frac{1}{C}\right)^{-1} \times e^{-2|k|z_0} = \left(1 + \frac{e^{-2|k|z_0}}{C}\right)^{-1} \qquad (6)$$

The passband power is met when k = 0 and we can define a cutoff wavenumber k_c corresponding to k for which the output is half of the passband power:

$$k_c = \frac{\ln(C)}{2z_0} \qquad (7)$$

3.4. Modelling parameters

Using an inverse modelling method is a fast, effective and repeatable way to compute a model on a large area with a fine gridding. It also removes part of human biases that are a risk when carrying forward modelling in which the model is manually modified until it fits a set of conditions that describe an acceptable Moho and meets the geophysical observations [*Aitken et al.*, 2013]. However, the whole model is based on the acceptance of the initial shallow geologic setting, on the precision of the topographic and gravimetric surveys and on the few parameters that are user-input: the layer densities, the reference Moho depth and the covariance parameter for the Moho inversion.

The geologic model we first used consisted of five layers, each characterized by a density: water, first sediment layer (syn-kinematic), second sediment layer (pre-kinematic), crust and mantle.

The crust and mantle density were chosen based on *Bécel et al.* [2009] P-wave velocities and on *Sobolev and Babeyko* [1994] P-wave velocity versus density curves. We chose a density of 2650 kg.m^{-3} for the upper crust as the P-wave velocities at the top and bottom of the layer are 6 and 6.2 km.s^{-1}. The lower crust P-wave velocity is 6.7 km.s^{-1}, corresponding to 2950 kg.m^{-3}. The values retained are also compatible with Christensen and Mooney [1995] average velocity versus average density curve. Seismic velocity models do not indicate that the proportion of upper and lower crust varies significantly or that lateral variations of density are present in each layer. With two third of upper crust and one third of lower crust we obtain an average density value of 2750 kg.m^{-3} for the whole crust. Mantle density is taken equal to 3330 kg.m^{-3}.

An upper/lower crust interface is included in the gravity model. The interface is defined at two third of the Moho depth. The location of the interface is thus calculated iteratively, until convergence is reached, from the depth of the Moho (inversion result). The results obtained with this layered crust model are not exactly identical to those obtained with a single layer crust of density 2750 kg.m^{-3}, but the difference is small: taking into account the upper/lower crust interface lowers the standard deviation of the final residual anomaly in the domain of study by about 0.6 x10^{-5} m.s^{-2} (0.6 mGal).

The syn-kinematic and pre-kinematic sediment thicknesses that we adopted from *Bayrakci et al.* [2013] model are identified with P-wave iso-velocity contours: the first layer refers to the field in which P-wave velocity is smaller than 4.2 km.s^{-1} and pre-kinematic sediments have P-wave velocities between 4.2 km.s^{-1} and 5.2 km.s^{-1}. To estimate the two sedimentary layer densities from these velocities, we used *Erickson and Jarrard* [1998] relation for siliciclastic water-saturated sediments:

$$V_p = 1.11 + 1.178\emptyset + \frac{0.305}{[(\emptyset + 0.135)^2 + 0.0725]} + 0.61(v_{sh} - 1)(X - abs(X))$$

Where $X = \tanh\big(20(\emptyset - 0.39)\big)$. V_p is the compressional wave velocity, v_{sh} the shale fraction and $\emptyset$ the porosity.

It has the advantage of including the shale fraction as a variable which allows us to evaluate reasonable uncertainties since sediments may change from very fine clay to coarser layers. We tested the relation with v_{sh} varying from 0 to 1. For a velocity of 4.2 km.s^{-1}, we obtained the limit values of 2400 kg.m^{-3} ($\emptyset = 0.15$) and 2630 kg.m^{-3} ($\emptyset = 0.01$), using 2650 for siliciclastic grain density. One should note that the value calculated with $v_{sh} = 1$ largely encompass the possible drifting described by Erickson and Jarrard [1998] when dealing with very low porosities. Then, considering a porosity for shallow clay rich sediments of 700 kg.m^{-3} [*Le Pichon et al.*, 1990], which is consistent with measurements on Marmara Sea sediment cores [*Aloisi et al.*, 2015], and an exponential porosity-depth law (Athy's law, [*Grall et al.*, 2012 and 2013]) from the sediment layer top to its floor, we obtain a range of 2070 to 2390 kg.m^{-3} for the average density of the first layer of sediment.

For the bottom limit of the second layer, we used the same equation and $v_{sh} = 0$ to determine a minimum density of 2600 kg.m^{-3} ($\emptyset = 0.03$). From this value and the one calculated at the layer top, we get an average minimum density for the second layer of sediment of 2530 kg.m^{-3} ($\emptyset = 0.07$). We then consider 2650 kg.m^{-3} as a maximum, for which there is no density contrast between the second layer of sediment and the upper crust.

The two ranges of density were scanned with a step of 20 kg.m^{-3} and all combinations were tested. Each time, we calculated the residual gravity after correcting for the Marmara Sea Basins without taking into account the Thrace Basin and the Black Sea sediments.

The comparison of the residual standard deviations indicates that the higher the density values are, the smaller the residual gravity anomaly is. If a homogeneous crustal density is assumed for the upper crust and the two sediment layers, (2650 kg.m^{-3}) the residual anomaly is very small, which would result in an almost flat Moho. However, this interpretation can be considered unrealistic in view of the seismic data. Nevertheless, the residual anomaly and calculated Moho geometry are strongly dependent on the average densities assumed for the sedimentary layers.

In the following, the discussion will be based on a mean model obtained with average density values of 2230 and 2590 kg.m^{-3} for syn-kinematic and pre-kinematic sediments, respectively. We will also consider that varying the density within the determined range yields the possible range of variation of Moho depth maps as constrained by gravity.

For the inversion of the corrected gravity field, two more parameters have to be set: the mean Moho depth and the covariance. The choice of the mean Moho depth was based on *Karabulut et al*. [2013] and set to 30 km. We preferred that value to the about 35 km depth inferred around the Marmara Sea in *Bécel et al.* [2009] as their distribution of receiver and sources does not constrain well the Moho depth outside the basins. It is also the reference value chosen by *Tiberi et al.* [2001] for their inversion of gravity data after correcting for the plunging African slab in the Corinth Rift area.

The covariance parameter has a direct impact on the Moho results. We tested covariance ranging from 10 to 50 and selected 25 as it gives the depth variation amplitude closest to the one observed by *Karabulut et al.* [2013] for the model with intermediate gravity values. This corresponds to a cutoff wavelength of about 120 km.

4. Results

Figure 5 shows the intermediate result of the gravity field corrected from the topography and the upper crust density variations, before inversion. Figure 6 shows the Moho depth and the final residual, which is the difference between the measured gravity and the modeled gravity. Results computed with the minimum and maximum sediment densities within the bounds we defined are also presented. Although the Moho depth variation amplitude changes, the geometry is very similar on results a. and b. and all three results show a “saddle” shaped

Moho. The thinning spreads further North than South of the Marmara Sea, considering 30 km depth as the default depth in a homogeneous crust, and the two shallowest zone are centered north of the Marmara Island and above the Çınarcık Basin. The rms of the difference between the depths of the two extreme models is 1 km. Hence the model is fairly robust to variations of the sediment densities within the reasonable bounds we defined.

The modeled gravity is the summation of on land Bouguer correction, basin effects on the gravity and the gravity anomaly produced by the inferred Moho and upper crust/lower crust boundary. Thus, observation of the gravity residual is representative of the model accuracy as it is the part of the gravity measurement not explained by our model.

As presented in Figure 6, with each of the sediment density pair inputs, we obtain a map with a residual gravity anomaly equal to $0 \pm 5 \times 10^{-5}$ $m.s^{-2}$ (0 ± 5 mGal) on the majority of our domain of study.

In the Marmara Sea, the residual is characterized by a positive “belt” spreading from East to West above the basins and along the southern shore. In the middle, the Marmara Island, the zone North of the Kapıdağ Peninsula and the İmralı Basin, are small areas with negative residuals. We will discuss separately the northern and the southern part of the positive “belt” as they probably result from two different mechanisms.

The northern part of the “belt” coincides with the deep basins and show the highest residuals at the location of the current depocenters in the Tekirdağ and the Çınarcık basins. This may be due to the fact that sediment layers are characterized by only one mean density, which may be too small for zones with a very thick sediment layer. Similarly, as the residual above the basins is decreased by highest density values, the density ranges we defined earlier may be overly shifted toward lower density values. Also, in this zone, the positive residual creates a pattern which coincides with the MARSITE cruise ship path. Thus, although the merging of the N/O Pourquoi Pas? and the satellite data suppressed an artifact in the east (see Figure 3), the two data source may not be consistent enough. We could probably lower this positive residual by normalizing the ship data with regards of the satellite data, instead of only matching the averages. But the area covered by the ship data is not wide enough to be representative and to allow such a correction. Part of the positive residual is also due to the fact that wavelength shorter than the geological model resolution are not compensated and cannot be lessened when adding the Moho interface. So short wavelength gravity variations are visible where they were recorded along the ship path.

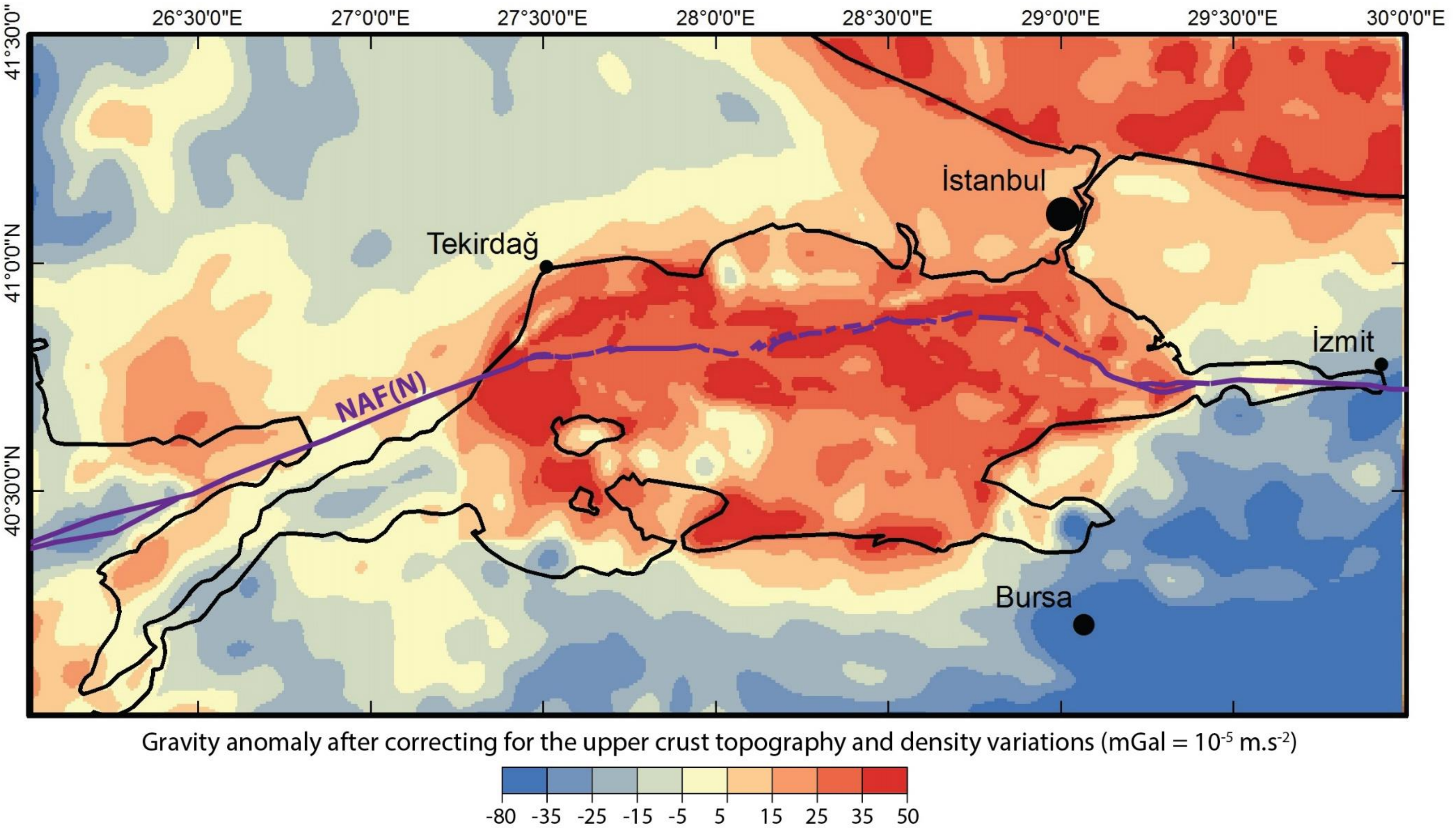

Figure 5. Gravity anomaly after correcting the measured gravity field using Bouguer calculation for the topography and the Parker method [Parker, 1972] for the sediment basins.

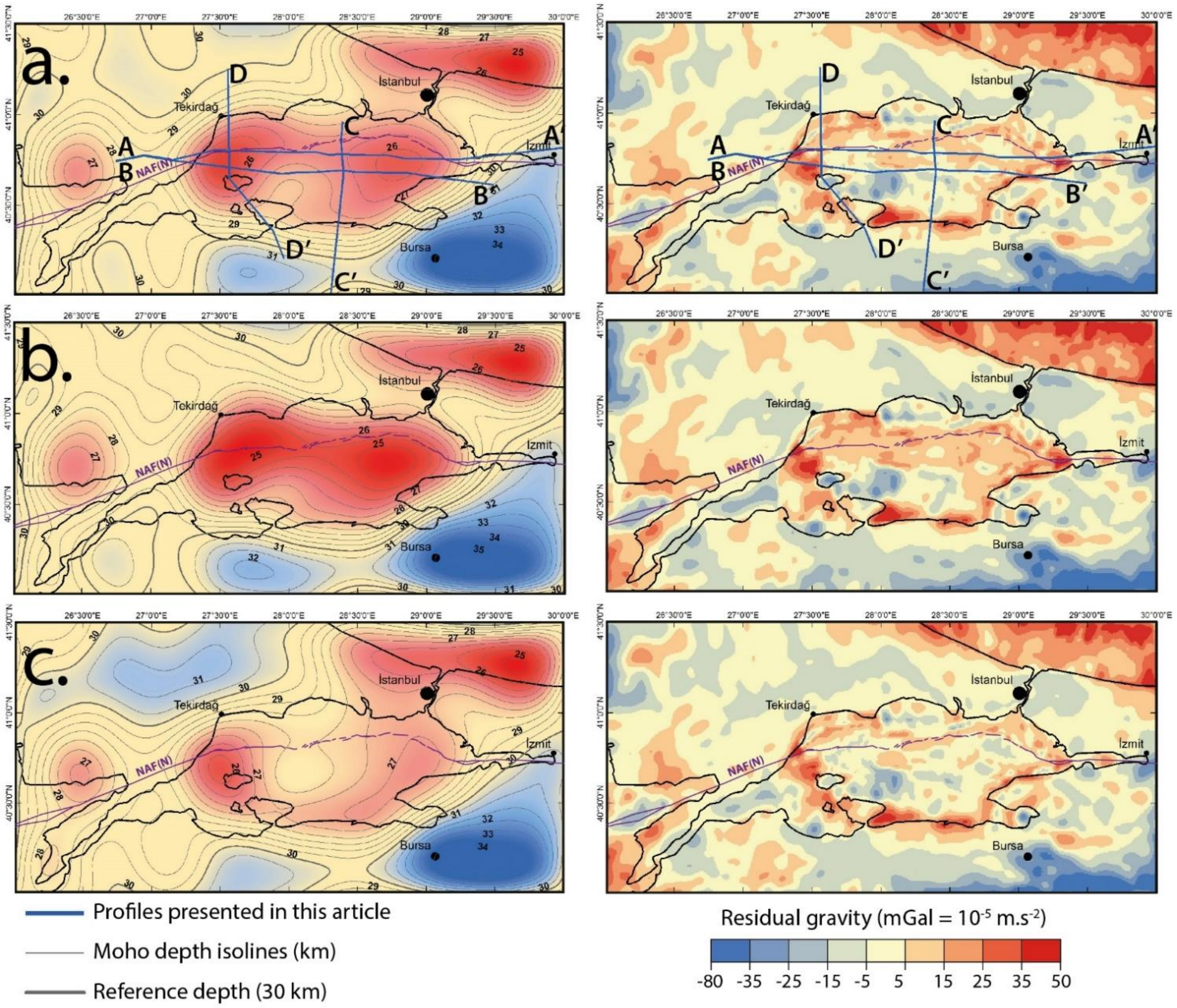

Figure 6. Moho depth topography and gravity residual computed with variable density for the syn-kinematic sediment layer and the pre-kinematic sediment layer with, respectively: a. 2.23 and 2.59 g.cm-^{3}, b. 2.07 and 2.53 g.cm-^{3} and c. 2.39 and 2.65 g.cm-^{3}. Thick blue lines: locations of profiles presented in Figure 7.

The southern part of the positive "belt", which spreads along the southern shore, coincides with a positive gravity anomaly in the initial gravity data (see Figure 3). The preservation of this positive anomaly as a residual, independently of the sediment densities, indicates that our model probably lacks a structure which should account for it. For instance, it could be an elastic flexure effect inside the upper crust related to the tilted blocks in the southern basins [*Bécel et al.*, 2009], as we have no constraint on the upper crust at that location.

Away from the Marmara Sea, at the limits of the area of study in the North-East and South-East directions, the overly bended Moho indicates an edge effect due to the fact that the Moho is approximated with Fourier transforms. This problem will not be discussed further as the area is large enough to avoid such effect near the Marmara Sea.

4.1. Compatibility with published geophysical studies

To assess the accuracy of our model, we here compare our results with previously published Moho depth data from geophysical surveys: *Bécel et al*. [2009] profiles based on Multi-Channel reflection Seismic (MCS) lines, on-land stations and OBSs, and *Karabulut et al.* [2013] 650 km long North-South profile based on a tomographic study. As the parameters in our study were chosen in order to reach a model close to those constructed by these geophysical surveys, it is expected that amplitude and main structures are alike. We will discuss the remaining differences.

In *Bécel et al.* [2009], three profiles based on marine multi-channel reflection seismic, Ocean Bottom Seismometers (OBSs) and onshore reflection/refraction records are presented. Figure 7 shows a comparison of these three profiles and of our results.

In wide-angle refraction-reflection modeling, reflections give information about the topography of the interfaces whereas refractions constrain the velocity of the medium, which in turn has an effect on the depth of the interfaces. On the far offset stations, the reflection from the top of the lower crust (PiP) and Moho (PmP) are clear. However, at the edges of the profiles, due to the sparse refraction sampling and the velocity-depth ambiguity, the depth of the interfaces are expected to be less accurate than in the regions sampled abundantly by both reflections and refractions (e.g. below the NMT the top of the crystalline crust is sampled abundantly by reflections from the basement and by refracted waves within the basement). Furthermore, even if *Bécel et al*. [2009] positioned the Moho at about 35 km away from the basin, this is an a priori depth and they found evidence only for 5 km of absolute Moho depth variation. Thus, we will focus on comparing the profiles under the NMT, where it is best constrained by seismic data.

The AA' profile [*Bécel et al.,* 2009] under the NMT shows a thinning almost constant under the main basins. Our 3D model is consistent with this 2D model under the basins, with a Moho depth at about 25 km and a slightly thicker crust in the central part of the Marmara Sea.

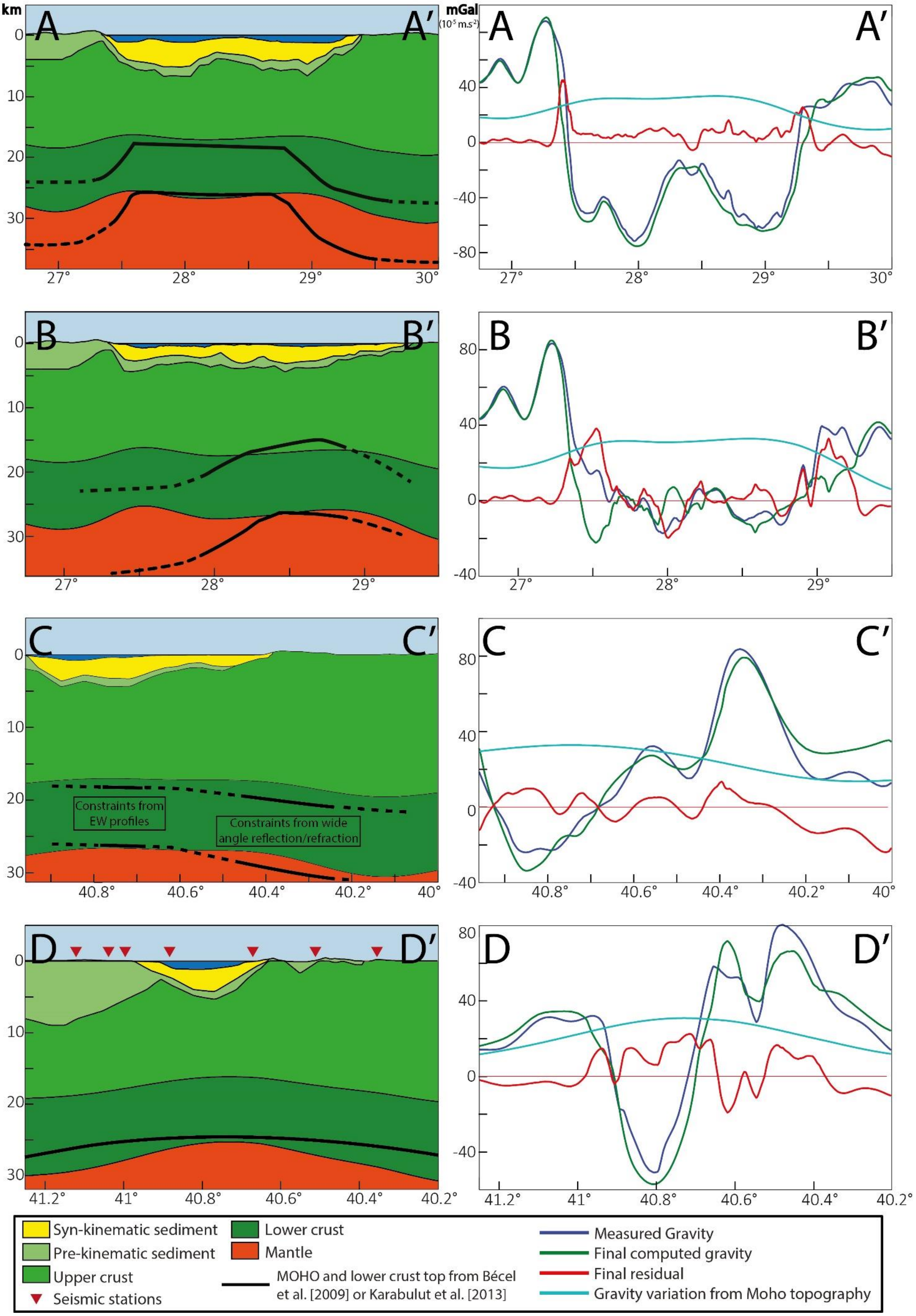
km
mGal (10^{-5} m.s^{-2})
A
A′
B
B′
C
C′
D
D′
0
10
20
30
27°
28°
29°
30°
40.8°
40.6°
40.4°
40.2°
40°
41.2°
41°
80
40
0
-40
-80
Constraints from EW profiles
Constraints from wide angle reflection/refraction
Syn-kinematic sediment
Pre-kinematic sediment
Upper crust
Seismic stations
Lower crust
Mantle
MOHO and lower crust top from Bécel et al. [2009] or Karabulut et al. [2013]
Measured Gravity
Final computed gravity
Final residual
Gravity variation from Moho topography

Figure 7. (previous page) Gravity, geological data and results along four profiles (see location on Figure 6.a.). Left column: geological setting, modeled Moho and modeled upper crust/lower crust boundary. Right column: gravity measurement, computed gravity, residual anomaly and gravity field induced by Moho depth variation. Profiles A., B., and C. coincides with profiles presented in Bécel et al. [2009] and profiles D. is localized on Karabut et al. [2013] cross-section. Bold black lines on the left column represent Bécel et al. [2009] Moho and lower crust depth on profiles A., B., and C., and Karabulut et al. [2013] Moho depth on profile D. Doted lines correspond to locations where seismic constraints are thin.

The consistency of the two models along the southern shelf E-W BB' is more questionable as *Bécel et al.* [2009] show a thinning under the limits of the İmralı Basin whereas our model gives a similar result as the profile under the NMT. However, the main data used to constrain this southern profile by *Bécel et al.* [2009] are shots along a MCS line, which was limited to the ship track East of Marmara Island. On the western extremity of this line, *Bécel* [2006] detected evidence of a deepening of the lower crust top and interpreted this as the edge of the thinning, concluding that the crust is un-thinned under the Marmara Island. But the dip they detected could in fact correspond to the edge of the thinning centered, in our model, under the Çınarcık Basin.

The third profile (CC') interpreted by *Bécel et al.* [2009] is oriented NS and shows that a thinning under the North Marmara Trough is required in order to fit the computed PmP waves travel time with records from the Oren on land station in the south. The profile in our model presents a shallower Moho overall but the inclination inferred from the Oren station of 4.3° is very close to the inclination in our model, at the location of *Bécel et al.* [2009] constraint on the Moho.

To conclude, our model is consistent with *Bécel et al.* [2009] model where seismic data give good constraints. But unlike *Bécel et al.* [2009], who determined that the thinning is localized under the main basins, we propose that the thinning zone is wider and extends southward, including below the Marmara Island anticline [*Le Pichon et al.*, 2013].

The 650 km long profile presented in *Karabulut et al.* [2013] was constructed based on a tomography study using receiver functions. Because only on land stations were used, the data spacing is not tight in the Marmara Sea and there are gaps of about 65 km in the north and 30 km in the south between the stations along the shores and the next stations on the profile. As our model amplitude in profile DD' was mainly based on *Karabulut et al.* [2013] study, we do observe the same depth in the middle of the Marmara Sea and away from the basins. However, the apparent wavelength of our model is different with a thinning spread on about 120 km compared to 220 km in *Karabulut et al.* [2013] model. Given that *Karabulut et al*. [2013] horizontal resolution is about 40 km, the two models are not inconsistent.

4.2. Isostatic model

To evaluate further the validity of our model, we compared it to an isostatic filtered model. The isostatic Moho model was calculated through an Airy mass compensation condition on columns of 35 km thickness and of about 0.4 km^2. The compensation was made to fit with an ideal column of 30 km of crust and 5 km of mantle. The basin model is the same as before, with two sediments layers. The resulting Moho was filtered through a Butterworth low-pass filter set to give the best correlation coefficient of the two models frequency signatures.

The result (see Figure 8.b) is close to the Moho inverted from gravity values, with two areas of maximum thinning in the eastern and western parts of the Sea of Mamara. Also, the western zone of thinning in the isostatic model is centered NE of the Marmara Island, not north of the island. This result is unsurprising as, by construction, the isostatically compensated Moho image is merely a filtered image of the basin geometry. The maximum thinning zones thus correspond to the areas with the highest thicknesses of basin fill. The range of Moho depth variations is also comparable, which indicates that the present day basin geometry is in large part isostatically compensated. However, local comparison with our model indicates that there is an isostatic deficit under the NMT but an excessive compensation under the southern basins where our modeled Moho is higher than the isostatic Moho.

The residual gravity anomaly (difference between measured gravity and modelled gravity anomaly) is significantly larger with the isostatic model than with the inversion results. This is because the Moho uplift in the isostatic model is too narrow to create a prominent gravity variation. Thus, the small amplitude of the gravity anomaly generated by the isostatic Moho uplift cannot compensate for the gravity anomaly in the Marmara Sea after basin correction (see Figure 5). As the amplitude of the gravity anomalies are filtered depending on wavelength and interface depth, according to equation (2), the Moho uplift would need to have a larger amplitude or to contain longer wavelengths in order to fit the gravity anomaly. A larger amplitude is not very realistic as it would imply that there is a net mass excess where the basins are deeper. But longer wavelengths is what our model suggests. In any case, a model based solely on local isostasy cannot explain the gravity anomaly.

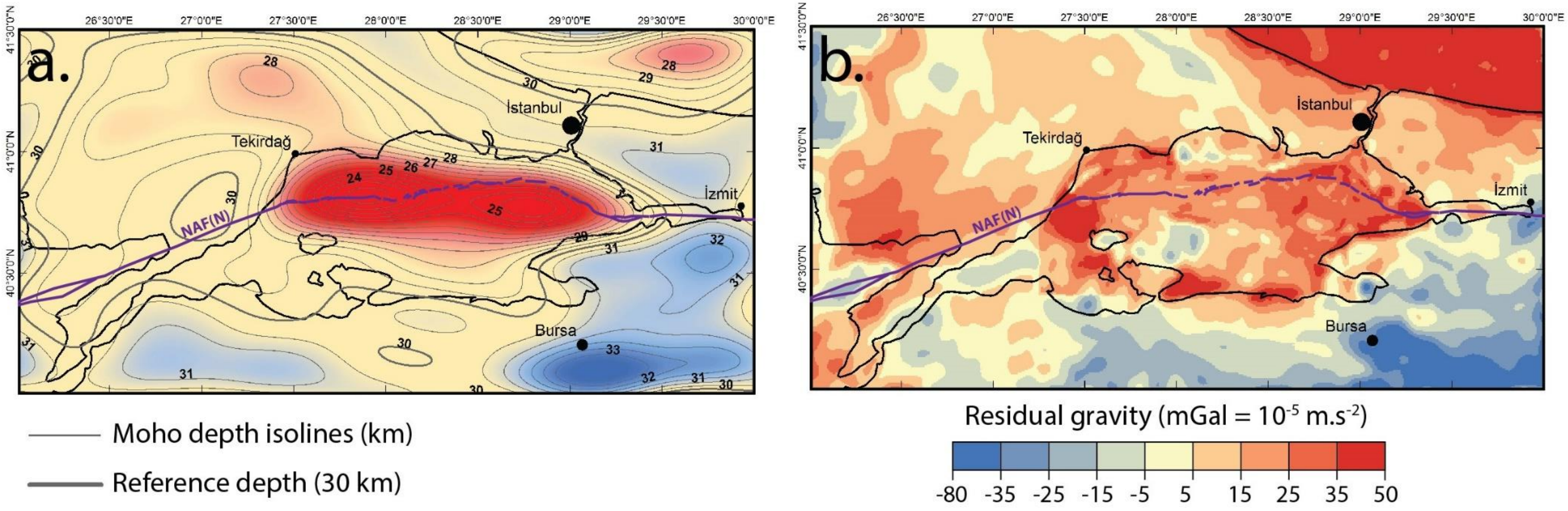

Figure 8. a. Moho depth and b. Gravity residual of the isostatic model. Geological setting, gravity data and sediment characteristics used as inputs are the same as in previous models. The compensation depth is 35 km and the reference crust thickness is 30 km The Moho topography is filtered to discard small wavelength. Apart from the filtering, it is a direct response to the geological model.

4.3. Uncertainties

The main factor that may compromise the accuracy of the Moho topography and of the various calculations based on it is that we did not considered laterally variable densities. As illustrated by *Aydin et al.* [2005], below the Sea of Marmara and south of it, Curie point depths are higher than 20 km. As a consequence, higher temperatures and lower densities in the lower crust and in the mantle are expected. This may not be problematic for the application of the Parker method as density variations at interface should not fluctuate significantly, but a thermal gravity correction could deal with gravity anomalies generated by lower densities [*Bai et al.*, 2014]. Since the temperature variations is oriented NS, such a correction would lower the visible divergence in the gravity anomaly before inversion (see Figure 5) between the North and the South. However, the amplitude of this anomaly is small compared to the anomalies dominating the Marmara Sea area. Only a small impact in the final result is expected. If this anomaly was corrected before inversion, we would predict a deeper Moho in the North and a relatively higher Moho in the South. This could in part explain the apparently thinner crust in our model beneath the Istanbul block, which appears as a relatively cold zone in the Curie point map [*Aydin et al.*, 2005].

Furthermore, we defined our sediment and upper crust limits from density and/or age contrasts, regardless of rock types. If this model is well constrained in the Marmara Sea from the seismic data, uncertainties increase away from the Sea. This effect adds up to the fact that the upper/lower crust density contrast is also solely constrained in the Marmara Sea by *Bécel et al*. [2009] deep surveys. However, the data coverage is sufficient to rule out the isostatically compensated model in which the Moho uplift would be mostly confined below the deep basins.

Another source of uncertainty is the likely existence of a damage zone with low P- and S-wave velocity and low density along the Main Marmara Fault. Since datasets in the Marmara Sea still lack a fine enough resolution to reveal the geometry and characteristics of such a zone, we did not integrate it in our model but used the characteristics of the San Andreas Fault low velocity zone to evaluate the impact that such a zone could have on the Moho model in the Marmara Sea. Recent studies based on the San Andreas Fault Observatory at Depth (SAFOD) project have shown that the damaged zone is about 200 m and extends at least as deep as 7 km [*Jeppson & Tobin*, 2015; *Li & Malin*, 2008]. We used the 2D equation by *Telford et al*. [1990] for calculating the 2D gravity effect of a vertical dyke (applied to a zone of low density along a fault). We considered a 200 to 300 m wide zone reaching the surface and going as deep as 15 km, which corresponds to the maximum depth of the brittle crust floor [*Schmittbuhl et al.*, 2016]. We evaluated the maximum value of the density anomaly to 400 kg/m^3 using velocity-density relationships proposed for the San Andreas fault damage zone [*Roecker et al.*, 2004]. We thus obtain a maximum anomaly accounting for the density loss along the fault of -8.9 mGal, which drops to -1.8 mGal 5 km away from the fault. As for the impact on the Moho modelling, the uplift of the Moho found after correcting for the effect of a damaged zone is increased by a maximum of 120 m under the fault, which has a negligible effect on the volume calculations we will carry in the discussion.

5. Discussion

The Moho depth variation model computed in this study shows a distribution of thinning which appears to roughly mimic the base of the syntectonic basins [*Bayrakci et al.*, 2013]. The Moho highs do not exactly match the upper crust lows but are both close to the two Marmara most active basins. The two highs are separated by an inflexion in the Moho roughly at the Central High location, where the minimum extension is observed in the North Marmara Trough. The thinning also appears to spread over a wider zone. This indicates that the stretching component of strain in the Marmara Sea has been distributed differently in the upper crust and at the Moho level, implying some ductile flow in the lower crust.

If this model is hardly compatible with any model based on rigid blocks, like *Armijo et al.* [1999] block model based on present day active fault geometry in the brittle crust, it shows a geometric compatibility with the low angle detachment system identified in the Eastern and Central Marmara Sea from seismic reflection and refraction profiles [*Bécel et al.*, 2010]. But the zone of crustal thinning still appears broader extending below the southern shelf and the Marmara Island. A more detailed comparison of the Moho topography and of the basement topography is presented in *Le Pichon et al.* [2015].

5.1. Overall extension in the Marmara Sea

To quantify the overall extension accommodated during the Marmara Sea basins formation, we considered the volume difference between the crust in our model and a reference pre-kinematic model with a constant 30 km thick crust and no sediment basins nor hills. Here, the term “crust”, refers to the lower and upper crust, as well as to the pre-kinematic sediment. In order to avoid interferences from older geological systems, we discarded zones where the Moho depth variations are influenced by Pre-Pliocene tectonics, for instance the Uludağ massif which exhumation occurred during the early Miocene [*Okay et al.*, 2008], the Black Sea, and the Thrace Basin. Figure 9 shows the final 19150 km^2 area we considered.

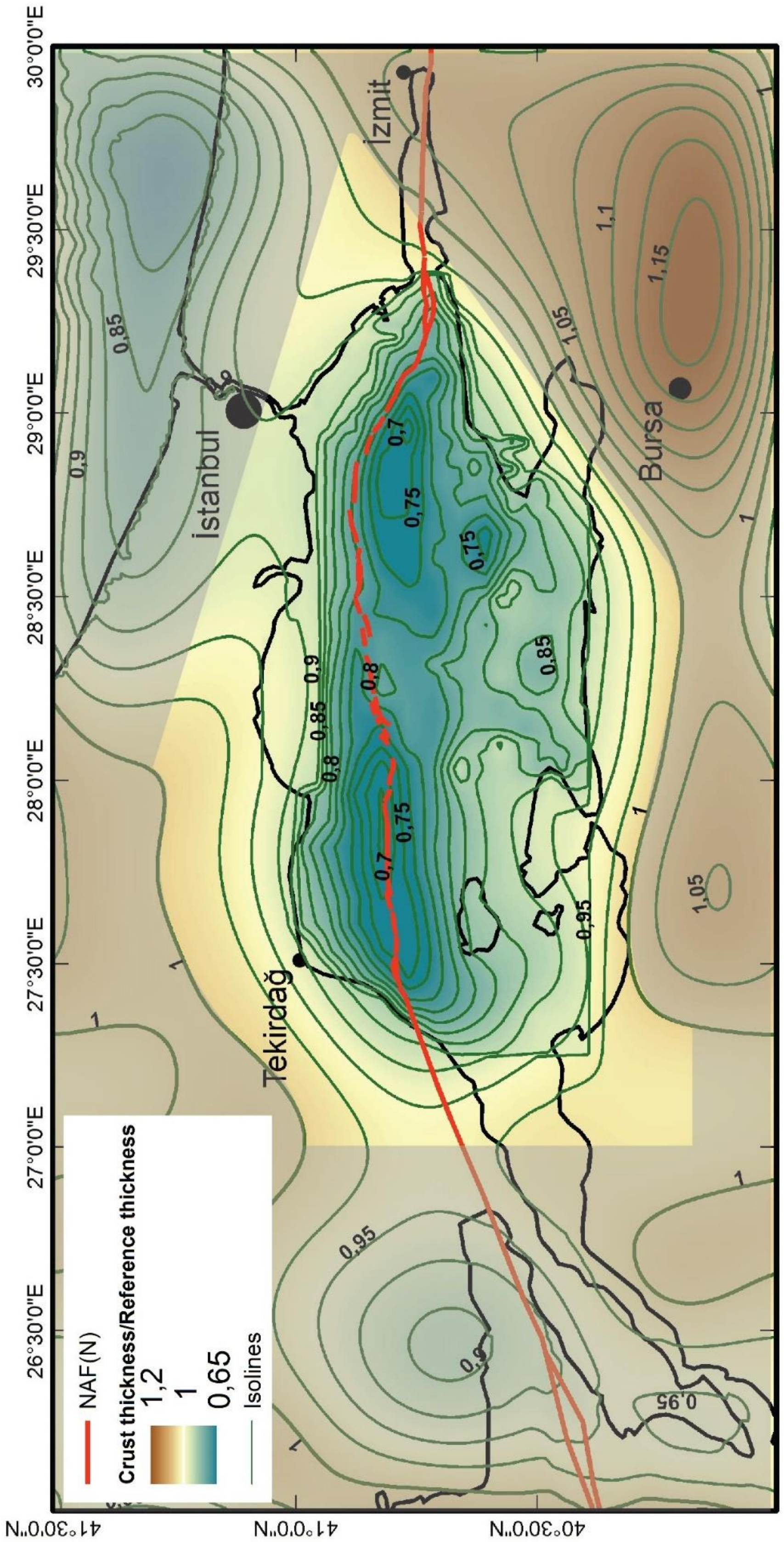

Figure 9. Thinning rate corresponding to our model crust thickness over 30 km reference thickness. The unshaded area correspond to the zone that was considered in a crust volume calculation to estimate a 2100±250 km^2 extension surface in the Marmara Sea.

We computed the proportion of the area that could be accommodated with this ideal crust, given the volume of crust in our model. We obtained that, with the volume of crust given by our model in the 19150 km^2 area we defined, a 30 km thick reference crust could cover only 17000±300 km^2. Thus, our model indicates a total of 2050±300 km^2 of extension during the formation of the Marmara Sea. Figure 10 shows a schematic explanation of this calculation. The uncertainty is obtained by varying the sediment densities within the defined bounds and varying the reference Moho depth by 2 km around the 30 km reference value, which corresponds to *Karabulut et al.* [2013] estimated uncertainty on Moho picks. Because the reference thickness is also an input for the Moho topography inversion, the uncertainty on "missing" surface may seem smaller than expected.

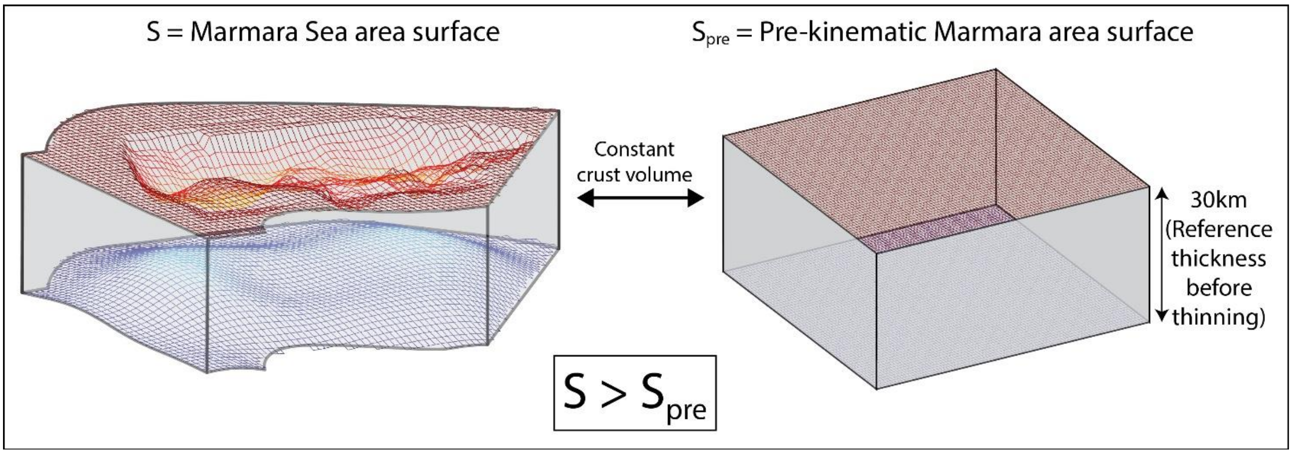

Figure 10. Schematic explanation of the extension surface calculation. The surface difference between the current model and the ideal pre-kinematic model corresponds to the extension. We compute the pre-kinematic block surface regardless of its shape.

Armijo et al. [2002] presented a reconstitution of the area at -5 Myr based on present day active fault geometry in the brittle crust. They delimited four rigid blocks creating two main zones where oblique slip and extension occur, along the deep basins and along the southern coast. A third zone, further south, will not be considered as it is in great part outside of the area we modeled. Between these two systems, an additional fault system identified beneath the Southern continental shelf, the Southern Marmara Fault, has been mostly active during the Pliocene [*Le Pichon et al.*, 2013]. The total slip on the Shelf Fault is not precisely known and this fault was interpreted as a dominantly transpressional, deformation with only local transtension associated with fault bends. A reconstitution assuming an offset of 85 km on the Ganos fault branch [*Armijo et al.*, 2002] yields a surface increase by extension of about 6900 km^2 with, respectively, 3200 km^2 and 3700 km^2 along the deep basins and the southern shelf. This is about 3 times the value we found. Matching those results would imply an average initial crust thickness of 42 km. Other parameters are displacement and slip obliquity. It is possible that the block model overestimates obliquity. Reducing obliquity in the Marmara Sea would increase compression generated at the fault bends in Ganos Mountain area in the West and Armutlu area in the East. This compression today results in active uplift, but did not result in an observable crustal thickening yet. We conclude that reducing the obliquity is unlikely to solve the discrepancy. More likely, the total 85 km slip assumed in the block model is an overestimate. The thinned domain that we obtain from gravity modeling appears wider than the Marmara Trough and extends southward beneath the shelf, but is not resolved as two distinct zones of extension. The distribution of crustal thickness thus obtained does not support the presence of a large component of localized extension along the southern fault system. Although the presence of active faults scarps running along the Southern Marmara coast between Gemlik Bay and Kapıdağ Peninsula can be argued based on geomorphology, the eastward connection of this fault system to Ganos Fault is unclear. A Southwestward prolongation and connection with the southern branch of the NAF is another possibility [e.g. *Şengör et al.*, 2014] that would produce less extension, and also less displacement along Ganos Fault. It is thus possible that the total extension across the Southern Marmara zone is much smaller than in the block model of *Armijo et al*. [2002]. In fact, in the block model, the extension in the northern zone alone is a better match for the extension we calculated over the whole Marmara Sea area.

In this total surface extension calculation, we used the reference 30 km depth as the thickness of the crust before deformation. However, in this area where the Hellenic subduction rollback has been active for more than 20 Myr [*Jolivet and Faccenna,* 2000], it is possible that a large scale thinning and smoothing by ductile flow in the lower crust has occurred, even though we do observe 30 km as the average value in the region around the Marmara Sea [*Karabulut et al.,* 2013; *Tiberi et al.,* 2001]. In that case, the construction of the Moho variation with regards of a local reference depth would still be valid but a more regional reference depth should be considered in the calculation of overall extension.

5.2. Tectonic regime evolution during the last 5 Myr

A complementary approach is to compare our estimate of finite extension with estimated present day rate of extension from geodesy. Geodetic data cannot constrain the distribution of motion within the Marmara Sea but the bulk extension of the domain comprised within the same area as the one we selected (see Figure 9) may be calculated from interpolated velocity fields [*Özeren and Holt,* 2010]. The deformation field in the Marmara Sea area was calculated based on a new mathematical approach based on solving for the elastic deformation sources [*Haines et al.*, 2015]. In zones, like the Marmara Sea, which have dense GPS data along the boundaries of the domain of interest, this approach provides an interpolation of the deformation field within the domain consistent with an assumption of elastic strain in a homogeneous upper crust. However, results are independent of assumptions on where faults are located, and thus cannot be used to ascertain slip rates on offshore faults. The areal strain is calculated from the divergence of the vertical derivatives of horizontal stress (VDoHS) rates, divided by an elastic constant, and is equal to the divergence of the velocity field. Using the GPS data presented in *Reilinger et al.* [2006], we calculated the extension rate in our domain by considering the areal strain integrated over a wide zone covering the entire thinned crust domain. This result does not depend on the details of the VDoHS field. We obtained an extension rate on our surface of 396 $km^2.Myr^{-1}$.

Thus, considering the total finite extension calculated before and assuming a stable extension rate similar to the present rate, the Marmara Sea extension could have been formed in 5.2±0.7 Myr. Although this time period could have accommodated a stable extension rate, there is little chance that the fault system and the way the extension was distributed has been steady as 5 Myr is considered as the maximal age for the incursion of the North Anatolian Fault system in the Marmara Sea [*Şengör et al.*, 2005; *Armijo et al.*, 1999]. In fact, variations with time of the rate, the width of the deformation zone and of the rate of motion are suspected [e.g. *Şengör et al.*, 2005]. *Grall et al.* [2012] identified a progressive change in basin subsidence distribution in the Marmara Central Basin, implying that the zone affected by extension has been wider during some time in the Pliocene, likely in relation with detachment systems identified in seismic reflection data [*Bécel et al.*, 2009]. *Le Pichon et al.* [2015] propose that a system analogous to the Corinth detachment system was active in the Pliocene between 4.5 and 3.5 Myr, prior to the initiation of the Main Marmara Fault, and accommodated strain at the tip of the propagating North Anatolian Fault. The beginning of this extension phase as described by *Le Pichon et al.* [2015] lies in the uncertainty range of our evaluation based on present day extension rate and Moho topography. We propose that the extension strain in the Marmara zone has been stable or slightly decreasing since the Pliocene, maintaining a constant overall regional extension, but that the incursion of the North Anatolian Fault system restructured the distribution of the extension from a wide zone with high-scale detachment and distributed extension to the current situation where extension is mostly carried along the Main Marmara Fault.

For the last 1.5 Myr, considering a geological slip rate of 18 mm/yr on the Main Marmara Fault [*Le Pichon et al.*, 2015; *Grall et al.*, 2013; *Kurt et al.*, 2013] and supposing that the extension was evenly carried along the 160 km long North Marmara Trough, our surface extension rate leads to an extension rate of 2.5 mm/yr and an average angular obliquity of 7.9° between velocity vector and local plate boundary orientation.

Based on the repartition of the crust thinning (see Figure 9), we can make a few assumptions on how the purely extensive system was functioning prior to the North Anatolian Fault propagation. We see that there is a striking difference between two zones, delimited approximately by a SW-NE line crossing the eastern tip of the Kapıdağ Peninsula and the Kumburgaz Basin. In the eastern zone, the thinning is stretched all the way to the southern coast line where the crust thickness is only 80 % of our reference thickness. In the western zone, only a small zone centered on the Tekirdağ Basin southern limit shows a crust thickness below 80 % of our reference thickness, and the Main Marmara Fault crosses the zone at the maximum of the thinned zone. In the east, the shifting of the fault in respect of the thinned zone could simply be the effect of the Çınarcık Basin fast subsidence [*Le Pichon et al.*, 2015], originating from the releasing bend [*Kurt et al.*, 2013]. On the other hand, in the west, there is no shifting of the thinning toward the Tekirdağ Basin depocenter. We explain this dissimilarity by a difference in the setting before the fault propagation. In the west, where evidence of a large-scale detachment is yet to be found, the extension may have been distributed on multiple fault zones. Thus, no well-defined zone of thinning was created. Whereas in the East, detachment functioning [*Bécel et al.*, 2009; *Le Pichon et al.*, 2015] caused a broad but well defined thinned zone. In this zone, the lower crust was weakened by isotherm rising and ductile flows were facilitated. After the propagation of the North Anatolian Fault northern branch, the extension was mostly carried by asymetrical basins along the main fault. However, in the eastern Marmara zone the extension system remained active, as indicated by steady-state subsidence in İmralı Basin [*Sorlien et al.*, 2012], and facilitated the equalization and the spreading of the Moho indentation by ductile flow from the south, maintaining a shift of the thinning location toward the South of the fault. In the following part, we quantify the ductile flow in the lower crust.

5.3. Upper and Lower crust extension budget and ductile flow in the lower crust

If stretching is independent of depth, as in McKenzie [1978] model, and if local isostatic compensation is applied at the Moho, the indentation of the Moho should nearly be a mirror image of the basin geometry. The results of the gravity inversion indicate that this is not the case in the Sea of Marmara and we argued that ductile flow in the lower crust could be at least part of the explanation. In the following we will show that the volume of lower crustal flow does not need to be large to explain the observations.

Let us divide the thinned crust area along latitude 40.7 °N into a northern domain containing the Northern Marmara Troughs and a southern domain (see Figure 11). We assume that the volume of the basins and of the Moho uplift are proportional to the stretching taking place in the upper crust and in the lower crust respectively. We also assume that ductile flow in the lower crust fully accounts for discrepancies in the stretching distribution between the upper crust and the lower crust. Thus, comparing the distribution of the basin volume and of the Moho indentation in each domain will give us a maximum value for ductile flow between the northern and the southern domain. Our model indicates that, in the upper crust, 69 % of the basin volume is in the northern domain while the rest, 31 %, is in the south. In the lower crust, only 55 % of the Moho uplift is in the northern domain and 45 % is in the southern domain (see Figure 11). We conclude that 14 % of the Moho uplift volume is moved between the northern and southern domain, compared with the case where the distribution of extension is the same in the upper and lower crust (69% vs 31%). This corresponds to 5.8 x 10^{12} m^3 of crust material that was displaced northward to accommodate for the Moho uplift. Considering that this volume is a maximization of the ductile flow in the lower crust, the maximum surface extension related to the ductile flow can be calculated knowing the ductile crust thickness.

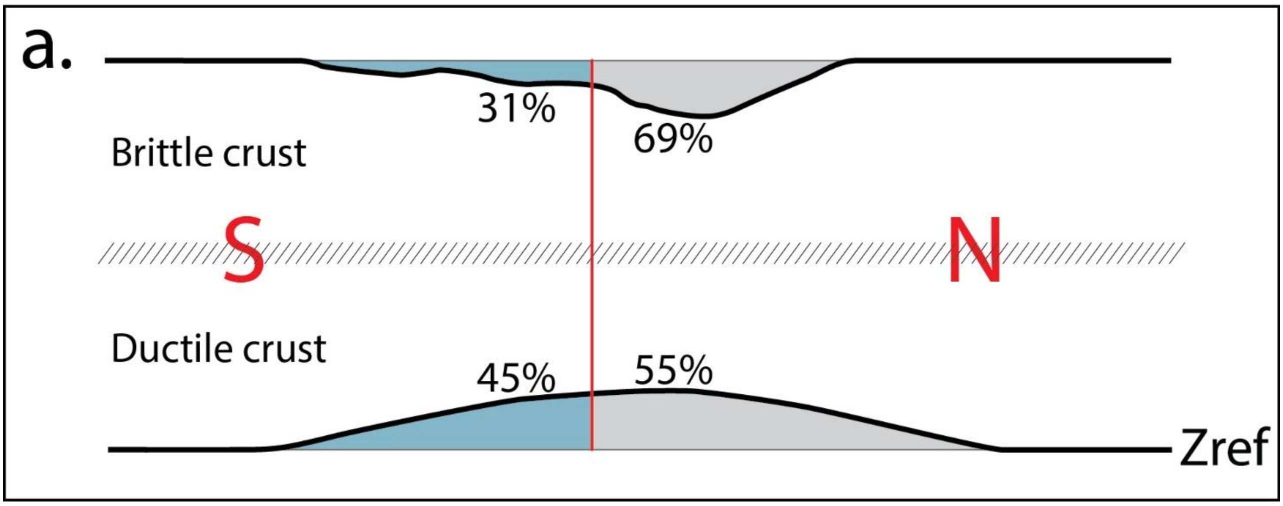

Figure 11. Schematic 2D illustration of the comparison between the basin volume in the upper crust and the Moho uplift in the lower crust. Considering that these volumes are proxies for the stretching, and that lower crust thinning that is not proportionally observed in the upper crust implies ductile flow, we find that 14% of the uplift in the lower crust is shifted from the northern block (N) to the southern block (S) and is related to lateral ductile flow.

Micro seismicity distribution indicates that the floor of the brittle crust is at around 15 km [*Schmittbuhl et al.*, 2016]. However, some lateral variations of the brittle crust thickness can be suspected as the geothermal gradient increases from north to south of the Marmara Sea. *Aydin et al.*, [2005] indicates that the Curie-point depth reaches about 24 km within Istanbul block in the north and decreases to about 12 km south of the Marmara Sea. Regional magnetic studies find an average Curie-point depth of 14.5 km in the Marmara Sea area, compatible with seismicity depth distribution [*Ates* et al., 2003], but the resolution of the spectral method used in both studies is insufficient to resolve the details of the North-South Curie-point gradient at the local scale. In addition, the maximum depth at which the upper crustal detachments could be imaged in the Eastern Marmara Sea is 13 km [Bécel et al., 2009]. We thus retain a brittle crust thickness of about 15 km, possibly thinner in extended domains. This corresponds to an initial ductile lower crust thickness of about 15 km.

We estimated earlier that the maximum volume of lower crust flow transferred from the southern to the northern domain to account for the lateral variation of lower crustal thickness compared to upper crustal thickness is 5.8×10^{12} m^3. The average surface of lower crust transferred is thus 390 to 585 km^2, assuming that the thickness of the ductile layer is in the 10-15 km range. This represents about 15-30% of the total 2050±300 km^2 surface extension during the Marmara Sea basin formation. Considering that the length of the Marmara Sea is 160 km., out of 12.8±1.9 km of extension perpendicular to the EW direction of the Main Marmara Fault, the shearing between upper and lower crust needed to explain the distribution of crustal thickness only amounts to 2.4 to 3.7 km. Even if our model is quite schematic and maximizes ductile flow in the lower crust, this maximum flow is relatively small compared to the total extension. This shows that moderate upper/lower crust decoupling can account for the observed distribution of extension in the upper and lower crust.

In fact, with a brittle crust thickness of about 15 km and a maximum sediment thickness of about 6 km, the Marmara Sea case fits *Petrunin and Sobolev* [2006] results of rheological models linking brittle crust thickness and sediment thickness, intermediate between the Gulf of Aqaba and the Dead Sea cases considered in their study. Some involvement of the lower crust is thus probably needed to account for the Moho uplift under the Marmara Sea as well as for the southward spread of the extended domain. Unlike under the Dead Sea, the crust is ductile enough for a partial compensation within the crust and some Moho uplift to occur but, unlike under the Death Valley, ductile flows are not sufficient to regionally flatten the Moho. Whether the Marmara Sea is more representative of strike-slip basins in continental crust worldwide cannot be assessed easily as cases with well-constrained Moho geometry are relatively few.

Several other well studied cases correspond to older basins with complex history (e.g. Songliao Basin; *Wang et al*., 2007; *Liu and Niu*, 2011) or to active basins with more advanced extension (e.g. Andaman Sea; *Morley and Alvey*, 2015). Moreover, the tectonics of the Marmara Sea are influenced by the interaction between the NAF strike-slip system and the Western Anatolian extension driven by the Aegean subduction [*Le Pichon et al.*, 2015]. We also noted a difference in the geothermal gradient North and South of the Marmara Sea [*Aydin et al.*, 2005]. The combination of these factors may have favored the development of crustal extension south of the present location of the main strike-slip fault.

6. Conclusion

Using the Parker method and a new inversion method we developed for this study, we corrected the free air gravity anomaly in the Marmara area from the topography and density structure of the sedimentary basins, and built a Moho depth model showing a saddle shaped uplift under the Marmara Sea. From a reference depth of 30 km, the Moho shows two main uplifts reaching over 25 km, centered north of the Marmara Island and below the İmralı and Çınarcık basins, and connected by a ridge staying above 27 km. The main novel contribution of this model is to show that the thinning is not limited to the NMT but extends further than the Marmara Sea coasts. While this finding is consistent with the hypothesis of an early phase of extension involving crustal scale detachments [*Becel et al., 2009*; *Le Pichon et al*., 2015], we propose that this early stage process is associated with a steady-state lower crustal flow toward the deep Marmara Trough in a continuously evolving fault system. The gravity residual after correcting for the whole basin and crust model shows that there is no remaining large wavelength anomalies which, together with the 1 km average Moho depth error, testifies for our model robustness.

The Moho topography map and the upper crust model constitute a 3D model of the crust. The comparison of this model with an ideal un-thinned crust of the same volume gave us the total surface extension during the formation of the Marmara Sea basins. We found 2050±300 km^2, corresponding to 12.8±1.9 km of extension in a direction normal to the plate boundary along the 160 km long Marmara Sea. When related to the current GPS-derived areal extension rate of 396 km^2.Myr^{-1}, it leads to an age of 5.2±0.7 Myr for the system. This age span is roughly compatible with the geological age of the Marmara Sea basins

The difference in the apparent distribution of extension at the upper crustal level, from basin geometry, and at the Moho level, from the gravity inversion, may be explained by minor decoupling between upper and lower crust deformation. A horizontal displacement in the lower crust of about 3 km toward the north (representing about 25 % of the total extension, and less than 6% of the total motion accommodated in the Marmara Sea strike-slip zone) can explain the amplitude of the Moho uplift south of the NMT. However, the relative contribution to the present day crustal structure of ductile lower crust deformation and early extension before the incursion of the North Anatolian Fault still needs to be assessed.

Finally, we propose that the Marmara Sea lower crust ductility is intermediate between the two much studied end-member cases of transform extension zone, the Dead Sea and the Death Valley, where no Moho uplift is observed. Moho uplift can be interpreted primarily as a consequence of crustal rheology but the boundary conditions (Aegean extension in the Marmara Sea case) can also influence the amount and distribution of crustal extension and should be taken into account when comparing with other strike-slip basins worldwide.

7. Acknowledgements

This work was funded by MARSITE FP7 EU project, by COST action FLOW, and by INSU support fund for scientific cruises. We thank the GENAVIR crew during the MARSITE cruise as well as the scientific team for their help and time spent on discussions and explanations during on-board operations. Special thanks to Patrick Le Roy for his detailed presentation of the N/O Pourquoi Pas? equipment. We thank Hayrullah Karabulut, Louis Geli, Celal Şengör and, more particularly, Xavier Le Pichon for discussions and constructive comments on the manuscript.

The satellite gravity data are available on the Scripps Institution of Oceanography (University of California San Diego) website (http://topex.ucsd.edu/index.html) and gravity data retrieved by the N/O Pourquoi Pas? gravimeter are available on the IFREMER data repository website (http://data.ifremer.fr/). All other sources used to build the geological model are published and referenced in the manuscript. Input files necessary to reproduce the model are available from the authors upon request (kende@cerege.fr).

8. References

Aitken, A. R. A., Salmon, M. L., & Kennett, B. L. N. (2013). Australia's Moho: A test of the usefulness of gravity modelling for the determination of Moho depth. *Tectonophysics*, *609*, 468–479. doi:10.1016/j.tecto.2012.06.049

Aloisi, G., Soulet, G., Henry, P., Wallmann, K., Sauvestre, R., Vallet-Coulomb, C., … Bard, E. (2015). Freshening of the Marmara Sea prior to its post-glacial reconnection to the Mediterranean Sea. *Earth and Planetary Science Letters*, 413, 176–185. doi:10.1016/j.epsl.2014.12.052

Armijo, R., Meyer, B., Hubert, A., & Barka, A. (1999). Westward propagation of the North Anatolian fault into the northern Aegean: Timing and kinematics. *Geology*. doi:10.1130/0091-7613(1999)027<0267:WPOTNA>2.3.CO;2

Armijo, R., Meyer, B., Navarro, S., King, G., & Barka, A. (2002). Asymmetric slip partitioning in the Sea of Marmara pull-apart: a clue to propagation processes of the North Anatolian Fault? *Terra Nova*, 14(2), 80–86. doi:10.1046/j.1365-3121.2002.00397.x

Aydin, I., Karat, H. I., & Koçak, A. (2005). Curie-point depth map of Turkey. *Geophysical Journal International*, 162, 633–640. doi:10.1111/j.1365-246X.2005.02617.x

Bai, Y., Williams, S. E., Müller, R. D., Liu, Z., & Hosseinpour, M. (2014). Mapping crustal thickness using marine gravity data: Methods and uncertainties. *Geophysics*, 79(2), G27–G36. doi:10.1190/geo2013-0270.1

Bayrakci, G., Laigle, M., Bécel, A., Hirn, A., Taymaz, T., Yolsal-Cevikbilen, S., & Team, S. (2013). 3-D sediment-basement tomography of the Northern Marmara trough by a dense OBS network at the nodes of a grid of controlled source profiles along the North Anatolian fault. *Geophysical Journal International*, 194(3), 1335–1357. doi:10.1093/gji/ggt211

Bécel, A. (2006) Structure Sismique de la Faille Nord Anatolienne en Mer de Marmara, Phd Thesis, Institut de Physique du Globe de Paris.

Bécel, A., Laigle, M., de Voogd, B., Hirn, A., Taymaz, T., Galvé, A., … Özalaybey, S. (2009). Moho, crustal architecture and deep deformation under the North Marmara Trough, from the SEISMARMARA Leg 1 offshore–onshore reflection–refraction survey. *Tectonophysics*, *467*(1-4), 1–21. doi:10.1016/j.tecto.2008.10.022

Bécel, A., Laigle, M., de Voogd, B., Hirn, A., Taymaz, T., Yolsal-Cevikbilen, S., & Shimamura, H. (2010). North Marmara Trough architecture of basin infill, basement and faults, from PSDM reflection and OBS refraction seismics. *Tectonophysics*, 490(1-2), 1–14. doi:10.1016/j.tecto.2010.04.004

Ben-avraham, Z., Hänel, R., & Villinger, H. (1978). Heat flow through the Dead Sea rift. *Marine Geology*, 28, 253–269. doi:10.1016/0025-3227(78)90021-X

Ben-Zion, Y., Peng, Z., Okaya, D., Seeber, L., Armbruster, J. G., Ozer, N., … Aktar, M. (2003). A shallow fault-zone structure illuminated by trapped waves in the Karadere-Duzce branch of the North Anatolian Fault, western Turkey. *Geophysical Journal International*, 152, 699–717.

Biddle, K. T., & Christie-Blick, N. (1985). Glossary - Strike-slip deformation, basin formation, and sedimentation. *Special Publication of the Society of Economic Paleontologists and Mineralogists,* 375–386.

Burchfiel, B. C., & Stewart, J. H. (1966). “Pull-apart” origin of the central segment of Death Valley, California. *Geological Society of America Bulletin,* 77(April 1966), 439–442. doi:10.1130/0016-7606

Christie-Blick, N., & Biddle, K. T. (1985). Deformation and basin formation along strike-slip faults. *Society for Sedimentary Geology,* 37, 1–34. doi:10.2110/pec.85.37.0001

Christensen, N. I., Mooney, W. D., & Christensen, N.I., Mooney, W. D. (1995). Seismic velocity structure and composition of the continental crust: A global view. *Journal of Geophysical Research*: Solid Earth (1978–2012), 100(B6), 9761–9788. doi:10.1029/95JB00259

De Voogd, B., Serpa, L., & Brown, L. (1988). Crustal extension and magmatic processes: COCORP profiles from Death Valley and the Rio Grande rift. *Geological Society of America Bulletin,* 100(October), 1550–1567. doi:10.1130/0016-7606(1988)100<1550:CEAMPC>2.3.CO;2

Erickson, S. N., & Jarrard, R. D. (1998). Velocity-porosity relationships for water-saturated siliciclastic sediments. *Journal of Geophysical Research*, 103, 30385. doi:10.1029/98JB02128

Feng, R., & McEvilly, T. V. (1983). Interpretation of seismic reflection profiling data for the structure of the San Andreas fault zone. *Bulletin of the Seismological Society of America,* 73(6A), 1701–1720. doi: 73:1701-1720

Fliedner, M. M., Ruppert, S., Malin, P. E., Park, S. K., Jiracek, G., Phinney, R. a., … Thompson, G. a. (1996). Three-dimensional crustal structure of the southern Sierra Nevada from seismic fan profiles and gravity modeling. *Geology*, 24(4), 367–370. doi:10.1130/0091-7613(1996)024<0367:TDCSOT>2.3.CO;2

Garfunkel Zvi and Ben-Avraham Zvi. (1996). The structure of the Dead Sea basin. Tectonophysics, 266, 155–176. http://doi.org/10.1016/S0040-1951(96)00188-6

Gómez-Ortiz, D., & Agarwal, B. N. P. (2005). 3DINVER.M: a MATLAB program to invert the gravity anomaly over a 3D horizontal density interface by Parker–Oldenburg’s algorithm. *Computers & Geosciences*, *31*(4), 513–520. doi:10.1016/j.cageo.2004.11.004

Grall, C., Henry, P., Tezcan, D., Mercier de Lepinay, B., Bécel, A., Geli, L., … Harmegnies, F. (2012). Heat flow in the Sea of Marmara Central Basin: Possible implications for the tectonic evolution of the North Anatolian fault. *Geology,* 40(1), 3–6. doi:10.1130/G32192.1

Grall, C., Henry, P., Thomas, Y., Westbrook, G. ., Cagatay, M. ., Marsset, B., … Géli, L. (2013). Slip rate estimation along the western segment of the Main Marmara 1 Fault over the last 405-490 ka by correlating Mass Transport Deposits. *Tectonics*, 32(6), 1587–1601. doi:10.1002/2012TC003255

Haines, A. J., Dimitrova, L. L., Wallace, L. M., & Williams, C. A. (2015). Enhanced Surface Imaging of Crustal Deformation: Obtaining Tectonic Force Fields Using GPS Data. Springer.

Hergert, T., & Heidbach, O. (2010). Slip-rate variability and distributed deformation in the Marmara Sea fault system. *Nature Geoscience*, 3(2), 132–135. doi:10.1038/ngeo739

Huvaz, O., Karahanoglu, N., & Ediger, V. (2007). The thermal gradient of the Thrace Basin, NW Turkey: correlation with basin evolution processes. *Journal of Petroleum Geology*, 30(1), 3–24. doi:10.1111/j.1747-5457.2007.00003.x

Jeppson, T. N., & Tobin, H. J. (2015). San Andreas fault zone velocity structure at SAFOD at core, log, and seismic scales. Journal of Geophysical Research, 1–15. doi: 10.1002/2015JB012043

Jolivet, L., & Faccenna, C. (2000). Meditterranean extension and the Africa-Eurasia collision. *Tectonics*, 19(6), 1095–1106. doi:10.1029/2000TC900018

Karabulut, H., Schmittbuhl, J., Özalaybey, S., Lengliné, O., Kömeç-Mutlu, a., Durand, V., … Bouin, M. P. (2011). Evolution of the seismicity in the eastern Marmara Sea a decade before and after the 17 August 1999 Izmit earthquake. *Tectonophysics*, 510(1-2), 17–27. doi:10.1016/j.tecto.2011.07.009

Karabulut, H., Paul, A., Afacan Ergun, T., Hatzfeld, D., Childs, D. M., & Aktar, M. (2013). Long-wavelength undulations of the seismic Moho beneath the strongly stretched Western Anatolia. *Geophysical Journal International*, 194(1), 450–464. doi:10.1093/gji/ggt100

Katzman, R., Brink, U. S. ten, & Lin, J. (1995). Three-dimensional modeling of pull-apart basins: Implications for the tectonics of the Dead Sea Basin. *Journal of Geophysical Research*, 100(B4), 6295–6312. doi:10.1029/94JB03101

Kurt, H., Sorlien, C. C., Seeber, L., Steckler, M. S., Shillington, D. J., Cifci, G., … Carton, H. (2013). Steady late quaternary slip rate on the Cinarcik section of the North Anatolian fault near Istanbul, Turkey. *Geophysical Research Letters*, 40, n/a–n/a. doi:10.1002/grl.50882

Laigle, M., Bécel, A., de Voogd, B., Hirn, A., Taymaz, T., & Ozalaybey, S. (2008). A first deep seismic survey in the Sea of Marmara: Deep basins and whole crust architecture and evolution. *Earth and Planetary Science Letters*, 270(3-4), 168–179. doi:10.1016/j.epsl.2008.02.031

Le Pichon, X., Henry, P., & Lallemant, S. (1990). Water flow in the Barbados Accretionary Complex. *Journal of Geophysical Research*, 95(B6), 8945–8967. doi:10.1029/JB095iB06p08945

Le Pichon, X., Saatc, R., & Tok, B. (2001). The active Main Marmara Fault. *Earth and Planetary Science Letters*, 192, 595–616.

Le Pichon, X., İmren, C., Rangin, C., Şengör, A. M. C., & Siyako, M. (2013). The South Marmara Fault. *International Journal of Earth Sciences*, 103(1), 219–231. doi:10.1007/s00531-013-0950-0

Le Pichon, X., Şengör, A. M. C., Kende, J., İmren, C., Henry, P., Grall, C., & Karabulut, H. (2015). Propagation of a strike-slip plate boundary within an extensional environment : the westward propagation of the North Anatolian Fault . Canadian Journal of Earth Sciences, 53. doi:10.1139/cjes-2015-0129

Li, Y.-G., & Malin, P. E. (2008). San Andreas Fault damage at SAFOD viewed with fault-guided waves. Geophysical Research Letters, 35(8), 1–6. doi: 10.1029/2007GL032924

Liu, Huafeng, Niu, Fenglin (2011). Receiver function study of the crustal structure of Northeast China: Seismic evidence for a mantle upwelling beneath the eastern flank of the Songliao Basin and the Changbaishan region. *Earthquake Science,* 24(1), 27-33. doi: 10.1007/s11589-011-0766-6

McKenzie, D. (1978). Some remarks on the development of sedimentary basins. *Earth and Planetary Science Letters,* 40(1), 25–32. doi:10.1016/0012-821X(78)90071-7

Morley, C. K., & Alvey, A. (2015). Is spreading prolonged, episodic or incipient in the Andaman Sea? Evidence from deepwater sedimentation. Journal of Asian Earth Sciences, 98, 446–456. doi:10.1016/j.jseaes.2014.11.033

Okay, a. I., Satir, M., Zattin, M., Cavazza, W., & Topuz, G. (2008). An Oligocene ductile strike-slip shear zone: The Uludag Massif, northwest Turkey--Implications for the westward translation of Anatolia. *Geological Society of America Bulletin*, 120(7-8), 893–911. doi:10.1130/B26229.1

Oldenburg, D. W. (1974). The Inversion and interpretation of gravity anomalies. *Geophysics*, *39*(4), 526–536.

Özeren, M. S., & Holt, W. E. (2010). The dynamics of the eastern Mediterranean and eastern Turkey. *Geophysical Journal International*, 183(3), 1165–1184. doi:10.1111/j.1365-246X.2010.04819.x

Parker, R. L. (1972). The Rapid Calculation of Potential Anomalies. *Geophysical Journal of the Royal Astronomical Society*, *31*(4), 447–455.

Pavlis, N. K., Holmes, S. A., Kenyon, S. C., & Factor, J. K. (2012). The development and evaluation of the earth gravitational model 2008 (EGM2008). *Journal of Geophysical Research: Solid Earth,* 117(B4). doi:10.1029/2011JB008916

Petrunin, A., & Sobolev, S. V. (2006). What controls thickness of sediments and lithospheric deformation at a pull-apart basin? *Geology*, 34(5), 389–392. doi:10.1130/G22158.1

Pfister, M., Rybach, L., & Simsek, S. (1998). Geothermal reconnaissance of the Marmara Sea region (NW Turkey): surface heat flow density in an area of active continental extension. Tectonophysics, 291(1–4), 77–89. http://doi.org/10.1016/S0040-1951(98)00032-8

Pollack, H. N., Hurter, S. J., & Johnson, R. (1993). Heat flow from the Earth’s interior: analysis of the global data set. *Reviews of Geophysics,* 31(3), 267–280. doi:10.1029/93RG01249

Rangin, C., Le Pichon, X., Demirbag, E., & Imren, C. (2004). Strain localization in the Sea of Marmara: Propagation of the North Anatolian Fault in a now inactive pull-apart. *Tectonics*, 23(2), n/a–n/a. doi:10.1029/2002TC001437

Reilinger, R., McClusky, S., Vernant, P., Lawrence, S., Ergintav, S., Cakmak, R., … Karam, G. (2006). GPS constraints on continental deformation in the Africa-Arabia-Eurasia continental collision zone and implications for the dynamics of plate interactions. *Journal of Geophysical Research*, 111(B5), B05411. doi:10.1029/2005JB004051

Robinson, A., Rudat, J., Banks, C. J., & Wiles, R. L. F. (1996). Petroleum geology of the Black Sea. *Marine and Petroleum Geology*, *13*(2), 195–223. doi:10.1016/0264-8172(95)00042-9

Roecker, S., Thurber, C., & McPhee, D. (2004). Joint inversion of gravity and arrival time data from Parkfield: New constraints on structure and hypocenter locations near the SAFOD drill site. Geophysical Research Letters, 31(12), 10–13. doi:10.1029/2003GL019396

Sandwell, D. T. (1987). Biharmonic s pline interpolation of GEOS-3 and SEASAT altimeter data. *Geophysical Research Letters*, *14*(2), 139–142.

Sandwell, D. T., & Smith, W. H. F. (1997). Marine gravity anomaly from Geosat and ERS 1 satellite altimetry. *Journal of Geophysical Research*, *102*(B5), 10039–10054. doi:10.1029/96JB03223

Sandwell, D. T., Garcia, E., Soofi, K., Wessel, P., Chandler, M., & Smith, W. H. F. (2013). Toward 1-mGal accuracy in global marine gravity from CryoSat-2, Envisat , and Jason-1. *The Leading Edge*, 892–899.

Sass, J. H., Lachenbruch, A. H., Galanis Jr., S. P., Morgan, P., Priest, S. S., Moses Jr., T. H., & Munroe, R. J. (1994). Thermal regime of the southern Basin and Range Province: 1 . Heat flow data from Arizona and the Mojave Desert of California and Nevada. *Journal of Geophysical Research*, 99(B11), 22093–22119.

Seeber, L., Emre, O., Cormier, M.-H., Sorlien, C. C., McHugh, C., Polonia, A., … Cagatay, N. (2004). Uplift and subsidence from oblique slip: the Ganos–Marmara bend of the North Anatolian Transform, western Turkey. *Tectonophysics*, 391(1-4), 239–258. doi:10.1016/j.tecto.2004.07.015

Şengör, A. M. C., Tüysüz, O., İmren, C., Sakınç, M., Eyidoğan, H., Görür, N., … Rangin, C. (2005). the North Anatolian Fault: a New Look. *Annual Review of Earth and Planetary Sciences*, 33(1), 37–112. doi:10.1146/annurev.earth.32.101802.120415

Şengör, A. M. C., Grall, C., Imren, C., Pichon, X. Le, Görür, N., Henry, P., … Siyako, M. (2014). The geometry of the North Anatolian transform fault in the Sea of Marmara and its temporal evolution: implications for the development of intracontinental transform faults. *Canadian Journal of Earth Sciences*, 51(February), 222–242. doi:10.1139/cjes-2013-0160

Schmittbuhl, J., Karabulut, H., Lengliné, O., & Bouchon, M. (2016). Seismicity distribution and locking depth along the Main Marmara Fault, Turkey. *Geochemistry, Geophysics, Geosystems*, 17(3), 954–965. doi:10.1002/2015GC006120

Siyako, M., & Huvaz, O. (2007). Eocene stratigraphic evolution of the Thrace Basin, Turkey. *Sedimentary Geology*, *198*(1-2), 75–91. doi:10.1016/j.sedgeo.2006.11.008

Smit, J., Brun, J.-P., Cloetingh, S., & Ben-Avraham, Z. (2008). Pull-apart basin formation and development in narrow transform zones with application to the Dead Sea basin. *Tectonics*, 27(6), 1–17. doi:10.1029/2007TC002119

Sobolev, S. V, & Babeyko, A. Y. U. (1994). Modeling of mineralogical composition, density and elastic wave velocities in anhydrous magmatic rocks. *Surveys in Geophysics*, *15*(5), 515–544. doi:10.1007/BF00690173

Sorlien, C. C., Akhun, S. D., Seeber, L., Steckler, M. S., Shillington, D. J., Kurt, H., … Diebold, J. B. (2012). Uniform basin growth over the last 500ka, North Anatolian Fault, Marmara Sea, Turkey. Tectonophysics, 518–521, 1–16. http://doi.org/10.1016/j.tecto.2011.10.006

Tarantola, Albert. (2005). Inverse Problem Theory and Methods for Model Parameter Estimation. *Society for Industrial and Applied Matematics*.

Telford, W. M., Geldart, L. P., & Sheriff, R. E. (1991) Applied Geophysics (2nd edition), *Cambridge University Press*. doi: 10.1002/gj.3350270119

Ten Brink, U. S., Ben-Avraham, Z., Bell, R. E., Hassouneh, M., Coleman, D. F., Andreasen, G., … Coakley, B. (1993). Structure of the Dead Sea pull-apart basin from gravity analyses. *Journal of Geophysical Research*, 98(B12), 21877. doi:10.1029/93JB02025

Tiberi, C., Diament, M., Lyon-Caen, H., & King, T. (2001). Moho topography beneath the Corinth rift area (Greece) from inversion of gravity data. *Geophysical Journal International*, 145, 797–808. doi:10.1046/j.1365-246X.2001.01441.x

Vening-Meinesz, F. A. (1931). Une nouvelle méthode pour la réduction isostatique régionale de l'intensité de la pesanteur. *Bulletin Géodésique, 29*, 33–51.

Wang, C., Rui, F., Zhengsheng, Y. A. O., & Xingjue, S. T. (1986). Gravity Anomaly and Density Structure of the San Andreas Fault Zone. *Pure and Applied Geophysics*, 124(1), 127–140.

Wang, P. J., Xie, X. A., Frank, M., Ren, Y. G., Zhu, D. F., & Sun, X. M. (2007). The Cretaceous Songliao basin: Volcanogenic succession, sedimentary sequence and tectonic evolution, NE China. Acta Geologica Sinica-English Edition, 81(6), 1002–1011. doi:10.1111/j.1755-6724.2007.tb01022.x

Watts, A. B., Karner, G. D., & Steckler, M. S. (1982). Lithospheric flexure and the evolution of sedimentary basin. *Philosophical Transactions of the Royal Society A*, 305(1489), 249–281. doi:10.1098/rsta.1982.0036

Watts, A. B., & Burov, E. B. (2003). Lithospheric strengh and its relationship to the elastic and seismogenic layer thickness. *Earth and Planetary Science Letters*, 213, 113–131. doi:10.1016/S0012-821X(03)00289-9

Zuber, M. T., Bechtel, T. D., & Forsyth, D. W. (1989). Effective elastic thicknesses of the lithosphere and mechanisms of isostatic compensation in Australia. *Journal of Geophysical Research,* 94, 9353–9367. doi:10.1029/JB094iB07p09353

CHAPITRE II

Etude directe et corrélation du réflecteur H1 « rouge » dans des carottes de sédiments - apports de la mission MARSITE

1. Introduction et motivation

Depuis 2009, une riche bibliothèque de relevés sismiques et, plus particulièrement, une campagne 3D en haute résolution dans le Haut Ouest, ont permis d'identifier des séquences répétitives dans la succession des sédiments des bassins. Ces séquences sont attribuées à des phénomènes périodiques, de l'ordre de 100.000 ans, liés aux variations passées du climat et du niveau de l'eau dans l'étendue lacustre ou marine Marmara. Sur cette base, des modèles d'âge ont été proposés. Ils reposent, dans la partie Est, sur la corrélation de deltas avec des épisodes de bas niveau dans le bassin d'İmralı Nord [*Sorlien et al.*, 2012] et, dans la partie Ouest, sur l'alternance de deux géométries différentes de dépôts sédimentaires [Grall et al., 2014]. Si les deux modèles sont reliés par une concordance supposée des principaux réflecteurs sismiques identifiables et par la similitude visuelle des séquences observées, aucune continuité le long de la Mer de Marmara ne permet de confirmer cette hypothèse. Et, si les deux modèles concordent sur l'interprétation des premiers cycles, coïncidant également avec l'extrapolation des taux de sédimentation mesurés sur des carottes atteignant 40 ka, des divergences d'interprétations sur les couches sédimentaires plus anciennes restent en suspens et les erreurs liées à l'extrapolation peuvent augmenter de façon très importantes avec la profondeur. Cependant, ces deux études représentent actuellement les seules tentatives d'établissement d'un modèle d'âge des sédiments en Mer de Marmara au-delà des derniers 15 000 ans.

Au-delà de la compréhension de l'effet des variations climatiques sur l'alternance des dépôts sédimentaires dans une zone aussi exceptionnellement impactée par la variation du niveau de la mer, la construction d'un modèle d'âge apporte des renseignements indirects sur le fonctionnement du système de failles. En effet, une étude menée par *Grall et al.* [2013] a mis au jour l'existence d'un complexe de glissement de terrain enfouis chevauchant la faille Nord-Anatolienne et dont les deux parties sont décalées par le mouvement de la faille. La mesure du décalage relatif a été rendu possible par les relevés sismiques 3D dans le Haut Ouest. En l'état actuel, cette mesure, couplée à l'interprétation des séquences stratigraphiques, permet d'estimer une vitesse moyenne de déplacement de la faille de 15.1–19.7 mm/a depuis le dépôt du glissement de terrain, estimé à 405–490 ka [*Grall et al*., 2013]. Des données d'âge basées sur des méthodes de datation rigoureuses devraient cependant être apportées pour valider ou invalider ce qui n'est pour le moment qu'une estimation.

C'est dans ce contexte que l'un des objectifs de la mission océanographique à bord du Pourquoi Pas ? a été pensé. En visant des zones érodées où des réflecteurs sismiques anciens affleurent presque au niveau du fond marin, ainsi que des zones de sédimentation condensée, des carottages d'environ 20 m devaient permettre d'étudier et de dater directement les sédiments des réflecteurs correspondant aux limites de séquences. Soutenues par des relevés sismiques « CHIRP » 3.5 kHz, permettant l'étude à haute résolution des horizons sismiques caractérisés en sismique HR, la troisième partie de la mission MARSITE visait à permettre la construction d'un modèle d'âge définitif jusqu'à environ 500 000 ans.

2. Modèle d'Age des Sédiments en mer de Marmara – Etat de l'art et questions en suspens

2.1. Répétitivité des cycles de sédimentation en relation avec la variation du niveau matin

A partir de l'observation de la géométrie des dépôts sédimentaires dans des données sismiques du Haut Ouest et du bassin d'İmralı, plusieurs modèles d'âge des sédiments en Mer de Marmara ont été proposés.

Au niveau du Haut Ouest, à proximité de la faille de Marmara, la sédimentation est constituée d'une alternance de couches drapées et d'unités de remplissage [*Grall et al.*, 2013 ; *Grall et al.*, 2014 (citation valable pour tout ce paragraphe)]. Les unités de remplissages présentent des variations latérales d'épaisseur importantes et des figures d'onlap à leur base tandis que les niveaux drapés ne présentent que de faibles variations d'épaisseur. De plus, des glissements de terrains sont visibles régulièrement au sein des unités de remplissage. Il a été proposé que les séquences de remplissage correspondent aux périodes de haut niveau marin tandis que les séquences drapées correspondraient aux périodes lacustres de la Mer de Marmara. Les épisodes de glissement de terrain, affectant en premier lieu les séquences de remplissage pourraient être induits par la réduction progressive de la salinité des eaux interstitielles par diffusion au début des périodes lacustres [*Grall et al.*, 2014].

Ainsi, d'après l'analyse proposée par *Grall et al.* [2014] et présentée en Figure 1, quatre séquences complètes seraient identifiables sur le relevé sismique 3-D du Haut Ouest.

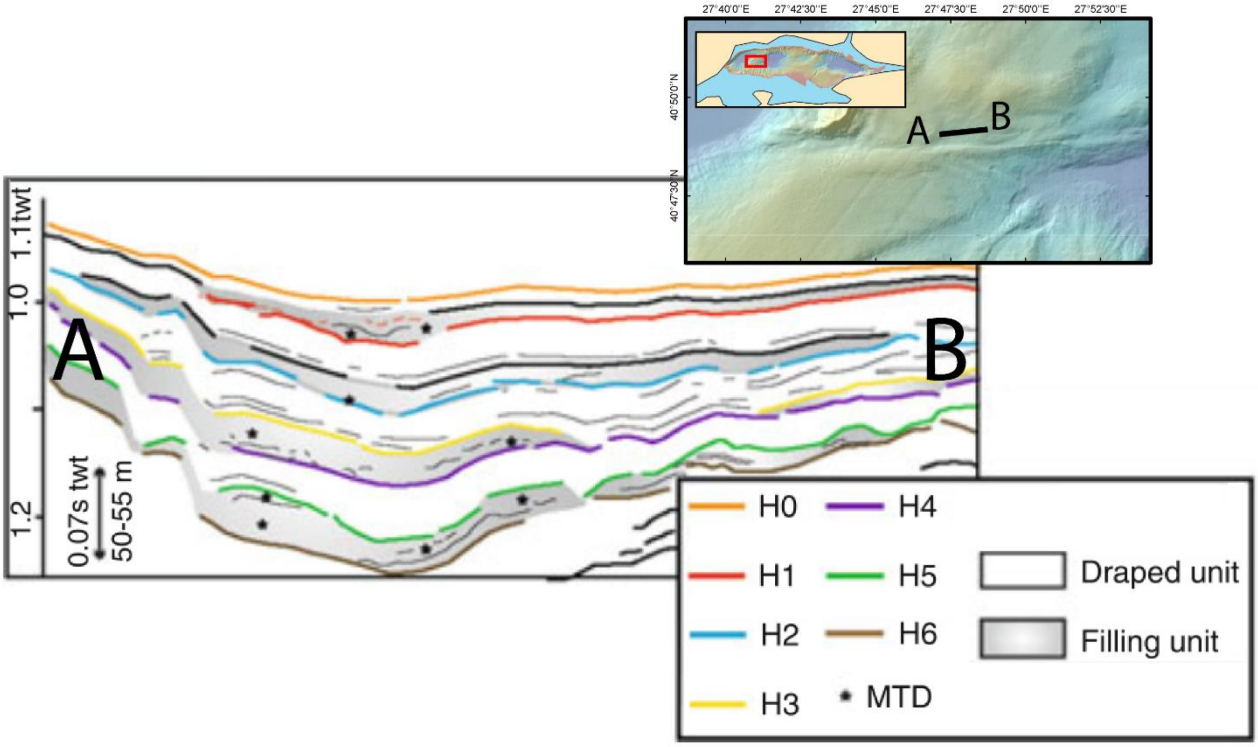

Figure 1. Profil sismique interprété du biseau est du Haut Ouest. Tous les MTD (Mass Transport Deposit, ou glissement de terrain) identifiés sont au sein de niveaux de remplissage. Quatre répétitions de la séquence sont observées. Figure de Grall et al. [2014] (localisation ajoutée).

Cette interprétation permettrait de remonter jusqu'au stade 11 avec les 4 cycles correspondant aux stades 1 à 5, 6 et 7, 8 et 9 et, pour finir, 10 et 11. Soit un modèle d'âge remontant jusqu'à 450 ka au niveau de l'horizon marron H6 (voir Figure 1). Cependant, compte tenu de la variation des amplitudes glacio-eustatiques lors des cycles successifs, il est possible que les cycles de 100 ka n'aient pas tous donné lieu à une déconnection complète au niveau des Dardanelles et à l'installation de conditions lacustres [*Grall et al.*, 2014]. Ceci laisse donc une ambiguité sur l'interprétation de ces séquences en termes de cyclicité à 100.000 ans.

De fait, la construction par *Grall et al.* [2013] d'un modèle d'âge reposant sur l'extrapolation de vitesses de sédimentation mesurées sur des carottes atteignant 40 ka [*Lericollais and Henry*, 2004] et tenant compte de la compaction a amené à formuler une autre hypothèse pour les horizons les plus profonds. Les intervalles entre les réflecteurs H4-H3, d'une part, et les réflecteurs, H6-H5, d'autre part, auraient une épaisseur trop importante pour pouvoir correspondre à un demi-cycle de 100 ka mais correspondraient plutôt à un cycle entier.

Si l'extrapolation des taux de sédimentation n'est pas compatible avec l'interprétation proposée des séquences stratigraphiques dans le Haut Ouest, il n'en est pas de même de l'interprétation de profils du bassin d'Imrali, à l'Est de la Mer de Marmara. En effet, une étude menée par *Sorlien et al.* [2012] reposant sur l'identification de dépôts de deltas a permis de construire un modèle d'âge très proche de celui proposé par *Grall et al.* [2013].

Dans cette étude, *Sorlien et al.* [2012] ont identifié des structures progradantes avec des « toplap » caractéristiques de deltas de bas niveau (voir Figure 2). Ils suggèrent que les deltas se sont formés lors des périodes froides, alors que le plateau sud de la Mer de Marmara était exposé et que le bassin d'Imrali servait de zone de drainage au réseau d'écoulement se développant sur le plateau. Les réflecteurs majeurs les plus superficiels ne sont cependant associés à aucun delta. *Sorlien et al.* [2012] propose, pour expliquer cette observation, que la profondeur du bassin d'Imrali aurait augmenté après le dépôt du réflecteur « bleu » H2 car la sédimentation ne compensait plus la subsidence. L'épaisseur de la couche d'eau, même en période glaciaire, était alors trop importante pour observer la formation de deltas dans le bassin.

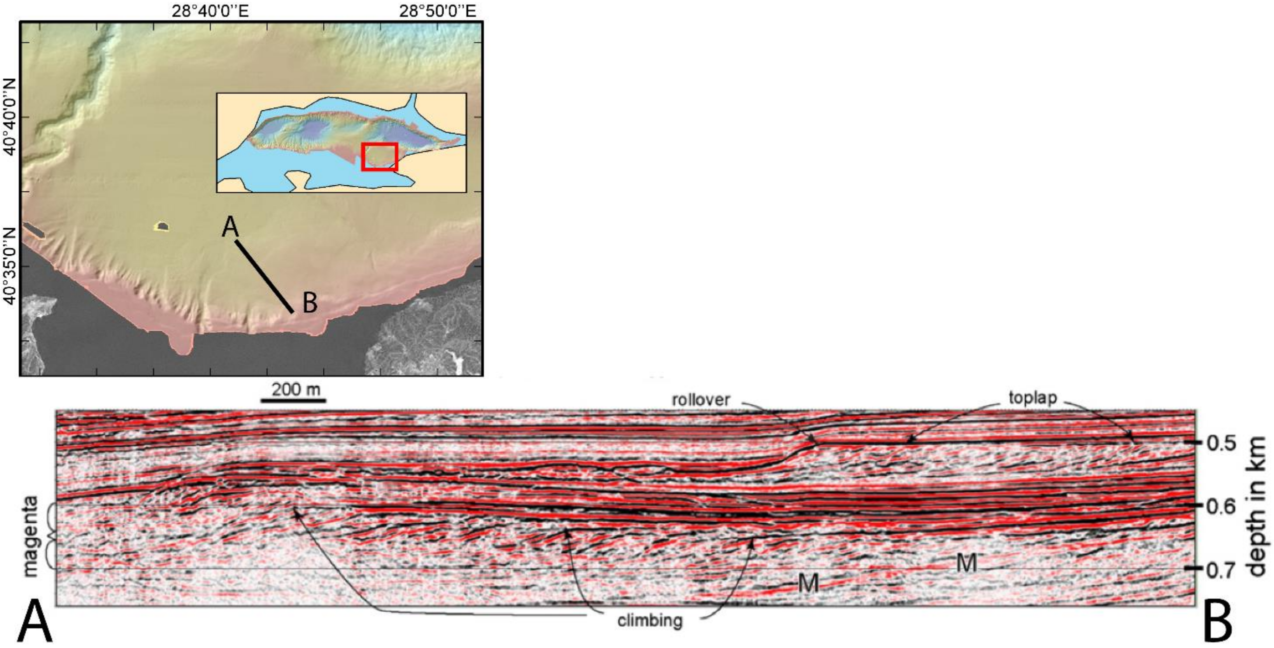

Figure 2. Gros plan sur le dépôt de delta sous-jacent au réflecteur "bleu" H2. M indique les réflexions multiples. Figure de Sorlien et al. [2012] (localisation ajoutée).

En s'appuyant sur ces observations *Sorlien et al.*, [2012] proposent également une construction de modèle d'âge. Dans un premier temps, ils calculent une datation du premier horizon « rouge » H1 à partir de l'extrapolation du taux de sédimentation mesuré sur une carotte atteignant ~17 ka [*Beck et al.*, 2007] et l'observation de niveaux à large « fanning » proche de la faille. Cette caractéristique serait due à un faible taux de sédimentation associé à un jeu continu de la faille lors des périodes de haut niveau marin. Cette approche permet de supposer un âge pour le réflecteur « rouge » H1 d'environ 110 ka, soit à la fin du stade 5e. Le modèle est ensuite extrapolé en utilisant à la fois le volume de sédiment, l'augmentation de l'inclinaison des horizons dans le bassin en profondeur et les décalages entre les horizons au niveau de failles normales. Les vitesses moyennes de sédimentation sur un cycle, d'inclinaison du bassin et du jeu des failles sont considérées constantes.

La Figure 3 présente le modèle d'âge proposé par *Sorlien et al.* [2012] (en pointillés) et celui proposé par *Grall et al.* [2013]. Les deux modèles coïncident tout à fait jusqu'au réflecteur « violet » H4 à 450 ka et restent cohérents, au regard des marges d'erreur, jusqu'au réflecteur « vert » H5 à environ 550 ka. Plus particulièrement, les deux modèles, en s'appuyant sur des études différentes, ont estimé un âge tout à fait semblable pour le premier réflecteur « rouge » H1, qui est le réflecteur le moins soumis aux approximations de l'extrapolation puisque le plus superficiel. Cependant, *Grall et al.* [2013] différencient les réflecteurs H1' et H1, qui sont attribués au début et à la fin du stade 5e, soit respectivement 130 ka et 109 ka, mais sont superposés au niveau de zones de sédimentation condensées.

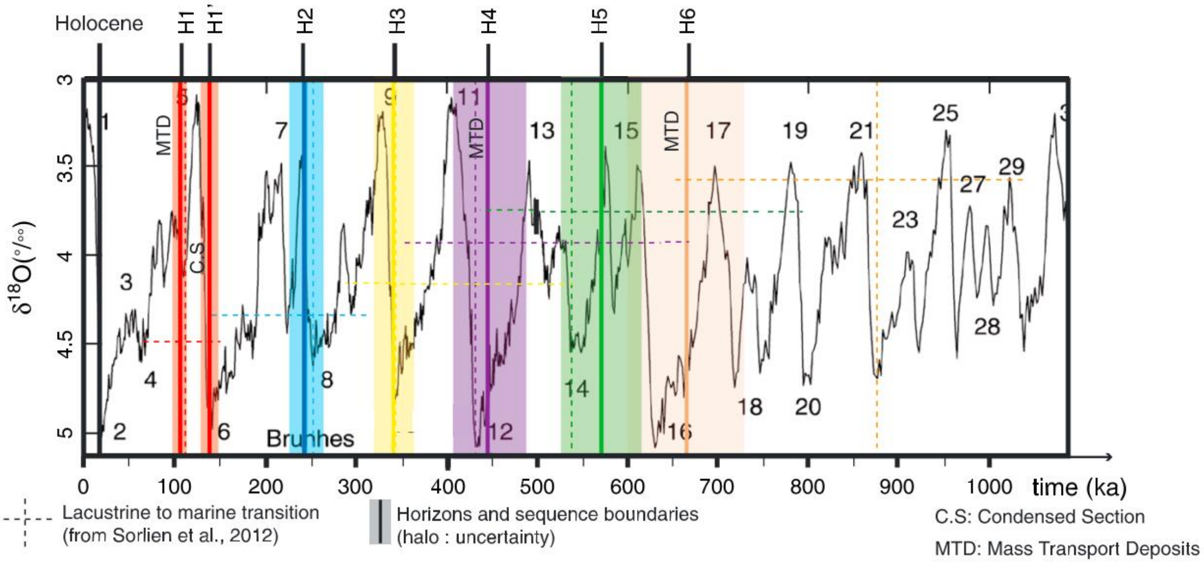

Figure 3. Modèles d'âge des principaux réflecteurs supérieurs de la Mer de Marmara construit par Grall et al. [2013] (traits continus) et Sorlien et al. [2012] (pointillés). Les couleurs des réflecteurs correspondent à celles de la Figure 1. Figure de Grall et al., [2013].

2.2. Identification de principaux réflecteurs sismiques en Mer de Marmara

La construction des modèles d'âge présentée précédemment s'est appuyée sur des réflecteurs aux caractéristiques permettant une identification aisée. Dans les deux cas, les réflecteurs ont été attribués à des limites de cycles, lorsque les conditions de sédimentation ont drastiquement varié. Cette hypothèse se comprend aisément puisque ce sont justement les variations de lithologie importantes qui vont créer les réflecteurs les plus forts.

L'existence d'incisions à travers la Mer de Marmara provoque la distinction entre un domaine Est et un domaine Ouest entre lesquels il n'est pas possible de suivre de manière continue les réflecteurs. Les caractéristiques des réflecteurs sont cependant suffisamment claires pour soutenir une correspondance entre les identifications réalisées sur les deux blocs.

Ci-après, une courte description des réflecteurs (depuis *Grall et al.* [2013]) :

- « rouge » H1 : premier réflecteur à forte amplitude et polarité négative (inverse de celle du fond marin).
- « rouge » H1' : réflecteur de la base de la séquence d' « onlap » dans laquelle est contenue H1 dans les bassins.
- « bleu » H2 : sous-jacent à H1 et H1'. Réflecteur caractérisé par des variations latérales de polarité et d'amplitude.
- « jaune » H3 : premier réflecteur sus-jacent à H4 et présentant une bonne continuité régionale.
- « violet » H4 : réflecteur à forte amplitude, polarité positive et constituant le toit d'un niveau transparent.
- « vert » H5 : semblable à H3 avec des variations topographiques plus marquées, indiquant un épisode d'érosion.
- « marron » H6 : semblable à H4, au sommet d'un niveau transparent.

Récemment, de nombreux profils sismiques « CHIRP » 3.5 kHz (profils de sondeur de sédiment) ont été relevés. A la profondeur en temps des réflecteurs sismiques décrits correspondent également des réflecteurs distinguables sur la très haute résolution des profils « CHIRP ». La possibilité de détecter ces réflecteurs à haute comme à très haute résolution confirme qu'il s'agit probablement de transitions lithologiques. S'il est difficile de différencier la plupart des réflecteurs directement sur les profils « CHIRP' », il est possible de les suivre, notamment dans des zones où ils sont trop proches pour être distingués à la résolution des profils de sismique usuelle. La Figure 4 présente une comparaison de l'aspect des premiers réflecteurs sur les deux types de données sismiques.

Les avantages des profils « CHIRP » sont particulièrement mis en avant lors des missions de carottage. En plus de faciliter la préparation en amont, les profils étant rapides à relever et à traiter, ils permettent de contrôler précisément les zones ciblées sur le moment, par exemple pour vérifier l'absence de poches de gaz. Leur résolution permet aussi d'évaluer finement les profondeurs auxquelles les différents réflecteurs seront situés dans la carotte.

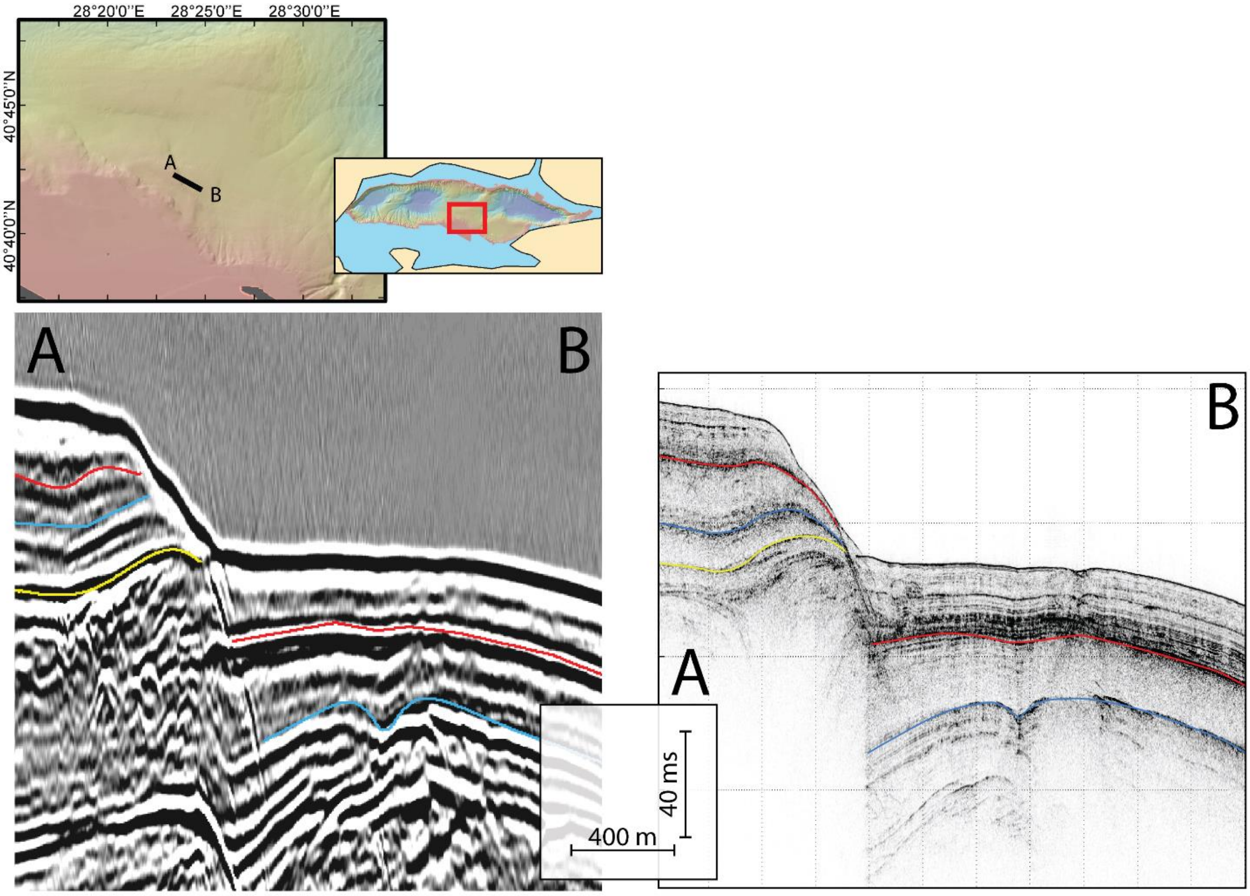

Piri-52 MRS-SBP-41

Figure 4. Comparaison d'un profil sismique HR(en amplitude) et d'un profil "CHIRP" 3.5 kH (en enveloppe de l'amplitude) dans le bassin d'İmralı avec identification de trois réflecteurs principaux. Dans le bloc Ouest, les réflecteurs sont faciles à discerner dans les deux types de données. Dans le bloc Est, le réflecteur « rouge » H1 fait partie d'un empilement de réflecteurs sur le profil « CHIRP » 3.5 kHz rendant difficile son identification et son suivi.

2.3. Objectifs de la mission Marsite pour l'étude direct des réflecteurs principaux

S'appuyant sur la riche base de données sismique HR et « CHIRP », le volet carottage de la troisième partie de la mission MARSITE a été planifié dans le but d'apporter des données nouvelles pour contraindre les modèles d'âge grâce à l'étude directe des sédiments. Des cibles ont été définies dans des zones où les réflecteurs principaux caractérisés par *Grall et al*. [2013] et *Sorlien et al*. [2012] sont suffisamment proches de la surface pour permettre de les traverser par carottage à piston.

Pour multiplier les chances de succès, plusieurs zones avec les mêmes objectifs ont été sélectionnées. Trois zones visaient à établir une chronologie récente, la plus continue possible, depuis le dépôt du réflecteur « rouge » H1 jusqu'à aujourd'hui. Deux autres zones ont, quant à elles, été choisies car elles devaient permettre d'atteindre des réflecteurs plus anciens, jusqu'au « violet » H4 dans le Haut Ouest

3. La Mission MARSITE en Mer de Marmara – volet carottage et obtention de profils sismiques CHIRP

3.1. Equipement

3.1.1. Le Pourquoi Pas ?

Le navire océanographique Pourquoi Pas ?, du nom du bateau du commandant Charcot, est un bateau océanographique de 108 m de long mis en service en 2005. Il est armé par le groupe GENAVIR et affrété 180 jours par an par l'IFREMER (Institut Français de Recherche pour l'Exploitation de la Mer) et 150 jours par an par la Marine Nationale. Il est équipé en permanence de deux sondeurs multifaisceaux, de courantomètres, d'un gravimètre, d'un sondeur de sédiment 3.5 kHz pour le relevé des profils « CHIRP », ainsi que d'une large gamme d'autres capteurs. Son pont est adapté au lancement et au suivi des opérations d'engins sous-marins, notamment le ROV Victor et le sous-marin de poche Nautile, tous deux propriétés de l'Ifremer. L'organisation des ponts extérieurs permet aussi d'intégrer temporairement des laboratoires mobiles installés dans des conteneurs.

Figure 5. Le Pourquoi Pas à Istanbul, avant le départ de la mission MARSITE.

Jusqu’à quarante scientifiques peuvent embarquer sur une mission. Les différents laboratoires et salles informatiques ainsi que la répartition des équipements sur le pont permettent de mener plusieurs opérations simultanément. Généralement, les activités scientifiques sont menées 24h/24. Lors de la mission MARSITE, les tâches opérées en continues, telle que la gestion des carotte prélevées, étaient assurées par des équipes organisées en quart, chacune travaillant deux quarts de 4h, espacés de 8h.

3.1.2. Le carottage par piston

Les carottes de la mission MARSITE ont toutes été prélevées par carottage à piston avec un carottier CALYPSO. Le fonctionnement de ce type de carottage repose sur un contrepoids pesant au-dessus du tube de carottage et lâché par un déclencheur à proximité du fond marin. Un piston intégré dans le tube reste à l’interface entre l’eau et le sédiment pendant la descente du tube et assure une dépressurisation qui limite les frottements.

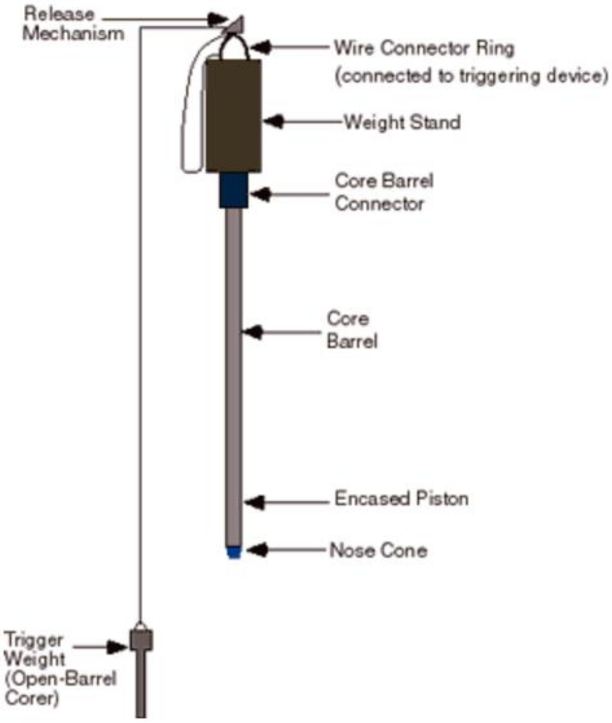

Figure 6. Schéma d’un carottier à piston. Figure de https://pubs.usgs.gov.

Lors de la mission MARSITE des tubes de 11.9, 23.4 et 24.5 m ont été utilisés. Aucune analyse des carottes n’a été réalisée à bord du navire. Les carottes ont été sciées en sections de 1 m de long, étiquetées et conditionnées pour être transportées à Brest et à Istanbul.

3.1.3. Le sondeur de sédiment

Comme indiqué en partie 2.2, la réalisation de « CHIRP » au cours d’une mission de carottage permet, en amont, de vérifier la situation de la zone ciblée et, en aval, de faciliter l’interprétation des niveaux lithologiques et des résultats d’analyses en relation avec les réflecteurs observés.

Le Pourquoi Pas ? est équipé d’un sondeur de sédiment développé par la société Triton-Elics. Il est constitué d’une antenne acoustique fixée à la coque dont les transducteurs servent à la fois pour l’émission et la réception du signal. La pénétration peut atteindre jusqu’à 100 m et la bande passante entre 1.8 kHz et 5.3 kHz permet une résolution inférieure à 30 cm [*http://flotte.ifremer.fr*]. Les relevés étaient directement traités à bord du Pourquoi Pas ? par la routine Matlab développée par Anne Pacault à l’IFREMER.

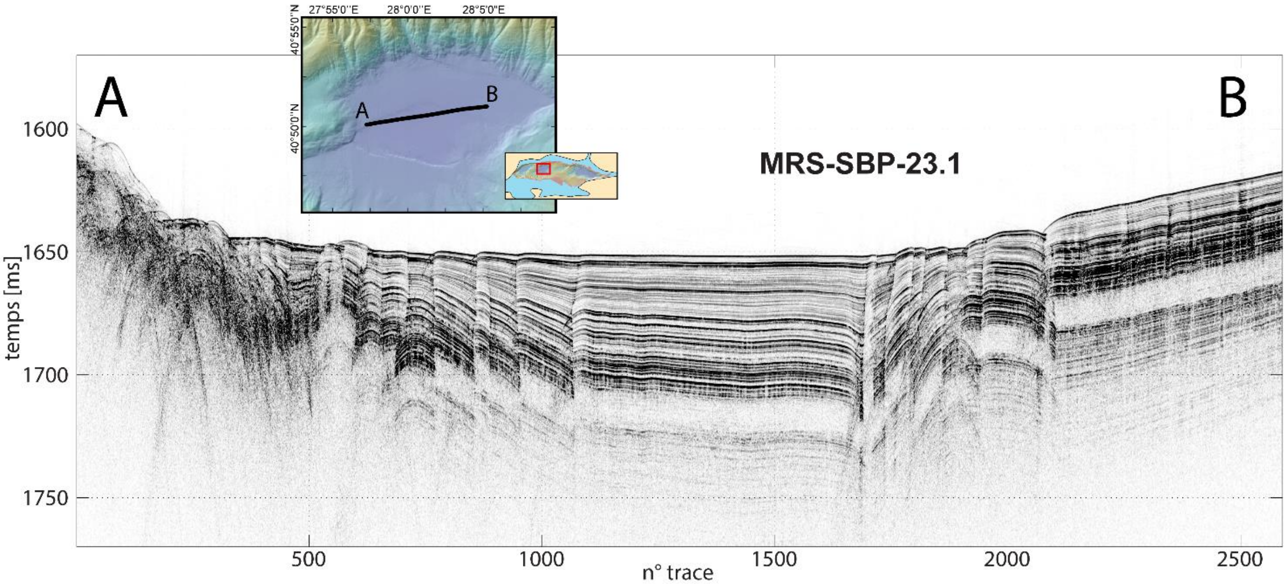

Figure 7. Exemple d’un profil “CHIRP” 3.5 kHz relevé pendant la mission MARSITE dans le Bassin Central et permettant de distinguer nettement des successions de failles.

3.1.4. Le Multi-Sencor core logger (IFREMER, Brest)

Le multi-sencor core logger (MSCL) est un appareil utilisé en routine comme première analyse des carottes de sédiments avant ou après leur ouverture. L’appareil peut être utilisé à bord des navires océanographiques en équipant un laboratoire mobile installé dans un conteneur. Cependant lors de la mission MARSITE, aucun MSCL n’était embarqué. Les carottes ont été analysées à postériori à l’IFREMER de BREST et à l’ITU (Université Technique d’Istanbul).

Les carottes prélevées dans l'Ouest de la Mer de Marmara ont été analysées à Brest, sur un banc MSCL GEOTEK mesurant la vitesse des ondes P, la susceptibilité magnétique et la densité par absorption gamma.

3.2. Sites de carottages et premiers bilan

3.2.1. Résumé des opérations

Toutes les carottes présentées ci-après ont été récupérées pendant la campagne MARSITE à bord du Pourquoi Pas ? Les carottes MRS-CS-22, MRS-CS-23, MRS-CS-24, MRS-CS-25 et MRS-CS-26 sont entreposées et étudiées au CEREGE tandis que les carottes MRS-CS-18, MRS-CS-20, MRS-CS-21 et MRS-CS-27 sont à l'ITU (voir Table 1). A bord, les sédiments contenus dans l'ogive (le dispositif disposé à l'extrémité du tube de carottage pour percer le sédiment) ont été récupérés lors de chaque carottage. Ils ont été étudiés afin de trouver d'éventuels marqueurs temporels dans le contenu en microfossiles pour une première estimation de l'âge maximum atteint. Cette partie présente les résultats de la campagne de carottage ainsi que les informations parfois apportées par le contenu des ogives.

Depuis, les carottes ont été ouvertes, décrites, photographiées et échantillonnées. Des analyses supplémentaires ont été menées sur les carottes conservées à l'ITU tandis que la carotte MRS-CS-22 a été l'objet d'une étude poussée, détaillée dans le chapitre III de ce manuscrit.

Seules les carottes prélevées pour l'étude chronologique au long terme (au moins jusqu'au réflecteur « rouge » H1) afin de contraindre le modèle d'âge des sédiments de la Mer de Marmara et d'établir la chronologie des variations de l'environnement entre marin et lacustre sont présentées dans ce manuscrit. Des carottes supplémentaires en vue de l'étude des turbidites déclenchées par des tremblements de terre ont également été récupérées dans les bassins à proximité des dépocentres.

Carotte	Longitude	Latitude	Zone	Bathymé-trie (m)	Longueur du tube (m)	Pénétra-tion	Récupé-ration	Dépôt
MRS-CS18	28,87958	40,66206	E Imrali N pente	291	24,5	73%	14,25	ITÜ
MRS-CS20	28,39274	40,70388	W Imrali escarpement	289	24,5	100%	18,9	ITÜ
MRS-CS21	28,39526	40,70284	W Imrali escarpement	277	24,5	73%	8,88	ITÜ
MRS-CS22	27,79906	40,83863	N Haut Ouest sommet	551	23,4	100%	20,42	CEREGE
MRS-CS23	27,82166	40,79283	S Haut Ouest pente	920	11,9	100%	10,32	CEREGE
MRS-CS24	27,82590	40,79033	S Haut Ouest pente	953	11,9	Non renseigné	8,9	CEREGE
MRS-CS25	27,82297	40,79206	S Haut Ouest pente	929	11,9	100%	10,65	CEREGE
MRS-CS26	27,82401	40,79144	S Haut Ouest pente	933	23,4	83%	17,59	CEREGE
MRS-CS27	28,40088	40,70049	W Imrali base escarpement	313	23,4	100%	20,65	ITÜ

Table 1. Coordonnées et caractéristiques des carottes récupérées lors de la mission MARSITE pour l'étude des lithologies liées aux réflecteurs sismiques principaux.

3.2.2. Le Nord du Haut Ouest

Dans le Nord du Haut Ouest, le carottage visait une zone prometteuse pour l'établissement d'une chronologie au-delà du réflecteur « rouge » H1. Le site se trouve à proximité d'un haut topographique, dans une zone où l'enregistrement sédimentaire est condensé, mais offre une épaisseur adéquate par rapport à la longueur du tube de carottage. Le positionnement de la cible sur une pente rend probable l'existence de hiatus ou de remaniements dus à des déstabilisations de la pente. Le positionnement exact a été choisi afin de viser une colonne dans laquelle les réflecteurs s'expriment nettement (voir Figure 8), tout en évitant le sommet de la pente où des échappements gazeux sont révélés par des échos sur les données de colonne d'eau des sondeurs multifaisceaux [*Dupré et al.*, 2015].

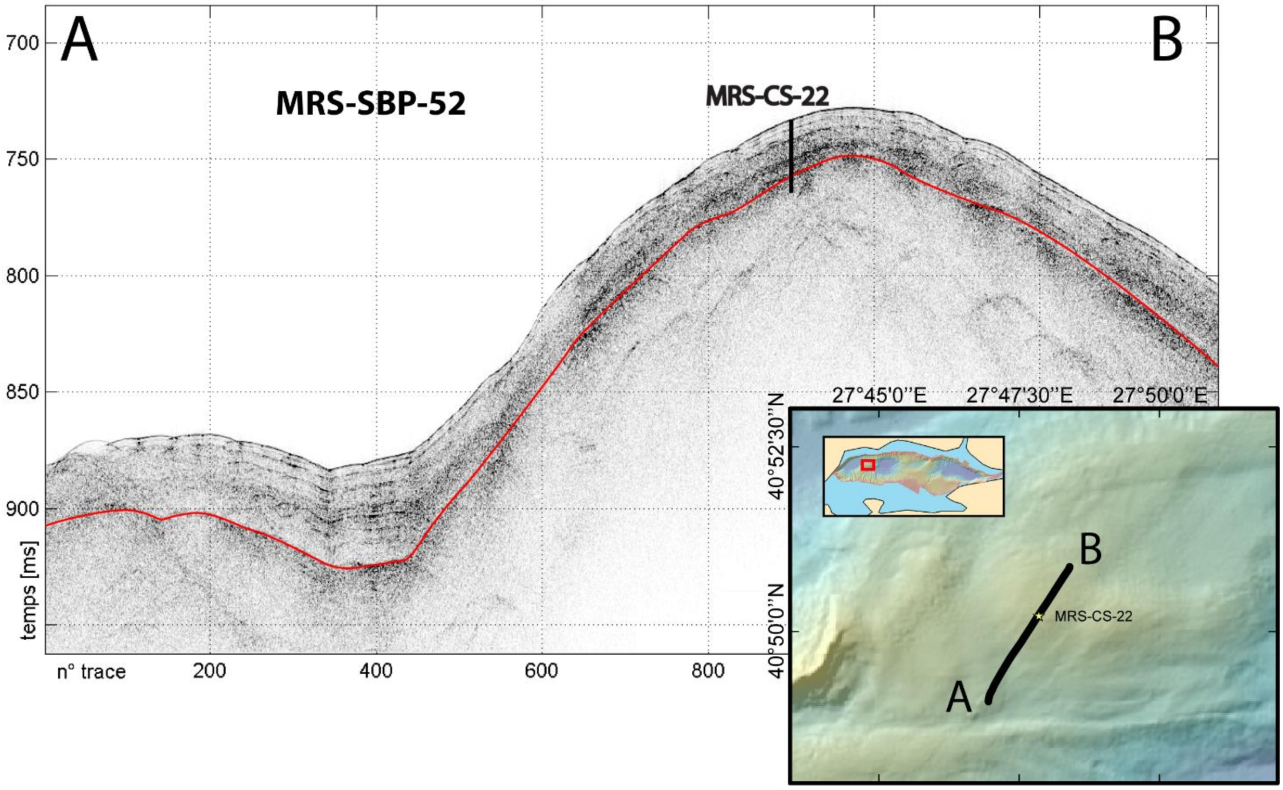

Figure 8. Localisation de la carotte de sédiment MRS-CS-22 dans le nord du Haut Ouest et représentation de la cible sur le profil « CHIRP » 3.5 kHz MRS-SBP-52.

Le carottage dans cette zone a été un succès. Le tube de 23.4 m a pénétré à 100%, dépassant largement la profondeur à laquelle doit se situer la transition lithologique responsable du réflecteur « rouge » H1.

Le tamisage du contenu de l'ogive a révélé un contenu en foraminifère extrêmement riche, aussi bien benthique que planctonique, ne laissant aucun doute sur l'origine marine des sédiments (voir Figure 9). Par ailleurs, le contenu en coccolites n'est pas dominé par *E.huxleyi* ce qui indique que l'échantillon est antérieur à la fin du stade MIS 5 ou début du stade MIS 4 (71 ka) [*Thierstein et al.*, 1977; *Flores et al.*, 1997]. Le bas du tube a donc atteint un niveau marin franc correspondant probablement au précédent interglaciaire.

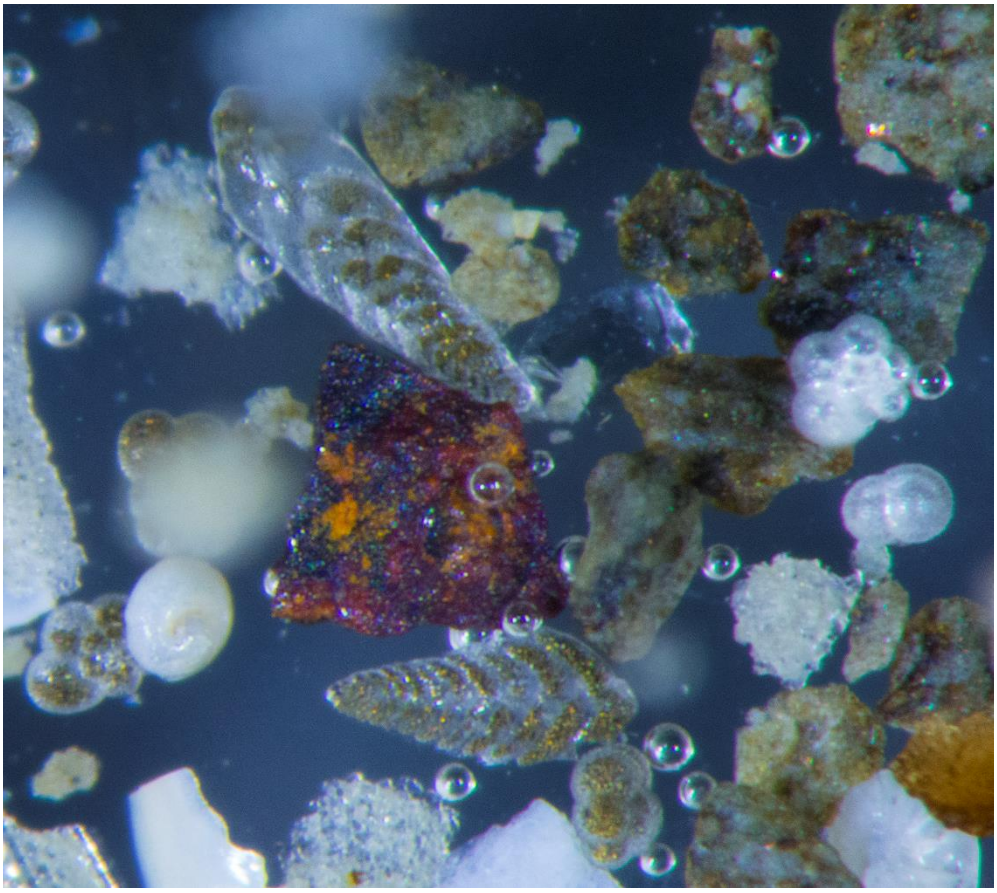

Figure 9. Photographie du rejet de tamis > 125 µm d'un échantillon de l'ogive de la carotte MRS-CS-22. Des foraminifères benthiques et planctoniques sont visibles. Les cristaux dorés sont de la pyrite précipitée dans les loges.

3.2.3. Le Sud du Haut Ouest – des sédiments anciens mais difficiles à exploiter

La zone ciblée dans le Sud du Haut Ouest présente une pente érodée le long de laquelle des réflecteurs anciens affleurent proche de la surface des sédiments. Quatre carottes ont été récupérées dans cette zone en visant à créer un recouvrement entre les carottes afin de récupérer une séquence complète jusqu'au réflecteur « violet » H4 dont l'âge est estimé à 450 ka (voir Figure 10). Cependant, l'instabilité de la pente et la difficulté de suivre les réflecteurs à proximité de la surface sur les deux types de profils sismiques laissait craindre l'existence de glissement de terrain sur les premiers mètres de l'empilement de sédiment.

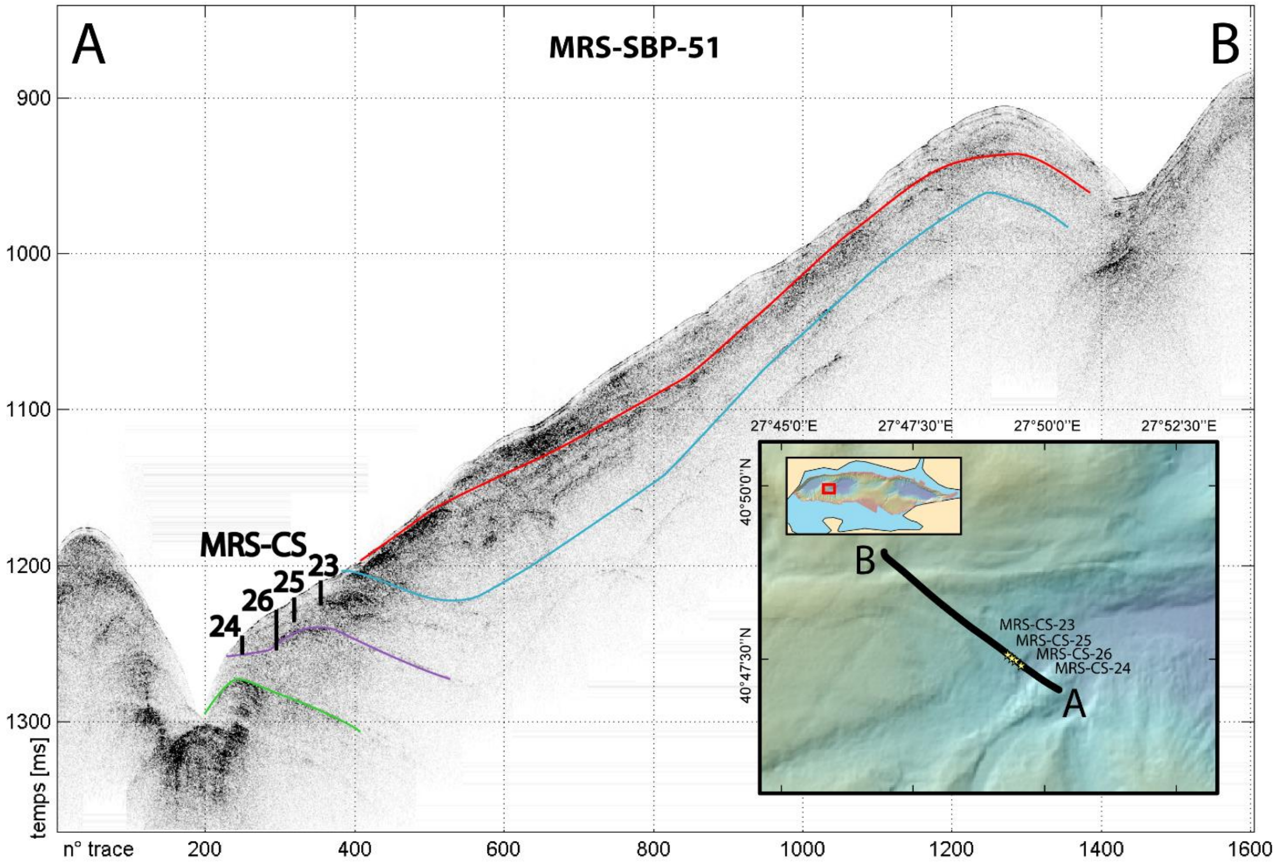

Figure 10. Localisation des carottes de sédiment prélevées sur une pente érodée dans le Sud du Haut Ouest et représentation des cibles sur le profil « CHIRP » 3.5 kHz MRS-SBP-51. L'échelonnement des cibles visait à récupérer une séquence continue par chevauchement des enregistrements. La difficulté à suivre les réflecteurs à proximité de la surface suggère la présence de perturbations dues à des glissements de terrain.

A l'origine, ces carottages devaient tous être réalisés avec des tubes d'une longueur supérieure à 20 m afin de maximiser les chances de pénétrer sous les niveaux perturbées par d'éventuels glissements de terrain. Cependant, les difficultés de pénétration lors de la mission obligèrent à réaliser 3 des 4 carottages avec des tubes plus courts (voir Table 1).

L'ouverture des carottes au CEREGE confirma hélas la présence de perturbations s'étendant parfois sur la totalité des carottes. Si certaines sections ne présentent qu'un pendage modéré des sédiments permettant de supposer une conservation de la chronologie des dépôts, d'autres présentent des perturbations plus importantes (e.g. plis isoclinaux « slump folds») rendant l'étude complexe.

Néanmoins, une étude préliminaire des fossiles des sédiments contenus dans les ogives a permis une première évaluation de l'âge maximum des sédiments récupérés. La Table 2 résume les résultats et les conclusions de cette analyse préliminaire.

	Coccolites	Conclusion
MRS-CS-23	Principalement des fossiles remaniés, prédominance d'*Emiliana huxleyi* dans les espèces en place	**MARIN fin MIS 5 ou MIS 1**
MRS-CS-25	Quelques *Gephyrocapsa ericsonii* et présence d'*Emiliana huxleyi*	**Probablement CONTINENTAL MIS 6 ou MIS 7**
MRS-CS-26	*Gephyrocapsa caribbeanica* abondante et *Gephyrocapsa ericsonii.* Pas d'*Emiliana huxleyi*	**MIS 7 ou MIS 8**
MRS-CS-24	Uniquement du remaniement	**CONTINENTAL**

Table 2. Résumé de l'étude des coccolites des ogives des carottes du sud du Haut Ouest.

Le contenu en diatomées et en foraminifères a également été évalué. Dans tous les échantillons ces fossiles représentent au maximum quelques débris et de rares individus dont l'état de conservation suggère du remaniement. Il est donc probable que les conditions environnementales étaient défavorables à la prolifération de ces organismes ou à la préservation des fossiles. Dans le cas des diatomées, une étude plus poussée des échantillons contenant des débris pourrait peut-être apporter des renseignements. A ce stade du travail, les conclusions de la Table 2 ne sont cependant basées que sur l'observation des coccolites.

La principale information apportée par cette étude est donnée par l'ogive de la carotte MRS-CS-26. L'absence d' E. Huxley pourrait indiquer un sédiment antérieur à 280 ka [*Thierstein et al.*, 1977 ; *Raffi et al.*, 2006]. Cependant, l'abondance de *G. Oceanica* pointe plutôt un âge postérieur à 270 ka [*Pujos*, 1988]. Le carottage a donc probablement atteint une époque proche de cette charnière au cours du MIS 7 (243-191 Ma) ou MIS 8 (300-243 Ma).

L'étude exhaustif des 50 m de sédiments de ces 4 carottes devrait donc permettre d'apporter de nouvelles informations pour la construction du modèle d'âge, à condition de réussir à distinguer les glissements de terrains, de réordonner éventuellement les dépôts et de pouvoir appliquer des méthodes de datation ou bien de trouver des indicateurs temporels indirects précis. A ce stade, les carottes ont été ouvertes, décrites et échantillonnées avec un pas de 20 cm en vue d'étude chimique, micropaléontologique et pour des tamisages. Elles sont conservées au CEREGE dans un conteneur frigorifique.

3.2.4. Les bassins d'İmralı

Une carotte a été prélevée dans le bassin d'İmralı Est et trois carottes dans le bassin d'İmralı Ouest avec ce même objectif de récupération de série temporelle plus ou moins longue.

La carotte MRS-CS-18 provient d'une pente du bassin d'İmralı Est. Le long de la pente, la série s'étale graduellement. Il était donc possible de choisir une section plus ou moins condensée. La cible finale visait à prélever plusieurs mètres sous le réflecteur « rouge » H1 afin d'aller au-delà de l'enregistrement de la carotte MRS-CS-22.

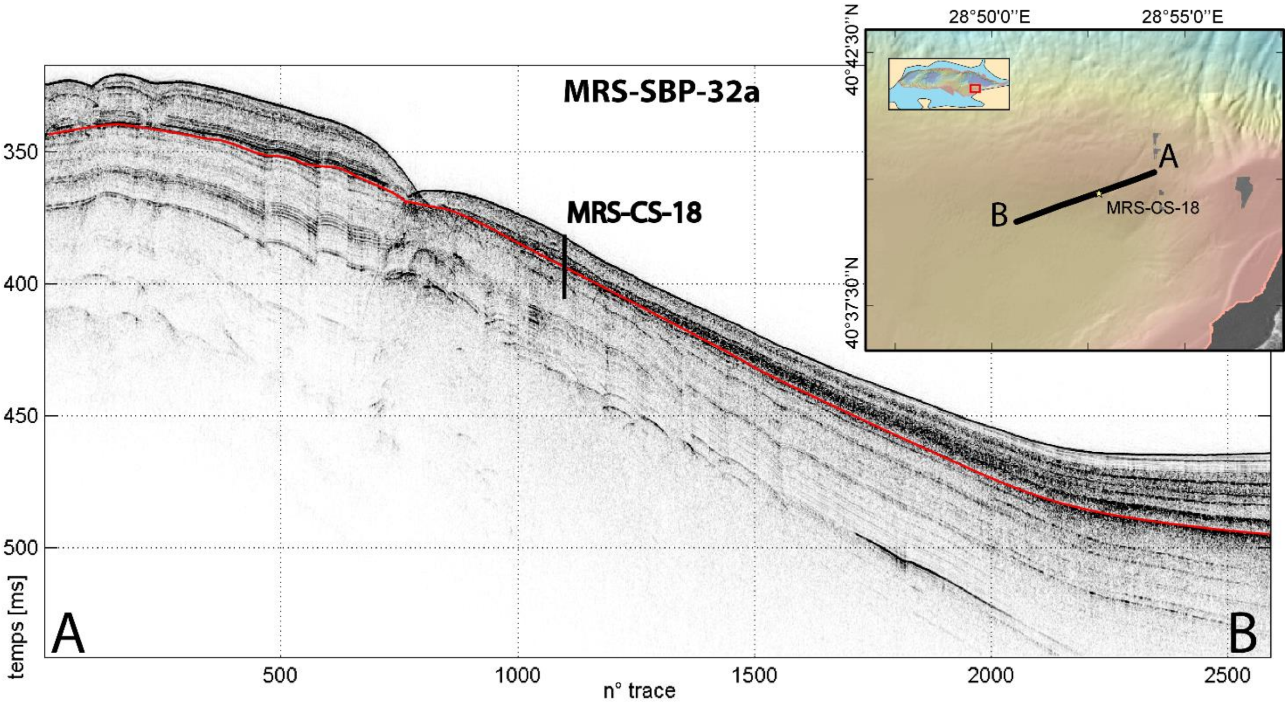

Figure 11. Localisation de la carotte de sédiment MRS-CS-18 dans l'Est du bassin d' İmralı et représentation de la cible sur le profil « CHIRP » 3.5 kHz MRS-SBP-32a.

Les carottes MRS-CS-20, MRS-CS-21 et MRS-CS-27 ont, elles, été prises de part et d'autre d'un escarpement de faille. Le site était très prometteur car les réflecteurs anciens semblaient accessibles et les profils « CHIRP » 3.5kHz ne montrent pas de dépôts de glissement de terrain le long de l'escarpement (voir Figure 12). Cependant, lors du carottage MRS-CS-21, le tube a plié entre les réflecteurs « rouge » H1 et « bleu » H2, probablement en traversant un niveau très riche en coquilles de moules zébrées, *Dresseina sp.*, typique de la faune d'eau douce pontocaspienne. Les trois séquences finalement récupérées sont donc, à nouveau, de bons enregistrements contenant l'épisode à l'origine du réflecteur « rouge » H1, mais n'atteignent pas les réflecteurs suivants.

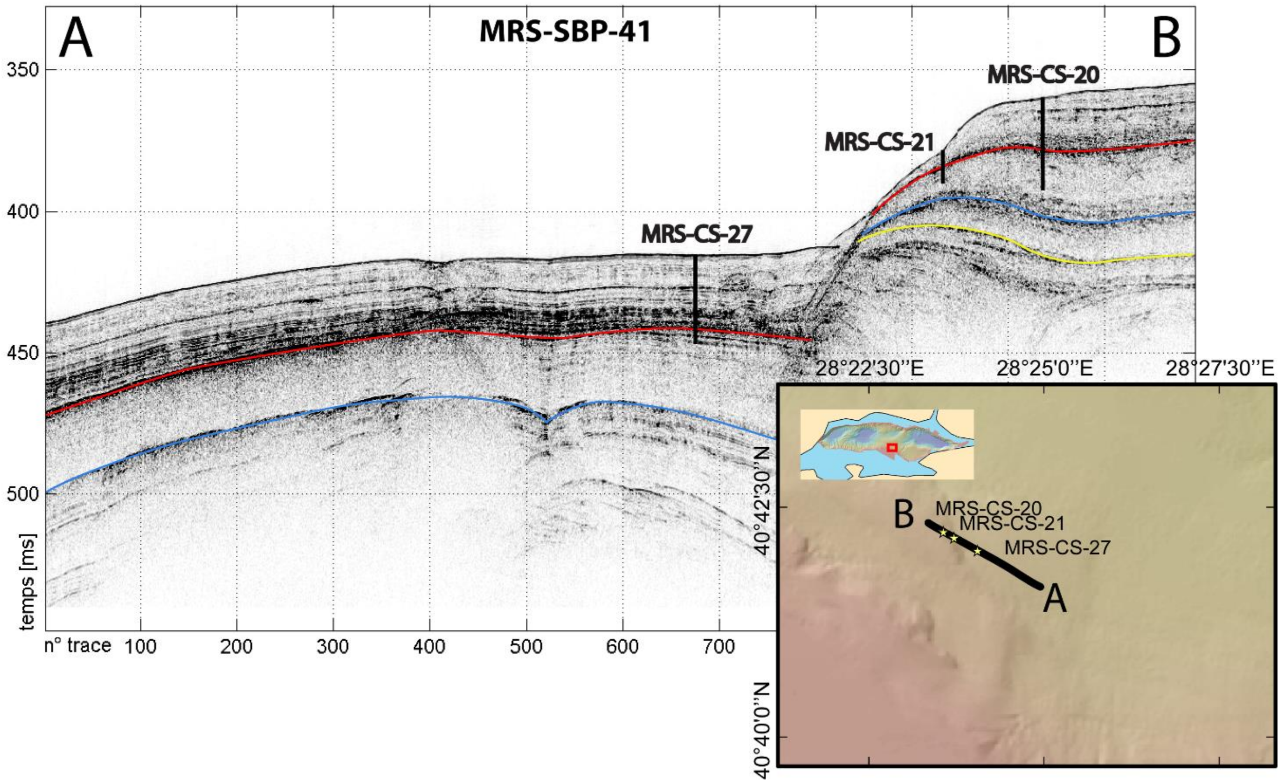

Figure 12. Localisation des carottes de sédiment MRS-CS-20, MRS-CS-21 et MRS-CS-27 dans l'Ouest du bassin d'İmralı et représentation des cible sur le profil « CHIRP » 3.5 kHz MRS-SBP-41.

4. Caractérisation du réflecteur H1 « Red » et vérification des corrélations par construction de synthétiques sismiques

Ce sont finalement 5 carottes récupérées lors de la mission MARSITE qui ont franchi le réflecteur « rouge » H1. Une étude des caractéristiques géophysiques de ces sédiments a été menée afin d'établir l'origine du réflecteur et de corréler précisément les niveaux de sédiments avec les profils sismiques.

Ce travail a permis, pour la première fois, d'expliquer l'origine du réflecteur « rouge » H1 dans les bassins de la mer de Marmara.

4.1. Lithologie des carottes MRS-CS-22, MRS-CS-18 et MRS-CS-27 et mesures de densité – Identification du H1 « Red »

La Figure 13 présente la lithologie détaillée de la carotte MRS-CS-22 ainsi que la densité des sédiments mesurée par transmission des rayons gamma au MSCL.

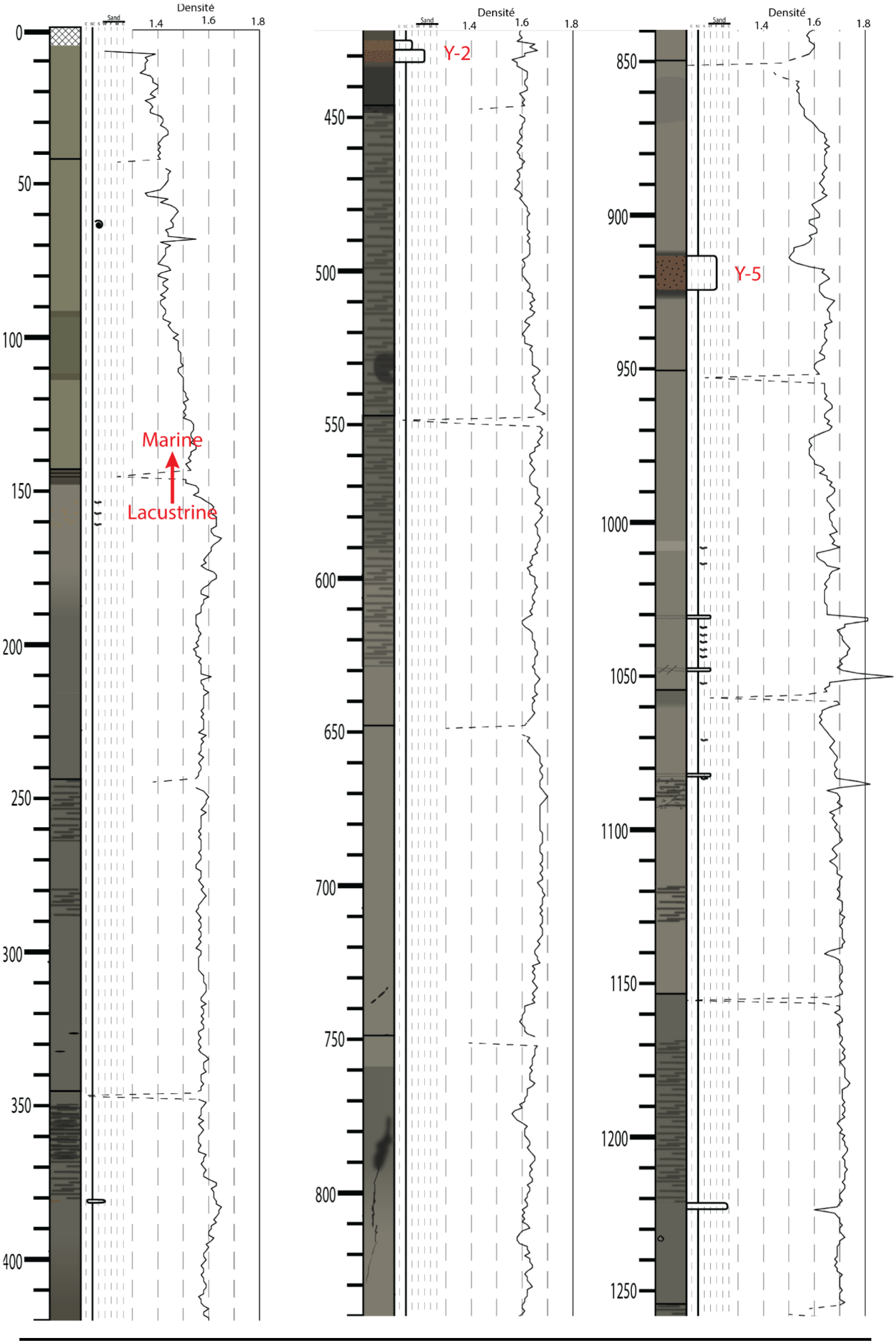
Densité
Sand
1.4
1.6
1.8
0
50
100
150
200
250
300
350
400
Marine
Lacustrine
Y-2
450
500
550
600
650
700
750
800
Y-5
850
900
950
1000
1050
1100
1150
1200
1250

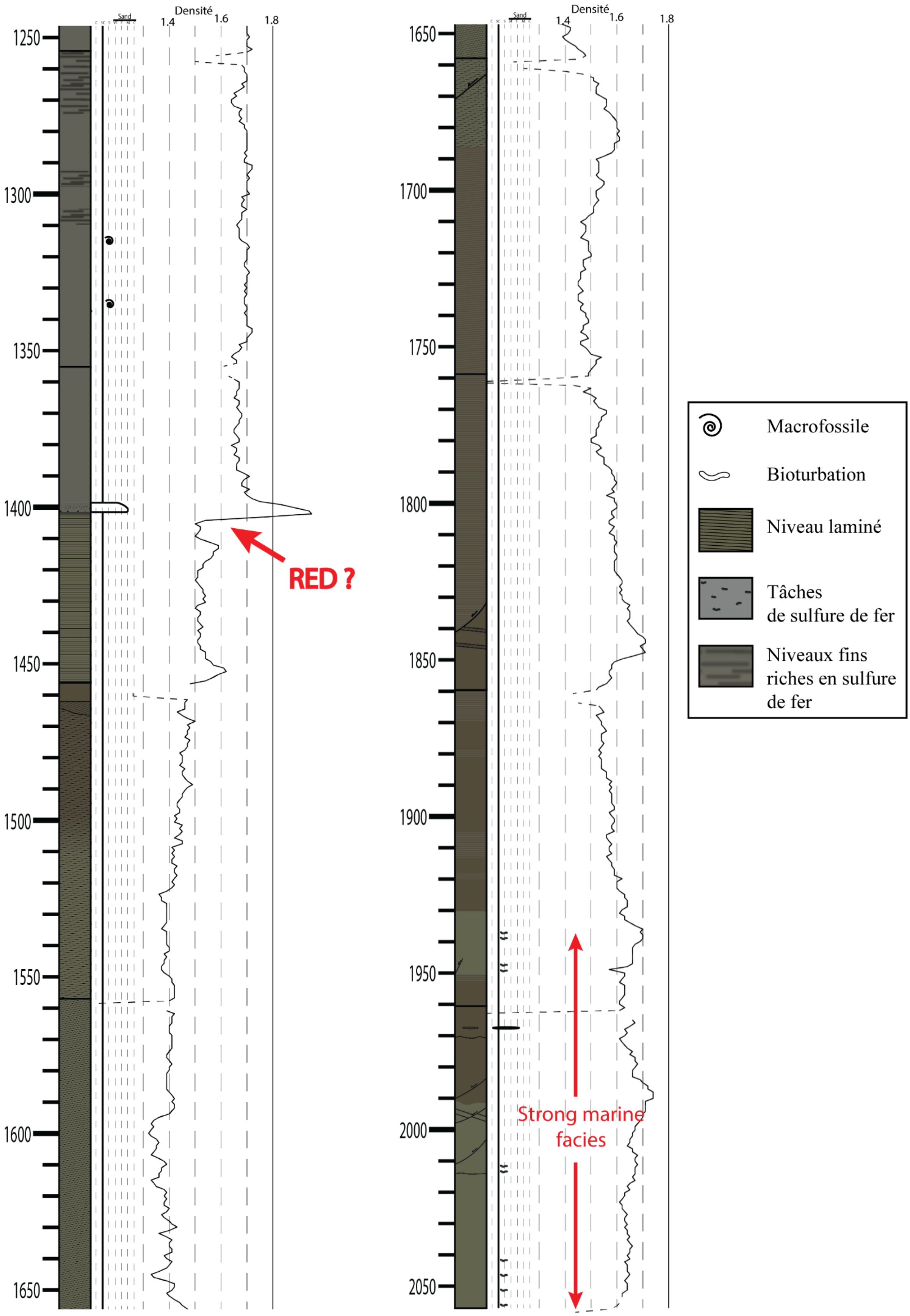

RED ?

Strong marine facies

Figure 13. (page précédente) Description lithologique détaillée de la carotte MRS-CS-22. Les couleurs reproduisent les observations faites avec la charte MUNSELL. La description a été faite quelques minutes après l'ouverture des sections. Les couleurs ont donc parfois rapidement varié. Par exemple, les zones noircies par la présence de sulfure de fer ont été oxydées et se sont éclaircies. Les densités indiquées en pointillées correspondent aux données relevées au niveau des extrémités de section et ont été nettoyées.

Les mesures de vitesse des ondes P obtenues ne sont exploitables que sur les premiers mètres des carottes et sont très bruitées (voir partir 4.2). Nous nous sommes donc basés exclusivement sur les densités mesurées pour estimer la position du réflecteur « rouge » H1(voir 13). La chute de densité située à 14 m, au niveau du passage d'un faciès laminé riche en matière organique à un faciès homogène est le meilleur candidat. Cette interface présente un contraste marqué de densité et la variation est stable, de part et d'autre de l'interface, pour être visible à la résolution des profils sismiques HR.

Cette hypothèse a été testée sur les autres carottes afin de déterminer si une chute comparable de densité se trouvait systématiquement à une profondeur dans la carotte cohérente avec la localisation du réflecteur.

La Figure 14 présente les densités mesurées sur 4 des 5 carottes ayant franchi le réflecteur « rouge » H1. Dans les 4 profils, une zone de chute abrupte de densité se trouve à une profondeur dans la carotte compatible avec la localisation du réflecteur « rouge » H1 identifié sur les profils sismiques (voir Figure 8, Figure 11 et Figure 12). La lithologie conforte l'hypothèse que le même événement est responsable de ces interfaces puisque les carottes MRS-CS-18, MRS-CS-20 et MRS-CS-27 présentent également une interface entre un faciès laminé en bas et un faciès homogène au-dessus.

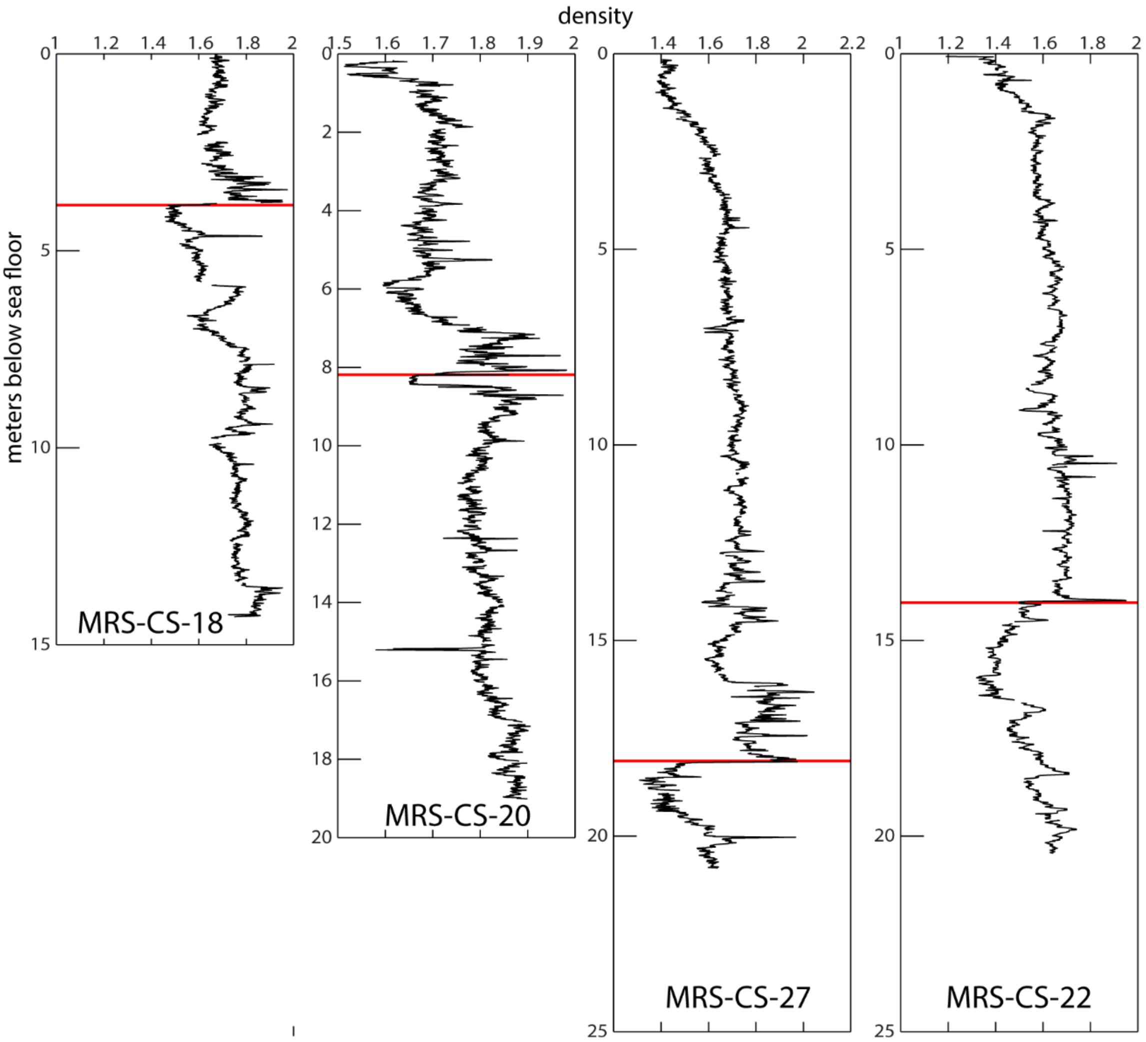

Figure 14. Densité mesurée le long des carottes MRS-CS-18, MRS-CS-20, MRS-CS-27 et MRS-CS-22. Les données ont été nettoyées des chutes de densités mesurées à chaque extrémité de section. Les traits rouges indiquent la localisation supposée du réflecteur « rouge » H1.

4.2. Vérification de la corrélation par construction de synthétiques sismiques HR

Afin de vérifier le lien entre la chute de densité et le réflecteur « rouge » H1, nous avons construit des synthétiques sismiques qui ont ensuite été corrélés avec les signaux sismiques les plus proches des points de carottages. Un synthétique sismique est une simulation de la propagation d'une onde sismique dans les sédiments de la carotte, à partir de ses caractéristiques géophysiques.

La première étape de la construction d'un synthétique est le calcul de l'impédance acoustique (AI) :

$$AI = \rho.Vp$$

Avec ρ la densité et Vp la vitesse des ondes P.

Mais nos valeurs de vitesse des ondes P ne sont exploitables que sur une longueur réduite des carottes. Au-delà, les mesures présentent trop d'atténuation pour être valide. Pour pouvoir malgré tout estimer l'impédance acoustique sur toute la longueur des carottes, nous avons évalué l'influence de la vitesse des ondes P sur le calcul. La Figure 15 présente la densité, la vitesse des ondes P et l'impédance acoustique sur les sections de la carotte MRS-CS-22 où le calcul est possible. On y remarque que si le signal Vp est plus bruité que la densité, sa variation relative est, elle, moindre. Les variations de l'impédance acoustique correspondent donc majoritairement aux variations de la densité.

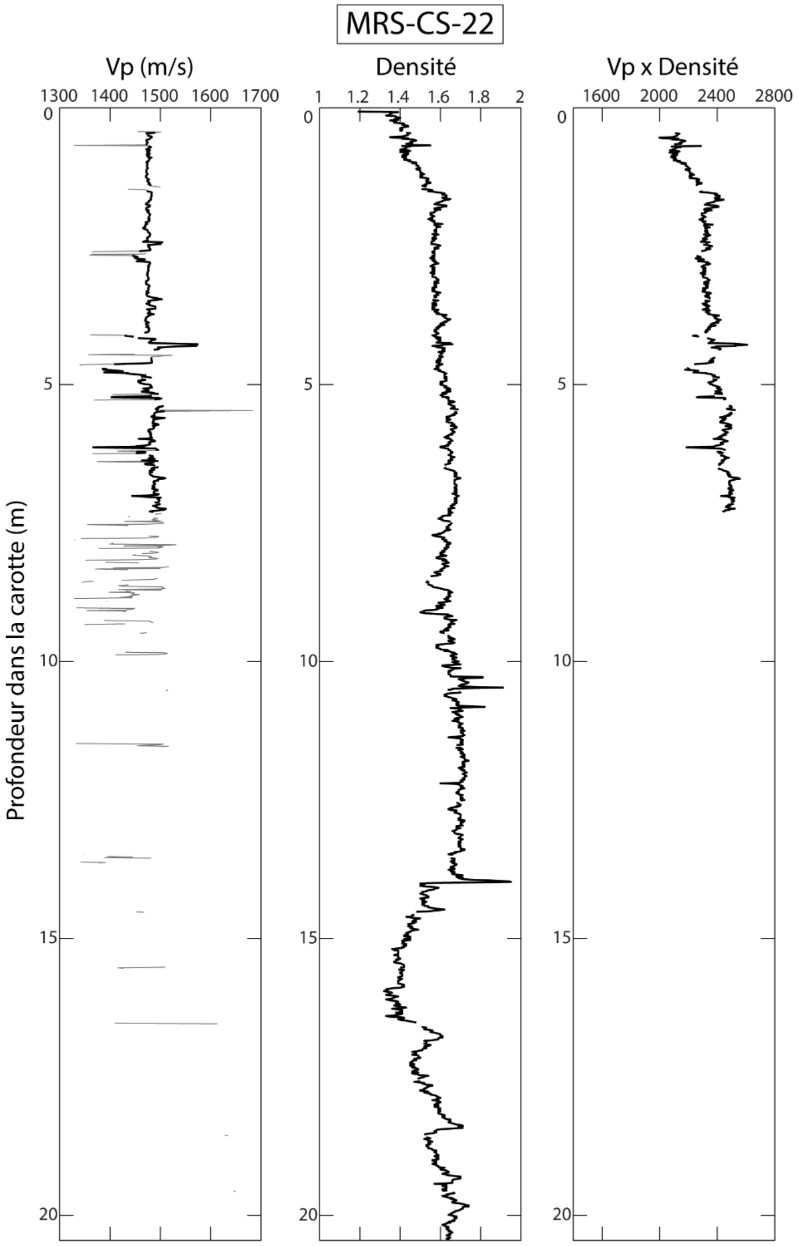

Figure 15. Calcul de l'impédance acoustique sur la carotte MRS-CS-22. Les valeurs grisées des mesures de Vp sont les données nettoyées. Elles correspondent à des artefacts d'une seule valeur aberrante ou bien aux mesures prises en extrémités de section. Les valeurs inexistantes de Vp correspondent à des mesures présentant trop d'atténuation.

En supposant cette caractéristique conservative sur l'ensemble des carottes, nous avons simplifié le calcul de l'impédance acoustique en considérant Vp constante. Cette simplification est évidemment drastique et implique que d'éventuels niveaux caractérisés par un fort gradient de vitesse des ondes P sans variations nette de densité ne seront pas matérialisés en un réflecteur sur les synthétiques. Cependant, les résultats montrent une belle coïncidence entre réflecteurs des synthétiques et réflecteurs des profils sismiques relevés, particulièrement dans les « CHIRP » 3.5 kHz (voir partie 4.3), ce qui suggère que la plupart des réflecteurs sismiques correspondent effectivement à des interfaces à forte variation de densité.

Le coefficient de réflexion (R) entre un point i et le point suivant est ensuite calculé selon la formule suivante :

$$R = \frac{AI_{i+1} - AI_i}{AI_{i+1} + AI_i}$$

Enfin, la convolution du profil de coefficient de réflexion par une ondelette semblable à celle utilisée pour le relevé des profils sismiques permet d'obtenir la simulation du signal dans la carotte. Pour les synthétiques de sismique HR, nous avons utilisé l'option de calcul de synthétiques intégrée au logiciel KINGDOM. Ce logiciel propose également de récupérer une ondelette à partir des données sismiques.

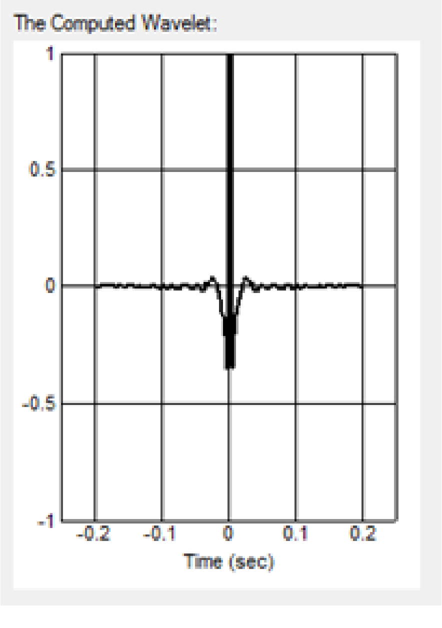

Figure 16. Ondelettes calculées par le logiciel KINGDOM à partir des données du profil pirmarmara_a2_b8, à proximité du point de carottage de la carotte MRS-CS-22. Il est également possible de créer des ondelettes théoriques. Les ondelettes de Ricker sont de bonnes approximations des ondelettes sismiques et sont couramment utilisées.

La corrélation du synthétique calculé et des traces sismiques est faite en considérant que la carotte a été compactée lors du carottage et que la longueur réelle de sédiment récupéré correspond à la longueur du tube multipliée par le pourcentage de récupération (voir Table 1) moins 50 cm correspondant à l'ogive. Cela revient donc à supposer que la colonne de sédiment a subi une compression homogène lors du carottage. Cette hypothèse est sans doute grossière mais elle est suffisante pour travailler à la résolution des profils sismiques HR. Le signal est ensuite placé par rapport au réflecteur du fond marin et en considérant une vitesse des ondes de 1500 m/s.

La Figure 17 présente le résultat pour la carotte MRS-CS-22.

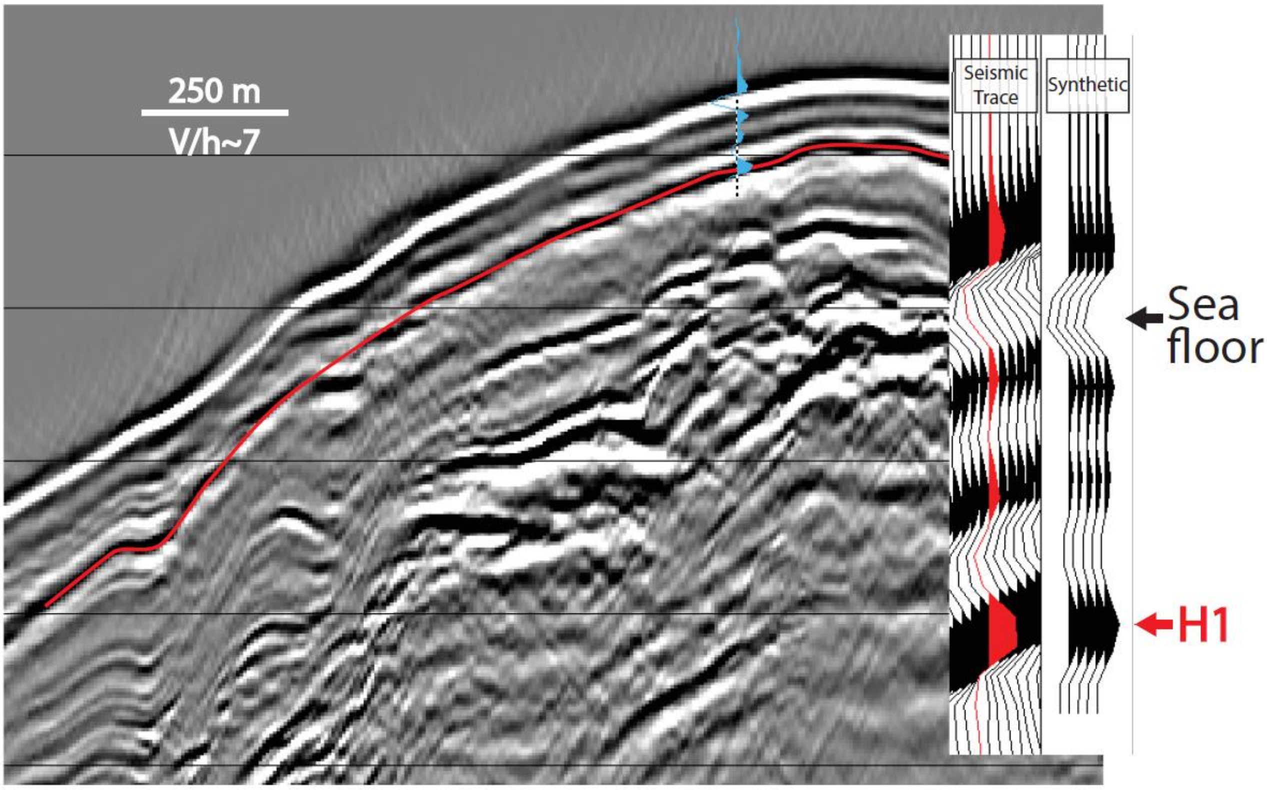

Figure 17. Comparaison du synthétique sismique de la carotte MRS-CS-22 et du profil sismique relevé au point de carottage. Les réflecteurs du fond marin et du « rouge » H1 sont bien corrélés avec le haut de la carotte et la position proposée pour le réflecteur « rouge » H1 dans la carotte. Les autres réflecteurs, plus faibles, ne sont que des latéraux des deux réflecteurs principaux.

La construction du synthétique sismique de la carotte MRS-CS-22 et sa comparaison avec les traces relevées à proximité immédiate du point de carottage révèle une corrélation quasiment parfaite entre les deux signaux. Cependant, seuls le fond marin et le niveau du réflecteur « rouge » H1 possèdent des caractéristiques géophysiques à l'origine d'un fort coefficient de réflexion. L'ondelette contient des latéraux à l'origine de pics secondaires interprétés comme des réflecteurs sur le profil. Quoi qu'il en soit, cette construction confirme notre hypothèse : l'origine du pic d'amplitude formant le réflecteur nommé « rouge » H1 est bien la chute de densité mesurée à 14 m dans la carotte.

Des synthétiques ont également été construits à partir des données des autres carottes. A nouveau, seules les densités ont pu être exploitées. La Figure 18 présente leur comparaison avec les traces sismiques aux points de carottage.

Seule la carotte MRS-CS-27 permet également de vérifier la correspondance entre le niveau de variation de densité et la détection d’un réflecteur dans les profils sismiques. La chute de densité dans la carotte MRS-CS-20 correspondant au faciès finement laminé est trop fine pour créer un réflecteur à la résolution des profils HR (voir Figure 14). Enfin, la carotte MRS-CS-18 est trop condensée et le réflecteur « rouge » H1 est sans doute superposé au premier latéral du réflecteur du fond marin.

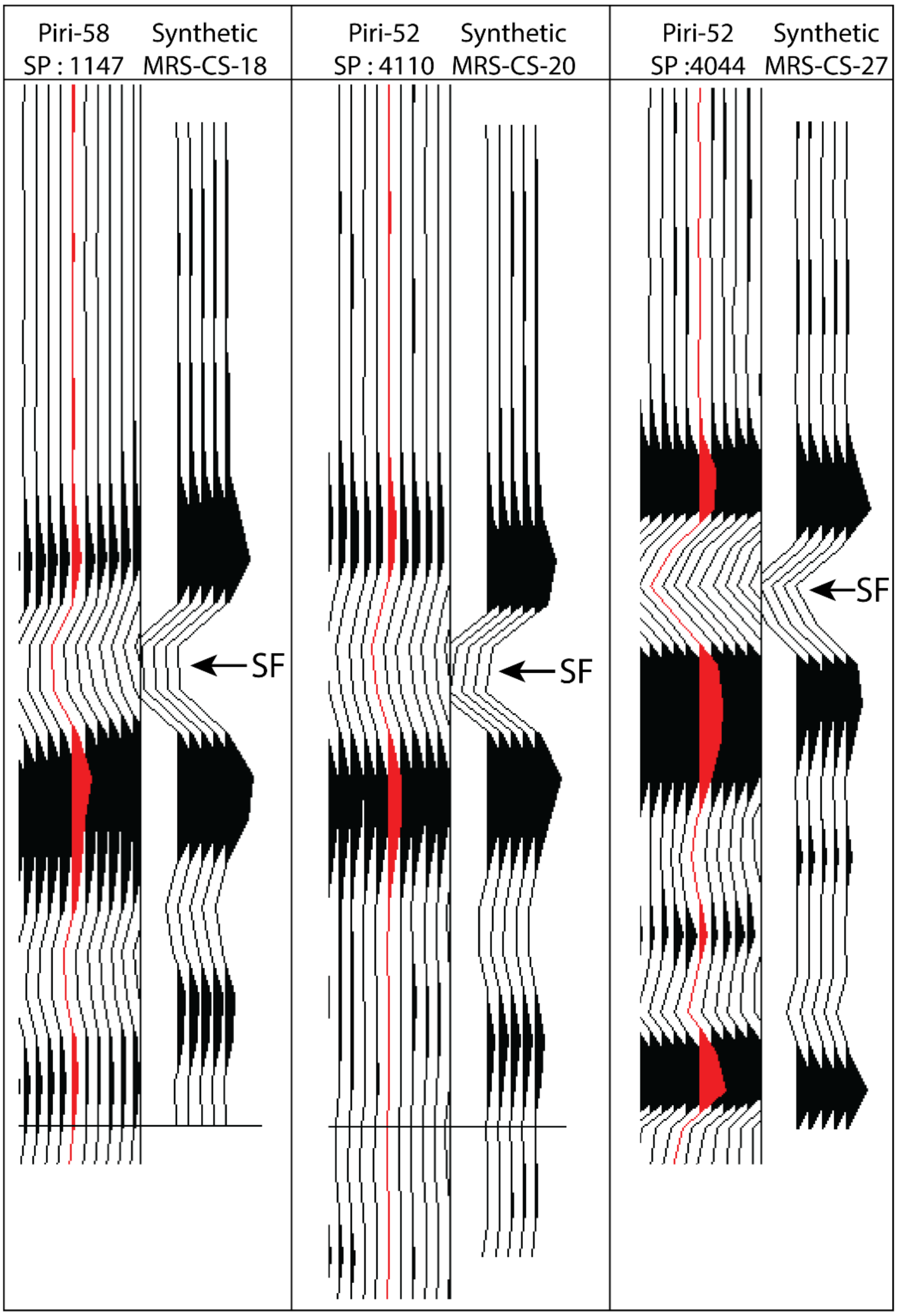

Figure 18. Comparaison des synthétiques des carottes MRS-CS-18, MRS-CS-20 et MRS-CS-27 avec les traces sismiques relevées à proximité des points de carottage. SF (Sea Floor) indique la position du réflecteur du fond marin. Seules les données de la carotte MRS-CS-27 permettent de corréler un deuxième réflecteur.

4.3. Vérification de la corrélation par construction de synthétiques sismiques « CHIRP » 3.5 kHz

Si la résolution des profils sismiques HR ne permet pas toujours de distinguer un réflecteur lié à la variation de densité ni d'établir une correspondance avec un réflecteur observé, les profils « CHIRP » 3.5 kHz, eux, donnent une image bien plus fine de l’empilement des sédiments.

Le logiciel KINGDOM ne proposant pas de travailler avec des ondelettes courtes telles que celles utilisées dans les relevées des « CHIRP » 3.5kHz, nous avons développé notre propre routine de construction des synthétiques avec MATLAB. La technique est exactement la même que celle détaillée pour les profils HR. Nous avons, toutefois, travaillé avec deux types d’ondelettes. La première, comme précédemment, était calculée à partir des profils sismiques, par auto-convolution des traces. La deuxième est une ondelette théorique de Ricker. Les deux versions ont donné sensiblement les mêmes résultats. Les synthétiques présentés dans cette partie ont été générés avec l’ondelette de Ricker. A cette résolution, on ne travaille plus avec les amplitudes mais avec l’enveloppe des amplitudes. Il n’y a donc pas de valeurs négatives.

La Figure 18 présente les synthétique des carottes MRS-CS-18, MRS-CS-20, MRS-CS-27 et MRS-CS-22 en superposition avec les profils « CHIRP » 3.5 kHz. Pour toutes les carottes, placer le profil synthétique en fonction du fond marin et de la vitesse des ondes ne permettait pas d’obtenir une corrélation satisfaisante. A chaque fois, il a été nécessaire de décaler le synthétique vers le bas en dessous du fond marin. Nous reviendrons sur ce point ultérieurement. Les synthétique ont alors été placés de façon à faire coïncider les pics des synthétiques et les niveaux de grande amplitude des profils. Seule la carotte MRS-CS-18 ne permet pas une corrélation précise pic/horizon, mais plutôt une corrélation entre une zone de pics et une zone d’horizons superposés.

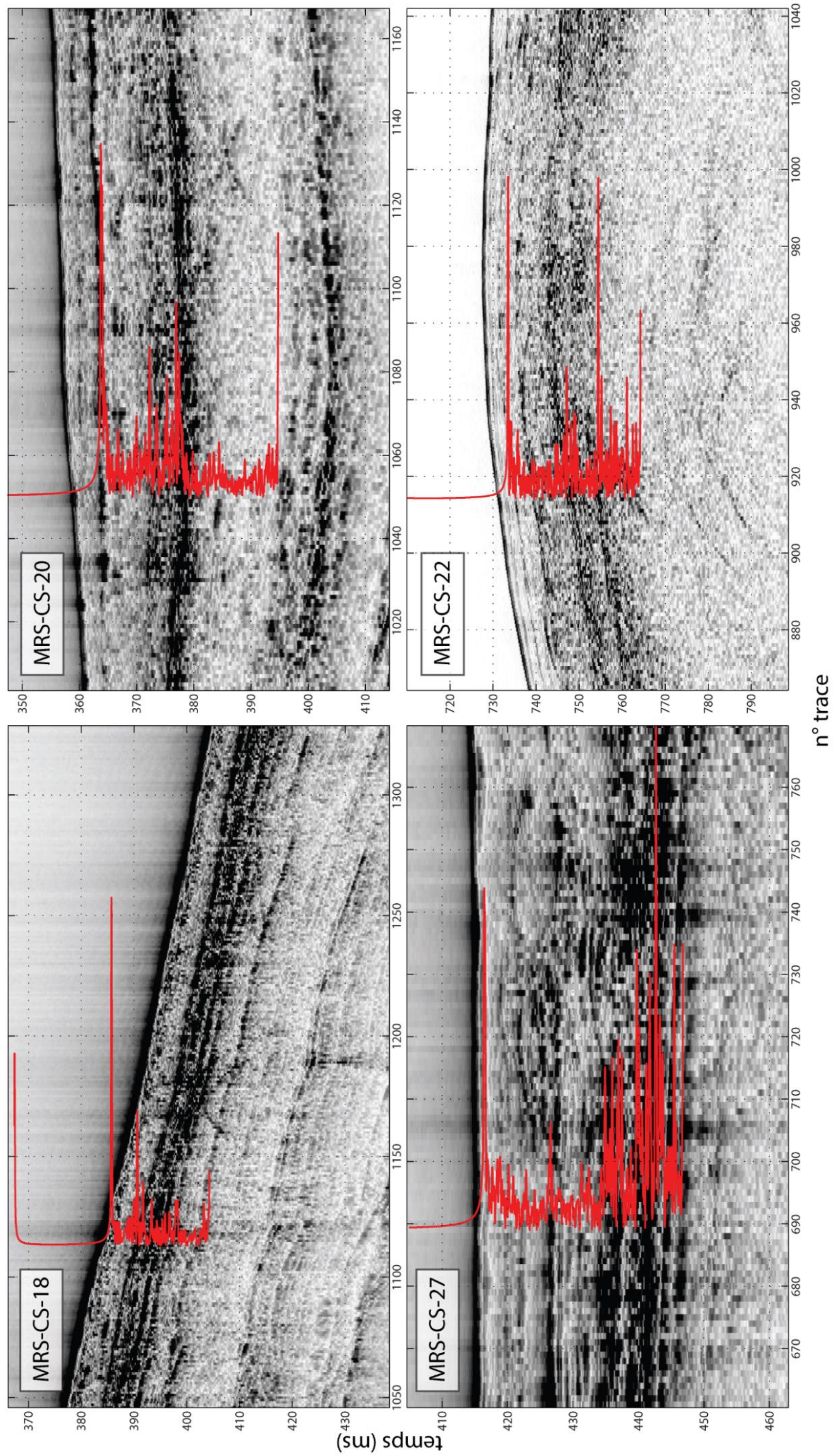
MRS-CS-18
MRS-CS-20
MRS-CS-27
MRS-CS-22
temps (ms)
n° trace
370
380
390
400
410
420
430
1050
1100
1150
1200
1250
1300
350
360
370
380
390
400
410
1020
1040
1060
1080
1100
1120
1140
1160
410
420
430
440
450
460
670
680
690
700
710
720
730
740
750
760
720
730
740
750
760
770
780
790
880
900
920
940
960
980
1000
1020
1040

Figure 19. (page précédente) Comparaison des synthétiques « CHIRP » des carottes MRS-CS-18, MRS-CS-20, MRS-CS-27 et MRS-CS-22 et des profils « CHIRP »3.5kHz relevés aux points de carottage. Les profils et les synthétiques présentent l'enveloppe du signal. La corrélation doit se faire avec les traces les plus proches de la verticale où a été placé le 0 des synthétiques. Le premier pic des synthétiques est provoqué par le contraste entre les premières densités mesurées sur la carotte et la densité de l'eau considéré au-dessus des sédiments. Cependant, ce pic ne représente pas le fond marin si le carottage n'a pas récupéré les sédiments les plus superficiels. Le dernier pic des synthétiques est également un artefact.

Dans un deuxième temps, aidé de la description lithologique des carottes (voir Figure 13) et de la représentation des synthétiques calculés en fonction de la profondeur le long de la carotte, nous avons expliqué l'origine des pics principaux des synthétiques en terme de variations lithologique. Ce travail permet, finalement, d'associer les horizons visibles sur les profils avec un événement observé dans la lithologie.

La Figure 20 présente le résultat pour la carotte MRS-CS-22. En plus de donner sans équivoque la position du réflecteur « rouge » H1, la corrélation permet d'interpréter les trois réflecteurs sus-jacents visibles. Un pic correspondant à la transition marin/lacustre est bien corrélé avec le premier réflecteur du profil « CHIRP ». Un deuxième pic, provoqué par les variations de densité d'un niveau de cendre volcanique, correspond à un horizon, au-dessus du réflecteur « rouge » H1. Enfin, un dernier niveau à forte amplitude dans le profil sismique peut être attribué à un autre niveau de cendre volcanique, même si les variations de densité dans la carotte ne créent pas de pic dans le synthétique.

Des identifications des deux niveaux de cendre volcanique ont été proposées dès la description lithologique de la carotte (voir 13) par rapprochement avec *Çağatay et al.* [2015]. Plus tard, les identifications proposées ont été vérifiées par analyse chimique de la composition des verres (voir Chapitre III). Le premier niveau correspond aux dépôts de l'éruption Cape Riva du Santorin il y a 22 ka (tephra marin Y-2) et le deuxième à l'éruption Campagnian Ignimbrite des Champs Phlégréens il y a 39 ka (tephra marin Y-5).

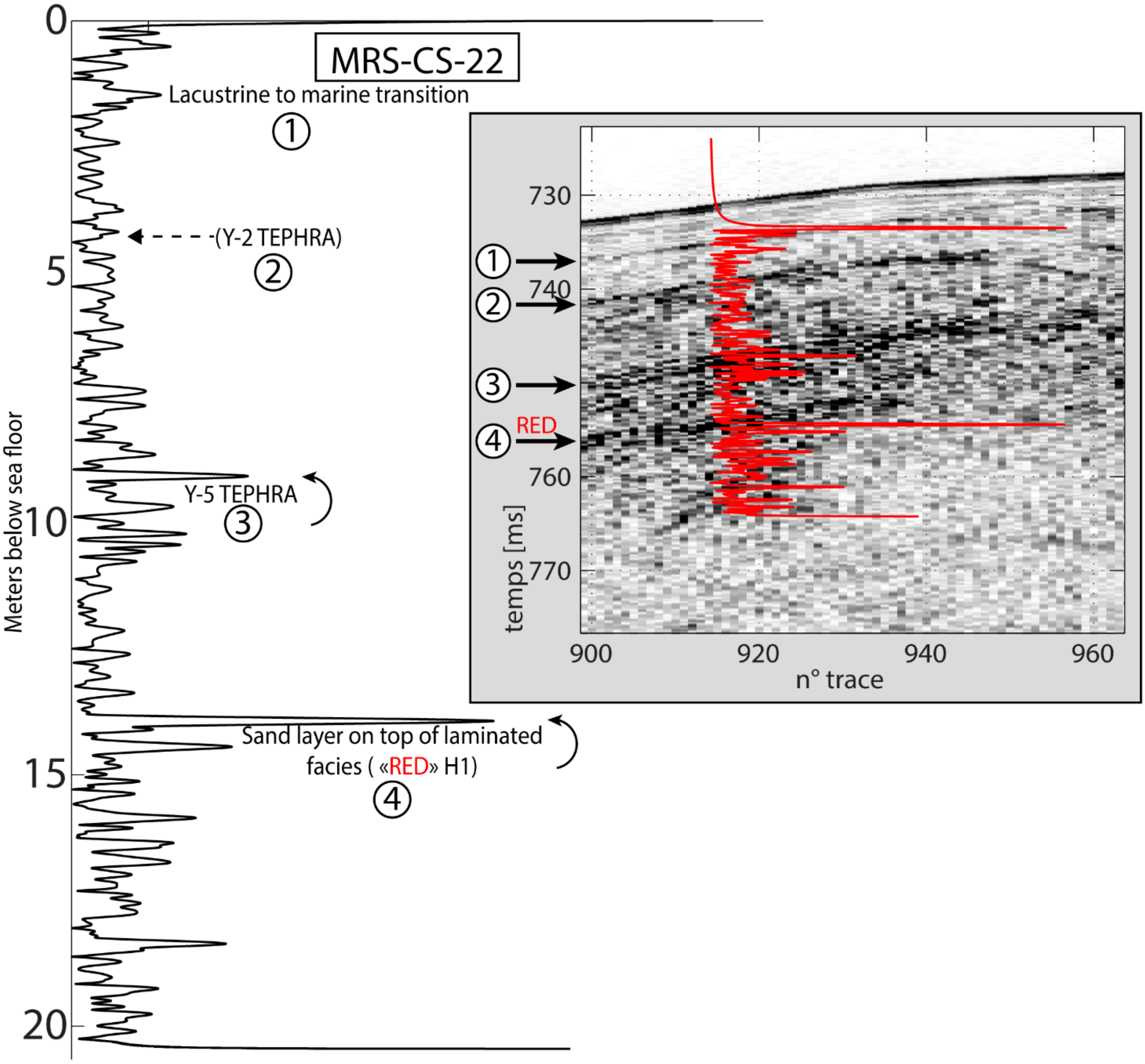

Figure 20. Identification de l'origine des pics du synthétique "CHIRP" de la carotte MRS-CS-22 et correspondance avec les réflecteurs observés sur le profil au point de carottage. Les variations géophysique de la carotte au niveau du tephra Y-2 ne créent pas de pic dans le synthétique. Cependant, la profondeur du réflecteur n°2 tel qu'il est calé par rapport aux autres niveaux correspond parfaitement à la profondeur du niveau de cendre Y-2 dans la carotte de sédiment.

La carotte MRS-CS-22 est celle offrant les corrélations les plus visibles avec des niveaux continus. Si les autres synthétiques comportent tous un pic suffisamment isolé ou bien des zones de pics permettant un calage avec les profils (voir Figure 18), l'interprétation complète n'est pas aussi aisée. Les synthétiques comportent généralement des pics correspondant à des faciès locaux, tels que des lentilles de sable, ou bien les profils comportent des réflecteurs nombreux qui ne permettent pas une interprétation certaine de chacun des réflecteurs rapprochés. Cependant, la profondeur à laquelle le niveau de chute de densité et de transition d'un faciès laminé à un faciès homogène est observé, correspond dans tous les cas à la profondeur à laquelle le réflecteur « rouge » H1 a été pointé, à la fois sur les profils « CHIRP » 3.5 kHz et sur les profils de sismique HR.

Ainsi la construction des synthétiques à la résolution des profils « CHIRP » 3.5 kHz permet de valider la correspondance entre le réflecteur « rouge » H1 et la variation de densité dans les sédiments liée à une interface entre sédiments homogènes et sédiments laminés riches en matière organique. L'interprétation de cette interface stratigraphique en termes d'événement environnementaux ou climatiques ou bien sa datation permettra donc une première validation ou invalidation des interprétations proposées par *Sorlien et al.* [2012], *Grall et al.* [2013] et *Grall et al.* [2014] pour la construction d'un modèle d'âge des sédiments de la Mer de Marmara.

Au-delà de cet objectif, la construction des synthétique a également permis la caractérisation de réflecteurs fins dans les profils « CHIRP » 3.5 kHz. Ce travail pourrait être poursuivi, par exemple pour l'identification de la transition marin/lacustre ou des niveaux de tephra sur d'autres carottes à travers toute la mer de Marmara afin de pouvoir contraindre la cartographie de ces niveaux sur les profils « CHIRP » 3.5 kHz. Ces trois événements étant précisément datés, une cartographie de leur dépôt permettrait d'établir des cartes d'épaisseur de sédimentation et d'étudier les éventuelles variations récentes de vitesse de sédimentation.

4.4. Apport des synthétiques sur la connaissance des phénomènes de compression et de pertes lors du carottage

Dans cette partie, on parlera de compression et d'étirement des sédiments en non pas de compaction et de décompactions. En effet, le phénomène décrit ici se produit dans le tube de carottage et n'implique pas de variation de teneur en eau mais seulement d'éventuelles variations de pression de fluide.

Les quatre corrélations présentées en Figure 19 ont été réalisées en supposant que le haut de la carotte ne correspond pas au fond du bassin mais qu'une épaisseur de sédiments a été perdue lors du carottage. La différence entre la profondeur du fond marin et celle du haut du synthétique correspond à une épaisseur de 0.9, 1.4, 1.8 et 4.8 m. Cette dernière valeur est celle de la carotte MRS-CS-20 que nous considérons comme une anomalie, peut-être liée à un décalage entre la cible et la position de carottage réelle sur la pente érodée. Les autres écarts de profondeur pourraient, eux, être dus à une récupération incomplète des sédiments. Par ailleurs, l'existence d'une compression ou d'une récupération incomplète est certaine puisque la pénétration des tubes de carottage a souvent atteint 100% sans que la longueur de sédiment récupérée n'atteigne celle du tube (voir Table 1).

La corrélation des réflecteurs identifiables de la carotte MRS-CS-22 permet de vérifier que les deux processus, perte et compression, interviennent ensemble. La Figure 21 présente une comparaison du synthétique « CHIRP » 3.5 kHz de la carotte et de la trace sismique relevée la plus proche. Les profils ont, cette fois, été calés par rapport au réflecteur et au pic n°1 correspondant à la transition marin/lacustre.

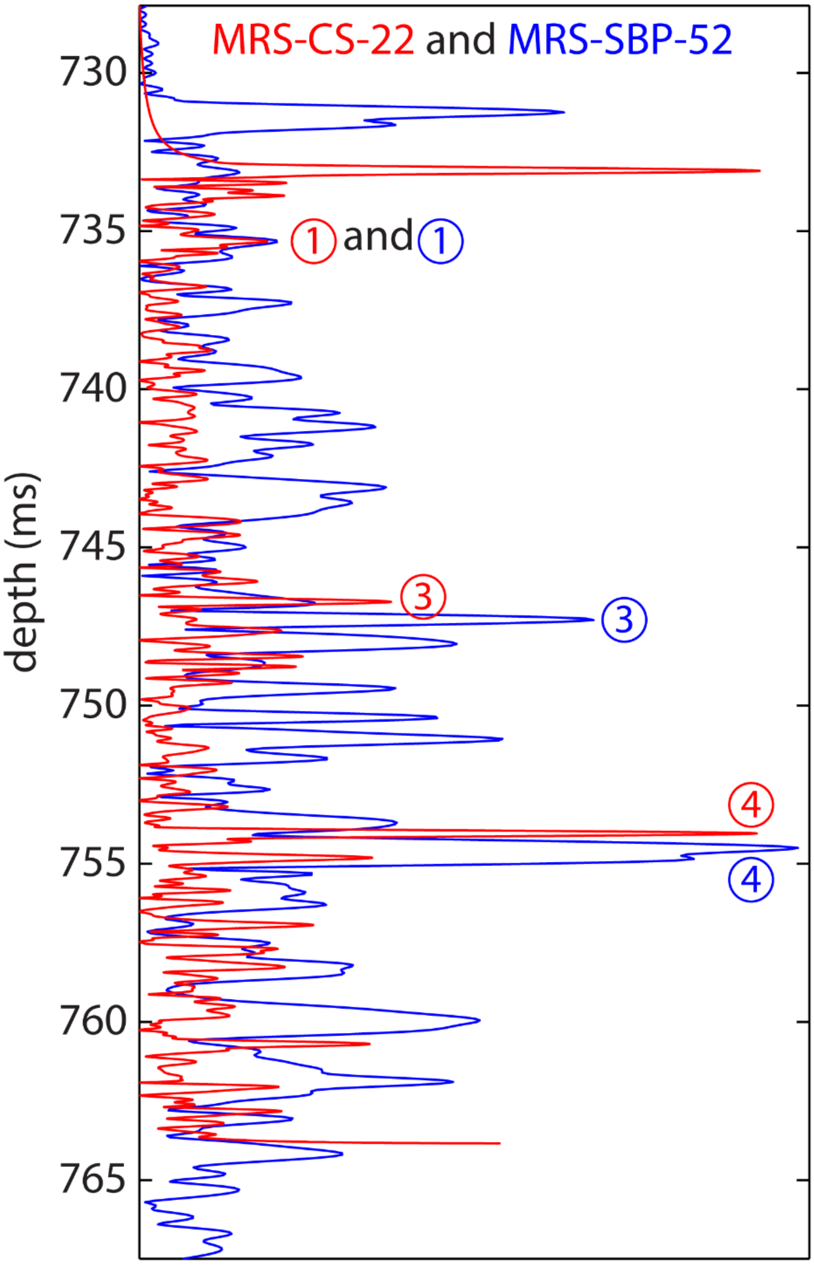

Figure 21. Synthétique "CHIRP' de la carotte MRS-CS-22 (en rouge) et enveloppe de la trace "CHIRP" la plus proche du point de carottage sur le profil MRS-SBP-52 (en bleu). Les deux profils sont calés par rapport au pic et au réflecteur correspondant à la transition marin/lacustre à environ 735 ms. Les numéros correspondent aux numéros de pic de la Figure 20. Le niveau de cendre volcanique Y-2 n'est détectable sur aucun des deux signaux.

Le niveau correspondant à la transition marin/lacustre constitue un bon point de calage de par la bonne similitude entre les deux signaux. Tous deux sont constitués d'un pic triple avec un pic central majeur. La transition se situe à une profondeur réelle dans la carotte de sédiment de 1.5 m mais elle est corrélée avec un pic à 4.1 ms sous le fond marin, soit 3 m. Il semble douteux que les premiers 1.5 m de la carotte aient subi une compression divisant son épaisseur de moitié. De plus, une telle compression serait visible dans le sédiment et se serait propagée plus profondément dans la carotte. Nous proposons donc qu'une épaisseur de sédiment, sans doute proche de 1.5 m, a été perdue en haut de la colonne lors du carottage.

En dessous, le décalage entre les niveaux corrélés 1et 3 (voir Figure 21), montre que le sédiment a été légèrement comprimé. Plus précisément, l'épaisseur de sédiment entre les niveaux corrélés 1 et 3 correspondrait à 9 m selon le profil « CHIRP » 3.5 kHz et à seulement 8.5 m dans la carotte. Soit une compression de 5.8%. Au contraire, la même comparaison entre les niveaux 3 et 4 aboutit à une épaisseur de sédiment de 5.4 m d'après le profil « CHIRP » 3.5 kHz et à 5.5 m d'après le synthétique. Cet écart est trop faible pour conclure à un étirement mais indique en tout cas une réduction de la compression.

En conclusion, nous proposons que, lors des carottages à piston avec le Pourquoi Pas ? pendant la campagne Marsite, trois phases se succèdent :

- Absence de récupération (perte des sédiments les plus superficiels)
- Récupération avec compression modérée des sédiments
- Récupération sans compression ou avec étirement

Si la comparaison des données des autres carottes amène à des conclusions semblables, la difficile corrélation des signaux ne permet pas d'aboutir à des résultats robustes. Ce travail ne donne donc qu'une première idée des phénomènes de perte, compression et étirement lors du carottage par piston. Des données d'autres carottes assorties à des profils « CHIRP » 3.5 kHz seraient nécessaires pour renforcer nos conclusions. Des informations sur des carottes plus longues permettraient notamment de déterminer s'il y a réellement une inversion de tendance avec un passage d'un processus de compression à un processus d'étirement, si un état stationnaire existe ou bien si un état stationnaire existe suivi d'un étirement des sédiments sous-jacents.

Enfin, le déroulement technique du carottage est à prendre en compte car plusieurs facteurs peuvent conduire à une mauvaise récupération des sédiments. Par exemple, l'ajustement de la longueur de la boucle de déclenchement est un paramètre à ajuster précisément en fonction de la profondeur du carottage et doit tenir compte de l'élasticité du câble parfois difficile à évaluer. Or, cet ajustement est plus difficile à faible profondeur d'eau, comme c'est le cas ici, car l'incidence de l'élasticité est alors moins importante. Un déclenchement tardif du piston produirait alors une pénétration sans récupération dans les premiers sédiments meubles puis une récupération imparfaite sur les mètres suivants, après déclenchement. Le même mécanisme peut survenir simplement si la détection du fond marin est mal ajustée et que le déclenchement n'est pas fait à la bonne profondeur.

5. Variations environnementales et dépôts ponctuels au niveau du réflecteur H1 « Red »

L'étude des réflecteurs sismiques et des synthétiques calculés à partir des données géophysiques des carottes a permis d'établir un lien entre le réflecteur « rouge » H1 et une transition entre deux faciès dans la colonne de sédiment. Mais l'objectif final de l'identification de ce réflecteur sismique est d'apporter des précisions au modèle d'âge des sédiments de la mer de Marmara. Pour rappel, *Sorlien et al.* [2012] proposent, pour le réflecteur « rouge » H1, un âge de 110 ka et *Grall et al.* [2013] proposent un âge de 109 ou 130 ka (pour les réflecteurs H1et H1', superposés à la position de la carotte MRS-CS-22).

Cette dernière partie mentionne quelques résultats présentés en détails dans le Chapitre III et présente des données additionnelles obtenues lors de l'étude des niveaux lithologiques au niveau de la transition à l'origine du réflecteur « rouge » H1.

5.1. Une évolution vers un milieu de plus en plus lacustre à l'origine de la variation de faciès

Toutes les carottes présentent la même transition lithologique d'un faciès vert laminé à un faciès gris homogène, plus dense, à l'origine du réflecteur « rouge » H1. Dans la carotte MRS-CS-22, l'identification de deux niveaux de cendres de 22 ka et 39 ka au-dessus et l'existence d'un niveau de sédiment marin franc en dessous permet de proposer une première fourchette temporelle pour les dépôts sédimentaires à la transition : entre 111 ka (fin de la dernière période de haut niveaux marin) et 39 ka. Cette fourchette correspond à une période allant du stade MIS 5d au stade MIS 3, c'est-à-dire une période comprise dans le dernier interglaciaire, alors que le niveau de la mer était plus bas qu'aujourd'hui. Les deux faciès étudiés sont donc des dépôts correspondant à un stade lacustre de la Mer de Marmara, ou bien à un stade intermédiaire.

La Table 3 présente les caractéristiques des deux faciès ainsi que de leur interface. Les observations sont valables pour toutes les carottes mentionnées précédemment. Les analyses ont été faites sur la carotte MRS-CS-22 ou bien proviennent d'études précédentes publiées pour le cas du faciès homogène. D'une carotte à l'autre, les conclusions de l'observation des faciès sont les mêmes. Cependant, les faciès ont des épaisseurs variables, notamment le faciès laminé qui fait plusieurs mètres dans la carotte MRS-CS-22, mais seulement quelques centimètres dans la carotte MRS-CS-20. De plus, dans la carotte MRS-CS-22, un niveau de sable érosif de 2 cm est à la transition. Dans les autres carottes, il n'y a pas toujours de niveau de sable précisément à l'interface et on trouve parfois plusieurs niveaux lenticulaires de sable.

	Observations (toutes carottes)	**Résultats d'analyse (MRS-CS-22 ou étude précisée)**
Faciès homogène	Argile silteuse grise homogène avec des zones à nombreuses « taches » de sulfure de fer. Fragments de Dreissena sp.	Ostracodes lacustres [*Vidal et al.*, 2010] vers le sommet du faciès. Contenu très pauvre en micro et macro fossiles. Diatomées d'eau douce (fragments, rares specimens intacts)
Niveaux de sables	Erosifs Grains moyens à fins Classement parfois visible.	Grains classés Principalement du quartz aux grains émoussés luisants.
Faciès laminés	Argile grise-verte luisante à nombreuses lamines blanches. Aucun macro-fossile.	Lamines blanches riches en carbonates. Diatomées d'eau douce à saumâtre abondantes Riche en matière organique (sapropel).

Table 3. Résumé des caractéristiques des faciès et des niveaux de sable à l'interface à l'origine du réflecteur « rouge » H1.

De ces différentes observations, il est possible de tirer plusieurs conclusions (pour plus de détails, voir le Chapitre III) :

- Le faciès laminé correspond à un environnement d'eau douce au moins dans la tranche d'eau superficielle.
- Le faciès laminé correspond à un environnement impropre à la vie dans les profondeurs des bassins au moins.
- Le faciès homogène correspond à un environnement lacustre oligotrophique.

Ainsi, les deux faciès correspondent à des stades au moins partiellement lacustres. Pour expliquer leurs différences, nous proposons que l'interface entre les deux faciès correspond à un basculement ayant réorganisé les masses d'eau lors de la désalinisation de la Mer de Marmara après le dernier interglaciaire. Une possibilité serait que le faciès laminé corresponde à un état stratifié de la colonne d'eau entre une masse inférieure d'eau plus ou moins salée et une couche superficielle d'eau douce provenant de la mer noire, alors que la connexion avec la

Mer Méditerranée était conservée mais ténue. La baisse du niveau sous le détroit des Dardanelles aurait alors accéléré la désalinisation en supprimant toute entrée d'eau de mer, ce qui aurait pu avoir comme conséquence finale l'homogénéisation des masses d'eau.

Cependant, un basculement dans la répartition des masses d'eaux aurait aussi pu survenir avant la déconnexion, au cours de la désalinisation graduelle liée à la réduction de la connexion entre la Mer de Marmara et la mer Méditerranée.

5.2. Origine des niveaux de sables à l'interface entre les faciès

Si la variation de densité à l'origine du réflecteur « rouge » H1 n'est liée qu'à la transition entre les deux faciès, cette interface est aussi caractérisée par des niveaux de sables qui peuvent peut-être apporter des informations supplémentaires sur l'origine des faciès. Le plus massif est celui présent à l'interface dans la carotte MRS-CS-22.

A première vue, ce niveau semble granoclassé verticalement, cependant une étude à très haute résolution de la granulométrie a révélé une stratification à l'intérieur du niveau. La Figure 22 présente les résultats obtenus.

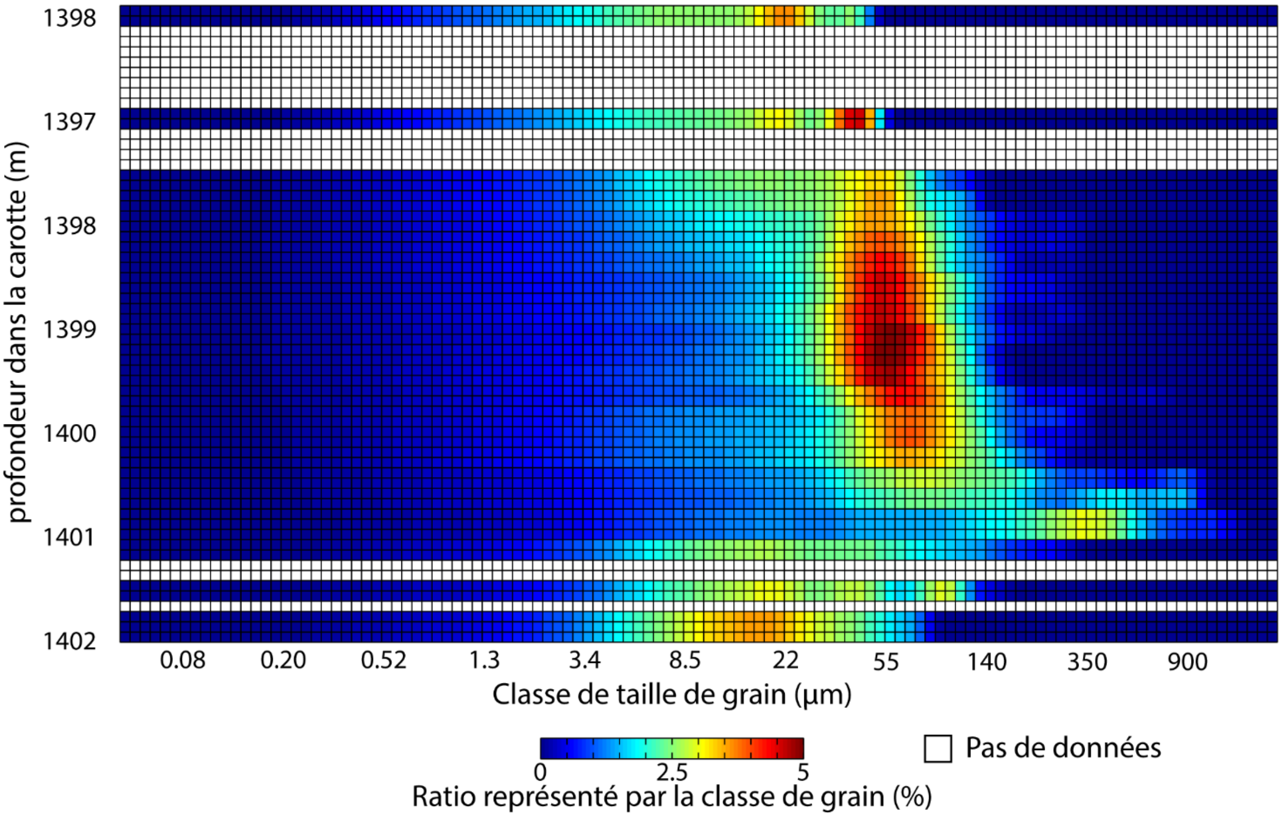

Figure 22. "Colormap" de la composition granulométrique à l'interface à l'origine du réflecteur 'rouge" H1.

Une première observation est que les matrices des deux faciès, laminé et homogène, sont comparables en terme de granulométrie. En effet, en dessous du niveau de sable à 1401 cm et au-dessus de 1398 cm, on observe le même ordre de répartition de la granulométrie entre 3.4 et 55 µm. Entre les deux faciès, l'étude révèle que le niveau de sable est en fait composé de deux niveaux distincts. La base, entre 1401 et 1401.3 cm est constituée d'une lamine de sable grossier de 140 à 900 µm. Le deuxième, plus fin, est composé de grains d'environ 22 à 140 µm. La juxtaposition des deux niveaux est à l'origine de l'apparent classement vertical. Indépendamment, les niveaux présentent plutôt un classement limité. Le deuxième niveau montre bien cependant une légère évolution vers des grains plus fins vers le haut. Les deux niveaux pourraient simplement correspondre aux grains transportés par le courant et aux grains mis en suspension à la suite d'un même événement.

De par l'absence de matrice fine dans les niveaux de sable, ceux-ci doivent correspondre à des événements courts et ayant sédimenté rapidement. De plus la succession de plusieurs niveaux de sable autour de la même interface dans les autres carottes supposent que plusieurs épisodes de mobilisation des sables ont eu lieu à cette période sur toute la Mer de Marmara. Nous proposons donc que ces dépôts correspondent à une période où des zones ont rapidement été exposées par émersion et sont devenues sujettes à l'érosion. Ce phénomène pourrait être lié à une période d'accélération de la chute du niveau de la mer.

Si l'interface étudiée est postérieure à la déconnexion de la Mer de Marmara avec la Mer Méditerranée, alors une chute rapide du niveau de l'eau est possible si les sédiments déposés dans le détroit ont subi une incision rapide par la rivière s'écoulant alors dans les Dardanelles. Une autre possibilité est que le lac Marmara s'est retrouvé avec un bilan hydrique négatif suite à un arrêt ou une forte diminution de l'apport d'eau douce en provenance de la Mer Noire. Cependant, cette deuxième hypothèse est plus discutable puisqu'aucun indice de concentration de la salinité n'a été identifié à ce jour [*Aloisi et al.*, 2015 ; Chapitre III de ce manuscrit]. Enfin, une accélération de la baisse de niveau pourrait simplement être due au fait que la mer de Marmara était encore connectée à l'océan global à une période où celui-ci a chuté plus rapidement. Sachant que notre interface se situe au milieu des dépôts interglaciaires, un bon candidat serait la fin du stade 5 [e.g. *Rohling et al.*, 2014].

La connaissance de la variation de la profondeur du détroit des Dardanelles pourrait permettre de statuer entre ces hypothèses. Or, cette question a des ramifications aussi bien en tectonique qu'en sédimentologie et reste encore sujette à débat. L'étude de terrasses dans le détroit [*Gökaşan et al.*, 2008] et de carottes du plateau nord [*Çağatay et al.*, 2009] ont permis de proposer une profondeur de 50 m avant la déconnexion et une profondeur de 85 m avant la reconnexion. Ceci impliquerait bien une incision du détroit pendant la phase lacustre. Si celle-ci s'est produite à la fois dans un cours laps de temps et après une période suffisante pour que la différence de profondeur entre les deux mers soit importante, alors une baisse rapide du niveau de la Mer de Marmara a pu se produire. Cependant, à ce jour, aucune donnée ne permet de placer temporellement d'éventuelles incisions et d'en prouver la simultanéité avec les dépôts de sables.

5.3. Estimation de l'âge de l'interface

Si l'étude isolée de l'interface « rouge » H1 ne permet pas d'estimer l'âge des dépôts, le reste de la carotte donne de précieux indices. Les éléments suivants sont détaillés dans le Chapitre III.

Tout d'abord, le faciès franchement marin sous-jacent au faciès laminé doit correspondre au stade 5e (130-115 ka), lorsque le niveau marin était comparable ou supérieur à aujourd'hui. Ensuite, la corrélation du contenu en Calcium déterminé par XRF avec celui de la carotte MD2430 [*Çagatay et al.*, 2015] suggère que le bas du faciès homogène correspond au stade 4 (71-57 ka). Enfin, les âges des deux niveaux de tephras sont cohérents avec ces estimations et suggèrent qu'il n'y a pas de hiatus important, au moins dans la plus grande partie du faciès homogène. Ainsi, l'interface entre les faciès homogène et laminé correspondraient à la fin du stade 5 et au début du stade 4 avec, éventuellement, des pertes dues à l'érosion sous les niveaux de sable.

Comme exposé précédemment, l'existence d'un changement soudain de faciès et les niveaux de sables érosifs pourraient tous deux être expliqués par une accélération de la baisse du niveau de la mer. Or, une telle accélération a eu lieu à la fin du stade 5. Nous proposons donc finalement que cette interface correspond à une transition hydrologique de la Mer de Marmara survenue entre 80 et 70 ka, pendant la baisse accélérée du niveau de la mer à la fin du stade MIS 5, associée au retournement et à l'homogénéisation des masses d'eau. Par ailleurs, la déconnexion avec la mer Méditerranée s'est sans doute produite pendant cette période (voir INTRODUCTION GENERALE, Figure 5).

5.4. Compatibilité avec les modèles d'âges établis

Ainsi, nous aboutissons à un âge pour le réflecteur « rouge » H1 se situant entre 80 et 70 ka, soit une estimation plus faible que les âges proposés par *Sorlien et al*. [2013] et *Grall et al*.

[2012]. A la lumière de ces nouvelles données, nous avons cherché, dans un premier temps, à expliquer comment cet âge aurait pu être surestimé dans ces deux études.

Sorlien et al. [2012] appuient leur estimation sur deux arguments. Le premier est une extrapolation basée sur une carotte atteignant 17 ka à 17 m sous le fond marin [*Beck et al.*, 2007]. Le réflecteur « rouge » H1 se trouvant à proximité et à 110 m sous le fond marin d'après les profils sismiques, ils estiment son âge à 110 ka. Cette extrapolation se base donc sur une vitesse moyenne de sédimentation depuis 17 ka qui n'exclue pas les taux faibles de la période marine actuelle. Par ailleurs, l'étude de la carotte MRS-CS-22 a montré que la vitesse de sédimentation a peut-être ralenti entre les stades 4 et 2 (voir Chapitre III), ce qui participerait donc à faire de cette vitesse moyenne une vitesse trop faible pour représenter toute la période glaciaire et donc conduirait à une surestimation de l'âge du réflecteur.

Sorlien et al. [2012] vérifient également cette estimation en étudiant des dépôts sédimentaires en éventail attribués aux périodes de haut niveau marin. Le réflecteur « rouge » H1 se situant juste au-dessus de l'un d'eux, l'âge de 110 ka est validé puisqu'il correspond à la fin du stade 5e pendant lequel le niveau marin était aussi haut qu'aujourd'hui. Cependant, la baisse du niveau marin, bien que rapide juste après le stade 5e [*Rohling et al.*, 2014] n'a peut-être pas conduit à un changement immédiat de la géométrie des dépôts. Une sédimentation encore lente pendant les stades MIS 5d à MIS 5b pourrait expliquer la géométrie des sédiments sous-jacents au réflecteur « rouge » H1.

Grall et al. [2013] utilise également une vitesse moyenne de sédimentation pour évaluer l'âge du réflecteur « rouge » H1. Cette vitesse, utilisée pour construire tout le modèle, se base sur la supposition que l'épaisseur de sédiment entre le fond marin et le téphra Y-5 de 39 ka est représentative de la vitesse moyenne sur un cycle de 100 ka composé à la fois de sédiments marins (vitesse lente de sédimentation) et lacustres (vitesse rapide de sédimentation). Mais cette hypothèse ne fonctionne pas pour le réflecteur « rouge » H1, qui est trop jeune pour que les dépôts sus-jacents soit représentatifs d'une moyenne sur un cycle de 100 ka. Certes, cette hypothèse est présentée comme une approximation et est sans doute valable pour estimer les âges des réflecteurs suivants si ceux-ci sont effectivement suffisamment espacés dans le temps pour représenter au moins des cycles de 100 ka. Cependant, l'estimation de l'âge du réflecteur « rouge » H1 ne devrait se faire qu'avec la vitesse de sédimentation correspondant au taux rapide des périodes de bas niveaux marins pour atteindre une meilleure précision. Par ailleurs, la vitesse moyenne proposée est sans doute également une sous-estimation de la réalité puisque la vitesse de sédimentation à la fin de la dernière période de bas niveau marin était peut-être plus faible que la moyenne sur toute la période de bas niveau marin (voir Chapitre III de ce manuscrit). Enfin, la présence de niveaux de sable au sommet des sapropèles indique qu'il y a pu y avoir un épisode d'érosion au cours de la transition entre les stades MIS5 et MIS 4 ce qui peut participer au décalage entre une longueur de sédiment réduite et la vitesse de sédimentation estimée.

Nos résultats ne constituent cependant pas une invalidation claire de ces modèles d'âge. Une possibilité est qu'elle met simplement en lumière un décalage dans l'estimation du positionnement des réflecteurs. Alors que les réflecteurs ont été attribués à des périodes proches des extrémums climatiques, nous proposons que le réflecteur « rouge » H1, et peut-être d'autres, correspondent plutôt à une variation hydrologique soudaine postérieure au maximum interglaciaire précédent.

Cependant, nous avons montré que l'estimation de la vitesse de sédimentation est sujette à débat. Les périodes sur lesquelles nous avons pu mesurer une vitesse de sédimentation (voir Chapitre III) montrent une grande variabilité et une vitesse moyenne sur toute la colonne est difficile à estimer sans connaitre la durée des périodes de haut niveau marin à vitesse de sédimentation réduite. Ces durées elles-mêmes ont d'ailleurs sans doute varié au cours du temps.

En conclusion, nous pensons que les futures informations apportées par des carottes atteignant des réflecteurs plus profonds seront décisives. A ce stade, la construction des modèles d'âge par simple interprétation des unités sédimentaires semble plus acceptable que l'utilisation de vitesse de sédimentation estimée sur des périodes très courtes. L'accès direct à des réflecteurs supplémentaires permettra d'établir si le positionnement du réflecteur « rouge » H1 au milieu de la baisse du niveau marin est cyclique et si un réflecteur équivalent est parfois observé lors de la remontée du niveau marin. Dans ce cas, peut-être aboutirons-nous à une confirmation du modèle proposé par *Grall et al.* [2014] qui s'appuie sur la répétition de deux types de géométries sédimentaires.

6. Conclusion

L'étude des synthétiques sismiques et de la lithologie des carottes ayant atteint le réflecteur « rouge » H1 a permis de :

- Comprendre l'origine du réflecteur « rouge » H1 d'un point de vue géophysique. Il est le résultat d'une augmentation de densité (du bas vers le haut) à l'interface entre deux faciès.

- Etudier l’origine lithologique de cette variation de densité. Elle correspond au passage d’un faciès laminé riche en matière organique à un faciès homogène moins riche en matière organique et, par voie de conséquence, moins riche en eau.
- Interpréter en termes de variation environnementale le passage d’un faciès à l’autre. Nous proposons que les deux faciès correspondent à des environnements lacustres ou sous influence d’un flux d’eau douce provenant de la mer noire et que la transition de l’un à l’autre s’est fait quand l’apport d’eau salée provenant de la mer méditerranée a été coupé, permettant une diminution de la salinité des masses d’eau profondes anoxiques et leur mélange avec les eaux de surface, éventuellement lors d’une accélération de la baisse du niveau marin.
- Proposer une datation de l’interface et donc du réflecteur « rouge » H1. L’identification de tephras, l’étude du contenu en fossiles, la lithologie et les analyses chimiques de la carotte MRS-CS-22 permettent de construire un modèle d’âge de la carotte qui suggère que l’interface s’est formé à la fin du stade MIS 5 ou au début du stade MIS 4 (entre 80 et 70 ka).

La différence entre cette datation et les datations proposées dans les modèles d’âges établis est attribuée à deux causes. La première est une sous-estimation systématique de la vitesse de sédimentation lorsque l’extrapolation se base sur des sédiments jeunes. La deuxième est que les variations de géométries sédimentaires ont systématiquement été attribuées à des changements dans l’organisation des dépôts survenant à grande proximité temporelle des extrémums climatiques. Or, nous avons montré que le réflecteur « rouge » H1 correspond à une période de transition au milieu de la dernière période glaciaire.

A ce jour, encore de nombreuses études peuvent être menées sur les carottes de sédiments récupérés lors de la campagne MARSITE pour contraindre d’avantage les modèles d’âge en Mer de Marmara. Les carottes provenant du sud du Haut Ouest seront difficiles à exploiter en raison d’un remaniement parfois important des sédiments, mais l’évaluation des âges à la base des carottes est prometteuse. A l’est, les carottes des bassins d’İmralı sont en cours d’étude et pourraient apporter des précisions sur les variations environnementales et sur la chronologie des dépôts depuis le dernier interglaciaire.

Références

Aloisi, G., Soulet, G., Henry, P., Wallmann, K., Sauvestre, R., Vallet-Coulomb, C., … Bard, E. (2015). Freshening of the Marmara Sea prior to its post-glacial reconnection to the Mediterranean Sea. *Earth and Planetary Science Letters*, *413*, 176–185. http://doi.org/10.1016/j.epsl.2014.12.052

Beck, C., Mercier de Lépinay, B., Schneider, J.-L., Cremer, M., Çağatay, M. N., Wendenbaum, E., … Jaouen, A. (2007). Late Quaternary co-seismic sedimentation in the Sea of Marmara's deep basins. *Sedimentary Geology*, *199*(1–2), 65–89. http://doi.org/10.1016/j.sedgeo.2005.12.031

Çağatay, M. N., Eriş, K., Ryan, W. B. F., Sancar, Ü., Polonia, A., Akçer, S., … Bard, E. (2009). Late Pleistocene–Holocene evolution of the northern shelf of the Sea of Marmara. *Marine Geology*, *265*(3–4), 87–100. http://doi.org/10.1016/j.margeo.2009.06.011

Çağatay, M. N., Wulf, S., Sancar, Ü., Vidal, L., Henry, P., Appelt, O., & Gasperini, L. (2015). The tephra record from the Sea of Marmara for the last ca . 70 ka and its palaeoceanographic implications. *Marine Geology*, 361, 96–110. http://doi.org/10.1016/j.margeo.2015.01.005

Dupré, S., Scalabrin, C., Grall, C., Augustin, J. M., Henry, P., Şengör, A. M. C., … Géli, L. (2015). Tectonic and sedimentary controls on widespread gas emissions in the Sea of Marmara: Results from systematic, shipborne multibeam echo sounder water column imaging. *Journal of Geophysical Research: Solid Earth*, *120*(5), 2891–2912. http://doi.org/10.1002/2014JB011617

Flores, J. A., Sierro, F. J., Francés, G., Vázquez, A., & Zamarreno, I. (1997). The last 100,000 years in the western Mediterranean: Sea surface water and frontal dynamics as revealed by coccolithophores. *Marine Micropaleontology*, 29(3–4), 351–366. http://doi.org/10.1016/S0377-8398(96)00029-1

Grall, C., Henry, P., Thomas, Y., Westbrook, G. ., Çağatay, M. N., Marsset, B., … Géli, L. (2013). Slip rate estimation along the western segment of the Main Marmara 1 Fault over the last 405-490 ka by correlating Mass Transport Deposits. *Tectonics*, *32*(6), 1587–1601. http://doi.org/10.1002/2012TC003255

Grall, C., Henry, P., Westbrook, G. K., Thomas, Y., Marsset, B., Borschneck, D., … Cifc, G. (2014). *Submarine Mass Movements and Their Consequences*, *37*, 595–603. http://doi.org/10.1007/978-3-319-00972-8

Gökaşan, E., Ergin, M., Özyalvaç, M., Sur, H. I., Tur, H., Görüm, T., … Özturan, M. (2008). Factors controlling the morphological evolution of the Çanakkale Strait (Dardanelles, Turkey). *Geo-Marine Letters*, *28*(2), 107–129. http://doi.org/10.1007/s00367-007-0094-y

Lericolais,G., and P.Henry (2004), Cruise report of Marmara VT/Marmacore 2, cruise IPEV VT68, Pujos, A. (1988). Spatio-temporal distribution of some Quaternary coccoliths. *Oceanologica Acta*, *11*(1), 65–77. Retrieved from http://www.scopus.com/inward/record.url?eid=2-s2.0-0023790925&partnerID=40&md5=db33b3d7e311b733aec2616002aa7e0c

Raffi, I., Backman, J., Fornaciari, E., Pälike, H., Rio, D., Lourens, L., & Hilgen, F. (2006). A review of calcareous nannofossil astrobiochronology encompassing the past 25 million years. *Quaternary Science Reviews*, *25*(23–24), 3113–3137. http://doi.org/10.1016/j.quascirev.2006.07.007

Rohling, E. J., Foster, G. L., Grant, K. M., Marino, G., Roberts, a P., Tamisiea, M. E., & Williams, F. (2014). Sea-level and deep-sea-temperature variability over the past 5.3 million years. *Nature*, *508*(7497), 477–82. http://doi.org/10.1038/nature13230

Sorlien, C. C., Akhun, S. D., Seeber, L., Steckler, M. S., Shillington, D. J., Kurt, H., … Diebold, J. B. (2012). Uniform basin growth over the last 500ka, North Anatolian Fault, Marmara Sea, Turkey. *Tectonophysics*, *518–521*, 1–16. http://doi.org/10.1016/j.tecto.2011.10.006

Thierstein, H. R., Geitzenauer, K. R., Molfino, B., & Shackleton, N. J. (1977). Global synchroneity of late Quaternary coccolith datum levels Validation by oxygen isotopes. *Geology*, *5*(7), 400–404. http://doi.org/10.1130/0091-7613(1977)5<400:GSOLQC>2.0.CO;2

Vidal, L., Ménot, G., Joly, C., Bruneton, H., Rostek, F., Çağatay, M. N., … Bard, E. (2010). Hydrology in the Sea of Marmara during the last 23 ka: Implications for timing of Black Sea connections and sapropel deposition. *Paleoceanography*, *25*(1), PA1205. http://doi.org/10.1029/2009PA001735

CHAPITRE III

Variations environnementales et hydrologie en mer de Marmara depuis le stade 5 (MIS 5)

Résumé étendu

En mer de Marmara, les modèles d’âge des sédiments sont basés sur l’interprétation stratigraphique de profils sismiques et sur les taux de sédimentation récents calculés sur des carottes de sédiments. Notamment, l’observation de l’alternance de niveaux de remplissages et de couches de sédiments drapés suggère une coïncidence avec les périodes de haut et de bas niveaux marins. Cette hypothèse, compatible avec les taux de sédimentation récents, permet de construire des modèles d’âge jusqu’à environ 650 000 ans. Cependant, jusqu’à aujourd’hui, aucun des réflecteurs sur lesquels s’appuient ces modèles n’avait été identifié et daté directement. Au cours de la campagne MARSITE en mer de Marmara, des zones précises permettant d’atteindre ces réflecteurs ont été choisies pour la récupération de carottes de sédiments. Ce papier présente les études menées sur la carotte MRS-CS-22 qui contient les couches responsables du réflecteur H1 « rouge », le réflecteur le plus récent sur lesquels s’appuient les modèles.

Le contenu de la carotte ne permettant pas de datation isotopique, une grande variété de techniques ont été appliquées afin de construire un modèle d’âge de la carotte. Deux techniques ont notamment permis de fixer des âges absolus : la téphrochronologie et le paléomagnétisme. A cela s’ajoutent des renseignements donnés par le signal Calcium issu des analyses XRF. En haut de la carotte, un pic déjà observé [*Reichel and Halbach.*, 2007; *McHugh et al.*, 2008] correspond à la reconnexion entre la mer de Marmara et la mer Méditerranée tandis que le signal du milieu de la carotte est corrélable avec le signal NGRIP δO^{18} [*Çagatay et al.*, 2015]. Enfin, les assemblages de microfossiles ont également été interprétés en termes de variation environnementale liée aux différents stades marins isotopiques (MIS).

Le résultat de cette étude multi proxy est un modèle d’âge s’étalant depuis environ 120 000 ans jusqu’à aujourd’hui et définissant 4 périodes. La première, à la base de la carotte, correspond à la fin du stade 5e. Durant cette période, l’environnement était marin, mais l’oxygénation de la base de la colonne d’eau diminuait graduellement, causant la disparition progressive des foraminifères. La deuxième partie est attribuée aux dépôts des stades 5d à 5a (70 à 114 ka). Ces sédiments, correspondant aux dépôts d’une phase transitoire, constituent un sapropel de plus de 4 m d’épaisseur comprenant deux sous évènements marqués par une accumulation encore accrue de matière organique. Durant cette période, la forte stratification des eaux a favorisé la préservation de la matière organique en profondeur tandis que la profusion de diatomées de surface révèle une eau douce à saumâtre en haut de la colonne d’eau. La troisième partie correspond à la longue période lacustre depuis le stade MIS 4 jusqu’au stade

MIS 2 (70 à 12 ka). Dans la carotte étudiée, les sédiments y sont particulièrement pauvres en contenu fossiles. Cependant, la baisse de la quantité de matière organique suggère une homogénéisation de la colonne d’eau et une meilleure oxygénation des eaux profondes, due à une désalinisation forte suite à une déconnection totale du détroit des Dardanelles. Enfin, la dernière partie correspond au stade marin actuel, riche en foraminifères.

Au-delà de permettre la reconstitution détaillée de l’évolution de l’environnement dans les bassins profonds de l’ouest de la mer de Marmara, les mesures géophysiques ont permis de situer, dans la carotte, la transition responsable du réflecteur « rouge » H1. Le réflecteur coïncide avec la forte variation de densité entre le sapropel léger et les dépôts lacustre sus-jacents et daterait donc de la limite MIS 5/MIS 4 il y a 70 000 ans. Sans remettre entièrement en question les modèles d’âges publiés, cette étude pourrait indiquer que les réflecteurs principaux interprétés correspondent à des transitions lithologiques brutales au milieu de phases de transitions climatologiques plutôt qu’à des extrémums climatologiques.

Enfin, en annexe, nous présentons un proxy pour la salinité basé sur l’étude du rapport entre les taux de Strontium et de Calcium. S’appuyant sur la variation de la précipitation de Strontium dans les carbonates en fonction de la concentration de Strontium dans l’eau, ce proxy semble indiquer une diminution graduelle de la salinité en mer de Marmara jusqu’à environ 50 000 ans.

1. Introduction

The Marmara Sea, confined between the Bosphorus Strait in the West and the Dardanelles Strait in the East, has been affected through time by climatic variations in a remarkable way. During glacial periods, the global sea level would fall close to or below the Dardanelle Strait, disconnecting the Marmara Sea from the Mediterranean. Conversely, sea level rise during warm periods would restore the connection with the Mediterranean Sea. As a result, the sediment column below must have recorded an alternation of marine and brackish or freshwater deposits. Seismic data from the Southern Marmara Shelf do show a stack of sediments with variable geometries and internal reflection characteristics that could correspond to the alternation of low-stand and high-stand periods [eg. *Sorlien et al.*, 2012; *Grall at al.*, 2013; *Grall et al.*, 2014]. Furthermore, coring campaigns have already reached sediments proving that lacustrine environments did exist during the last low-stand period [eg: *Lericollais and Henry*, 2004; *McHugh et al.*, 2008; *Eriş et al.*, 2011; *Vidal et al.*, 2010; *Çağatay et al.*, 2009, 2015]. The environmental transitions during the late Pleistocene-Holocene recorded in the sediments have been extensively studied in order to describe the evolution of the water level and salinity in the Marmara Sea and, thereby, of the connections with the Mediterranean Sea and the Black Sea. However, few cores retrieved so far contain a recording going beyond Marine Isotope Stage (MIS) 4. *Çağatay et al*. [2009] described a set of nine cores retrieved off the Prince Islands and Çekmece on the Northern Shelf which included a sedimentary succession with erosional surfaces. They estimated the oldest sediments to belong to the lacustrine period MIS 6 and they described the last marine to lacustrine transition which included the deposition of two marine sapropels with a lacustrine interval in between. However, because the core contained discontinuities, a precise age model of the facies transition is yet to be defined.

Thus, a continuous record since MIS 5 would complete these studies and give a first glance at how the lacustrine environment gradually established itself after the last interglacial. Furthermore, an age-depth model since MIS 16 has been constrained from seismic profiles based on 7 main seismic reflectors that were documented as separating the alternations of high-stand and low-stand sediments [*Sorlien et al.*, 2012; *Grall et al.*, 2013; 2014]. A continuous record of the last transitions correlated with seismic data could give a first confirmation of the proposed age models for the uppermost reflector which estimated age is ~105 ka.

2. Materials and Methods

The R/V Pourquoi Pas ? core MRS-CS-22 presented in this study is a 20,6 m piston core retrieved from the Western High during the MARSITE cruise in October 2014.

2.1. Choice of the coring location

Retrieving a close to complete sequence of events in the length of a piston core limits the span of the targeted time interval. Thus, extensive inspection of sub-bottom profiles (3.5 kHz) and seismic lines were carried in order to identify good coring locations for the Marmara Cruise (2014) onboard the R/V Pourquoi Pas ?. Condensed stack on topographic highs and eroded slopes where the main seismic reflectors where within reach were selected. About half of the cores were planned to reach further than the last interglacial while the other half was positioned at locations that could offer a complete depositional record since the last interglacial within the core length. Core MRS-CS-22, described in this paper, is one of the latter. Additional targets close to the Kumburgaz basin depocenter were selected for turbidite studies. Figure 1 presents the target locations of all cores retrieved during the Marsite cruise.

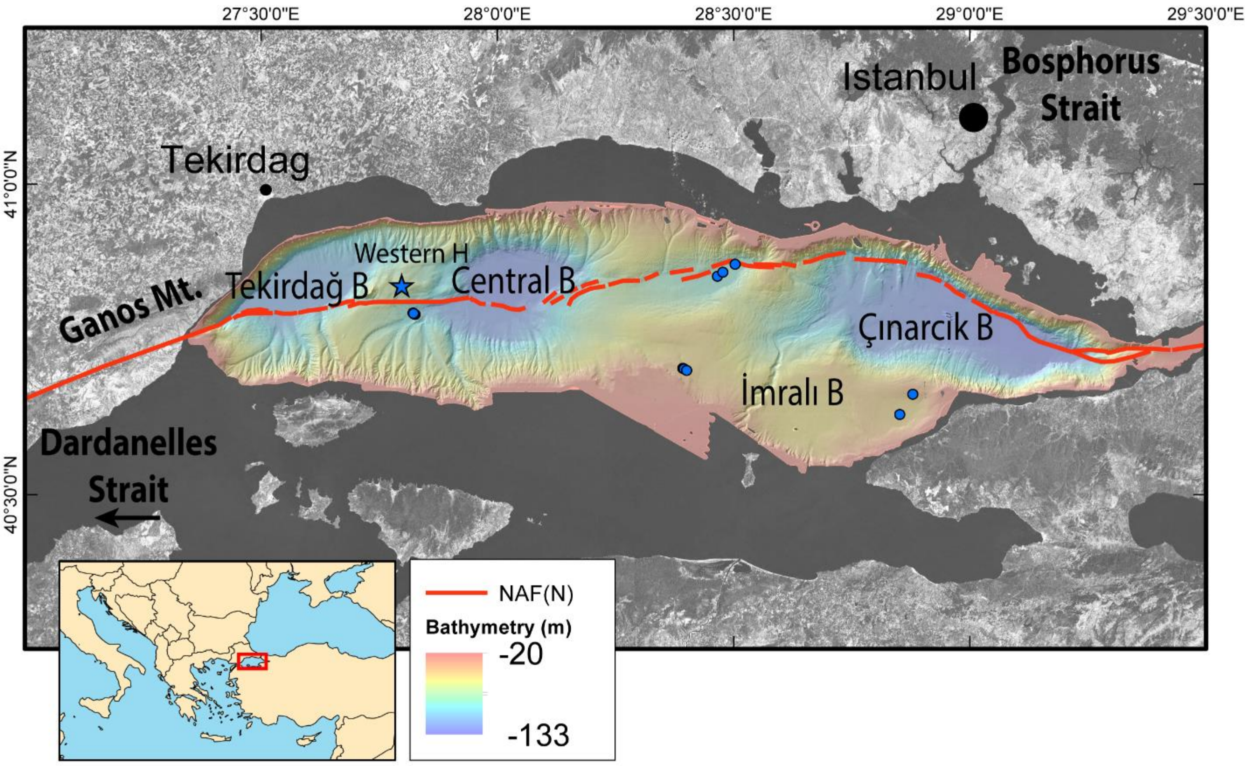

Figure 1. Locations of piston cores retrieved during the MARSITE cruise Leg 3 onboard the R/V Pourquoi Pas ?. Blue star: core MRS-CS-22. Blue points: other cores. NAF(N): Northern branch of the North Anatolian Fault (simplified from Şengör et al. [2014]). B: Basin. H: High. Bathymetry data are from the EM300 multibeam survey.

The location of core MRS-CS-22 was chosen to reach a condensed record of the stratigraphy while avoiding possible gas pockets close to the top of a topographical high. According to seismic line interpretations, the core contains the first main reflector: a high amplitude with negative polarity reflector named H1 by *Grall et al*., [2013] (see Figure 2) which age is estimated to correspond to 105±13 ka from extrapolation of sedimentation rates in the Western High [*Grall et al*, 2013]. Correlation of seismic horizons over the entire Marmara Sea is challenging as deep canyons cut the southern slope. However, H1 being the first high-amplitude negative polarity reflector below the sea floor and supposing that this characteristic is conservative in the whole sea, it can be correlated to horizon Red-1 identified in the eastern Marmara Sea and whose age was evaluated at around 110 ky from sedimentation rate extrapolation [*Sorlien et al.*, 2012].

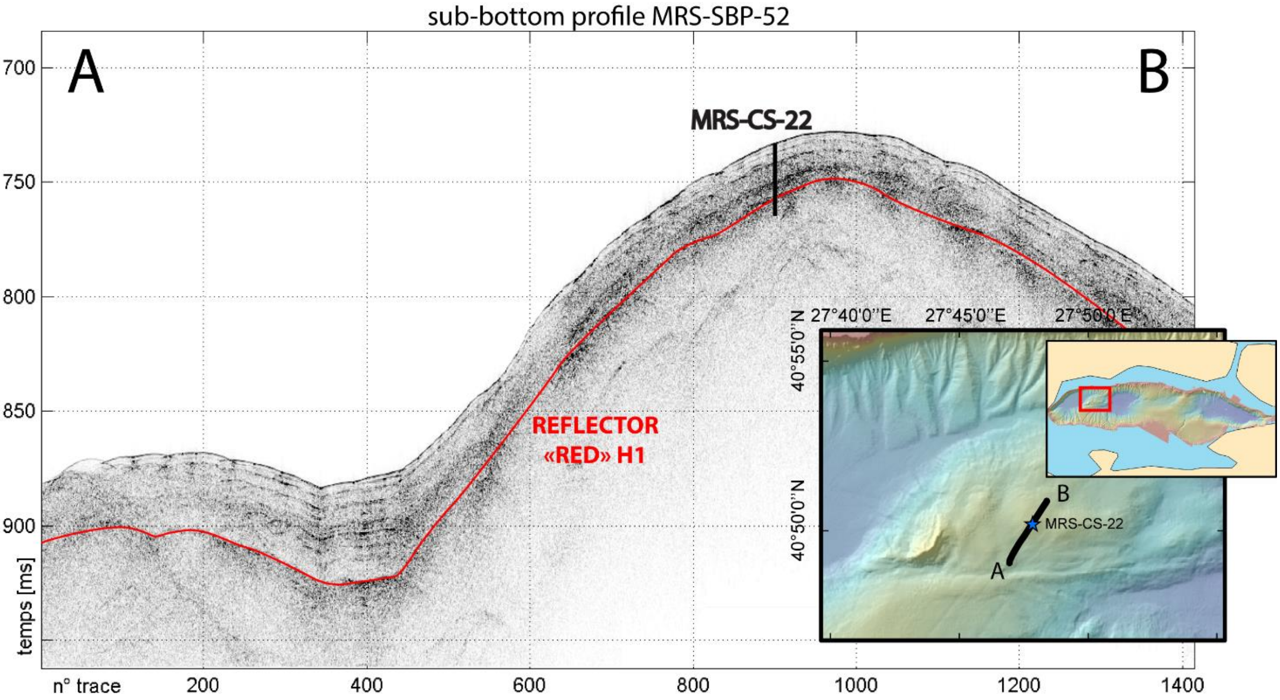

Figure 2. Location and estimated penetration of core MRS-CS-22 on MRS-SBP-52 sub-bottom profile (3.5 kHz). The uppermost seismic reflector used in Grall et al. [2013] age model is represented. Its position was inferred from correlation with high resolution seismic data. Its age is estimated at about 105-110 ka [Sorlien et al., 2012; Grall et al., 2013].

2.2. MSCL measurements, core description and sampling

Prior to the opening, core MRS-CS-22 was run through a GEOTEK multi-sensor core logger at the IFREMER laboratory in Brest (France). Bulk density from gamma-ray absorption, magnetic susceptibility and P-wave velocity were measured with a 1 cm step.

The core was opened, described and photographed in CEREGE (France). Slices of about 30 cc were collected every 20 cm and additional smaller samples were taken from interesting features like massive sand layers or volcanic ash layers.

2.3. Geochemical analysis and crystallography

All 21 sections were run through an ITRAX core scanner (COX, analytical Systems) at CEREGE for µ-XRF analysis of Ca, Ti, Cr, Rb, Sr, Fe, Mn, K, Zr, Ba, Si, S, Cl and Br at 5 mm resolution, using a Mo tube at 30 kV, 45 mA and 15 s counting time. Sections 15 to 20, with thin laminations, were re-analyzed with the same setting but a 0.5 mm resolution.

For calibration of the µ-XRF data, we selected samples with a 1 m spacing on the whole core plus additional samples on interesting facies or at minimum and maximum of the µ-XRF elemental counts. Since the facies in the upper sections of core MRS-CS-22 are similar to those already described and studied in other cores [*Beck et al.*, 2007; *Vidal et al.*, 2010, *Çağatay et al.,* 2015] we focused primarily on new features found in the lower part of the core for these additional samples. Major and trace elements were measured by ICP-MS (Agilent 7500ce) on homogenized freeze-dried samples dissolved in HF (3 mL) and HNO_3 (2 mL). Total Organic Carbon (TOC) and total carbon was measured with a gas chromatographic elemental analyzer on the same freeze-dried material.

Finally, samples from the same positions were freeze dried and ground in an agate mortar for XRD analysis of the crystallography. Measures were achieved on a PANanalytical X'Pert PRO θ/θ diffractometer set at 40 kV and 40 mA with a cobalt cathode. The samples were analyzed between 5° and 75° (2θ) with a 0.033° step and a counting time of 5 s. Mineral phases were then identified using the X'Pert Highscore (PANanalytical) Plus software with the PDF2 and ICDD (International Center for Diffraction Data) databases.

All analysis were conducted at CEREGE (Aix-en-Provence, France).

2.4. SEM tephra analysis

Two thick layers of volcanic glass shards were identified. Samples collected in the middle of each ash layer were wet sieved with a 150 µm screen then dry-sieved at 63 µm. The coarse fractions were dispersed on double-sided carbon pads at the bottom of 1" diameter moulds and embedded in epoxy resin. After hardening, the surface of the stubs was polished using 1200 grit SiC then suspensions of 6, 3, and 1 microns diamond. The analysis were performed at CEREGE on a Scanning Electron Microscope (SEM) (Hitachi S3000-N SEM) fitted with a Bruker Energy

Dispersive Spectrometer (EDS) and a Spirit analyser. The SEM was operated at 15 kV, with probe currents ca. 2nA. Microanalyses were calibrated using various natural and synthetic standards. All analyses were recorded while scanning the beam over regions ca. 10 microns large, in order to minimize Na loss.

2.5. Rock magnetism

Paleomagnetism measurements were conducted on core MRS-CS-22 as an additional way to set age tie-points. Analysis were conducted at CEREGE on U-channels with a superconducting rock magnetometer 760R (2G enterprises). The natural remanant magnetization (NRM) was measured before and after alternating field demagnetization with field steps of 15, 20, 30, 40 and 80 mT. The last step achieved a complete elimination of the NRM. The anhysteretic remanant magnetization (ARM) was then measured at the same demagnetization steps after being imparted in a 80 mT alternating field (AF) coupled with a 0.1 mT direct field.

2.6. Micropaleontology

Because the fossil content of core MRS-CS-22 is very irregular, we first sampled with a coarse resolution of 1 m. Samples were wet sieved through 63 µm and 125 µm screens for analysis of the coarser fraction. As most of those samples had little or no microfossil content, the sampling resolution was refined to 20 cm only on the last 2 m were very rich benthic foraminifera assemblages were found. The biogenic content in the fraction > 125 µm was handpicked in the samples with poor content. The samples with rich marine foraminifera assemblages were split until about 300 foraminifera could be handpicked in one sub-sample. The assemblages were described up to the genera. Smear slides were also prepared to evaluate the content in coccoliths and diatoms.

2.7. Granulometry

Finally, to assess the origin and variability of the detrital fraction input, granulometry analysis was achieved with a resolution of 1 m plus some additional samples from sand layers or close to facies changes.

3. Results

3.1. Lithology

Core MRS-CS-22 consists of four units showing three main facies.

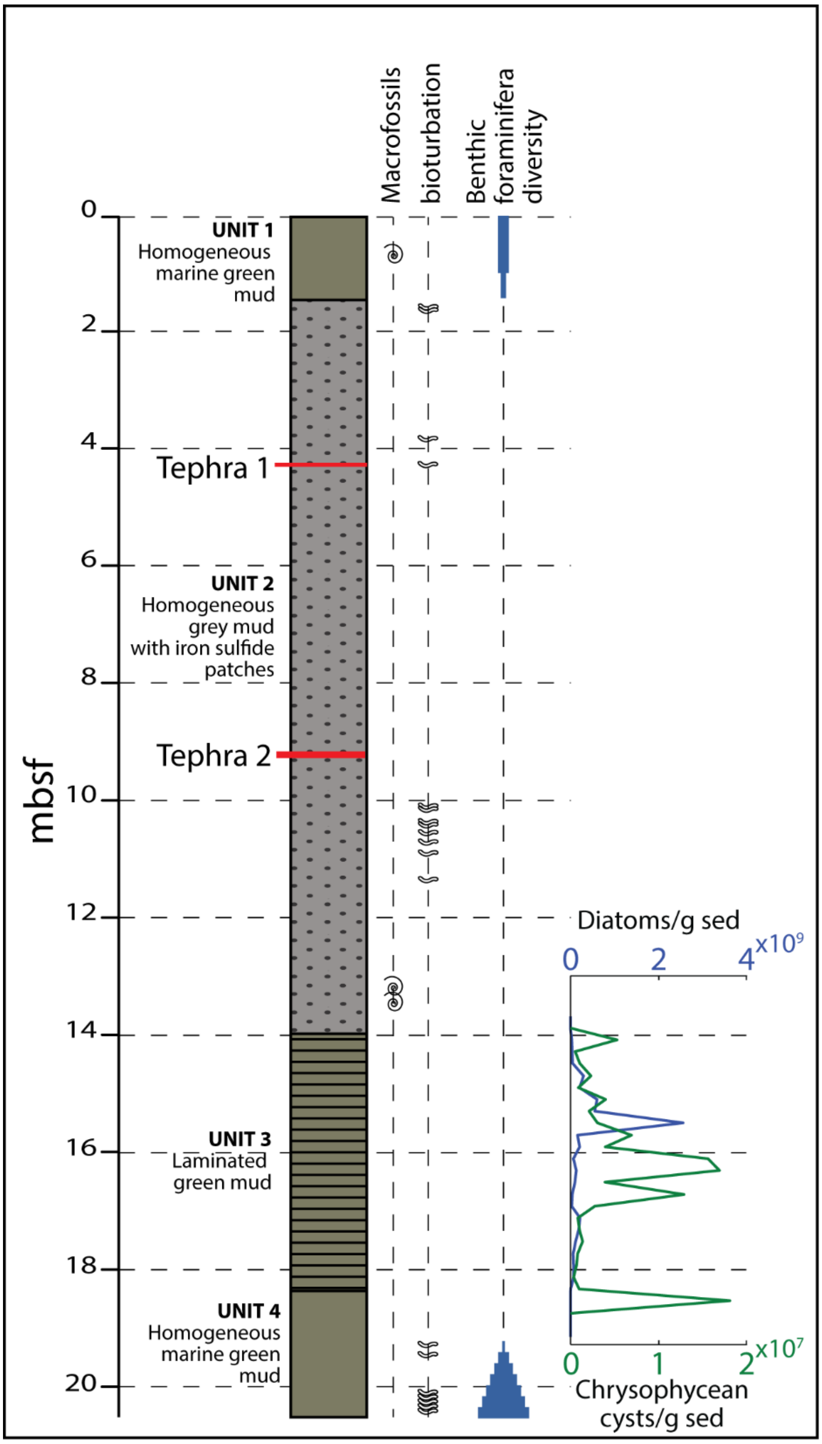

Figure 3. Stratigraphy of core MRS-CS-22 and main results of fossils analysis. The foraminifera diversity graphic is a qualitative scheme that shows the location in the core of the foraminifera disappearance. Details are given in part 3.4.

The first 1.5 m thick unit at the core top is a marine homogeneous silty olive gray mud with rare echinoderm macroscopic fragments. Microscopic fossils in this unit include bivalves, gastropods, echinoderms and foraminifera fauna dominated by *Uvigerina* sp. and planktonic genera. Near the base of the unit, a 10 cm thick darker and lightly laminated layer containing up to 2% wt organic carbon in its middle part probably corresponds to the main lower Holocene Sapropel deposited between 12.3 and 5.7 cal ka BP [*Çağatay et al.*, 2015; *Aksu et al.*, 2002].

Unit 2 is a 12.5 m thick homogeneous grey mud with zones of abundant sulfide spots. A few bioturbations can be observed at the top and in the middle of the unit. The proximity with a zone of gas escape at the top of the topographic high is here visible as the facies is marked by some vertical fractures filled with sulfide. Around 10.5 m and 12 m, we observe centimetric sand layers and some small listric faults that could indicate an impairment of the sediment. A few fragments of *Dreissena* sp. shells were found near the bottom of the unit but macroscopic fossils are absent otherwise. The sieving revealed that microfossil content is also poor. This unit has been previously documented [*Vidal et al.*, 2010; *Çağatay et al.*, 2015] as a lacustrine unit with a fauna indicating fresh-brackish bottom water, at least during the deposition of the upper part of the unit. The transition between this unit and the laminated unit below is marked by a well-sorted sand layer with an erosive base.

Unit 3 is a very finely laminated green mud. The lamination size being at the limit of the XRF resolution (0.5 mm) on most of the unit, only the thickest laminae allow to interpret the color variations. Comparison of XRF results with pictures of the core shows that white laminae correspond to Ca-rich layers (See Figure 4) while SEM-examination shows abundant idiomorphic carbonate crystals. The alternation of laminae is probably due to annual variations corresponding to phytoplankton bloom caused by hot summer months or by water mixing during spring. In either case, the mechanism is the same: CO_2 assimilation during phytoplankton growth by photosynthesis increases the pH which decreases the carbonate solubility [*Leng and Marshall.*, 2003]. This unit contains no macroscopic fossils or fragments and is devoid of sand layers. Sieving revealed rare transported fossil fragments and some fish bones. However, smear slides show that the unit is rich in diatoms, and also contains chrysophycean cysts. The diatoms are brackish water species and freshwater species with some tolerance to salt. The good preservation of the laminae, the high TOC content, the abundance of freshwater diatoms and the absence of any trace of benthic organisms indicates that Unit 3 is a thick sapropel deposited in calm, probably under stratified water conditions with anoxic bottom waters and brackish or fresh upper waters.

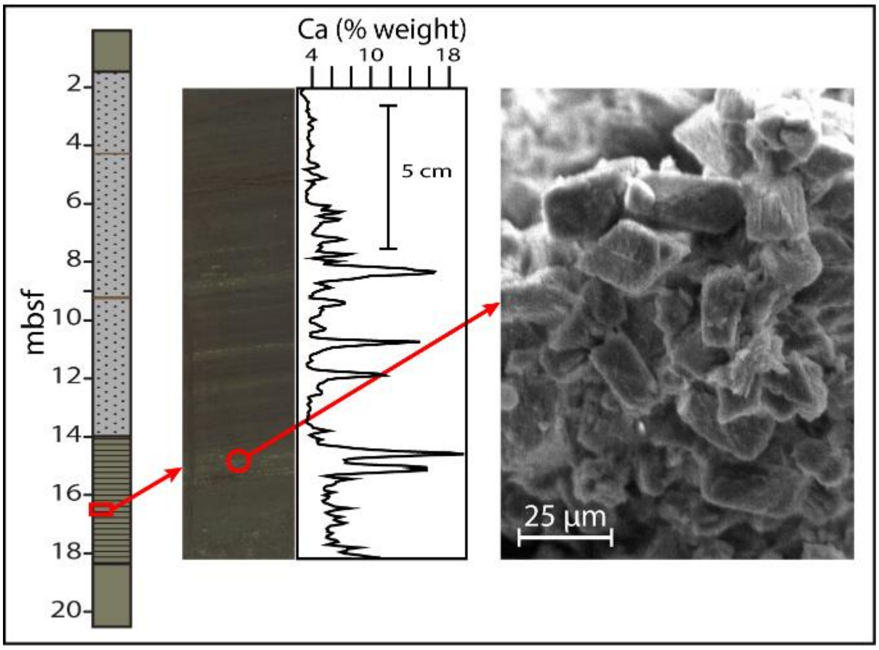

Figure 4. Composition of the white laminae in unit 3 of core MRS-CS-22. The XRF data shows a correlation of light zones with thick laminae and Ca peaks. The observation of a white lamina on the REM shows idiomorphic calcite crystals.

As some parts of the unit are tilted and as listric faults are observed near the top and the bottom of the unit, sedimentation gaps may exist in the sediment record. However, the very good preservation of the laminae and their limited tilt warrant that the chronological sequence is preserved and that no significant displacement occurred.

Unit 4 is similar to Unit 1 in terms of lithological content and facies. It consist of a homogeneous olive grey silty mud with bioturbations, silt patches and sand lenses. The unit does not contain any macroscopic fossils, although sieving revealed a very rich benthic foraminifera fauna indicating a strong marine environment.

3.2. Tephrochronology

Two tephra were identified in core MRS-CS-22 (see Figure 3).

The first one is a 7-cm dark olive gray layer lying at 4.25 mbsf. It mainly consists of elongated or vesicular pumices and some bubble-wall shards. Pyrite crystals at the surface of glass shards can be observed on the REM and XRD measurements indicate the presence of plagioclase, chlorite, gypsum and quartz.

The second tephra, at 9.12 mbsf is a 10 cm thick olive grey consisting almost exclusively of bubble wall glass shards. XRD analyses show that the tephra contains biotite, sanidine, gypsum and quartz.

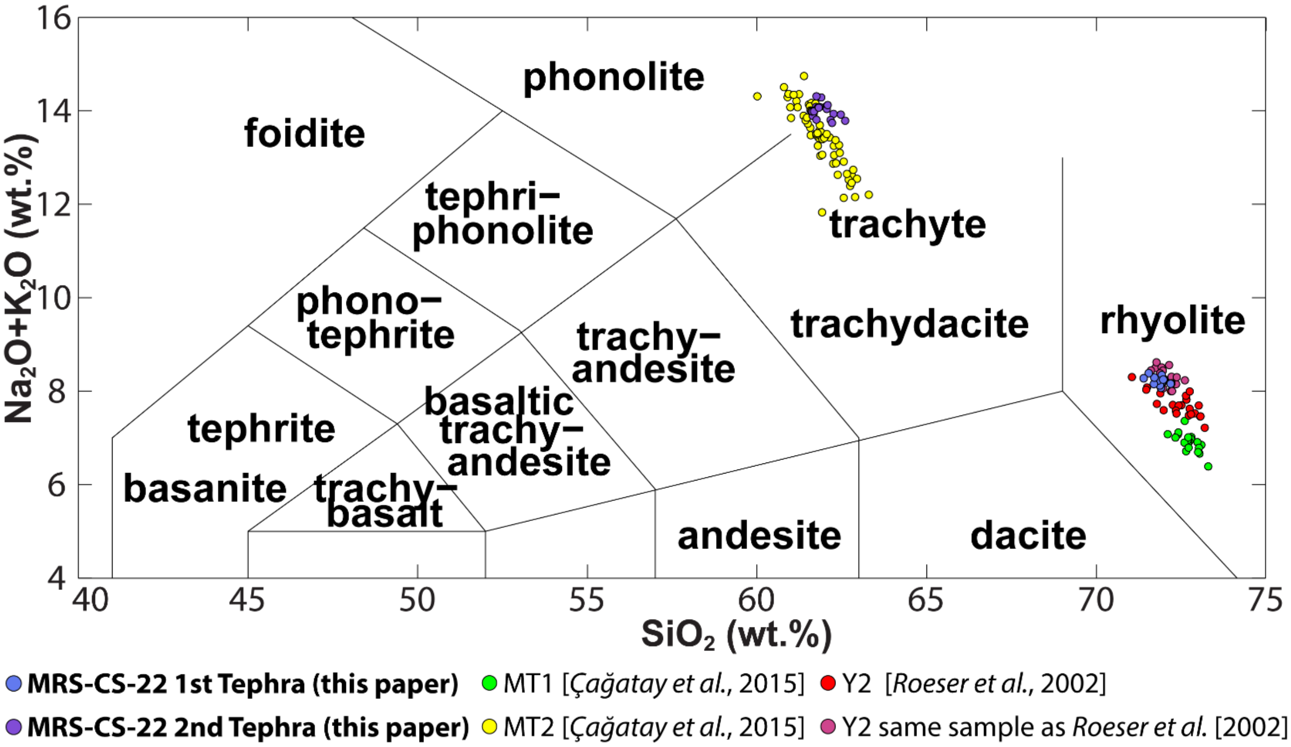

Figure 5. Total Alkali Silica diagram with data from this paper and from previous tephra studies.

Tephra layers in the Marmara Sea have been previously described by *Wulf et al*., [2002], *Aksu et al.* [2008] and *Çağatay et al*. [2015]. The description of the two tephras in core MRS-CS-22 as well as their stratigraphic position strongly support that they correspond to the MT1 and MT2 tephra documented by *Çağatay et al.* [2015] who correlated them with the Cape Riva eruption of Santorini at 22 ka (marine tephra Y-2) and with the Campanian ignimbrite eruption of the Phlegrean Fields in Italy at 39 ka (marine tephra Y-5). To verify this assumption, we performed chemical analysis on a SEM fitted with an EDS. The results are shown on a Total Alkali Silica (TAS) diagram in Figure 5. The upper tephra alkali/silica composition corresponds to a rhyolite and the lower one to a phonolitic-trachytic, which is consistent with our hypothesis. Also, our results are very close to *Çağatay et al.* [2015] data, with a smaller scattering. Furthermore, we analyzed a sample from the Y-2 marine tephra that was already analyzed by *Roeser et al*. [2002] and found a perfect correspondence with our sample. Hence we consider that the two successive eruptions in core MRS-CS-22 correspond to the two successive eruptions described by *Çağatay et al.* [2015] with estimated ages of 22 ka and 39 ka.

3.3. Paleomagnetism

Paleomagnetism measurements in core MRS-CS-22 gave us results of high quality. Figure 6 present the relative paleointensity, as well as the declination and inclination variations. The relative paleointensity is the mean of the NRM after the demagnetization at 15, 20 and 30 mT divided by the mean of ARM at the same demagnetization thresholds. At the top of the core, about one meter of sediment seems to have been disturbed during coring or section splitting and present chaotic results. Below, from 1 m to about 17 m, the declination and inclination directions are remarkably stable, with variations corresponding to the position of lows in the paleointensity. From 17 m to the bottom of the core, the paleointensity is too weak to reveal any variations. However, declination and inclination seem to have recorded a succession of short excursions during this interval.

We interpreted the main excursions by starting with the Laschamp event as the occurrence of the 39 ka tephra leaves little doubt on its position. The Laschamp event is a brief episode of inversion of the magnetic field that occurred at 40 ka with a drop in the field intensity that lasted about 2 ka [eg: *Bonhommet & Zähringer*, 1969; *Laj et al*., 2000; *Lund et al.*, 2005]. Since the second tephra is dated at 39 ka, the Laschamp event must coincide with the major paleointensity drop right below the volcanic ash layer. One should note that even without the tephra, there would be little doubt about the Laschamp event position as it is the last major drop of the paleointensity and as the overall aspect of the paleointensity variations is similar enough with published datasets [eg : *Thouveny et al.*, 2004; *Nowaczyk et al*., 2013].

After the Laschamp event, only one major excursion is well documented: the Mono Lake excursion [*Liddicoat & Coe*, 1979]. Its age is still debatable but recent studies are pointing at around 32 ka [*Wagner et al.*, 2000; *Benson et al.*, 2003]. In core MRS-CS-22, this excursion must correspond to the paleointensity low at about 7 m. Although there are more than one low between the two tephras, this is the only one that present excursional declination and inclination measurements and its position between the two tephras is consistent with its estimated age.

The last excursion that can be used as a clear age tie-point in core MRS-CS-22 is the drop in the paleointensity at about 13 m that coincides with an excursional behavior of the declination and inclination. We attribute this recording to the Norwegian-Greenland Sea excursion at 64.5 ka. [*Bleil & Gard*, 1989; *Nowaczyk & Baumann*, 1992; *Nowaczyk et al.*, 2013].

The interval with low NRM from about 16.5 m to the bottom of the core could correspond to the period of low paleointensity between 95 and 125 ka. [*Thouveny et al.*, 2004]. However, without further investigations, we cannot exclude the possibility that the magnetism in these sections was badly preserved or recorded. Furthermore, the inclination and declination here show a number of small excursional behavior that has not been observed before [eg: *Guyodo & Valet*, 1999; *Thouveny et al.*, 2004] making it hard to attribute any of the peaks to one known excursion. Nevertheless, we can conclude that the top of this interval at 16.5 m cannot be older than 95 ka as it post-date the end of the low paleointensity interval.

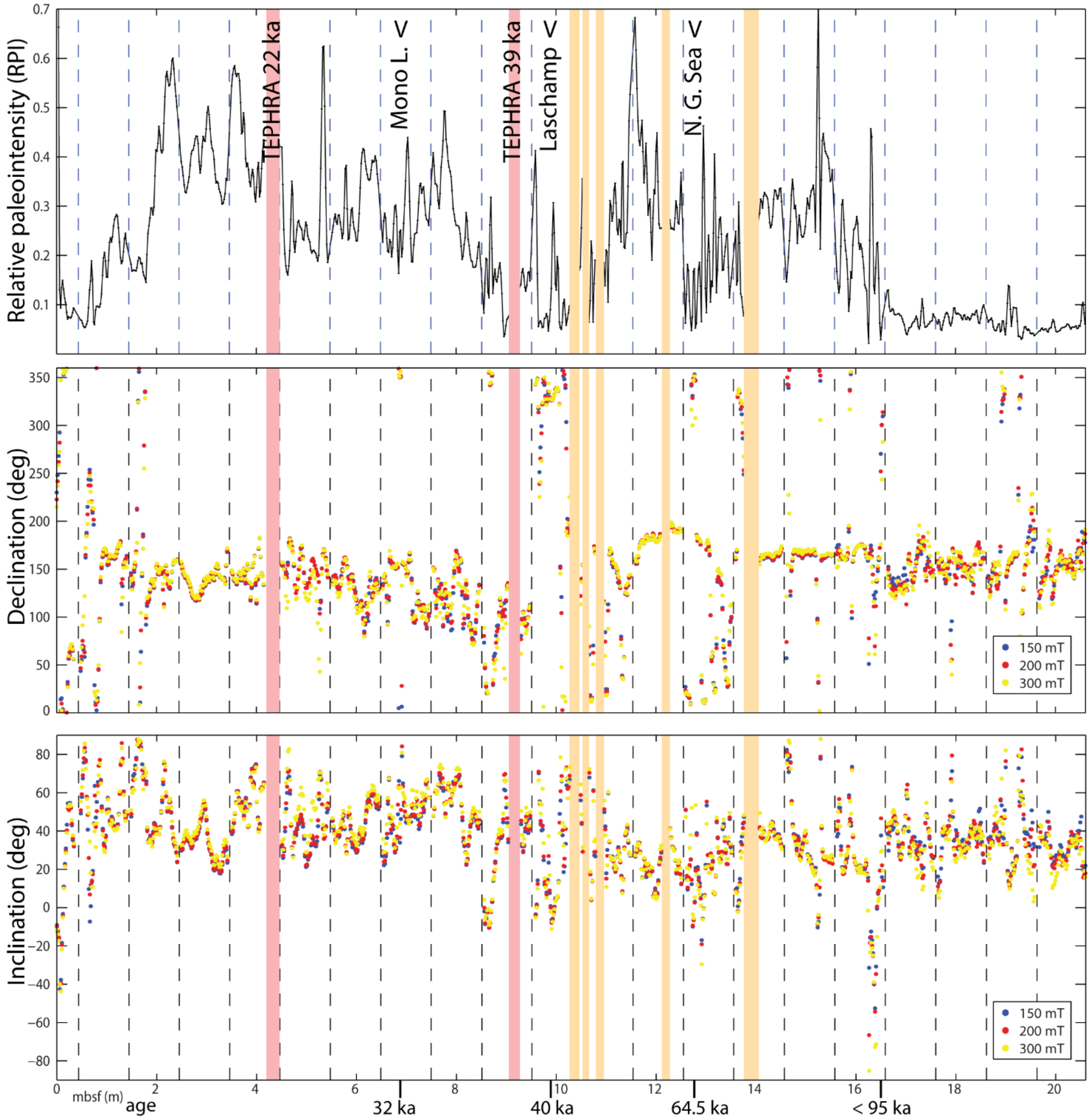

Figure 6. Relative Paleointensity (RPI), declination and inclination of NRM measured on core MRS-CS-22. The RPI is the mean of NRM after demagnetization at 15, 20 and 30 mT divided by the mean of ARM at the same demagnetization thresholds. Data at the position of volcanic ashes (red) and observed sand layers (yellow) were removed. Sections limits are represented by vertical dotted lines. Measurements over 4 cm at each section extremities

were systematically removed. Supposed positions of the Laschamp, Mono Lake and Norwegian Greenland Sea excursions are shown, as well as the age tie-points deduces from the correlations.

3.4. Fossil content and foraminifera assemblages

Core MRS-CS-22 fossil content is drastically different along the various depositional units (see Figure 3).

Starting from the bottom of the core, the foraminifera fauna in Unit 4 is rich in various benthic genera, including some that require an oxic environment such as *Cibicidoides* spp. or *Quinqueloculina* spp. [*Kaiho et al.*, 1994] (see Figure 7). In fact, on a length of 1 m, upward, the assemblage goes from a mix of 29 genera including these oxic indicators to an assemblage containing only 5 genera: *Brizalina* spp., *Hyalinea* spp., *Bolivina* spp., *Melonis* spp. and *Bulimina* spp., all able to live in low oxygen environment. [*McHugh et al*., 2008; *Kaiho et al*., 1994]. Although the presence of these 5 genera is not meaningful itself, as they can also prosper in oxic environment, the gradual decrease of the variety as well as the disappearance of oxic indicators is a striking illustration of the gradual loss of oxygen in the bottom water. Thus, according to the fossil content, Unit 4 represents the end of a rich marine period evolving toward an environment that prevents oxygenation of the bottom water mass.

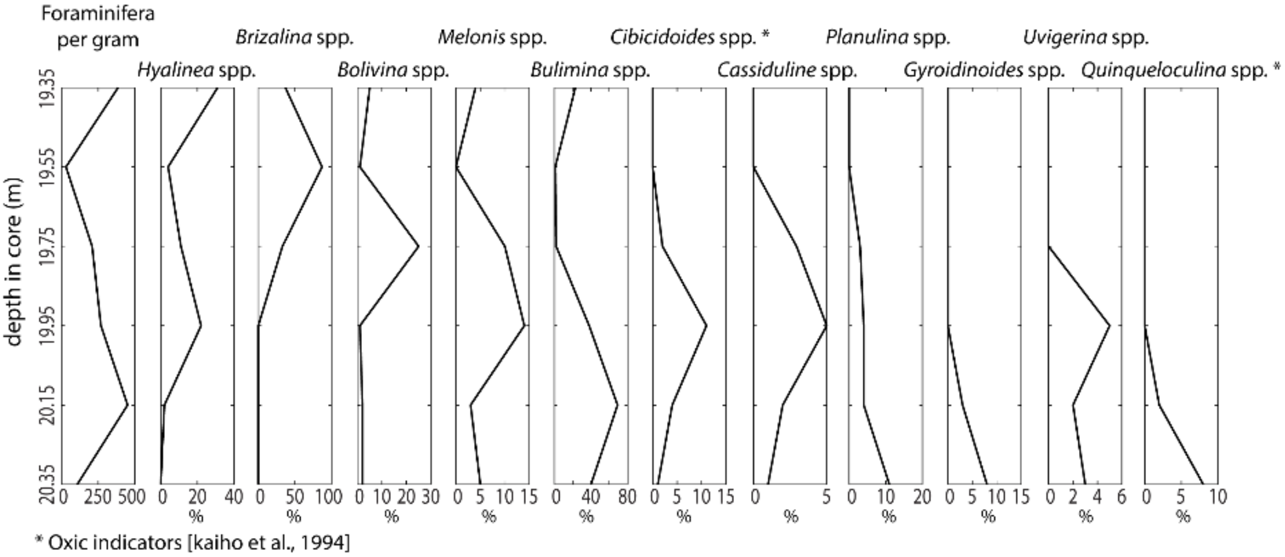

* Oxic indicators [kaiho et al., 1994]

Figure 7. Main foraminifera genera in assemblages at the bottom of Unit 4. Genera that represent at least 5% of one sample are shown. The lowermost sample contains 29 different genera including oxic indicators while the uppermost only contains the 5 genera represented here on the left. All 5 can bear suboxic conditions. The next sample upward does not contain foraminifera.

The fossil content of the sapropelic laminated Unit 3 is limited to Crisophycean cists and to freshwater to brackish diatoms, with assemblages dominated by S*tephanodiscus medius*

S.hantzschii and *S.neoastrea*. Fragments of *Entomoneis calixasini*, only described in the Marmara Sea [*Pailles et al.*, 2014] were also found.

S.hantzschii is a freshwater to brackish water species frequently occurring in rather eutrophic slow running rivers and lakes [*Houk et al*., 2014]. Interestingly, a mass development of small *S.hantzschii* was observed in the mixing zone of brackish and fresh waters of the Tangarog Bay of the Azov Sea [*Kovaleva et al*., 2014]. *E.calixasini*, considered as a benthic species because of its large winged morphology [*Round et al.*, 1990], was found associated to *S.hantzschii*. *S. neoastrea* is also a fresh to brackish waters species, inhabiting the littoral and pelagic zones of lakes. It was also found in meso to eutrophic alkaline lakes and in slow running rivers [*Houk et al*,. 2014]. In contrast *S.medius* is generally regarded as a freshwater species [*Houk et al.*, 2014].

The presence of fresh to brackish water planktonic organisms and the perfect preservation of laminae in the sediments suggests that the water was stratified, with freshwater oxic conditions at the surface and anoxic, bottom water. The resemblance between these facies and the Black Sea present-day laminated facies [*Ross et al*., 1970] is misleading as the carbonate content is here authigenic (see Figure 4) while it consists of coccolithophorids in the Black Sea.

Unit 2 is the poorest in terms of fossil content. Except for a few gastropods and some poorly preserved, probably transported foraminifera, only a few *Dreissena* sp. shell fragments and some ostracodes were found. *Dreissena* sp. is a mollusk which was previously reported in lacustrine sediments of the Marmara Sea [*Aksu et al.*, 2002; *Çağatay et al*.; 2009; *Gasperini et al.*, 2011; *Aloisi et al.*, 2015]. Ostracodes were found along the whole unit although their number is insufficient for an assemblage study. The species identified (mainly *Candona* sp., and *Loxoconcha* sp.) are consistent with previous observations [*Vidal et al.*, 2010] and indicate that the ostracod fauna in the Marmara Sea during the lacustrine stage was influenced by the Black Sea fauna [*Boomer at al.*, 2010]. As no obvious event could have caused the complete disappearance of diatoms in an increasingly lacustrine environment, the absence of diatom fossil is probably due to the dissolution of silica bioclasts after a change of the water alkalinity. The limited number of other kind of fossils, such as ostracods, could simply come from the fact that core MRS-CS-22 was retrieved at a depth close to the limit at which most lacustrine organisms can live.

Finally, Unit 1 is rich in foraminifera, with a majority of benthic species. Since the reconnection with the Mediterranean Sea and the increase of the salinity has been studied in depth before [e.g.: Çağatay et al., 2000; *Eriş et al.*, 2010; *Vidal et al.*, 2010; *McHugh et al.*, 2008], we will not give further details on this unit.

3.5. Terrigenous fraction

The detrital content of core MRS-CS-22 is rather constant, with two grain size families centered on 18 and 5 µm along the whole core except on punctual event deposits (ash layers and sand). Quartz, muscovite, feldspar (mainly Albite), and clinochlore, are the detrital minerals identified in all samples, except in ash layers, in core MRS-CS-22. The stability of both the detrital grain composition and size indicate that the variability of detrital inputs was limited. Thus, the facies and composition variabilities in core MRS-CS-22 are probably more related to changes in the biogenic and chemical fraction rather than to variability of the terrigenous fraction.

3.6. Geochemistry

We measured Ca, Ti, Cr, Rb, Sr, Fe, Mn, K, Zr, Ba, Si, S, Cl, Br and inc/coh (Compton scatter-incoherent/Rayleigh scatter-coherent) using µ-XRF, and calibrated Ca, Ti, Cr, Rb, Sr, Fe, Mn and K with ICP-MS measurements. In addition, we obtained quantitative Mo and U contents from the ICP-MS. As a first approach of the results, we performed a Principal Component Analysis (PCA) on the centered and normalized µ-XRF data.

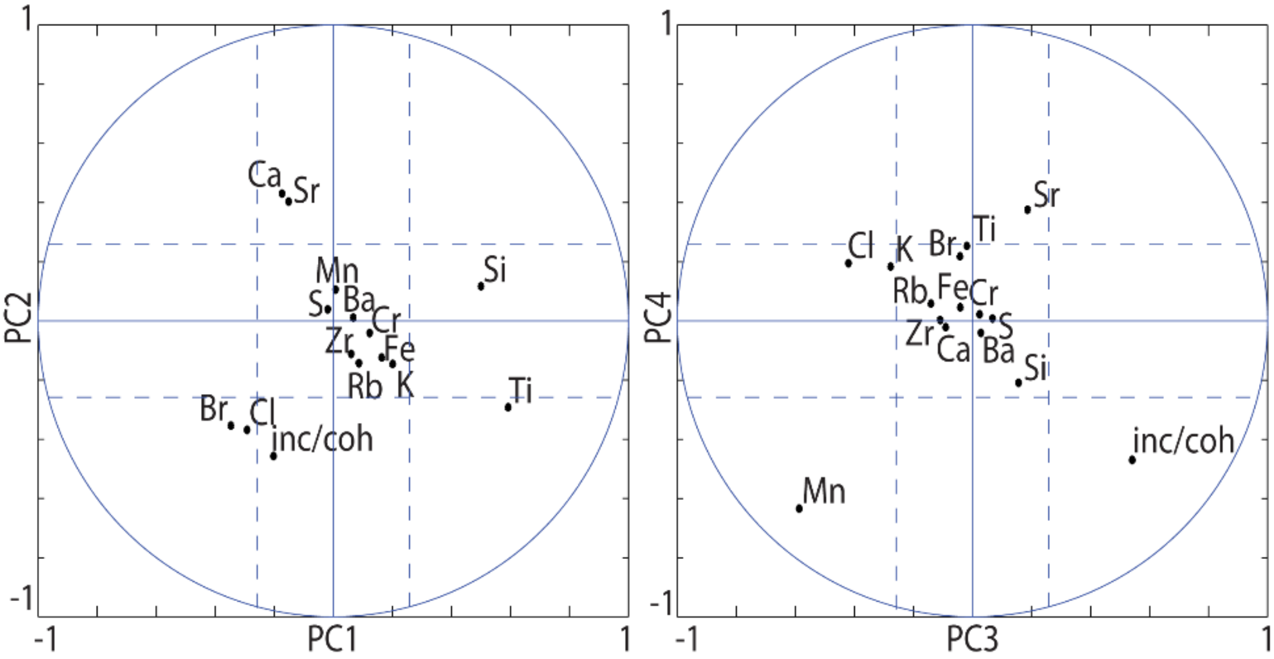

Figure 8. XRF variable positions along the four principal component axis of the Principal Component Analysis (PCA) achieved on µ-XRF data. The dashed lines represent the square root of the mean contribution. Considering one axis, a variable will be considered significant for the axis interpretation if it is further than the corresponding line.

XRF variable positions along the 4 main axis resulting of the ACP are shown in Figure 8. We selected 4 principal axis as it fulfills the Kaiser criterion [*Kaiser*, 1960] as well as the "elbow" method [*Cattell*, 1966]. The first main axis mainly represents the terrigenous fraction with Ti and Si and is opposed to the organic content and interstitial water fraction represented by Br, Cl and inc/coh [i.e. *Croudace et al*., 2006; *Ziegler et al*., 2008]. The second axis, also opposed to the interstitial water fraction, measures mainly the Calcite content, and correlated with the Sr content. This also indicates that the Sr content mostly corresponds to the carbonate fraction. The third and fourth main axis are both related to the Mn and inc/coh content.

Three domains can be identified along the core, following the lithological units.

Unit 1 and 4 are the marine facies. They both show a high Ca content and a very high Sr content, probably partly due to the presence of magnesian-calcite [*Ohde and Kitano*, 1984] as revealed by XRD measurement. Unit 2, the homogeneous lacustrine facies, shows a declining Br, inc/coh and Cl content, related to compaction, and multiple Ca and Sr peaks. Finally, the finely laminated facies recorded many redox variation with peaks of U, Mo, Mn and Ba forming cycles that could be related to the biogenic activity.

4. Discussion

4.1. Correlation of the Ca content with NGRIP data

From the Ca content in core MRS-CS-22, as revealed by XRF measurements, we propose two age tie-points.

The first tie-point is based on the prominent Ca peak observed between 1.5 and 1.8 mbsf reaching up to 18 wt.% Ca, before the lacustrine to marine facies change (See Figure 9). This peak has been observed before and has been attributed to authigenic carbonate precipitation due to the mixing of marine and fresh water after the reconnection at ~12 ka near the beginning of MIS 1 [*Reichel and Halbach.*, 2007; *McHugh et al*., 2008; *Çağatay et al.*, 2015].

The second one is actually a set of tie-points based on observations similar than *Çağatay et al*. [2015]. In their study of core MD01-2430, also retrieved from the Western High in the Marmara Sea, *Çağatay et al*. [2015] compare the ICP-MS Ca content in the lacustrine unit with the oxygen isotope record of the North Greenland Ice Core Project (NGRIP) [*Andersen et al.*, 2004] to build a NGRIP tuned age model. Their conclusion is based on the similarities of the two signals and on the hypothesis that higher Ca-concentrations correspond to authigenic carbonate precipitation promoted by primary production during warmer Greenland Interstadials

(GI) and can be correlated with other NGRIP isotope data. Their model is corroborated by the comparison with Ca content in a core from the southeastern Black Sea and with pollen records from Greece [*Çağatay et al*., 2015].

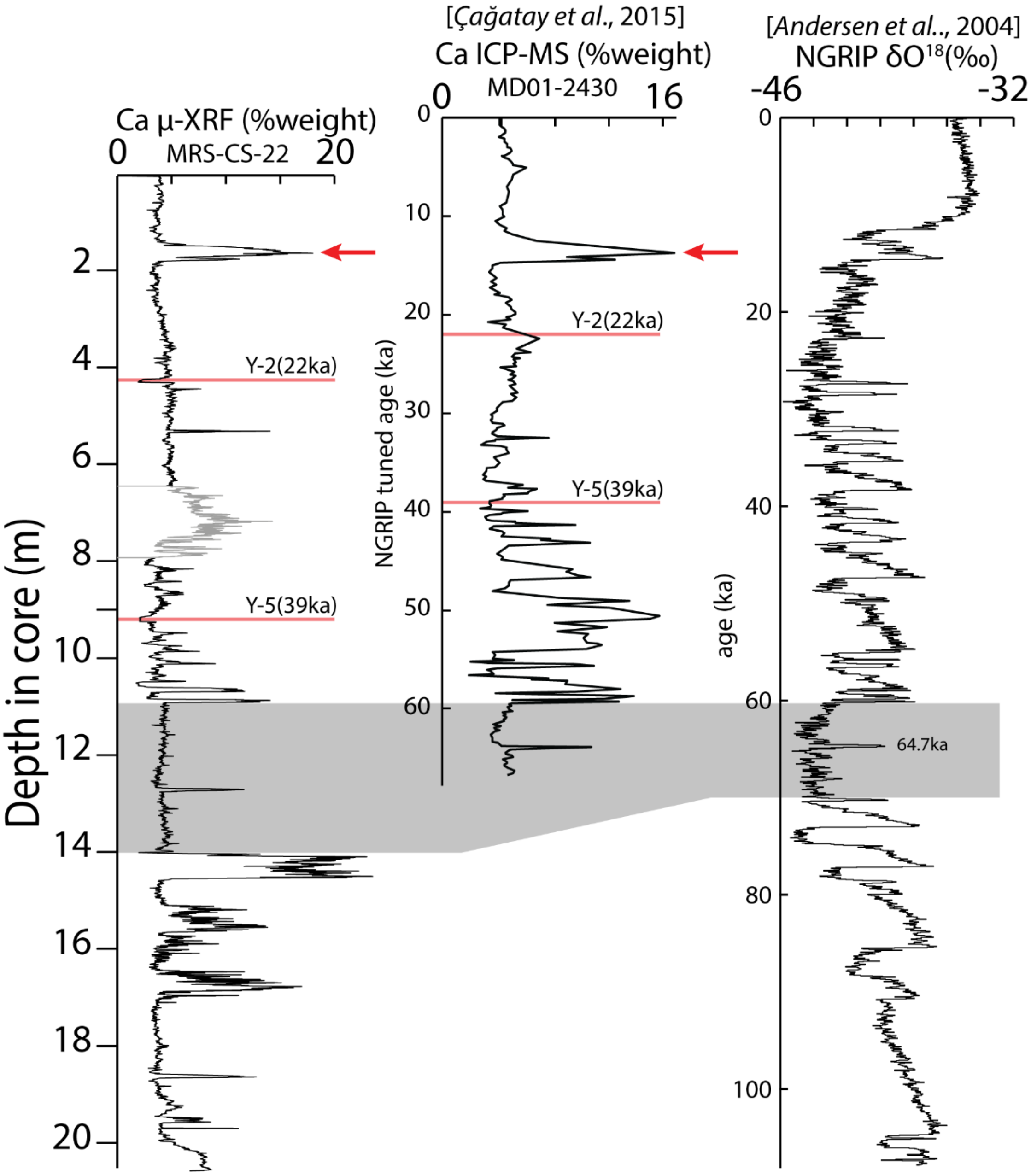

Figure 9.µ-XRF Ca content of core MRS-CS-22, ICP-MS Ca content of MD01-2430 [Çağatay et al., 2015] and oxygen isotope record of the North Greenland Ice Core Project (NGRIP) [Andersen et al., 2004]. The similarity of the three signals during MIS4 is highlighted by the shaded grey area while the two red arrows point toward the Ca peak that has been observed in multiple cores at the last lacustrine/marine transition [Reichel and Halbach., 2007; McHugh et al., 2008]. The grey section in the MRS-CS-22 data is inconsistent with other chemical measurements.

In this study, we compared the μ-XRF Ca data in core MRS-CS-22 with the ICP-MS Ca content in MD01-2430 together with the NGRIP oxygen isotope record, to obtain similar tuning on core MRS-CS-22 (Figure 9). If the Ca content in cores MRS-CS-22 and MD01-2430 are similar in the upper parts, correlations of individual Ca peaks between core MRS-CS-22 and the NGRIP data does not seem possible. However, Ca content between 11 and 14 mbsf in core MRS-CS-22 shows a strong similarity with core MD01-2430 and with the NGRIP signal between 60 and 70 ka. This segment is characterized by a period of relative loss of productivity, interrupted only by one peak that could correspond to the NGRIP peak at 64.7 ka.

The correlation of a limited interval of the Ca signal is debatable. If the two segments are indeed synchronous, then why is there no co-variations of the signals on both sides of this interval? From the other data, we can propose two reasons. First, the μ-XRF Ca signal in our core between about 6.5 and 8 m shows unexpected variations. The peaks in that section are not consistent with the ICP-MS results nor with the Total Inorganic Carbon measurements. A possibility is that the XRF recorded the effect of gypsum precipitation at the surface of the core. The second reason that could explain the bad co-variations of the signal is the presence of a hiatus. Between about 10 and 11 mbsf in core MRS-CS-22, the presence of multiple sand layers and listric faults indicate that the sediment column may have been altered. Also, if the correlation is correct, the existence of a hiatus at this location would be consistent with the positioning of the two tephras in cores MRS-CS-22 compared to core MD01-2430. Moreover, this correlation is perfectly consistent with the location of the 64.5 ka Norwegian-Greenland excursion recording, near the central 64.7 ka Ca peak.

4.2. Construction of an age model

Figure 10 summarizes the information described in the previous parts of this article that are used as age tie-points. They consist of the two tephras, the paleomagnetism events and the Ca μ-XRF tie-points. The last age indication is given by the disappearance of foraminifera at the end of the core.

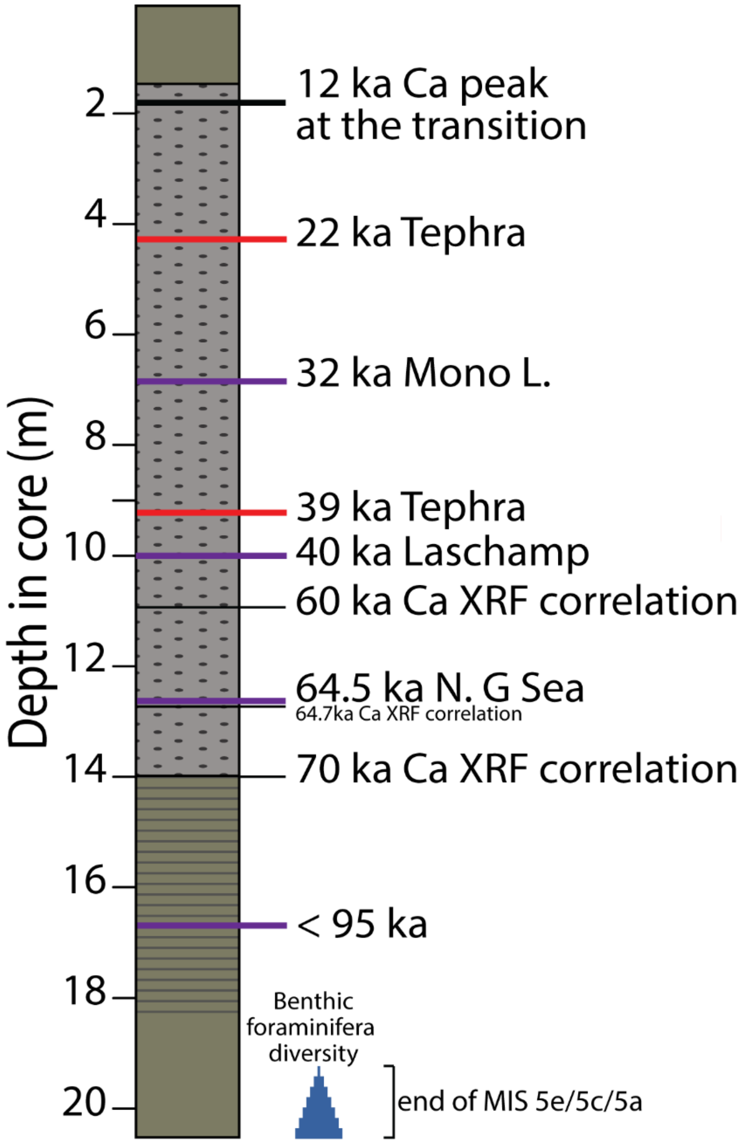

Figure 10. Schematic summary of all the dating points presented in this study. Dating points are given by tephras (Red), paleomagnetism (Violet) the Ca content (Black) and by the foraminifera content of the core bottom. Thin black lines were used to indicate the three debatable correlations of the Ca content.

As exposed in part 3.3.4, we consider that the gradual disappearance of foraminifera, starting with the genera needing oxic conditions, is an effect of oxygen loss caused by the formation of water column stratification. This is corroborated upward by the fossil content in Unit 3 with fresh to brackish diatoms and no trace of any benthic life. Thus, Unit 4 must correspond to a transition leading to conditions propitious for the stratification of the water column. Since the core bottom is undoubtedly marine, we propose that the transition corresponds to a decrease of the water level that reduced the connection with the Mediterranean Sea at the Dardanelles strait, leading to a situation where water input was dominated by freshwater. Considering the ages already inferred along the core, this transition must correspond to the end of one of the MIS 5 high-stands: MIS 5e, MIS 5c or MIS 5a. The coccoliths observed in the core catcher confirm that the core bottom cannot be younger. They show a dominance of *Gephyrocapsa* sp. over *E.huxleyi*. This indicates that the bottom sediments precede the inversion of dominance between *Gephyrocapsa* sp. and *E.huxleyi* which occurred between the late MIS 5 and MIS 4 [*Thierstein et al.*, 1977; *Flores et al.*, 1997]. Finally, considering the limited number of facies variations, it is unlikely that the core bottom is older than MIS 5e.

We now consider the sea-level variations during MIS 5 (see Figure 11). Although the sea-level variation from MIS 5e to MIS 5a seems small compared to the Dardanelles' present-day sill depth, it may not have been the case if the sill was then at a higher position. The determination of the sill depth variations in the past is a difficult question with tectonic and sedimentary implications. In Figure 11, we represented the sparse information available today from a morphological study of the Dardanelles strait [*Gökaşan et al.*, 2008]. One correspond to a depth before the disconnection while the other one corresponds to a depth before the reconnection [*Gökaşan et al.*, 2008; *Çağatay et al.*, 2009]. No precise date has been proposed but it does suggest that the sill was at a higher position before the last disconnection. And because marine water flows below the freshwater, the marine flow must have been predominantly affected by a reduction of the connection at the Dardanelles, even without a complete disconnection. For instance, today, the westward freshwater flow occupies 20 to 30 m at the top of the water column [*Özsoy et al.*, 1996 ; *Beşiktepe et al., 1994*]. With a sill depth at about 40-50 m (Figure 11) and supposing a comparable freshwater mass, the marine eastward water circulation at the sill could occupy at most 20 to 30 m during MIS 5.

Depending on the method used for relative sea-level modeling, the sea-level drop at the end of MIS 5e was of a few meters to more than 20 m [e.g. Medina-Elizalde, 2013; Rohling et al., 2014]. Thus, with a sill depth at 40-50 m, conditions for a trapping of the marine bottom water mass in the Marmara Sea may have appeared. The same effect after MIS 5c is less likely as the water level drop was reversed in the following substages. Finally, the major decrease of the water level at the end of MIS 5a probably caused a total disconnection and could also have created a stratification. However, this last hypothesis implies that the correlation of the Ca content during MIS 4 is wrong, as well as the correlation of the Norwegian-Greenland excursion at 64.5 ka since MIS 4 would then correspond to the laminated Unit 3 above the foraminifera disappearance. We will however consider both hypothesis in the following and consider a Model **a** in which the core bottom corresponds to the end of MIS 5e and a Model **b** in which it corresponds to MIS 5a.

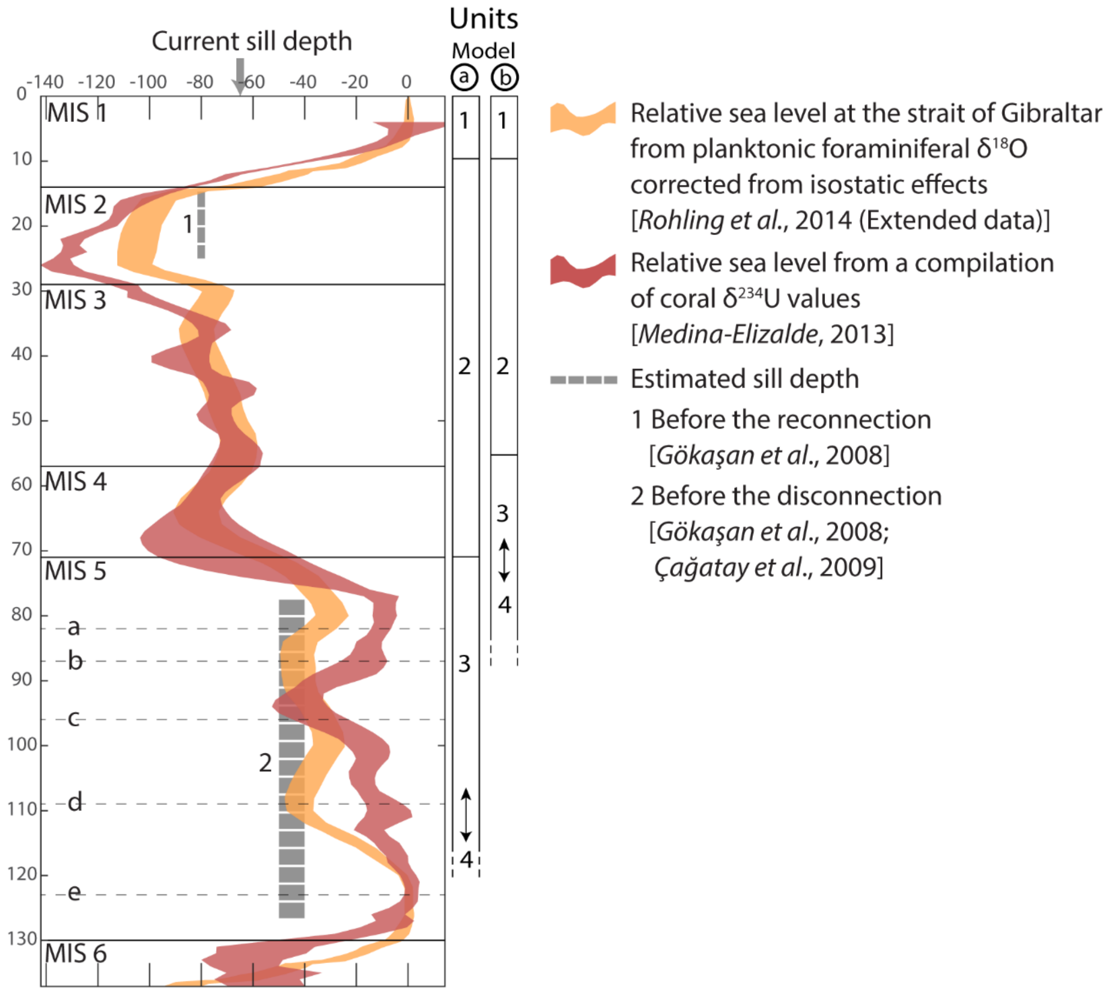

Figure 11. Representation of the two sill depth estimation during the last cycle with two relative sea-level depth model [Medina-Elizalde, 2013; Rohling et al., 2014]. On the right, the correlation with MRS-CS-22 sedimentary Units is showed for the two models we propose.

The correlation of the sedimentary Units with the sea-level for these two models is presented in Figure 11 while Figure 12 shows the two corresponding age models. Since the first samples in the core bottom recorded a decrease in the foraminifera diversity, we assumed that the core bottom was deposited when the sea-level was already decreasing. Thus, we plotted it during the decreases at the end of MIS 5e or MIS 5a with error bars encompassing all the duration of the decrease.

Figure 12 also presents the corresponding sedimentation rates. However, these rates cannot be perfectly accurate as, in addition to the potential existence of unidentified hiatus and the effect of sediment compaction, the model is probably affected by differential compaction or extension occurring during the coring. Furthermore, comparison of the geophysical property of the core and of seismic profiles indicates that the top of the sediment column was not recovered. Thus, 15 m/s for the current day sedimentation rate is probably an under-estimation.

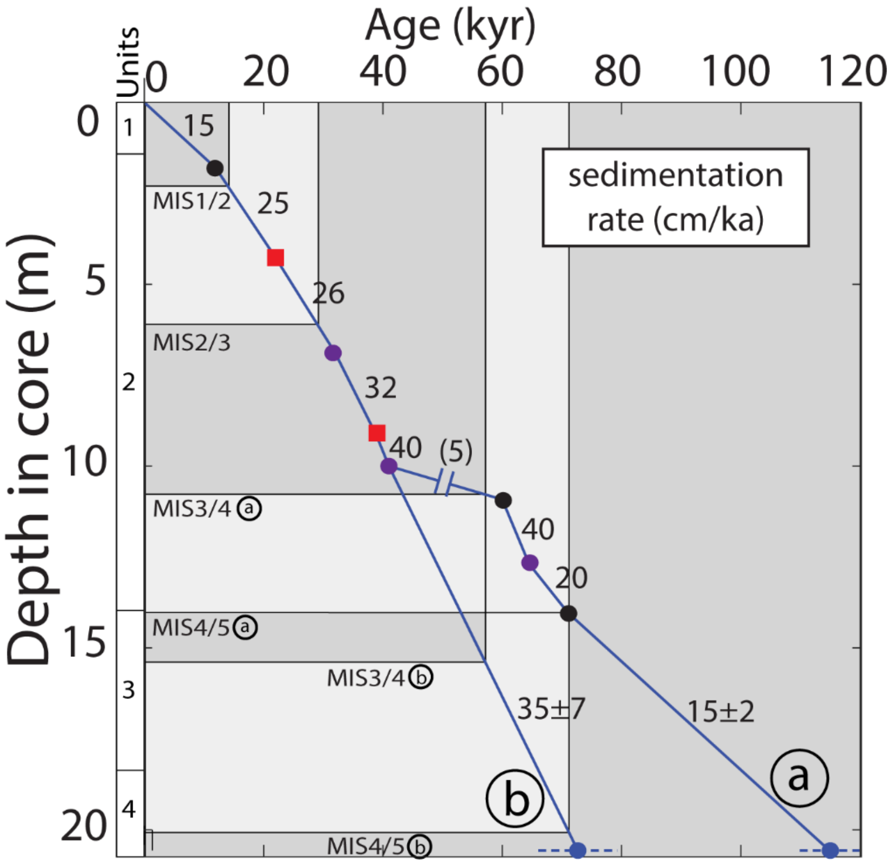

*Figure 12. Age models for core MRS-CS-22 based on the data presented in Figure 10 and corresponding sedimentation rates. Model **a** positions the core bottom during the sea-level drop at the end of MIS 5e while Model **b** positions it at the end of MIS 5a. Model **b** does not take into account the correlation made on the Ca content nor the Norwegian-Greenland Sea excursion of the paleomagnetism. The truncation in Model **a** indicates the location of a supposed hiatus.*

According to Model **a**, the sedimentation rate varies from 15 cm/ka, during the marine phases and during the deposition of the laminated unit, to 20-40 cm/ka during the lacustrine phases. These sedimentation rates are consistent with previous core studies that show a slower sedimentation after the reconnection [*Vidal et al*., 2010] and with the interpretation of seismic data suggesting higher sedimentation rate during the lacustrine phases [*Sorlien et al*., 2012].

According to Model **b**, the mean sedimentation rate was of 35 cm/ka during MIS 4 and a part of MIS 3.

4.3. Environmental and hydrological variations since MIS 5

Based on the age model and on all our observation presented here, we propose a reconstitution of the variation of the hydrology and environment since MIS 5e (Model **a**) or MIS 5a (Model **b**).

*4.3.1. Model **a***

During MIS 5e, the foraminifera assemblages in core MRS-CS-22 indicates a rich marine environment with an oxic bottom water. At the end of this stage, the gradual disappearance of oxic indicators suggests a gradual change in the water masses exchanges. As the water level started to drop, the connection at the Dardanelles was dwindled. Although the sea level at this time probably did not decrease below the sill depth, the limited connection may have had an impact on the water circulation by preventing enough marine water incursion and by decreasing the marine water circulation and mixing. Thus, the bottom water was progressively trapped and its oxygen content dropped.

We suggest that the disconnection may never have been total but that the marine influx did increase during the moderate high-stand of MIS 5c and MIS 5a. Indeed, a small continuous marine influx could have maintained the strong stratification by sustaining the high salinity and mass of the bottom water and preventing its gradual dilution.

Despite the substage variations, the hydrology and environment in the Marmara Sea from MIS 5d to MIS 5a must have been stable enough so that the deposits consist solely of finely laminated green mud. The absence of any kind of bottom water fossils or bioturbation and the high Total Organic Carbon (TOC) content indicate that the bottom water was depleted in oxygen, as inferred from the preceding gradual disappearance of foraminifera during MIS 5e. In fact, the high TOC content defines this facies as a more than 4-meter sapropel. The presence of diatoms and chrysophycean cysts indicates that the top of the water column was oxygenated and probably not fully marine nor fresh as most diatom species are adapted to a brackish environment. Thus, we do observe a testimony of the stratification that appeared at the end of MIS 5e.

Following our hypothesis, the beginning of MIS 4 would coincide with the second major lithological change. Since the beginning of MIS 4 corresponds to an important drop of the Mediterranean water level this could indeed explain the transition from the laminated Unit 3 to the homogeneous Unit 2. Furthermore, if, as suggested by the relative sea-level variations, the Marmara Sea was never completely disconnected from the Mediterranean Sea during MIS 5, this transition could correspond to the effective disconnection.

The base of Unit 2 is characterized by a 2-cm erosive sand layer. Similar sand layers were found at the same facies boundary in other cores retrieved during the MARSITE cruise in the eastern basins. In some cores, there are multiple sand layers close to the facies change and the boundary itself is not affected. Thus, the whole period of transition from MIS 5 to MIS 4 may have been propitious to sand layers formation in the whole Marmara Sea. We propose that when the water level dropped below the shelves level, vast surfaces were destabilized and landslips occurred all around the Marmara Sea. This is consistent with *Çağatay et al*. [2009] findings of reflector unconformities on the shelves indicating erosive events during MIS 4.

The absence of lamination and a few bioturbated levels in Unit 2 suggest that the stratification was not as strong as it was during the deposition of Unit 3. A possibility is that the gradual dilution of marine water finally resulted in a situation where the equilibrium maintaining the two water masses apart was altered. The two masses mixed and the homogenized new mass continued to evolve toward a lacustrine composition by gradual dilution. Additionally, or alternatively, the freshwater inputs at this time may have become too small to maintain the stratification.

The sparse available knowledge on the variations of the Dardanelles Strait depth makes it difficult to evaluate the state of the connection during MIS 4 to MIS 2. Considering the assumed strait depths before the disconnection and before the reconnection (see Figure 11), the strait was probably eroded by the water flow powered by its base level drop during the whole low-stand period. A possibility is that the two seas were regularly connected again. However, the connection was probably small, without major impact on the Marmara Sea stratigraphy or hydrology. This is consistent with the fact that Unit 2 is very homogeneous along its 12.5 m. However, if Model **a** is correct, then the hiatus between 60 and 40 ka could hide the traces of a more significant reconnection during MIS 3.

The lacustrine Unit 2, the marine Unit 1 and the transition from the first one to the second one have been the subject of numerous studies [e.g. *Reichel & Halbach*, 2007; *McHugh et al*., 2008; *Vidal et al*., 2010; *Aloisi et al*., 2015]. Because no new elements were revealed by core MRS-CS-22, we suggest referring to those studies for more details.

4.3.2. Model ***b***

Our Model **b** starts at the end of MIS 5a (Figure 11 and Figure 12). It assumes that both Unit 4 and Unit 3 were deposited during the sea-level drop. If the sill depth at the Dardanelles was around 40 to 50 m, the connection must have been quickly reduced or cut. In the first case, marine inputs from the Mediterranean must have been limited while, in the second case, water exchange were limited to light water outflow inducing only a very slow ventilation and dilution of the marine bottom water mass.

At the top of the laminated Unit 3, the transition to the homogeneous lacustrine Unit 2 above could coincide with the end of MIS 4. A possibility is that the transition marks the end of a period of incision through the strait triggered by the sea-level decrease. The deposition of the laminated Unit3 would correspond to a time when the Marmara Sea was disconnected from the Mediterranean before being connected again through the incision of the strait. Model **b** would then be similar to Model **a** with the possible existence of an alternation of periods of total disconnection and of small reconnection during MIS 3 and MIS 2.

4.4. Conclusion on the two models

Several facts make us favor Model **a**. First, Model **b** makes it difficult to explain the sand layers at the Unit 3/Unit 2 transition. Because these sand layers are found in the whole Marmara Sea at the unit transition, it must correspond to a massive event at the scale of the Marmara Sea. Thus, placing it during the major drop at the end of MIS 5a makes more sense than positioning it at the end of the sea-level drop. Secondly, although the Ca μ-XRF correlation may seem controversial, its perfect consistency with the Norwegian-Greenland Sea excursion is an argument in its favor. And if the correlation is correct then the top of Unit 3 age is 70 ka at least, considering that erosion may have occurred, making it impossible to fit with Model **b**.

Furthermore, the variations of the Total Organic Carbon, diatom fossils and Chrysophycean cysts content along the sapropelic Unit 3 (see Figure 13) could coincide with periods of high and low productivity, possibly corresponding to climatic variations. Correlating this unit with MIS 5 and its substages could explain such variations. At this time, available data seem insufficient to propose a robust precise correlation of the substages. But additional TOC data points as well as an analysis of the pollen content may help precise the model in a near future.

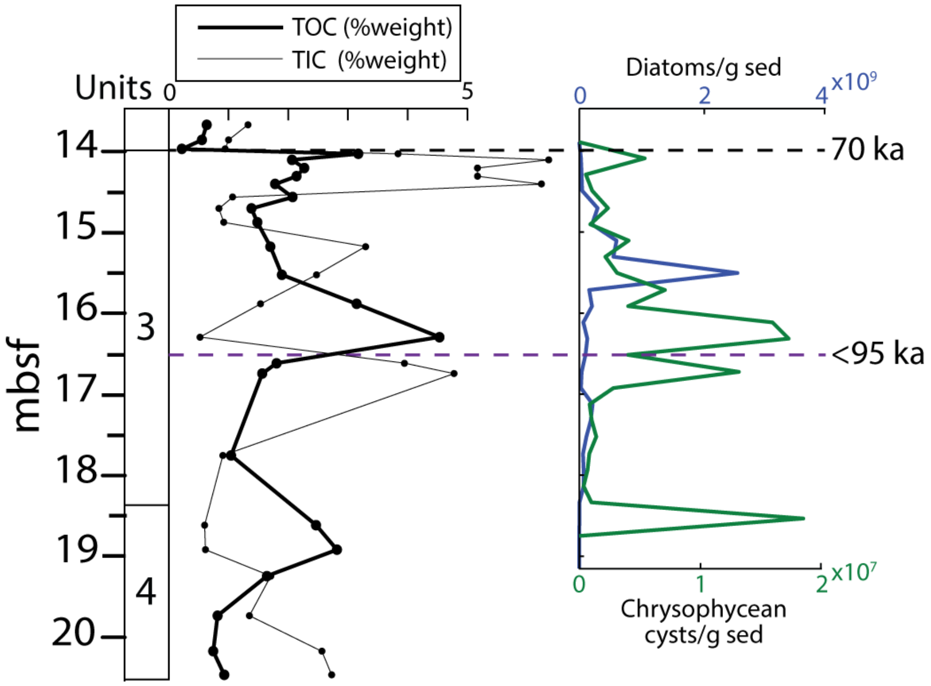

Figure 13. Total Organic and Inorganic Carbon content in Units 3 and 4 of core MRS-CS-22 (left) and diatoms and chrysophycean cysts content (right).

Finally, the last argument supporting Model **a** is the carbon content itself. The exact mechanism ruling the formation of sapropels has been the object of multiple studies [i.e. *Rohling et al.*, 2015 (see for a synthesis); *Grant et al.*, 2016] but it is commonly admitted that the paloproductivity takes part in the process. And while the productivity may not have always been very high during MIS 5d to MIS 5a, it must have been reduced during the sea-level decrease and during the low-stand of MIS 4. Thus, again, this support Model **a** which correlates the sapropel with MIS 5.

5. Conclusions

By targeting a topographic high in the Marmara Sea, the MARSITE cruise coring leg was aiming at retrieving a close to complete record in the Sea of Marmara since the last interglacial. Core MRS-CS-22 proved to fulfill that aim and, if the record is probably indeed incomplete, the only suspected hiatus could be positioned at the beginning of MIS 3.

Based on paleomagnetism, chemical, tephra and fossil analyses, we constructed two age models of the sediment in the Marmara Sea and proposed a reconstruction of paleo-environment and hydrology since the last marine stage in the Marmara Sea. Although no absolute dating method could be applied on this core, the age model tie-points that we propose are consistent to one another. A first model starts at the end of MIS 5a while the other one starts at the end of MIS 5e. Based on the comparison of the models, we favor the latter.

If this hypothesis is correct, then it would be the first time that sediments are described in the Marmara Sea since MIS 5 first substage.

Based on foraminifera assemblages, we suggest that the base of the core corresponds to the sea-level drop at the end of MIS 5e, and that a stratification of the water masses provoked a decrease of the bottom water oxygenation. A few meters above, a correlation of the Ca content points at the end of MIS 5a right at the top of a laminated facies. Those two tie-points delimits a segment consisting mostly of a 4 m sapropel that was deposited from MIS 5d to MIS 5a. The high organic carbon content, the preservation of fine laminae and the presence of fossils of brackish to freshwater planktonic diatoms indicate that, during this whole period, the Marmara Sea water column was highly stratified.

Core MRS-CS-22 also gives us a better understanding of the hydrology variations after the last fully marine period. To explain the durability of conditions propitious to the sapropel deposition in the basins, we propose that the Marmara Sea was not fully disconnected before the end of MIS 5a but that a mince salt water influx prevented the bottom water salinity from being gradually diluted. Alternatively, the stratification was controlled by the freshwater inputs that were reduced as the temperature decreased. At the end of MIS 5, a rapid sea-level drop exposed the shelves to the erosion, causing the deposition of sand layers in the basins, while the Marmara Sea was finally disconnected from the Mediterranean Sea. However, this disconnection may not have been permanent during MIS 4 to MIS 2 since the sill depth was probably increased by erosion powered by the water base level drop and since high amplitude sea-level variations happened during MIS 3. Nevertheless, we suggest that the hydrology was persistently modified at the end of MIS 5.

Core MRS-CS-22 was also the first extensively studied core that contains the “RED” H1 reflector used by *Sorlien et al*. [2011] and *Grall et al*. [2013] as a base for their seismic horizon age model and which age was estimated to be about 110 ka. However, correlation of high resolution seismic profiles and “CHIRP” 3.5 kHz seismic profiles with the synthetic profile generated from geophysical characteristics of core MRS-CS-22 indicates that the “RED” reflector originates in the density difference at the limit between Unit 3 and Unit 2. The age of the “RED” horizon would therefore only be of about 70 ka. Since the age models proposed by *Sorlien et al*. [2011] and *Grall et al*. [2013] are based on the observation of repetitive sequences, other reflectors could also be shifted.

References

Aksu, A. E., Hiscott, R. N., Kaminski, M. A., Mudie, P. J., Gillespie, H., Abrajano, T., & Dogan, Y. (2002). Last glacial-Holocene paleoceanography of the Black Sea and Marmara Sea : stable isotopic , foraminiferal and coccolith evidence. *International Journal of Marine Geology, Geochemistry and Geophysics*, 190, 119–149.

Aksu, A. E., Jenner, G., Hiscott, R. N., & Işler, E. B. (2008). Occurrence, stratigraphy and geochemistry of Late Quaternary tephra layers in the Aegean Sea and the Marmara Sea. *Marine Geology*, 252(3–4), 174–192. http://doi.org/10.1016/j.margeo.2008.04.004

Aloisi, G., Soulet, G., Henry, P., Wallmann, K., Sauvestre, R., Vallet-Coulomb, C., … Bard, E. (2015). Freshening of the Marmara Sea prior to its post-glacial reconnection to the Mediterranean Sea. *Earth and Planetary Science Letters*, 413, 176–185. http://doi.org/10.1016/j.epsl.2014.12.052

Andersen, K. K., Azuma, N., Barnola, J.-M., Bigler, M., Biscaye, P., Caillon, N., … White, J. W. C. (2004). High-resolution record of Northern Hemisphere climate extending into the last interglacial period. *Nature*, 431(7005), 147–151. http://doi.org/10.1038/nature02805

Benson, L., Liddicoat, J., Smoot, J., Sarna-Wojcicki, A., Negrini, R., & Lund, S. (2003). Age of the Mono Lake excursion and associated tephra. *Quaternary Science Reviews*, 22(2–4), 135–140. http://doi.org/10.1016/S0277-3791(02)00249-4

Bertine, K. K. (1972). The deposition of molybdenum in anoxic waters. *Marine Chemistry*, 1(1), 43–53. http://doi.org/10.1016/0304-4203(72)90005-9

Beşiktepe, Ş. T., Sur, H. I., Özsoy, E., Latif, M. A., Oğuz, T., & Ünlüata, Ü. (1994). The circulation and hydrography of the Marmara Sea. *Progress in Oceanography, 34*(4), 285–334. http://doi.org/10.1016/0079-6611(94)90018-3

Bonhommet, N., & Zähringer, J. (1969). Paleomagnetism and potassium argon age determinations of the Laschamp geomagnetic polarity event. *Earth and Planetary Science Letters*, 6(1), 43–46. http://doi.org/10.1016/0012-821X(69)90159-9

Bleil, U., & Gard, G. (1989). Chronology and correlation of Quaternary magnetostratigraphy and nannofossil biostratigraphy in Norwegian-Greenland Sea sediments. Geologische Rundschau, 78(3), 1173–1187. http://doi.org/10.1007/BF01829339

Boomer, I., Guichard, F., & Lericolais, G. (2010). Late Pleistocene to Recent ostracod assemblages from the western Black Sea. *Journal of Micropalaeontology*, 29(2), 119–133. http://doi.org/10.1144/0262-821X10-003

Çağatay, M. N., Eriş, K., Ryan, W. B. F., Sancar, Ü., Polonia, A., Akçer, S., … Bard, E. (2009). Late Pleistocene–Holocene evolution of the northern shelf of the Sea of Marmara. *Marine Geology*, 265(3–4), 87–100. http://doi.org/10.1016/j.margeo.2009.06.011

Çağatay, M. N., Wulf, S., Sancar, Ü., Vidal, L., Henry, P., Appelt, O., & Gasperini, L. (2015). The tephra record from the Sea of Marmara for the last ca . 70 ka and its palaeoceanographic implications. *Marine Geology*, 361, 96–110. http://doi.org/10.1016/j.margeo.2015.01.005

Cattell, R. B. (1966). The scree test for the numbers of factors. *Multivariate Behavioral Research*, 1(2), 245–276. http://doi.org/10.1207/s15327906mbr0102

Croudace, I. W., & Rothwell, R. G. (2015). Micro-XRF Studies of Sediment Cores: Applications of a non-destructive tool for the environmental sciences (Developments in Paleoenvironmental Research). *Tracking Environmental Change Using Lake Sediments. Volume 2: Physical and Geochemical Methods* (Vol. 2). http://doi.org/10.1007/978-94-017-9849-5

Eriş, K. K., Çağatay, M. N., Akçer, S., Gasperini, L., & Mart, Y. (2011). Late glacial to Holocene sea-level changes in the Sea of Marmara: new evidence from high-resolution seismics and core studies. *Geo-Marine Letters*, 31(1), 1–18. http://doi.org/10.1007/s00367-010-0211-1

Gasperini, L., Polonia, A., Çağatay, M. N., Bortoluzzi, G., & Ferrante, V. (2011). Geological slip rates along the North Anatolian Fault in the Marmara region. *Tectonics*, 30(6). http://doi.org/10.1029/2011TC002906

Grall, C., Henry, P., Thomas, Y., Westbrook, G. ., Çağatay, M. N., Marsset, B., … Géli, L. (2013). Slip rate estimation along the western segment of the Main Marmara 1 Fault over the last 405-490 ka by correlating Mass Transport Deposits. *Tectonics*, 32(6), 1587–1601. http://doi.org/10.1002/2012TC003255

Grall, C., Henry, P., Westbrook, G. K., Thomas, Y., Marsset, B., Borschneck, D., … Cifc, G. (2014). Submarine Mass Movements and Their Consequences. *Advances in Natural and Technological Hazards Research*, *37*, 595–603. http://doi.org/10.1007/978-3-319-00972-8

Grant, K. M., Grimm, R., Mikolajewicz, U., Marino, G., Ziegler, M., & Rohling, E. J. (2016). The timing of Mediterranean sapropel deposition relative to insolation, sea-level and African monsoon changes. *Quaternary Science Reviews*, *140*, 125–141. http://doi.org/10.1016/j.quascirev.2016.03.026

Flores, J. A., Sierro, F. J., Francés, G., Vázquez, A., & Zamarreno, I. (1997). The last 100,000 years in the western Mediterranean: Sea surface water and frontal dynamics as revealed by coccolithophores. *Marine Micropaleontology*, 29(3–4), 351–366. http://doi.org/10.1016/S0377-8398(96)00029-1

Houk V., Klee R. & Tanaka H. (2010). Atlas of freshwater centric diatoms with a brief key and descriptions. Part III. Stephanodiscaceae A. Cyclotella, Tertiarius, Discotella. *Fottea* 14 (supplement): 1---530.

Houk V., Klee R. & Tanaka H. (2010). Atlas of freshwater centric diatoms with a brief key and descriptions. Part IV. Stephanodiscaceae B. Stephanodiscus, Cyclostephanos, Pliocaenicus, Hemistephanos, Stephanocostis, Mesodictyon & Spicaticriba. Fottea

Kaiho, K. (1994). Benthic foraminiferal dissolved-oxygen index and dissolved-oxygen levels in the modern ocean. *Geology*, 22(8), 719–722. http://doi.org/10.1130/0091-7613(1994)022<0719:BFDOIA>2.3.CO

Kaiser, H. F. (1960). The Application of electronic computers to factor analysis. *Educational and Psychological Measurement*, XX(1), 141–151. http://doi.org/10.1177/001316446002000116

Kovaleva, G. V., Povazhnyy, V. V., Zolotareva, A. E., Makarevich, P. R., & Matishov, D. G. (2014). Temporary ice microalgae community in Taganrog Bay of the Azov Sea. *Oceanology*, 54(5), 618–623. http://doi.org/10.1134/S0001437014050087

Laj, C., Kissel, C., Mazaud, A., Channell, J. E. T., & Beer, J. (2000). North Atlantic palaeointensity stack since 75ka (NAPIS-75) and the duration of the Laschamp event. *Philosophical Transactions of the Royal Society A: Mathematical, Physical and Engineering Sciences*, 358(1768), 1009–1025. http://doi.org/10.1098/rsta.2000.0571

Leng, M. J., & Marshall, J. D. (2004). Palaeoclimate interpretation of stable isotope data from lake sediment archives. *Quaternary Science Reviews,* 23(7–8), 811–831. http://doi.org/10.1016/j.quascirev.2003.06.012

Lericolais,G., and P.Henry (2004), Cruise report of Marmara VT/Marmacore 2, cruise IPEV VT68,

Liddicoat, J. C., & Coe, R. S. (1979). Mono Lake geomagnetic excursion. *Journal of Geophysical Research: Solid Earth*, 84(B1), 261–271. http://doi.org/10.1029/JB084iB01p00261

Lund, S. P., Schwartz, M., Keigwin, L., & Johnson, T. (2005). Deep-sea sediment records of the Laschamp geomagnetic field excursion (∼41,000 calendar years before present). *Journal of Geophysical Research B: Solid Earth*, 110(4), 1–15. http://doi.org/10.1029/2003JB002943

McHugh, C. M. G., Gurung, D., Giosan, L., Ryan, W. B. F., Mart, Y., Sancar, U., … Çağatay, M. N. (2008). The last reconnection of the Marmara Sea (Turkey) to the World Ocean: A paleoceanographic and paleoclimatic perspective. *Marine Geology*, 255(1–2), 64–82. http://doi.org/10.1016/j.margeo.2008.07.005

Medina-Elizalde, M. (2013). A global compilation of coral sea-level benchmarks: Implications and new challenges. *Earth and Planetary Science Letters*, *362*, 310–318. http://doi.org/10.1016/j.epsl.2012.12.001

Nowaczyk, N. R., & Baumann, M. (1992). Combined high-resolution magnetostratigraphy and nannofossil biostratigraphy for late Quaternary Arctic Ocean sediments. *Deep Sea Research Part A, Oceanographic Research Papers*, *39*(2 PART 1). http://doi.org/10.1016/S0198-0149(06)80021-X

Nowaczyk, N. R., Frank, U., Kind, J., & Arz, H. W. (2013). A high-resolution paleointensity stack of the past 14 to 68 ka from black sea sediments. *Earth and Planetary Science Letters*, *384*, 1–16. http://doi.org/10.1016/j.epsl.2013.09.028

Ohde, S., & Kitano, Y. (1984). Coprecipitation of strontium with marine Ca-Mg carbonates. *Geochemical Journal*, 18, 143–146. http://doi.org/10.2343/geochemj.18.143

Ostroff, C. R., Karlander, E. P., & Van Valkenburg, S. D. (1980). Growth rates of Pseudopedinella Pyriforme (Chrysophyceae) in response to 75 combinations of light, temperature and salinity. *Journal of Phycology*, 16(3), 421–423. http://doi.org/10.1111/j.1529-8817.1980.tb03054.x

Özsoy, E., Latif, M. A., Sur, H. I., & Goryachkin, Y. (1996). A review of the exchange flow regime and mixing in the Bosphorus Strait. *Bulletin de l'Institut Océanographique, 17*(1996), 187–204. Retrieved from http://cat.inist.fr/?aModele=afficheN&cpsidt=3101944

Paillès, C., Poulin, M., Boudouma, O., Pierre, C., Paddock, M., & Cleve, T. (2014). Entomoneis calixasini sp . nov ., a new fossil diatom from the Turkish Marmara Sea sediments. *Diatom Research*, 29(4), 411–422. http://doi.org/10.1080/0269249X.2014.921645

Reichel, T., & Halbach, P. (2007). An authigenic calcite layer in the sediments of the Sea of Marmara—A geochemical marker horizon with paleoceanographic significance. *Deep Sea Research Part II: Topical Studies in Oceanography*, 54(11–13), 1201–1215. http://doi.org/10.1016/j.dsr2.2007.04.008

Rohling, E. J., Foster, G. L., Grant, K. M., Marino, G., Roberts, a P., Tamisiea, M. E., & Williams, F. (2014). Sea-level and deep-sea-temperature variability over the past 5.3 million years. *Nature*, 508(7497), 477–82. http://doi.org/10.1038/nature13230

Rohling, E. J., Marino, G., & Grant, K. M. (2015). Mediterranean climate and oceanography, and the periodic development of anoxic events (sapropels). *Earth-Science Reviews*, *143*, 62–97. http://doi.org/10.1016/j.earscirev.2015.01.008

Ross, D. a, Degens, E. T., & Macilvaine, J. (1970). Black sea: recent sedimentary history. *Science (New York, N.Y.)*, 170(3954), 163–165. http://doi.org/10.1126/science.170.3954.163

Round F.E., Crawford R.M. & Mann D.G. (1990). The diatoms. Biology and morphology of the genera. *Cambridge University Press*, Cambridge. 747 pp.

Shackleton, N.J., et al. (2000). MD952042 Oxygen and Carbon Isotope Data, IGBP PAGES/World Data Center A for Paleoclimatology Data Contribution Series #2000-066. *NOAA/NGDC Paleoclimatology Program*, Boulder CO, USA.

Şengör, A. M. C., Grall, C., Imren, C., Pichon, X. Le, Görür, N., Henry, P., … Siyako, M. (2014). The geometry of the North Anatolian transform fault in the Sea of Marmara and its temporal evolution: implications for the development of intracontinental transform faults. *Canadian Journal of Earth Sciences*, 51(February), 222–242. doi:10.1139/cjes-2013-0160

Siddall, M., Rohling, E., Almogi-Labin, a, Hemleben, C., Meischner, D., Schmelzer, I., & Smeed, D. a. (2003). Sea-level fluctuations during the last glacial cycle. *Nature*, *423*(June), 853–858. http://doi.org/10.1038/nature01687.1.

Sorlien, C. C., Akhun, S. D., Seeber, L., Steckler, M. S., Shillington, D. J., Kurt, H., … Diebold, J. B. (2012). Uniform basin growth over the last 500ka, North Anatolian Fault, Marmara Sea, Turkey. *Tectonophysics*, 518–521, 1–16. http://doi.org/10.1016/j.tecto.2011.10.006

Thierstein, H. R., Geitzenauer, K. R., Molfino, B., & Shackleton, N. J. (1977). Global synchroneity of late Quaternary coccolith datum levels Validation by oxygen isotopes.

Geology, 5(7), 400–404. http://doi.org/10.1130/0091-7613(1977)5<400:GSOLQC>2.0.CO;2

Thomsen, H. A., Zimmermann, B., Moestrup, Ø., & Kristiansen, J. (1981). Some new freshwater species of Paraphysomonas (Chrysophyceae). *Nordic Journal of Botany*, *1*(4), 559–581. http://doi.org/10.1111/j.1756-1051.1981.tb00724.x

Thouveny, N., Carcaillet, J., Moreno, E., Leduc, G., & Nérini, D. (2004). Geomagnetic moment variation and paleomagnetic excursions since 400 kyr BP: A stacked record from sedimentary sequences of the Portuguese margin. *Earth and Planetary Science Letters*, 219(3–4), 377–396. http://doi.org/10.1016/S0012-821X(03)00701-5

Vidal, L., Ménot, G., Joly, C., Bruneton, H., Rostek, F., Çağatay, M. N., … Bard, E. (2010). Hydrology in the Sea of Marmara during the last 23 ka: Implications for timing of Black Sea connections and sapropel deposition. *Paleoceanography*, 25(1), PA1205. http://doi.org/10.1029/2009PA001735

Wagner, G., Beer, J., Laj, C., Kissel, C., Masarik, J., Muscheler, R., & Synal, H. A. (2000). Chlorine-36 evidence for the Mono Lake event in the summit GRIP ice core. *Earth and Planetary Science Letters*, 181(1–2), 1–6. http://doi.org/10.1016/S0012-821X(00)00196-5

Wulf, S., Kraml, M., Kuhn, T., Schwarz, M., Inthorn, M., Keller, J., … Halbach, P. (2002). Marine tephra from the Cape Riva eruption (22 ka) of Santorini in the Sea of Marmara. *Marine Geology*, 183(1–4), 131–141. http://doi.org/10.1016/S0025-3227(01)00302-4

Ziegler, M., Jilbert, T., de Lange, G. J., Lourens, L. J., & Reichart, G.-J. (2008). Bromine counts from XRF scanning as an estimate of the marine organic carbon content of sediment cores. *Geochemistry, Geophysics, Geosystems*, 9(5), n/a-n/a. http://doi.org/10.1029/2007GC001932

ANNEXE AU CHAPITRE II

Detailed evolution of the Marmara Sea salinity and oxygenation during the last deconnection from Strontium and redox element proxies

The calibrated Strontium and Calcium content in core MRS-CS-22 is one of the result of the XRF analysis combined with the ICP-MS results. As shown in Figure 14, the ratio between the two elements along the core varies between 2.10^{-3} in the middle of Unit 2 and almost 1.10^{-2} in the uppermost marine facies (Unit 1). Since this ratio is lower in brackish and fresh water than in marine water, we tried to establish if the Sr-Ca ratio variations in core MRS-CS-22 could be related to variations in the water supply.

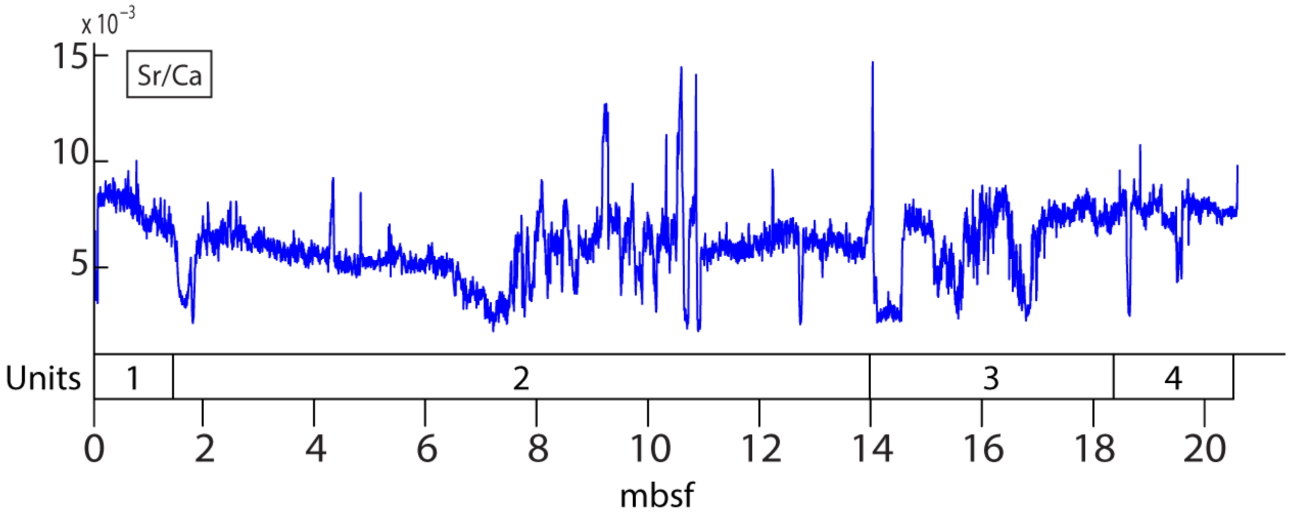

Figure 14. Sr/Ca content in core MRS-CS-22.

The Sr and Ca elements are predominantly stocked in carbonates. In an ideal case in which only calcite would precipitate, Sr/Ca would depend on one activity coefficient defined as [*Kinsman and Holland*, 1969]:

$$k_{Sr} = \left(\frac{Sr^{2+}}{Ca^{2+}}\right)_{calcite} \bigg/ \left(\frac{Sr^{2+}}{Ca^{2+}}\right)_{solution}$$

For calcite, we have k_{Sr} = 0.14 at 25°C and k_{Sr} = 0.08 at 100°C [*Kinsman and Holland*, 1969]. Considering a linear dependence with temperature, similarly to the aragonite coefficient [*Kinsman and Holland*, 1969], we obtain k_{Sr} = 0.148 at 15°C below the halocline [*Beşiktepe et al*., 1994]. During marine stages, Sr/Ca in water will get closer to the Mediterranean Sea value, close to the average ocean value of 18.5 mg/g [*Culkin and Cox*, 1966; *Major et al*., 2006]. On the opposite, during lacustrine stages, the Sr-Ca ratio should tend to the Sr-Ca ratio of river inputs transiting through the Black Sea with Sr/Ca of about 4.8 mg/g [*Major et al*., 2006]. Thus, if all the Sr and Ca are contained in calcite, we should observe Sr-Ca ratio varying between 2.74 mg/g during marine stages and 0.71 mg/g during lacustrine stages.

In our core, Sr/Ca values are high compared to these estimation because the terrigenous content interferes with the linear signal. By plotting Sr in function of Ca (Figure 15), locations of individual calcite peaks where the terrigenous fraction is insignificant and Sr-Ca is close to a linear function appear. Thus, linear regression based on chemical data at the precise location of these peaks will give the Sr-Ca ratio in calcite as the curve slope.

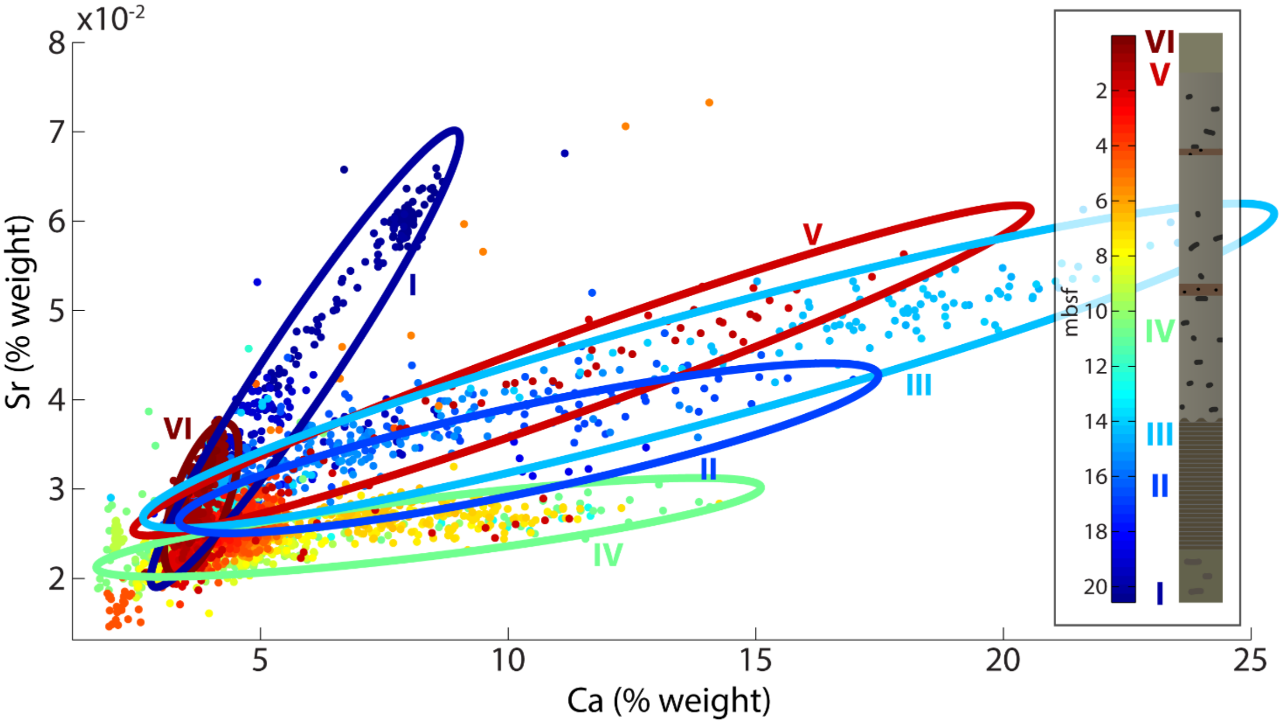

Figure 15. Sr-Ca plot (XRF data calibrated with ICP-MS) along the core depth. Ovals are highlighting zones rich in calcite where a clear Sr/Ca ratio appears. This first approach shows that sediments deposited in an environment that we supposed stratified or lacustrine (II and III) have a smaller ratio than marine sediments (V, VI and). The yellow points close to the green points of zone IV correspond to the calcium inconsistent values and are not considered.

Based on this observation, we carefully identified all Ca peaks in the core that are synchronous with Sr, ignoring Sr rich sand layer, the Ca inconsistent measurements (see Figure 9) and peaks that are too small to be clearly differentiated from the terrigenous fraction. For each peak, we performed a least-square method linear regression.

Table 1 details the results, with the location of each singularized peak, the number of points considered and the correlation coefficient. Figure 16. shows two examples of peak data with their linear regression as well as the stack of all linear regression curves.

Peak number	**mbsf (start-end)**	**Number of points**	**linear regression *y=ax+b***		**Correlation coefficient (R2)**	**Facies Unit**	**Sr/Ca (mg/g) in solution with kSr = 0.148**
			a	**b**			
1	0.10-0.91	159	8.96E-03	-3.14E-03	0.56	1	60.6
2	1.49-1.74	45	1.98E-03	2.11E-02	**0.93**	2	13.4
3	10.60-10.72	25	4.90E-04	2.20E-02	0.53	2	3.3
4	10.85-10.92	15	4.56E-04	2.25E-02	0.63	2	3.1
5	14.04-14.53	99	1.16E-03	2.91E-02	0.74	3	7.9
6	15.11-15.50	79	1.69E-03	2.29E-02	**0.80**	3	11.4
7	16.46-16.55	19	2.40E-03	2.15E-02	0.74	3	16.2
8	16.68-16.75	15	1.41E-03	2.40E-02	**0.89**	3	9.5
9	16.78-16.87	19	1.26E-03	2.32E-02	**0.85**	3	8.5
10	19.98-20.55	115	6.60E-03	7.55E-03	**0.96**	4	44.6

Seawater (global average) [*Major et al.*, 2006]	18.5 mg/g
River average in Black Sea [*Major et al.*, 2006]	4.8 mg/g

*Table 1. Result of linear regression of Sr-Ca data on calcite peaks. The regressions were performed on Matlab with the least-square method. The slope **a** represents the Sr/Ca ratio in calcite and gives, following equation (1), an estimation of the Sr/Ca ratio in the water at the time of Calcite precipitation.*

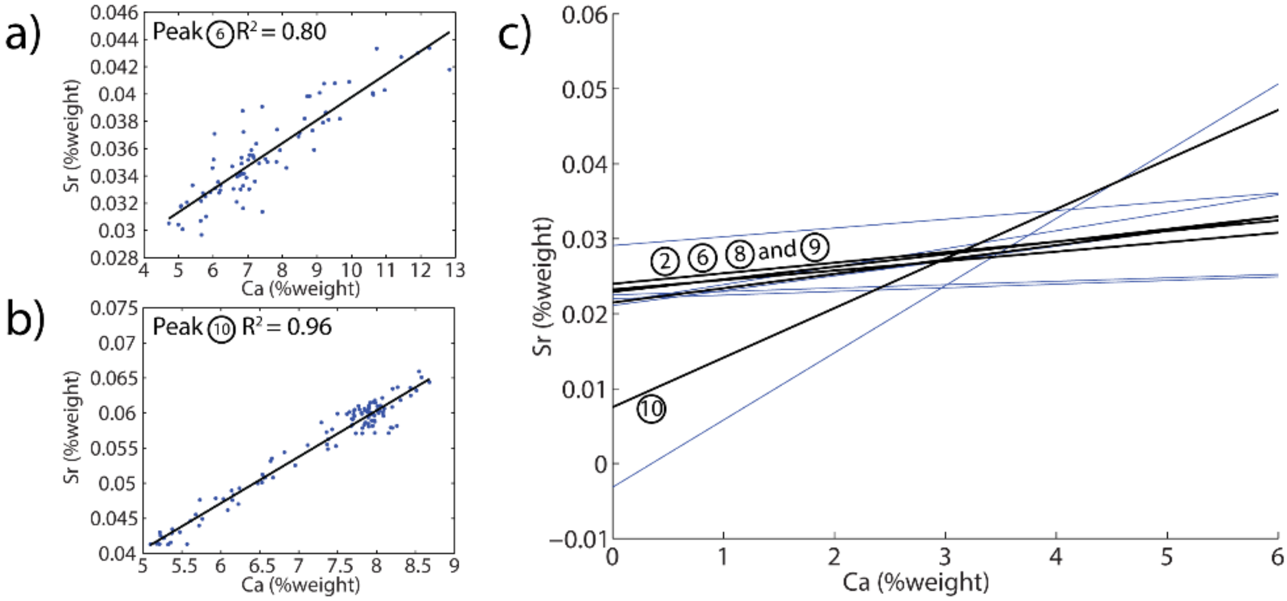

Figure 16. a) and b) Sr-Ca data points and linear regression of calcite peaks number 6 and 10 (see corresponding depth in Table 1). c) Results of all linear regression. Bold black lines are the regressions with $R^2 > 0.80$. Peak number 10 corresponds to the bottom marine facies where the presence of Magnesian-rich calcite increases the Sr/Ca ratio and where the terrigenous fraction may contain a different Sr base level. Peaks 2, 6, 8 and 9 with R2 > 0.8

have similar linear regression coefficient and indicate a base level of Strontium between $2.1x10^{-2}$ *and* $2.4x10^{-2}$.

However, k_{Sr} varies depending on the considered carbonate. The aragonite k_{Sr} at 15°C is 1.15 [*Kinsman and Holland*, 1969], Magnesian-rich calcite k_{Sr} is about 4 [Ohde & Kitano, 1984] while dolomite k_{Sr} is about half of the calcite k_{Sr} [*Jacobson and Usdowski*, 1976]. Thus, we can expect in marine water a Sr-Ca ratio of 21.3, 7.4 and 1.4 mg/g in, respectively, aragonite, Magnesian-rich calcite and dolomite and of 5.5, 2.0 and 0.4 mg/g for the same carbonates in lacustrine water. In MRS-CS-22, XRD results show that calcite is always dominant, although traces of aragonite and of dolomite do exist on most samples. Furthermore; Magnesian-rich calcite at the core extremities could be significant and affect the Sr-Ca ratio. We will assume that the dominance of calcite is strong enough to neglect other carbonates, except at the core extremities.

Peaks 1 and 10 correspond to the marine Units. Calculation of water Sr-Ca ratio with equation (1) and $k_{Sr} = 0.148$ yields $Sr/Ca \approx 44.6$ mg/g in solution during the deposition of the core bottom, which is two to three times the ratio value in the ocean [*Major et al*., 2006]. It confirms that, during marine stages, the Sr fraction contained in calcite is not representative of the entire Sr fraction. XRD results suggest that Magnesian-rich calcite is present. However, even if Sr co-precipitation in high Mg-calcite can be about four times that of the co-precipitation in low Mg-calcite, the Mg-calcite signal in XRD result is not wide enough to entirely explain the Sr/Ca increase. More likely, a variation in the terrigenous fraction is also responsible. Also, the small correlation coefficient of peak 1 makes the very high calculated slope doubtful.

Peak 2 corresponds to the calcite peak attributed to the precipitation triggered by marine and fresh water mixing after the reconnection [*Reichel and Halbach*., 2007], which is consistent with the high Sr/Ca in solution that correspond to 2/3 of marine water. Finally, peaks 3 to 9 belong to Units 2 and 3 and show a higher Sr/Ca slope during Unit 3. Sr/Ca in Unit 2 corresponds to less than 1/5 of marine water while Sr/Ca calculated in Unit 3 correspond to 1/4 to 1/2 of marine water.

Thus, it illustrates that, during the deposition of Unit 2 and 3, there was no steady-state and the water column inputs were varying with a gradual diminution of the marine water portion. Based on lithology, fossil content and previous studies, we proposed that Unit 2 was deposited after the Dardanelles disconnection and that the underlying Unit 3 was deposited while marine inputs from the Mediterranean was thin but persisting. These new results are consistent with this hypothesis.

But these calculations are limited to locations where calcite fraction is high enough to emerge from the terrigenous fraction. If this terrigenous fraction is stable and if our regressions are correct, the lines in Figure 16 should converge at the fraction representative of the terrigenous base level. Since there is no clear intersection of the lines, we will consider a Ca base level between 0 %wt and 3 %wt. Taking the mean of the y-intersect values (ignoring peak 5) we obtain a base level for Sr aof $2.2\text{x}10^{-2}$ %wt.

We used this base levels to correct the Sr and Ca weight fraction before calculating Sr/Ca. Figure 17 Shows the result. Again, we find that the Sr/Ca ratio is greater in Unit 3 than in Unit 2, supporting that the laminated facies was deposited in a transitional phase, in terms of salinity, after the full marine environment of Unit 4 and before the strong lacustrine environment of Unit 2.

But, looking at the curve with 0%wt as the Ca base level (in blue in Figure 17), a striking result is that, from 16.6 to 10 mbsf, a close to linear decrease of Sr/Ca appears, followed by a period of stability from 10 to 3 mbsf. If 0 %wt Ca is the Ca terrigenous base level along Units 2 and 3, it could support that the salinity loss was gradual then reached its minimum at 10 mbsf. Afterward, the salinity may have been steady until the reconnection. However, this interpretation can be accepted only if the high amplitude variability before and after this segment is explained.

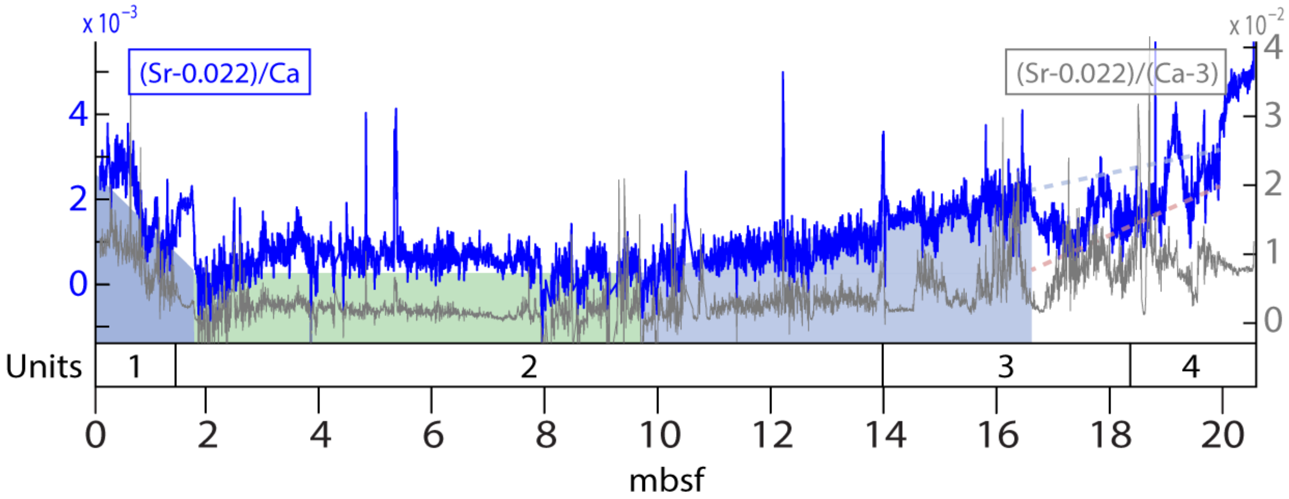

Figure 17. Sr/Ca ratio in core MRS-CS-22 with Sr and Ca value corrected from the base level of terrigenous inputs. Points with Ca lower than 3 %wt were removed as they probably correspond to zones deprived of any carbonate. The two base level were inferred from the linear regressions performed at the positions of Ca peaks. As the Ca base level is unclear, we plotted two possibilities. The blue and green areas as well as the blue and red dotted lines are illustrating the interpretation of the the 0 %wt Ca base level alone (see details in text).

At the core extremities, as we saw previously, the presence of high Mg-calcite is probably responsible for the high Sr/Ca ratio.

Below 16.6 msf, periodic low Sr/Ca values could be explained by the fact that this portion of the core was perturbed, as small faults were observed from 16.6 mbsf to the core bottom. However, it would hardly explain the amplitude of variability between the peaks and the lows in this section. Another possibility, if we consider that the water masses were stratified during most of Unit 3 deposition, is that the stratification establishment was not instantaneous but rather erratic, starting at 19.3 mbsf with two episodes of mixing, respectively corresponding to the deposition of sediments from 19 to 18 mbsf and from 17.6 to 16.6 mbsf. During episodes of mixing, the total salinity was better distributed in all the water volume, but still decreasing, as supported by the decrease of the signal in the lows (see red dotted line in Figure 17). Similarly, the highs in the curve are in the continuity of the 16.6 to 10 mbsf portion and could correspond to the continuous loss of salinity during better stratified periods. The fact that the Sr-Ca ratio decreases faster in the lows could also be explained by this hypothesis. As salinity loss occurs through the water discharge at the Dardanelle straight, salt will be expelled faster if the top of the water column is rich in salt. Thus, during periods of mixing, the outflow at the Dardanelles will cause a faster decrease of the salinity. A third hypothesis could be that the calcite formed during this lows in the signal was precipitated higher in the stratified water column, incorporating less Sr as the water was less salty. It is also possible that a conjunction of these factors caused the observed variability. A poorer stratification would explain the fastest decrease during the signal lows while a different origin could account for the significant gap between the high and low Sr/Ca values.

Thus, we propose that the Sr-Ca ratio indicates that the salinity started decreasing even before the foraminifera disappearance, at 19 mbsf in our core. Then the salinity loss was gradual and reached its minimum at 10 mbsf. In the core, this depth corresponds to a segment with probable material loss. Thus, we can only estimate an age between 40 and 60 ka. Afterward, the salinity remained stable in a lacustrine environment until the reconnection.

However, if we now consider the curve with 3% wt Ca as the base level, this scenario is not so obvious. The Sr-Ca ratio in Unit 2 still appears as the period with the lower salinity but the evolution toward this stage is way more chaotic and fitting a decreasing trend would be arguable. We do know, from granulometric and XRD analysis, that terrigenous inputs were somewhat stable. However, a constant size grain does not imply invariant Ca and Sr inputs and the XRD results without a precise quantification cannot support this fact either. Thus, the reality may have varied between the two curves.

To conclude, we described a new salinity proxy based on the study of the Sr-Ca ratio and on the determination of the Sr and Ca base level of the terrigenous inputs. Our reasoning stands on multiple hypothesis, the main one being that other carbonates than calcite are negligible. Also, further analysis could help precise the terrigenous base level or discriminate between the two models we proposed. However, the trend that we brought out is clear enough to suggest that it is not hazardous. Thus, testing this proxy on other cores and other areas could be promising.

References

Beşiktepe, Ş. T., Sur, H. I., Özsoy, E., Latif, M. A., Oğuz, T., & Ünlüata, Ü. (1994). The circulation and hydrography of the Marmara Sea. *Progress in Oceanography*, 34(4), 285–334. http://doi.org/10.1016/0079-6611(94)90018-3

Çağatay, M. N., Eriş, K., Ryan, W. B. F., Sancar, Ü., Polonia, A., Akçer, S., … Bard, E. (2009). Late Pleistocene–Holocene evolution of the northern shelf of the Sea of Marmara. *Marine Geology*, 265(3–4), 87–100. http://doi.org/10.1016/j.margeo.2009.06.011

Culkin, F., & Cox, R. A. (1976). Sodium, potassium, magnesium, calcium and strontium in sea water. *Deep Sea Research and Oceanographic Abstracts*, 13(5), 789–804. http://doi.org/10.1016/0011-7471(76)90905-0

Jacobson, R. L., & Usdowski, H. E. (1976). Partitioning of strontium between calcite, dolomite and liquids: An experimental study under higher temperature diagenetic conditions, and a model for the prediction of mineral pairs for geothermometry. *Contributions to Mineralogy and Petrology*, 59(2), 171–185. http://doi.org/10.1007/BF00371306

Kinsman, D. J. ., & Holland, H. . (1969). The co-precipitation of cations with CaCO3—IV. The co-precipitation of Sr2+ with aragonite between 16° and 96°C. *Geochimica et Cosmochimica Acta*, 33(1), 1–17. http://doi.org/10.1016/0016-7037(69)90089-1

Major, C. O., Goldstein, S. L., Ryan, W. B. F., Lericolais, G., Piotrowski, A. M., & Hajdas, I. (2006). The co-evolution of Black Sea level and composition through the last deglaciation and its paleoclimatic significance. *Quaternary Science Reviews*, 25(17–18), 2031–2047. http://doi.org/10.1016/j.quascirev.2006.01.032

Ohde, S., & Kitano, Y. (1984). Coprecipitation of strontium with marine Ca-Mg carbonates. *Geochemical Journal*, 18, 143–146. http://doi.org/10.2343/geochemj.18.143

Reichel, T., & Halbach, P. (2007). An authigenic calcite layer in the sediments of the Sea of Marmara—A geochemical marker horizon with paleoceanographic significance. Deep Sea Research Part II: *Topical Studies in Oceanography*, 54(11–13), 1201–1215. http://doi.org/10.1016/j.dsr2.2007.04.008

CONCLUSION ET PERSPECTIVES

Les trois parties de ce mémoire constituent une reconstitution de l'évolution de la Mer de Marmara à des échelles de temps et d'espace fort éloignées. Cependant, la question à laquelle nous avons chaque fois tenté de répondre, par des méthodes aussi diverses que la géophysique, la modélisation ou la géochimie, est celle de la continuité dans le temps de l'évolution de la mer de Marmara ou, plus précisément, la question de l'extrapolation possible des caractéristiques actuelles et récentes connues du système de faille de la mer de Marmara et de son système hydrique.

Dans la première partie, nous avons proposé une modélisation de la géométrie 3D actuelle de la croûte basée sur les anomalies de gravité mesurées dans la région de la mer de Marmara. Si cette étude ne permet pas d'apporter des renseignements sur l'époque de l'incursion de la faille Nord-Anatolienne, elle est cependant compatible avec les modèles suggérant qu'un stade purement extensif aurait précédé l'incursion de la faille Nord-Anatolienne [*Le Pichon et al.*, 2003 ; *Gökaşan et al.*, 2003 ; *Rangin et al.*, 2004].

En supposant une épaisseur de croûte de référence correspondant à l'épaisseur avant l'extension crustale associée à la formation de la mer de Marmara, nous avons pu calculer l'extension totale dans la région depuis la formation des premiers bassins il y a environ 5 Ma. Ramenée à l'extension actuelle mesurée par GPS, cette extension totale correspond à une vitesse d'extension quasi constante depuis 5 Ma. Ainsi, notre modèle suggère que les contraintes extensives dans la région ont peu varié depuis l'époque précédant l'incursion de la faille Nord-Anatolienne en mer de Marmara, alors que les contraintes extensives n'étaient pas encore dissipées le long de la faille comme c'est le cas aujourd'hui. La région représenterait en quelque sorte la sommation d'un système transformant dextre sur un système extensif préexistant.

L'étude de la géométrie du modèle montre de plus, que la répartition de l'extension avant l'incursion de la faille a pu influer sur la géométrie actuelle du réseau. En effet, entre les blocs Ouest et Est, des différences de morphologies de la croûte pourraient s'expliquer par des mécanismes variables de répartitions des contraintes extensives qui auraient provoqué un amincissement plus localisé de la croûte à l'Est. Lors de l'arrivée de la faille Nord-Anatolienne à l'aplomb de la mer de Marmara, cette fragilisation aurait pu diriger la propagation de la faille en la forçant à se localiser dans la croûte plus cassante à la bordure de l'amincissement. A l'Ouest, où aucune trace de grand détachement n'a été observée, l'accommodation de l'extension a pu se faire de manière plus diffuse aboutissant à un amincissement de la croûte plus limité mais plus étalé. Dans cette zone, la faille de Marmara s'est propagée au centre de l'amincissement. Ainsi, nous suggérons que la géométrie de la croûte, liée à l'histoire tectonique de la région, a pu être déterminante lors de la construction et de la segmentation du réseau de la faille de Marmara.

Dans les deuxième et troisième parties de ce manuscrit, nous avons détaillé les études menées avant, pendant et après la campagne MARSITE en mer de Marmara autour de la récupération de carottes dans le Haut Ouest pour l'étude de niveaux de sédiments liés aux réflecteurs observés en sismique et utilisés pour la construction de modèles d'âges. Le but final était de pouvoir confirmer ou infirmer les modèles d'âges proposés par le passé et sur lesquels reposent les estimations de vitesse de la faille Nord-Anatolienne à l'échelle de 500 ka [*Sorlien et al.*, 2012, *Grall et al.*, 2013].

Les sites choisis devaient tous permettre de traverser l'un des réflecteurs intégrés dans les modèles d'âges, dans la longueur d'un carottier à piston. La vérification de la correspondance entre les réflecteurs sismiques et les sédiments extraits lors des carottages s'est faite grâce à la comparaison de synthétiques sismiques, basés sur les variations de densité des sédiments, et des enveloppes sismiques des profils à 3.5 kHz « CHIRP » ;

Les carottes extraites du site Sud et censées contenir des enregistrements échelonnés jusqu'à environ 450 ka n'ont pas donné les résultats escomptés. La longueur des tubes n'a pas permis de percer suffisamment loin sous des dépôts de glissement de terrain. Cependant, l'inclinaison limitée de certaines portions laisse espérer la possibilité de reconstituer une partie de la chronologie des sédiments.

Au contraire, la carotte MRS-CS-22, extraite au Nord de la faille Nord-Anatolienne et contenant les dépôts correspondant au réflecteur « rouge » H1 à l'âge estimé à environ 105 ka, a présenté une colonne de sédiments en place ou très légèrement incliné avec cependant quelques niveaux probablement érodés. Entre le sommet et la base de la carotte MRS-CS-22, aux fossiles marins, différents faciès lacustres se succèdent qu'on peut attribuer à des variations environnementales, elles-mêmes liées aux variations de la connexion entre la mer de Marmara et la mer Méditerranée au niveau du Détroit des Dardanelles depuis le dernier interglaciaire. Pour construire un modèle d'âge, nous nous sommes donc appuyés sur la détermination des conditions paléo-environnementales afin de corréler les stades isotopiques marins (MIS) avec les variations observées de faciès. Ce modèle a été complété par d'autres méthodes de datation : la téphrochronologie et le paléomagnétisme. L'association de ces méthodes a ainsi permis de dater précisément le réflecteur H1 et d'en comprendre la signification. Le modèle finalement obtenu n'a pas confirmé l'âge de 105 ka proposé pour le réflecteur « rouge » H1 puisqu'il indique un âge, plus jeune, de 70 ka.

Ainsi, le réflecteur « rouge » H1 correspondrait à la fin du stade 5, quand le niveau de la mer a brusquement chuté à une époque qui a pu marquer la déconnection totale entre les deux mers. D'un point de vue géophysique, le réflecteur est généré par une interface entre un faciès laminé léger riche en matière organique et un facies sus-jacent pratiquement stérile. Au niveau de l'interface, on trouve un niveau de sable érosif classé qui pourrait être le résultat de déstabilisations de pentes sur les plateaux quand ceux-ci se sont trouvés immergés. Ce même événement a été enregistré dans les carottes extraites dans les bassins Est ce qui confirme un événement global à l'échelle de la mer de Marmara.

L'incompatibilité n'est pas totale entre les modèles d'âges construits par extrapolation sur observation des données sismiques et l'âge indiqué par notre étude pour le réflecteur « rouge » H1. En effet, une des hypothèses essentielles des modèles était le rapport entre les variations climatiques et les réflecteurs majeurs, ce qui expliquait leur répétitivité au fil des cycles. De ce point de vue-là, notre étude apporte une confirmation : le réflecteur « rouge » H1 correspond bien à une variation majeure d'environnement. Cependant, contrairement à ce qui avait été supposé, cette variation ne correspond pas à la baisse du niveau de la mer de la fin du stade MIS 5e mais à la baisse de la fin du stade MIS 5a.

La propagation d'un nouveau taux de sédimentation moyen sur un cycle se basant sur la profondeur des dépôts de la base de la carotte rapportée à une zone non érodée pourrait permettre de reconstruire les modèles d'âges. Cette nouvelle estimation reviendrait à rajeunir les dépôts sous-jacents à H1 d'environ un tiers des âges proposés jusqu'à maintenant. Finalement, en suivant la méthode de *Grall et al.* [2013], on obtiendrait une vitesse estimée de la faille d'environ 23 à 30 mm/a. Or, cela correspond à un mouvement sur la faille de Marmara égal, voire supérieur, au mouvement des plaques [e.g. *Reilinger et al.*, 2006 ; 2010] alors même qu'il est actuellement admis qu'une partie du mouvement est accommodée sur les branches méridionales et sur des failles secondaires [*Flerit et al.*, 2003 ; 2004; *Reilinger et al.*, 2006 ; *Hergert & Heidbach*, 2010 ; *Hergert et al.*, 2011].

C'est pourquoi nous suggérons que la répétitivité des séquences sédimentaires est plus fiable que la seule estimation d'un taux moyen de sédimentation et que, si la corrélation des réflecteurs avec les stades isotopiques est probablement à revoir dans le sens d'un rajeunissement, les modèles existants ne sont pas non plus invalidés à ce stade.

Deux points majeurs pourraient permettre de progresser sur l'interprétation des réflecteurs plus profonds sans accéder directement aux dépôts. Le premier est l'origine du réflecteur H1' qui constitue la base de la séquence d'onlap sous le réflecteur H1, dans les bassins. L'apparence et la polarité semblable des deux réflecteurs suggèrent une répétitivité de l'épisode menant à H1, mais il est difficile de concilier ceci avec les variations du niveau de la mer depuis le stade MIS 5e. Le deuxième point est celui de l'origine des réflecteurs aux caractéristiques géophysiques différentes. En supposant que les mêmes variations environnementales lors des précédents cycles ont également conduit à la déposition de sapropels légers au début des périodes de baisse du niveau marin, d'autres réflecteurs négatifs forts devraient être observés. Des réflecteurs à polarité variable, comme le « bleu » H2, ou positive, comme le « violet » H4 ne peuvent donc pas avoir la même origine. La corrélation de ces réflecteurs avec les courbes paléo-climatiques ne peut donc se faire en associant tous les réflecteurs principaux à des périodes climatiquement semblables.

L'étude des carottes extraites dans le Sud du Haut Ouest pourrait être décisive à ce sujet. D'après les données sismiques, la carotte MRS-CS-26 contient le réflecteur « violet » H4. L'identification précise de la position de l'interface à l'origine du réflecteur pourrait permettre la caractérisation des variations environnementales, sans forcément mener à une datation. Associée à la nouvelle évaluation du taux de sédimentation moyen sur un cycle, cette information pourrait permettre de repositionner le réflecteur dans le modèle d'âge. De plus, le réflecteur « violet » H4 étant semblable au réflecteur « marron » H6 et les deux réflecteurs étant respectivement associés aux réflecteurs « jaune » H3 et « vert » H5, c'est sur le modèle entier que ce travail pourrait permettre d'avancer.

Pour terminer, bien que la finalité de notre étude ait été tournée vers la caractérisation du système de faille en mer de Marmara, les techniques employées ont permis de compléter les connaissances concernant les évolutions paléo-environnementales et paléo-océanographiques de la région. Si la reconnexion et la re-salinisation de la mer de Marmara ont plusieurs fois été décrites [*McHugh et al.*, 2008 ; *Çağatay et al.*, 2009 ; *Aloisi et al.*, 2015], nous avons pu identifier, pour la première fois, la séquence quasi complète de la désalinisation et de la déconnexion de la mer de Marmara. Nous avons également pu montrer qu'une stratification forte s'est installée pendant les stades MIS 5d à MIS 5a. Or, c'est cette période de forte stratification qui a mené au dépôt d'un sapropel de plusieurs mètres, lui-même à l'origine du réflecteur H1. Peut-être un travail sur la modélisation des interactions entre les masses d'eau en fonction de la géométrie des bassins, de l'ouverture des détroits et de la composition des flux entrants pourrait-il permettre de caractériser les conditions menant à une stratification. Ceci pourrait à la fois faciliter l'interprétation des réflecteurs, en permettant de poser des hypothèses sur les épisodes passés de dépôts de sapropels, et donner des informations sur l'état des connections aux périodes où ce type de dépôts sont directement observés dans des carottes.

Références :

Aloisi, G., Soulet, G., Henry, P., Wallmann, K., Sauvestre, R., Vallet-Coulomb, C., … Bard, E. (2015). Freshening of the Marmara Sea prior to its post-glacial reconnection to the Mediterranean Sea. *Earth and Planetary Science Letters, 413*, 176–185. http://doi.org/10.1016/j.epsl.2014.12.052

Çağatay, M. N., Eriş, K. K., Ryan, W. B. F., Sancar, Ü., Polonia, A., Akçer, S., … Bard, E. (2009). Late Pleistocene–Holocene evolution of the northern shelf of the Sea of Marmara. *Marine Geology*, *265*(3–4), 87–100. http://doi.org/10.1016/j.margeo.2009.06.011

Flerit, F., Armijo, R., King, G. C. P., Meyer, B., & Barka, A. (2003). Slip partitioning in the Sea of Marmara pull-apart determined from GPS velocity vectors. *Geophysical Journal International*, *154*(1), 1–7. http://doi.org/10.1046/j.1365-246X.2003.01899.x

Flerit, F., Armijo, R., King, G., & Meyer, B. (2004). The mechanical interaction between the propagating North Anatolian Fault and the back-arc extension in the Aegean. *Earth and Planetary Science Letters*, *224*(3–4), 347–362. http://doi.org/10.1016/j.epsl.2004.05.028

Gökaşan, E., Ustaömer, T., Gazioglu, C., Yucel, Z. Y., Öztürk, K., Tur, H., … Tok, B. (2003). Morpho-tectonic evolution of the Marmara Sea inferred from multi-beam bathymetric and seismic data. *Geo-Marine Letters*, *23*(1), 19–33. http://doi.org/10.1007/s00367-003-0120-7

Grall, C., Henry, P., Thomas, Y., Westbrook, G. ., Çağatay, M. N., Marsset, B., … Géli, L. (2013). Slip rate estimation along the western segment of the Main Marmara 1 Fault over the last 405-490 ka by correlating Mass Transport Deposits. *Tectonics*, *32*(6), 1587–1601. http://doi.org/10.1002/2012TC003255

Hergert, T., & Heidbach, O. (2010). Slip-rate variability and distributed deformation in the Marmara Sea fault system. *Nature Geoscience*, *3*(2), 132–135. http://doi.org/10.1038/ngeo739

Hergert, T., Heidbach, O., Bécel, A., & Laigle, M. (2011). Geomechanical model of the Marmara Sea region-I. 3-D contemporary kinematics. *Geophysical Journal International*, *185*(3), 1073–1089. http://doi.org/10.1111/j.1365-246X.2011.04991.x

Le Pichon, X., Chamot-Rooke, N., Rangin, C., & Şengör, A. M. C. (2003). The North Anatolian fault in the Sea of Marmara. *Journal of Geophysical Research*, *108*(B4), 1–20. http://doi.org/10.1029/2002JB001862

McHugh, C. M. G., Gurung, D., Giosan, L., Ryan, W. B. F., Mart, Y., Sancar, U., … Çağatay, M. N. (2008). The last reconnection of the Marmara Sea (Turkey) to the World Ocean: A paleoceanographic and paleoclimatic perspective. *Marine Geology*, *255*(1–2), 64–82. http://doi.org/10.1016/j.margeo.2008.07.005

Rangin, C., Le Pichon, X., Demirbag, E., & Imren, C. (2004). Strain localization in the Sea of Marmara: Propagation of the North Anatolian Fault in a now inactive pull-apart. *Tectonics*, *23*(2), n/a-n/a. http://doi.org/10.1029/2002TC001437

Reilinger, R., McClusky, S., Vernant, P., Lawrence, S., Ergintav, S., Cakmak, R., … Karam, G. (2006). GPS constraints on continental deformation in the Africa-Arabia-Eurasia continental collision zone and implications for the dynamics of plate interactions. *Journal of Geophysical Research*, *111*(B5), B05411. http://doi.org/10.1029/2005JB004051

Reilinger, R., McClusky, S., Paradissis, D., Ergintav, S., & Vernant, P. (2010). Geodetic constraints on the tectonic evolution of the Aegean region and strain accumulation along the Hellenic subduction zone. *Tectonophysics*, *488*(1–4), 22–30. http://doi.org/10.1016/j.tecto.2009.05.027

Sorlien, C. C., Akhun, S. D., Seeber, L., Steckler, M. S., Shillington, D. J., Kurt, H., … Diebold, J. B. (2012). Uniform basin growth over the last 500ka, North Anatolian Fault, Marmara Sea, Turkey. *Tectonophysics*, *518–521*, 1–16. http://doi.org/10.1016/j.tecto.2011.10.006

ANNEXE A – Code MATLAB pour la correction du champ de gravité et la modélisation de la croûte par inversion du résiduel

Cette première annexe présente les fonctions développées pour le CHAPITRE 1. Seules les fonctions les plus intéressantes sont reproduites ici. Les fonctions techniques telles que celle permettant de construire les matrices de gravité à partir des fichiers de données initiaux sont disponibles sur demande à kende@cerege.fr.

Ci-dessous, un exemple de script appelant la fonction principale :

```
% Extract topography/bathymetry from file
[X, Y, Z] = PreProcessData('DATA/topo.xyz', 0, 0);
% Extract observed gravity from file with same X and Y
[G] = PreProcessDataXY('DATA/G.dat', X, Y);
% Extract topography after a 20km window gaussian filtering from
file
% with same X and Y
[Z20] = PreProcessDataXY('DATA/marsmootop20.xyz', X, Y);
% Extract depth of first and second layer of sediment floor from
% file with same X and Y. The function modifies Bayrakci et al.
% (2013) data to account for the Black Sea and the Thrace Bassin
% sediments.
[Zsed1, Zsed2] = LoadSedWithBlackSeaAndThrace(X,Y);

% cell size
dy = -0.6532;
dx = 0.6611;

memo = 30000; % reference moho depth (m)
rho1 = 2230;  % sediment 1 density
rho2 = 2590;  % sediment 2 density

cov = 25; % covariance for the gravity inversion

[G, Gb20, grav, grav1, grav2, grav3, grav4, moho, newres, X, Y,
Zsed1, Zsed2, UCLC] = ModelCrust(X, Y, G, Z, Z20, Zsed1, Zsed2, dx,
dy, rho1, rho2, cov, memo);
```

```
function [G, Gb20, grav, grav1, grav2, grav3, grav4, moho,
newres, X, Y, Zsed1, Zsed2, UCLC] = ModelCrust(X, Y, G, Z,
Z20, Zsed1, Zsed2, dx, dy, rho1, rho2, cov, memo)

[m,n] = size(Z);

% BOUGUER correction coefficient
b = -0.1118; % mgal/m
bsed = -6.67384e-8 * 2 * pi * rho2 * 100;

% Calculation of the Bouguer correction on positive topography
Gb20 = zeros(m,n);
for i = 1:m
    for j=1:n
        if Z20(i,j)>0 && Zsed2(i,j) <=0
            Gb20(i,j) = - b*Z20(i,j);
        elseif Z20(i,j)>0 && Zsed2(i,j) > 0
            Gb20(i,j) = - bsed*Z20(i,j);
        else
            Gb20(i,j)= 0;
        end
    end
end

% Setting Z=0 for positive topography
Zshave = zeros(m,n);
for i = 1:m
    for j = 1:n
        if Z(i,j) > 0
            Zshave(i,j) = 0;
        else
            Zshave(i,j) = Z(i,j);
        end
    end
end

% density variation at interfaces
drho1 = rho1 - 1030;
drho2 = rho2 - rho1;
drho3 = 2750 - rho2;
drho4 = 3330 - 2750;

% Calculation of the gravity field generated by density
% variations at each interface
disp('topo')
[grav1] = gravpred2(Zshave, m, n,dy,dx,drho1);
 disp('Zsed1')
[grav2] = gravpred2(Zsed1, m, n,dy,dx,drho2);
 disp('Zsed2')
[grav3] = gravpred2(Zsed2, m, n,dy,dx,drho3);
```

```
% Anomaly due to the water, the first and the second layer of
% sediment:
grav = grav1 + grav2 + grav3;

% Residual anomally after correcting for Bouguer anomaly and
% known density interfaces
res=G-Gb20-grav;

% Anomally inversion and calculation of moho depth
disp('MOHO')
[moho,newres]=mohopred(res, m, n,dy,dx,drho4, memo, cov);

% new density values at interfaces when considering upper and
% lower crust
drhoSed2UC = 2650-rho2;
drhoUCLC = 2950 - 2650;
drhoLCM = 3330 - 2950;

% new gravity anomaly from the density variation at the
% sed2/UC interface
[grav3] = gravpred2(Zsed2, m, n,dy,dx,drhoSed2UC);

% Iterative calculation of the LC/UC interface depth :
% - Calculation of LC/UC depth from whole crust thickness
% - Calculation of gravity field generated from the density
% variation at the UC/LC interface
% - Calculation of new moho depth from the new gravity final
% anomaly
for it = 1:10
    moho = moho - memo;
    UCLC = Zsed2 + (moho - Zsed2) .* (2/3);

    disp('UCLC')
    [grav4] = gravpred2(UCLC, m, n,dy,dx,drhoUCLC);

    % Anomaly due to the water, the first, the second layer of
      sediment end
    % the Lower Crust/ Upper Crust boundary:
    grav = grav1 + grav2 + grav3 + grav4;

    % Residual anomally after correcting for Bouguer anomaly
      and 'grav'
    res = G - Gb20 - grav;

    disp('MOHO')
    % Anomally inversion and calculation of moho depth
    [moho,newres] = mohopred(res, m, n,dy,dx, drhoLCM, memo,
    cov);
end
end
```

This function was modified from a first version written by Gaye Bayrakci.

```
function [predgrav] = gravpred2(bathy, m, n,dy,dx,drho)
% Application of the Parker method [Parker, 1972] for the
% calculation of the gravity anomaly generated by the density
% variation 'drho' at a depth 'bathy' in a grid of size 'm'
% and 'n' representing cells of size 'dy' and 'dx'.

bathy=abs(bathy);

B=zeros(size(bathy));

me=(min(min(bathy))+max(max(bathy)))/2;

bathy=me-bathy;
G=6.673e-11;%m^3/kg/s^2
mm=ceil(m/2+1);
nn=ceil(n/2+1);
kx=zeros(size(bathy));
ky=zeros(size(bathy));
k=zeros(size(bathy));

%Beginning forward transformation.
if n==1
    for i=1:mm
    k(i,1)=2*pi*(i-1)/(dy*m);
    end
    if(mod(m,2)~=0)
    k(mm:end,1)=k(mm-1:-1:2,1);
    else
    k(mm+1:end,1)=k(mm-1:-1:2,1);
    end
    k=.001*k;
else
    %making kx and ky matrices.
    %making the x vector matrix
    for i=1:nn
    kx(1,i)=2*pi*(i-1)/(dx*n);
    end
    if(mod(n,2)~=0)
    kx(1,nn:end)=kx(1,nn-1:-1:2);
    else
    kx(1,nn+1:end)=kx(1,nn-1:-1:2);
    end
    for i=1:m
    kx(i,:)=kx(1,:);
    end
    %kx=kx*.001;
    %making the yvector matrix
```

```
    %making the y
    for i=1:mm
    ky(i,1)=2*pi*(i-1)/(dy*m);
    end
    if(mod(m,2)~=0)
    ky(mm:end,1)=ky(mm-1:-1:2,1);
    else
    ky(mm+1:end,1)=ky(mm-1:-1:2,1);
    end
    for i=1:n
    ky(:,i)=ky(:,1);
    end
    %ky=ky*.001;
    k=.001*sqrt(kx.^2.+ky.^2);
end
% Making phi Y and B
BB=zeros(size(B));
% disp('NEW')
i=1;
a0 = sum(sum(abs((k).^(i-1).*fft2(bathy.^i)/factorial(i))));
a = a0;

% increasing number of Fourier term until variation is
% insignificant
while a > a0/1e6
 DB=(k).^(i-1).*fft2(bathy.^i)/factorial(i);
 BB=BB+DB;
 a=sum(sum(abs(DB)));
 b=sum(sum(abs(BB)));
 delg1k=2*pi*G*drho*BB.*exp(-(k*me));
 c=sum(sum(abs(delg1k)));
 s=sprintf('%g   %g   %g',a, b, c);
 %disp(s);
 i=i+1;
end

% Calculating the gravity components

gravk=delg1k;

% Bringing it back to the land of space domain
predgrav=1e5*real(ifft2(gravk));
predgrav=reshape(removemean(reshape(predgrav,1,m*n)),m,n);
```

```
function [moho,newres] = mohopred(res, m, n,dy,dx,drho, me,
covar)
% Application of the Parker method [Parker, 1972] and of
% Tarantola [2005] solution for linear least square problem
% for the calculation of the moho depth from inversion of a
% residual gravity anomaly field.
% 'res' is the residual field, 'drho', the density contrast at
% the moho interface and 'me' is the mean estimated moho
% depth.

% t=6000;
BB=zeros(size(res));

G=6.673e-11;%m^3/kg/s^2


mm=ceil(m/2+1);
nn=ceil(n/2+1);
kx=zeros(size(res));
ky=zeros(size(res));
k=zeros(size(res));
% Beginning forward transformation.
if n==1
    for i=1:mm
    k(i,1)=2*pi*(i-1)/(dy*m);
    end
    if(mod(m,2)~=0)
    k(mm:end,1)=k(mm-1:-1:2,1);
    else
    k(mm+1:end,1)=k(mm-1:-1:2,1);
    end
    k=.001*k;
else
    % making kx and ky matrices.
    % making the x vector matrix
    for i=1:nn
    kx(1,i)=2*pi*(i-1)/(dx*n);
    end
    if(mod(n,2)~=0)
    kx(1,nn:end)=kx(1,nn-1:-1:2);
    else
    kx(1,nn+1:end)=kx(1,nn-1:-1:2);
    end
    for i=1:m
    kx(i,:)=kx(1,:);
    end

    % making the y vector matrix
    for i=1:mm
    ky(i,1)=2*pi*(i-1)/(dy*m);
    end
```

```
    if(mod(m,2)~=0)
    ky(mm:end,1)=ky(mm-1:-1:2,1);
    else
    ky(mm+1:end,1)=ky(mm-1:-1:2,1);
    end
    for i=1:n
    ky(:,i)=ky(:,1);
    end

    k=.001*sqrt(kx.^2.+ky.^2);
end


% calculating first order moho from residual
gg=2*pi*G*drho;
resk=1e-5*fft2(res);
mohok=(exp(-(k*me)).*(exp(-2*k*me)+1/covar).^(-1)).*resk;
mohok=mohok/gg;
moho=real(ifft2(mohok));

i=1;
a0 = sum(sum(abs((k).^(i-1).*fft2(moho.^i)/factorial(i))));
a = a0;

gravk=zeros(size(k));

while a > a0/1e6
 DB=(k).^(i-1).*fft2(moho.^i)/factorial(i);
 BB=BB+DB;
 a=sum(sum(abs(DB)));
 gravk=gg*BB.*exp(-(k*me));
 i=i+1;
end

% Bringing it back to the land of space domain
grav=1e5*real(ifft2(gravk));
newres=res-grav;
```

ANNEXE B – Code MATLAB pour la génération et la représentation des synthétiques sismiques

La fonction principale prend en entrée :

- le fichier SEGY traité du profil « CHIRP » 3.5 kHz le plus proche
- la longueur de la carotte
- les données de densité de la carotte en fonction de la profondeur dans la carotte
- la profondeur en temps du haut et du bas de la carotte
- éventuellement, la vitesse du son dans le sédiment pour la conversion profondeur-temps (auquel cas, la profondeur en temps du bas de la carotte est recalculée).

Ci-après, un exemple des représentations générées avec les données de la carotte MRS-CS-22 et le SEGY MRS-SBP-52 suivi des codes MATLABL des fonctions.

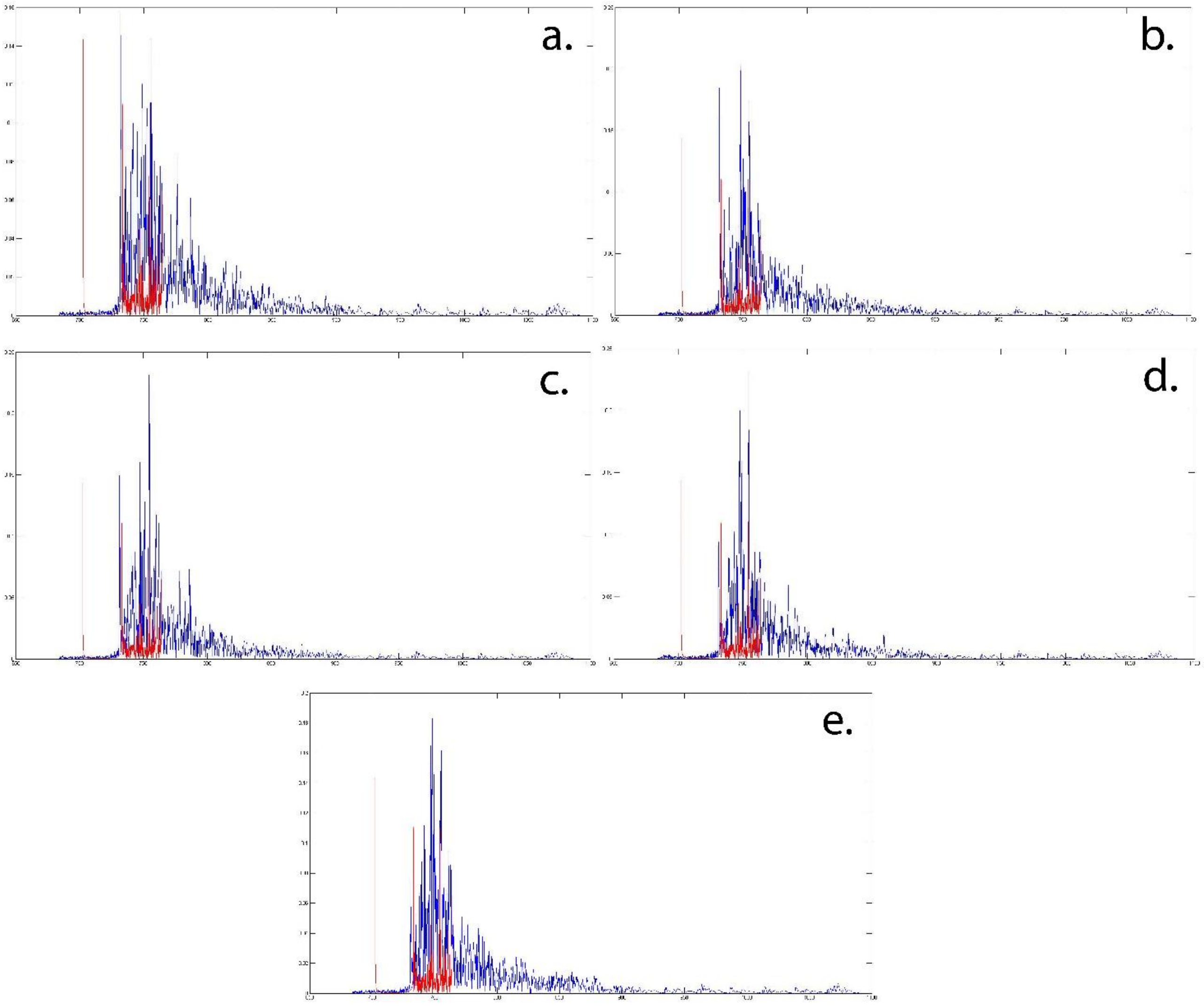

Figure 1. Représentation de l'enveloppe du synthétique sismique de la carotte MRS-CS-22 superposée aux 5 traces sismiques « CHIRP » 3.5 kHz les plus proches.

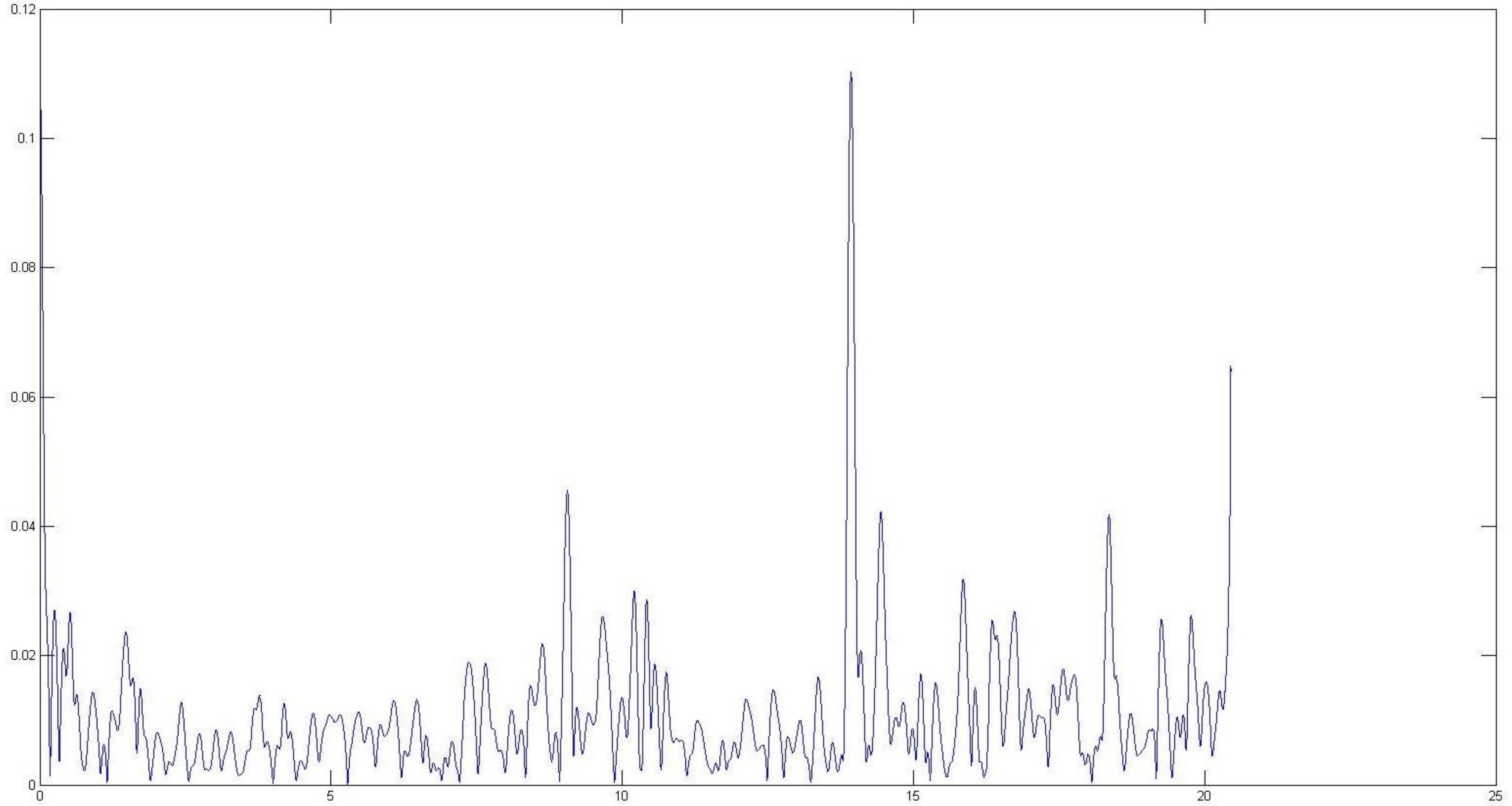

Figure 2. Représentation du synthétique sismique de la carotte MRS-CS-22 en fonction de la profondeur dans la carotte. Cette figure permet notamment de d'identifier l'origine d'un pic du point de vue stratigraphique par comparaison avec les descriptions.

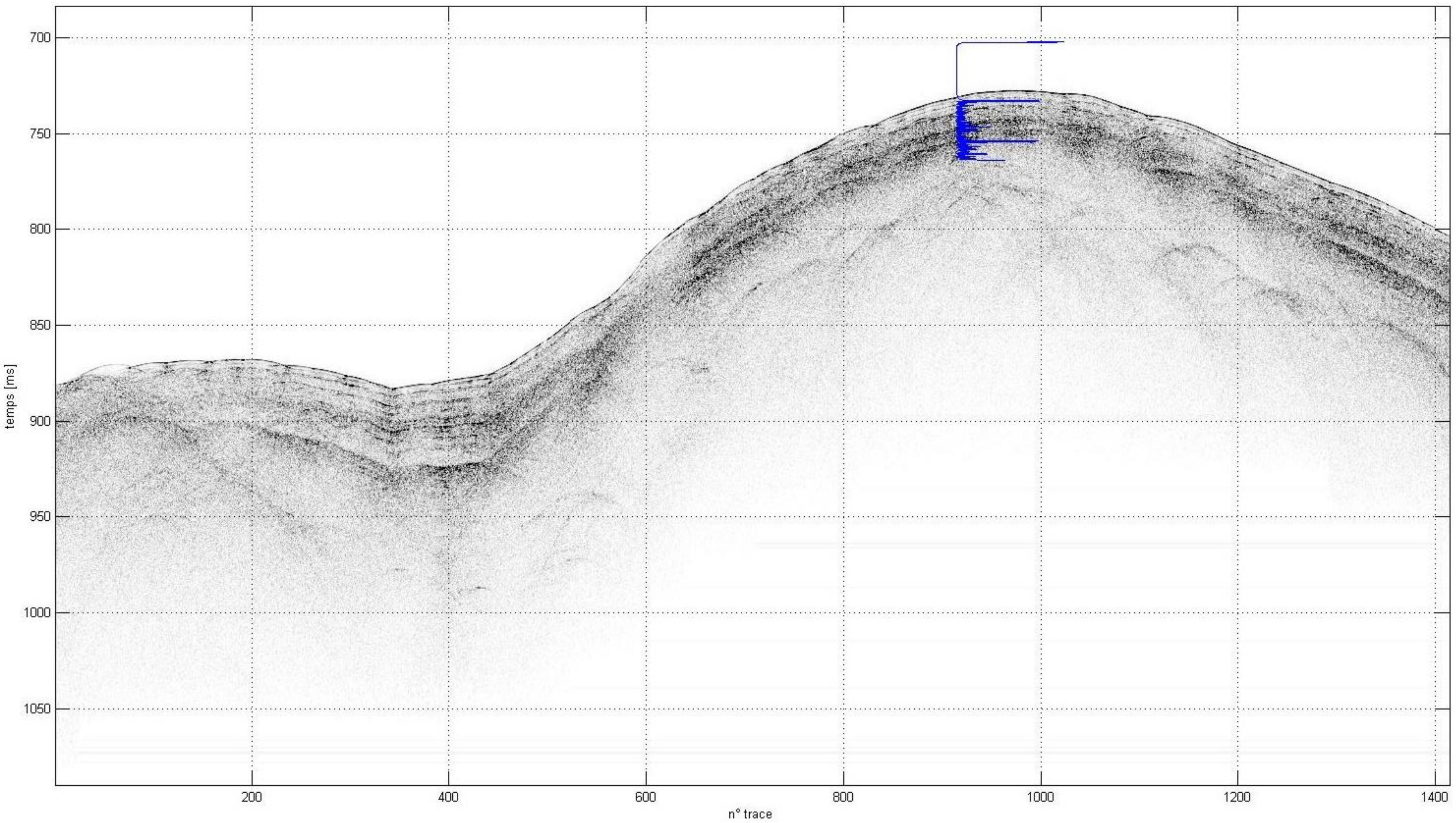

Figure 3. Profil sismique « CHIRP » 3.5 kHz et synthétique de la carotte MRS-CS-22 placé à la profondeur supposée et au niveau du Shot Point le plus proche. Des zooms de cette figure sont présentés dans le CHAPITRE II.

```
function [Synth, TimeSynth, DataShot, TimeShot] =
ShowSyntheticOnCHIRP( fileMSCL, fileSEGY, Di, Df, x, y, V,L)
% Lecture d'un fichier SEGY CHIRP, calcul du synthétique à
% partir des données de densité le long d'une carotte,
% représentation du résultat le long de la carotte et représentation
% comparée au données
% CHIRP.


% FileMSCL : fichier nettoyé
%   1ère colonne : profondeur en m
%   2ème colonne : densité
%   3ème colonne : Vp (optionel et non utilisé dans cette
% version)
% FileSEGY : fichier SEGY traité (process.SEG) SANS calcul
%            d'enveloppe
% Di : profondeur en s du haut de la carotte
% Df : profondeur en s du bas de la carotte
%      Si V ~= 0, Df est recalculé en fonction de Di et V
% x : longitude en degrés décimaux
% y : latitude en degrés décimaux
% V : Vitesse des ondes pour le calcul depth -> time en m/s
%     Si V=0, V est recalculé en fonction de Di et Df
% L : Longueur de la carotte.


%Calcul du synthétic
[Synth, TimeSynth, V]=Synthetic(fileMSCL,Di,Df,V,L);
disp(['Wave speed for depth->Time conversion = ', num2str(V), '
m/s.'])

%Extraction des données CHIRP
[~,b,~,c,Data] = sbp_litsegy(fileSEGY);

% Extraction de trois vecteurs contenant la latitude, la
% longitude et la profondeur en temps des données CHIRP.
Xcoor = mean([c.XSourceCoordinate; c.XReceiverCoordinate]);
Ycoor = mean([c.YSourceCoordinate; c.YReceiverCoordinate]);
TimeShot =
c.LagTimeShotRecording(1):b.ReelSampleInterval/1000:c.LagTimeShotRec
ording(1) + b.ReelSampleInterval/1000 *(b.ReelSamplesPerTrace-1);

% Extraction des données CHIRP (amplitude)
NbPings = size(c.TraceSequenceLine,2);
for itr = 1:NbPings
    Data(:,itr) = abs(hilbert(Data(:,itr)));
end
```

```
% Recherche du Shot Point le plus proche des coordonnées de la
carotte
I = FindClosestTrace(x,y,Xcoor,Ycoor);

% Affichage de 5 plots : le synthétique superposé aux 5 traces les
plus
% proches.
for i = -2:2
    figure(i+4)
    plot(TimeShot,Data(:,I+i));
    hold on
    plot(TimeSynth,Synth,'r')
end

% Extraction de la trace au shot point le plus proche (pour output)
DataShot = Data(:,I);

% Affichage du synthétique superposé au profil CHIRP
M = 5; m = mean(Synth); Synth = Synth ./ m .* M;
X = 1:NbPings;
figure(7); imagesc(X,TimeShot,Data); grid on; box on;
xlabel('n° trace'); ylabel('temps [ms]');
colormap(flipud(colormap('gray')));
palette = [0.002 0.10];
caxis(palette); colorbar;
hold on
plot(Synth + I,TimeSynth)
end
```

```matlab
function I = FindClosestTrace(x,y,X,Y)
% Recherche du Shot Point le plus proche du point de carottage
X = convert_dms2ddec(X);
Y = convert_dms2ddec(Y);
min = 99999999999999;
I = 0;
for i = 1:length(X)
    d = sqrt((X(i)-x)*(X(i)-x)+(Y(i)-y)-(Y(i)-y));
    if d < min
        min = d;
        I = i;
    end
end
end
```

```matlab
function ddec = convert_dms2ddec(dms)
% Conversion deg, min, sec en degrés décimaux
signe   = sign(dms);
dms     = abs(dms);
d       = floor(dms/1e6);
m       = floor((dms - d*1e6) /1e4);
s       = (dms - d*1e6 - m*1e4) /1e2;
ddec    = signe .*(d + m/60 + s/3600);
end
```

```
function [synth, timenew,V]=Synthetic(file,Di,Df,V, L)

% lecture du fichier.txt de données de densité le long de la carotte
M = textread(file);
depth = M(:,1);
density = M(:,2);

% Calcul de V si V=0. Sinon, recalcul de Df à partir de V et Di
if V == 0
    V = M(end,1)/(Df-Di)*2;
else
    Df = Di + 2*L/V;
end

% Construction de l'échelle de temps et prolongement de la densité
% avec d = 1 dans l'eau
DTWT=Df-Di;
temp = linspace(0,DTWT,length(density));
time = transpose([temp-temp(end),temp(2:end)]);
density = [ones(length(density)-1,1);density];

% Calcul de l'ondelette de Ricker
[R,~] = Ricker(3500,150,0.000005);

% Interpolation de la densité pour obtenir un signal de même
% fréquence que le signal de l'ondelette de Ricker
timenew = (time(1):0.000005:time(end));
time(isnan(density))=[]; %getting rid of NaNs
density(isnan(density))=[]; %getting rid of NaNs
densitynew = interp1(time,density,timenew,'linear','extrap');

% "padding" de la densité
densitynew = [densitynew ones(1,500)*densitynew(1,end)];

% Calcul du synthétique à partir de la densité seule
AI = densitynew .* 1500;
RefCoef = ones(size(AI));
for i = 2:length(AI)
    RefCoef(i) = (AI(i)-AI(i-1))/(AI(i)+AI(i-1));
end
synth=conv(RefCoef,transpose(R),'same');
synth = synth(1,1:end-500);

% Calcul de l'enveloppe de l'amplitude
synth = abs(hilbert(synth()));

% Ajout de la profondeur en temps du haut de la carotte
timenew = timenew + Di;
```

```
% Représentation du signal en fonction de la profondeur dans la
% carotte
figure(1)
i = abs(length(timenew)/2)+1;
z = linspace(depth(1),depth(end),length(timenew)-i+1);
plot(z,synth(i:end));

% Conversion du temps en ms
timenew = timenew.*1000;

end
```

```
% Fonction écrite par Dylan Mikesell et disponible sur github.com
% Seule l’en-tête est reproduite ici.

function [rw,t] = Ricker(f,n,dt,t0,t1)
%RICKER creates a causal ricker wavelet signal
%
%   RICKER creates and plots a default causal ricker wavelet with:
%
%       peak frequency   = 20 Hz
%       sampling time    = 0.001 seconds
%       number of points = 100;
%       peak location    = 1/F = 1/20Hz
%
%   RW = RICKER(...) returns the default wavelet in RW.
%
%   [RW,T] = RICKER(...) returns the time vector in T.
%
%   Specifying parameters of peak frequency (F, Hz), number of 
points (N),
%   and sampling time (DT) are specified by the syntax:
%
%       [RW,T] = RICKER(F)
%       [RW,T] = RICKER(F,N)
%       [RW,T] = RICKER(F,N,DT)
%
%   [RW,T] = RICKER(F,N,DT,T0) creates a ricker wavelet with peak 
centered
%   at T0.
%
%   [RW,T] = RICKER(F,N,DT,T0,T1) creates a 2 dimensional symmetric
%   ricker wavelet with sift in 1st dimension of T0 and second 
dimension of
%   T1.
%
%   Example 1:
%       ricker % plots a 20 Hz Ricker Wavelet over 0.1 seconds
%
%   Example 2:
%    % create a ricker wavelet with 40 Hz, 200 points, and 0.02 s 
between
%    % samples
%    [rw,t] = ricker(40,200,0.002);
%    plot(t,rw), xlabel('Time'), ylabel('Amplitude')

% Define inputs if needed
```

```
% Fonction écrite par Anne Pacault pour l'IFREMER
% Seule l’en-tête est reproduite ici.

function [TextHeader,BinaryHeader,ExtendedHeader,TraceHeader,Data] =
sbp_litsegy(fname)
%*******************************************************************
*******
% function [TextHeader,BinaryHeader,ExtendedHeader,TraceHeader,Data]
= sbp_litsegy(fname)
%-------------------------------------------------------------------
-------
% programme pour l'exploitation des données des SDS de l'ifremer
%-------------------------------------------------------------------
-------
% Fonction qui permet de lire un fichier SEGY.
% Hypothèse : toutes les traces ont le même nombre d'échantillons.
%
% INPUT :
% - fname : nom du fichier à lire
%
% OUTPUT :
% - TextHeader: 3200 bytes (40 lignes de 80 caractères, en ASCII ou
EBCDIC)
% - BinaryHeader: 400 bytes
% - ExtendedHeader : n*3200 bytes (option)
% - TraceHeader : 240 bytes pour chaque trace
% - Data : données au format IBM, float32, int8, int16 ou int32
%*******************************************************************
*******
% ifremer - pacault - 17/01/2012
%*******************************************************************
*******
```

ANNEXE C- Propagation of a strike-slip plate boundary within an extensional environment: the westward propagation of the North Anatolian Fault

This annex has been published as:

Pichon, X., Şengör, A. M. C., **Kende, J**., İmren, C., Henry, P., Grall, C., & Karabulut, H. (2015). Propagation of a strike-slip plate boundary within an extensional environment : the westward propagation of the North Anatolian Fault . *Canadian Journal of Earth Sciences, 53*. http://doi.org/10.1139/cjes-2015-012

NRC Research Press

ARTICLE

Propagation of a strike-slip plate boundary within an extensional environment: the westward propagation of the North Anatolian Fault[1]

Xavier Le Pichon, A.M. Celâl Şengör, Julia Kende, Caner İmren, Pierre Henry, Céline Grall, and Hayrullah Karabulut

Abstract: We document the establishment of the Aegea–Anatolia/Eurasia plate boundary in Pliocene–Pleistocene time. Before 2 Ma, no localized plate boundary existed north of the Aegean portion of the Anatolia plate and the shear produced by the motion of Anatolia–Aegea with respect to Eurasia was distributed over the whole width of the Aegean – West Anatolian western portion. In 4.5 Ma, a shear zone comparable to the Gulf of Corinth was formed in the present Sea of Marmara. The initial extensional basins were cut by the strike-slip Main Marmara Fault system after 2.5 Ma. Shortly after, the plate boundary migrated west of the Sea of Marmara along the northern border of Aegea from the North Aegean Trough, to the Gulf of Corinth area and to the Kefalonia Fault. There, it finally linked with the northern tip of the Aegean subduction zone, completing the system of plate boundaries delimiting the Anatolia–Aegea plate. We have related the change in the distribution of shear from Miocene to Pliocene to the formation of a relatively undeforming Aegea block in Pliocene that forced the shear to be distributed over a narrow plate boundary to the north of it. We attribute the formation of this block to the northeastward progression of the oceanic Ionian slab. We propose that the slab cuts the overlying lithosphere from asthenospheric sources and induces a shortening environment over it.

Résumé : Nous documentons l'établissement de la limite entre la plaque de la Mer Égée–Anatolie et celle de l'Eurasie au Pliocène–Pléistocène. Avant 2 Ma, aucune limite de plaque n'était localisée au nord de la portion égéenne de la plaque anatolienne et le cisaillement produit par le mouvement de la plaque anatolienne–égéenne par rapport à l'Eurasie était distribué sur toute la largeur de la portion ouest de l'Égée–Anatolie occidentale. Il y a 4,5 Ma, une zone de cisaillement comparable au golfe de Corinthe a été formée dans ce qui est l'actuelle mer de Marmara. Les bassins d'extension initiaux ont été recoupés par le système de failles de décrochement principal de Marmara après 2,5 Ma. Peu de temps après, la limite de la plaque a migré à l'ouest de la mer de Marmara, le long de la bordure nord de l'Égée, de la fosse nord de l'Égée à la région du golfe de Corinthe et jusqu'à la faille de Kefalonia. Là, elle est finalement jointe à l'extrémité nord de la zone de subduction égéenne, complétant ainsi le système de limites de plaques délimitant la plaque Anatolie–Égée. Nous avons relié le changement de la distribution du cisaillement, entre le Miocène et le Pliocène, à la formation d'un bloc égéen relativement peu déformé au Pliocène; cela a forcé la distribution du cisaillement sur une mince limite de plaque au nord du bloc. Nous attribuons la formation de ce bloc à la progression de la plaque plongeante de l'océan ionien vers le nord-est. Selon nous, la plaque plongeante a coupé la lithosphère sus-jacente des sources de l'asthénosphère, provoquant un environnement de raccourcissement au-dessus de la plaque plongeante. [Traduit par la Rédaction]

Introduction

McKenzie (1970, 1972) first described the westward extrusion of Anatolia–Aegea in terms of plate tectonics, following Ketin's pre-plate tectonics suggestion in 1948. GPS results have confirmed that one could describe the Anatolian extrusion to a first approximation in terms of rigid rotations (Le Pichon et al. 1993, 1995; McClusky et al. 2000, 2003; Reilinger et al. 1997, 2006; Le Pichon and Kreemer 2010). The northern boundary of this plate separates the Anatolia–Aegea plate to the south from the Eurasia plate to the north and is presently characterized along its whole 2100 km length by dextral strike-slip at a rate of ~24 mm/year. To the east, the portion of the boundary north of Anatolia corresponds to the 1200 km North Anatolian Fault (NAF) that propagated westward since 13–11 Ma (Şengör et al. 2005). The NAF reached the Gulf of İzmit in the Sea of Marmara ca. 4 Ma (Le Pichon et al. 2014), although shear related deformation in the broader Marmara region had already commenced in the late Miocene (Şengör et al. 2005) (see Fig. 1 for the tectonic map of Aegea – western Anatolia and Figs. 1 and 2*b* as a key to geographic and geologic features in the Marmara area). To the west (see Fig. 1), the additional 900 km

Received 31 July 2015. Accepted 18 October 2015.

Paper handled by Editor Ali Polat.

X. Le Pichon. Professeur Honoraire au Collège de France, Europôle de l'Arbois, Bât. Trocadéro, BP 80 13 545 Aix-en-Provence cedex 04 France.
A.M.C. Şengör. İstanbul Teknik Üniversitesi, Maden Fakültesi, Jeoloji Bölümü, Avrasya Yerbilimleri Enstitüsü, Ayazağa 34469 İstanbul, Turkey; Honorary Research Associate, The Natural History Museum, Cromwell Road, London SW7 5BD, UK.
J. Kende and P. Henry. CEREGE, CNRS-Aix Marseille Université, Marseille, France.
C. İmren. İstanbul Teknik Üniversitesi, Avrasya Yerbilimleri Enstitüsü, Ayazağa 34469 İstanbul, Turkey.
C. Grall. Lamont–Doherty Earth Observatory, Columbia University, Marine Geology and Geophysics, Palisades, NY 10964-8000, USA.
H. Karabulut. Kandilli Rasathanesi, Boğaziçi Üniversitesi, Kandilli, İstanbul, Turkey.
Corresponding author: A.M. Celâl Şengör (email: sengor@itu.edu.tr).

[1] This paper is part of a special issue that honors the careers of Kevin C. Burke and John F. Dewey.

Can. J. Earth Sci. **53**: 1416–1439 (2016) dx.doi.org/10.1139/cjes-2015-0129

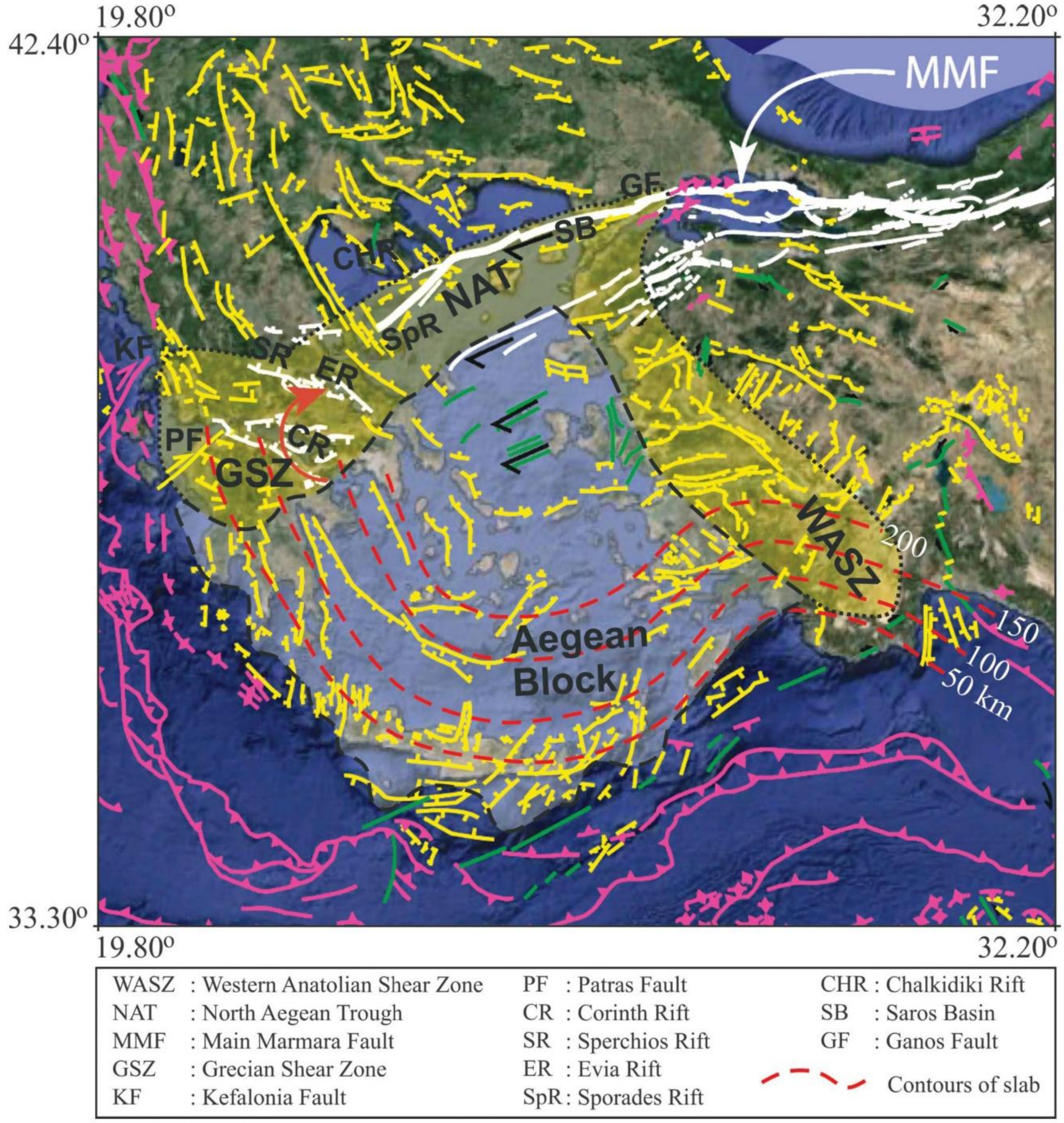

Fig. 1. Tectonic map of Aegea – western Anatolia. Violet-coloured markings indicate shortening structures, yellow indicates normal faults, green indicates left-slip faults, and white indicates the dextral North Anatolian Fault family including the normal faults of the Grecian Shear Zone (Şengör 1979). All faults are Quaternary, as they cut Quaternary deposits established by sequence correlations in the Sea of Marmara. Following the rule of Allen (1975), we assume all faults are active or potentially so. The light-colored, presently undeforming Aegean block revealed by geodesy is limited by dashed lines. The dashed red contours of the Aegean slab are after Gudmundsson and Sambridge (1998). The two yellowish shear zones that limit the Aegean Block, the Grecian Shear Zone (GSZ) and North Aegean Trough (NAT) to the north with clockwise rotation and the Western Anatolian Shear Zone (WASZ) to the east with counterclockwise rotation, absorb ~20–25 mm/year of shear, dextral for the northern zone and sinistral for the eastern zone. The figure is modified from Şengör and Zabcı (2016).

of plate boundary are complex (Şengör 1979; Şengör et al. 1982; Goldsworthy et al. 2002; Armijo et al. 2002; Le Pichon and Kreemer 2010; Shaw and Jackson 2010; Floyd et al. 2010; Royden and Papanikolaou 2011; Pérouse et al. 2012). The plate boundary follows successively from east to west: the NAF in the Sea of Marmara, called the Main Marmara Fault (MMF) by Le Pichon et al. (2001); the Ganos Fault; the North Aegean Trough (NAT), formed by the Saros Basin to the east and the Sporades Basin to the west; the Grecian Shear Zone (GSZ), a broad zone of shear named by Şengör (1979); and finally, joining through the dextral Kefalonia Fault, the Aegean subduction zone, where the 200 Ma Ionian oceanic slab is subducted at a rate of 34 mm/year (Pérouse et al. 2012).

The central theme of this paper concerns the mode of establishment of such a strike-slip plate boundary since 13–11 Ma when the Aegea–Anatolia plate was first initiated. We attempt to understand

Fig. 2. (*a*) Proposed tectonic map of Aegea – Western Anatolia ca. 4 Ma. White lines indicate the westward propagating North Anatolian dextral system, which has just reached the area of the present Sea of Marmara that is occupied by a system of clockwise rotating normal-fault bounded blocks similar to the Grecian Shear Zone (GSZ), with extensional decollements in front of the tip of the North Anatolian Fault (NAF). Modified from Şengör and Zabcı (2016). (*b*) Index map of geographic and geologic features within the Sea of Marmara area discussed in the text.

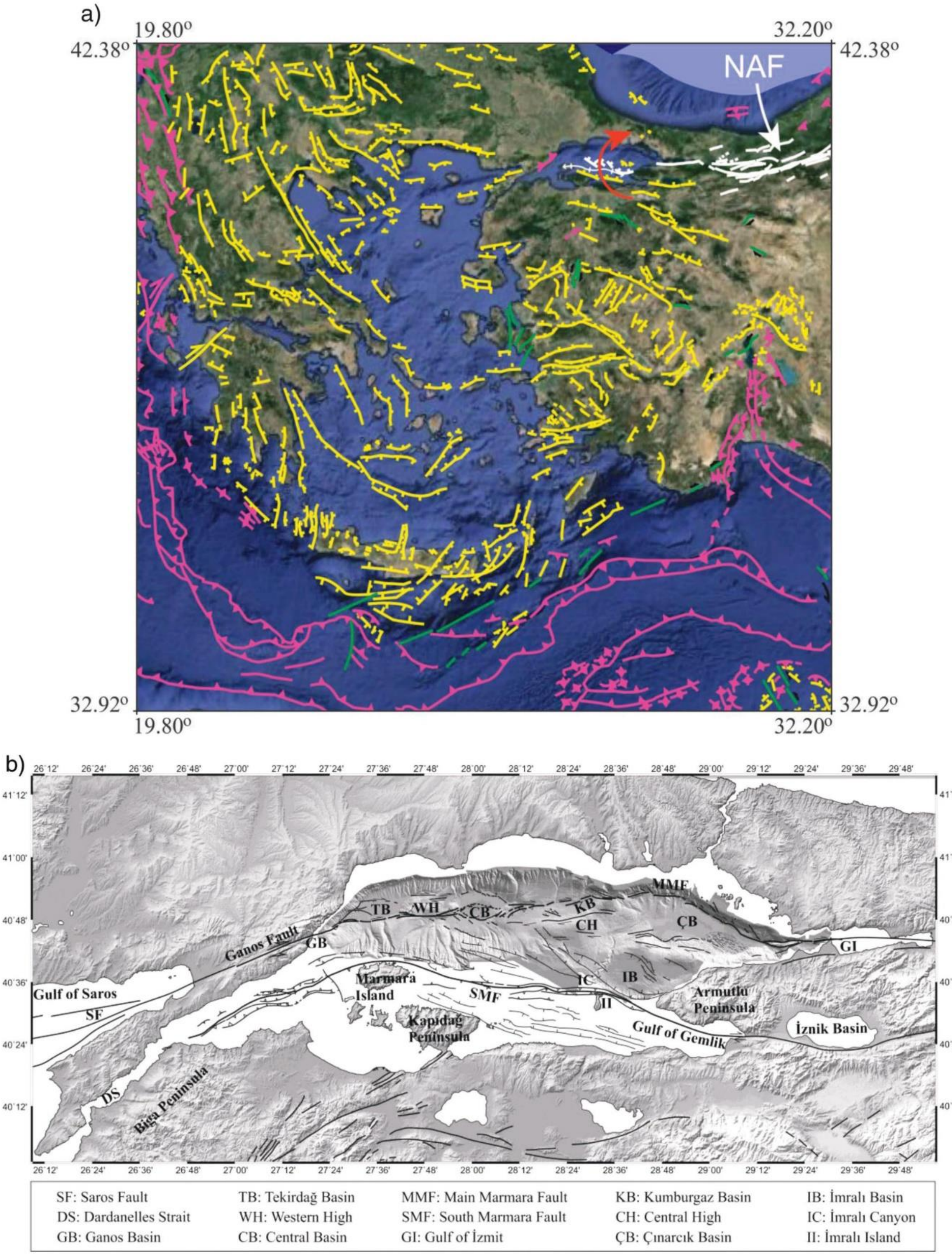

better why a localized pure strike-slip fault has progressively propagated westward as emphasized by Şengör et al. (2005). An essential character of both Anatolia and Aegea is that their geological history suggests very thin or even absent lithospheric mantle (e.g., Şengör 1982). Thus the Aegea–Anatolia plate corresponds to a huge ductile mass. Further, the western Aegean portion is subject to north–south extension because of the roll-back of the peri-Aegean subduction (Le Pichon and Angelier 1981; Le Pichon 1982). The ductility of this lithospheric mass and the presence of an important north–south extensional component on its western Aegean portion will occupy a prominent place in our investigation of the formation of this plate boundary. The transition from the well-defined NAF to the east to the more complex Aegean boundary to the west occurs within the Sea of Marmara. We will devote the principal part of this paper to a discussion of the genesis of the Sea of Marmara, as it enlightens the mode of propagation of the NAF through it. We will use new data and interpretations that have been partly published by Grall et al. (2012, 2013), Le Pichon et al. (2014), and Şengör et al. (2014), and those that are still to be published (J. Kende, P. Henry, G. Bayrakçı, S. Özeren, and C. Grall, in review).

The present tectonic regime of the NAF and its mechanical behavior

The portion of the NAF east of the Sea of Marmara

We first examine the behavior of the NAF east of the Sea of Marmara. The NAF there, throughout its length, is a stable localized pure dextral strike-slip fault with only local pull-apart and push-up segments (Şengör et al. 2005). The rate of geological motion has been established at ~18 mm/year (18 mm/year over 10 ky by Hubert-Ferrari et al. (2002), 18.6 mm/year over 3 ky by Kozacı et al. (2009), and 15–20 mm/year in a compilation made by Kozacı et al. (2009)). This rate is ~75% of the geodetic slip rate, which suggests that 25% of the displacement is taken outside of the main fault plane, presumably along minor faults on both sides of it.

We wish to emphasize an important point concerning the temperature structure of the upper lithosphere along the NAF. This is illustrated by the variation in the Curie point (580 °C for magnetite) depth as mapped by Aydın et al. (2005, fig. 4). The NAF follows the 20 km depth contour of the Curie point. Immediately to the south, the Curie point depth rises to less than 10 km. Thus, the lower crust and mantle are highly ductile to the south of the fault and much less to the north where the NAF keeps its course. The mapping of Aydın et al. (2005) demonstrates that the NAF keeps north of the boundary of the ductile lower crust and mantle zone. This observation leads us to propose that the NAF would not stabilize unless the whole crust is in the brittle domain. Otherwise, it has no roots and rapidly looses its "memory". Geologists have long indicated that the geological history of Anatolia suggests that no lithospheric mantle is present there (e.g., Şengör 1982). One can thus understand why the attempts to enter the bulk of Anatolia, by the Ovacık and Sungurlu faults, were unsuccessful and why the NAF has followed the northern limit of this ductile mass.

The NAF in the Sea of Marmara

Le Pichon et al. (2001) showed that the prolongation of the NAF within the Sea of Marmara, which they called the MMF, is a single throughgoing dextral strike-slip fault system that enters the Sea through the Gulf of İzmit and joins the Ganos Fault at its western extremity. The geological slip rate along the eastern Çınarcık portion of this fault has been established to be 18.5 mm/year (12.6–29.4 mm/year, 18.5 mm/year mean rate) over 500 ky by Kurt et al. (2013). Grall et al. (2013) found a rate of 15.1–19.7 mm/year over 405–490 ky to the west on the Western High (see Fig. 2*b*). On the Ganos Fault, Aksoy (2009) found 15.1–19.7 mm/year over 20 ky and Meghraoui et al. (2012) 17 ± 5 mm/year over 1000 years. Thus, the geological slip rate across the Sea of Marmara is ~18 mm/year as on the main eastern portion of the NAF. The NAF motion is consequently integrally transferred from the NAF to the Ganos Fault through the MMF. As for the NAF to the east of the Sea of Marmara, the rate along the MMF is also ~75% of the geodetic slip rate, which suggests again that 25% of the displacement is taken outside of the main fault plane.

Many authors have assumed the continuity of the rate of motion at the entrance of the Sea of Marmara. They consequently consider that the motion along the NAF there is distributed between a Marmara branch and a Gemlik branch to the south (see Fig. 2*b*). For example, Gasperini et al. (2011) have measured a strike-slip rate of 4 mm/year on the southern branch. Should these 4 mm/year be deducted from the 18 mm/year on the eastern NAF to obtain the rate of the MMF? Le Pichon et al. (1999) pointed out that this would be true only if the block between the two branches, which they called the Marmara block, had the same motion as the Anatolia block, which would be most unlikely. If the Marmara block has an independent motion, then the motion of this block can be adjusted in such a way that the rate is the same on the eastern NAF and the MMF to avoid any velocity discontinuity that would be otherwise mechanically very difficult to sustain. This is indeed what was found by Meade et al. (2002), Le Pichon et al. (2003), Reilinger et al. (2006), Le Pichon and Kreemer (2010), and other authors since, who have introduced in their GPS solution an independent Marmara block.

Note, however, that Gasperini et al. (2011) have measured average rates of ~9 mm/year on the NAF in the Gulf of İzmit by measuring offsets of a river channel that was drowned ~10 ky ago. This is about half the geological slip rate found to the east on the NAF and to the west in the Çınarcık Basin. This discrepancy is puzzling.

It is remarkable that the MMF follows the same 20 km Curie point limit along the northern edge of the Çınarcık Basin as along the eastern NAF. The portion of the MMF that follows the northern border of the Çınarcık Basin within the eastern Marmara Sea corresponds to a stable localized strike-slip fault (Karabulut et al. 2002, 2011; Bulut et al. 2009; Örgülü 2011; Kurt et al. 2013). While the MMF is entirely contained within the thickly sedimented deep Marmara Basin, another fault system called South Marmara Fault (SMF) by Le Pichon et al. (2014) was active in Pliocene time over the whole less-sedimented southern shelf of the Sea of Marmara. Some activity is still related to this southern fault system. On the southern edge of the İmralı Basin, Armijo et al. (2002) have described an active extensional system connected to the NAF in the Gulf of İzmit by a right-lateral fault along the shore of Armutlu Peninsula. Current fault activity does not seem continuous along the southwest, transtensional, edge of the İmralı Basin (see Fig. 2*b*), but a number of active normal faults appear to distribute the extensional component of strain within the basin (Şengör et al. 2014). Morever, subsidence at the depocenters proceeds at a steady rate since 0.4 Ma at least (Sorlien et al. 2012). Although little seismic activity is recorded in this area, it is possible that the growth of the İmralı Basin may still today accommodate some significant strain.

The MMF crosses the 20 km Curie point limit west of Çınarcık, as it changes direction to the west–southwest toward the Ganos Fault, to enter a hot lower crust and upper mantle area (Aydın et al. 2005). By doing so, it also enters into the serpentinite and mélange-dominated Intra-Pontide suture, which may also affect the mechanical behavior of the fault (see Le Pichon et al. 2014, fig. 1*b*). There, in the western and central Sea of Marmara, this localized strike-slip fault appears to coexist with remnants of an extensional system, as demonstrated by significant distributed extensional seismic activity to the south of it (Altınok and Alpar 2006; H. Karabulut, unpublished data, 2015). This western portion of the MMF is thus best understood as an intermediate type of boundary, where a localized strike-slip fault has just been established within a previously existing broad zone of shear affecting the ductile lower crust and upper mantle.

The NAF west of the Sea of Marmara

From the Ganos Fault westward into the Gulf of Saros, the Curie point depth increases again to more than 20 km and the Ganos – Saros Gulf Fault is indeed a stable pure strike-slip portion that corresponds to the westernmost extent of the stable pure strike-slip NAF (Karabulut et al. 2006). Recently, the 24 May 2014 M_w 7.0 earthquake confirmed the pure dextral strike-slip nature of the fault along the Saros Basin, all the way to 25°E (Görgün and Görgün 2015). Gasperini et al. (2011), using the same approach as in the Gulf of İzmit, confirmed the existence of dextral strike-slip along the Saros Fault. However, they evaluated the rate as only ~10 mm/year over the last 10 ky post-glacial period. This discrepancy with the geodetic slip rate of 22–24 mm/year (Le Pichon and Kreemer 2010; Pérouse et al. 2012; Müller et al. 2013) is similar to the discrepancy in the Gulf of İzmit and suggests that there might be some systematic bias in their evaluation. Morever, we pointed out above that trenching studies estimate slip rate on Ganos Fault at 17 ± 5 mm/year (Meghraoui et al. 2012; Aksoy 2009) over similar periods of time.

We conclude that the rate of dextral strike-slip motion is indeed constant from the NAF to the western extremity of the Gulf of Saros Fault along the prolongation of the NAF at a geodetic slip rate of ~24 mm/year. However, as discussed above, although the geological slip rate also appears to be constant at ~18 mm/year, it is only ~75% of the geodetic slip rate. We proposed above that this discrepancy between geodetic and geologic rates may indicate that ~25% of the displacement is taken outside of the main fault plane.

The western portion of the NAF: the undeforming Aegea block, the Ionian slab, and the two shear zones that limit it

We now move westward within the Aegean domain. A remarkable result established by the geodetic surveys of Aegea is the existence of an essentially undeforming Aegea block limited by two shear zones (Reilinger et al. 2006; Floyd et al. 2010; Le Pichon and Kreemer 2010; Royden and Papanikolaou 2011; see Fig. 1). The northern shear zone, as mentioned above, has been called GSZ by Şengör (1979, 1982). It absorbs ~20–25 mm/year of dextral slip. To the east, the Western Anatolian Shear Zone (WASZ) absorbs ~20 mm/year of sinistral slip. Both zones are characterized by distributed extension across several extensional asymmetric rifts with decollement, accompanied by rapid rotation at ~5°/My, clockwise for the dextral GSZ and counterclockwise for the sinistral WASZ (see detailed references below).

The rates of rotation mentioned above of ~5°/My should be detected by paleomagnetic measurements if they persevered over several million years. Such rotations have indeed been detected (Kissel et al. 2003; Van Hinsbergen et al. 2005, 2010). They are clockwise in the western Aegean region and may have reached as much as 40° between 15–13 and 8 Ma with an additional 10° after 4 Ma (Van Hinsbergen et al. 2005). They are counterclockwise within the eastern Aegean region in the WASZ and have been measured as ~20° between 16 and 5 Ma (Van Hinsbergen et al. 2010). These finite rotations thus qualitatively agree with the present geodetic rotations. Of course, paleomagnetic techniques can only detect rotations of relatively short radius. The absence of detectable paleomagnetic rotations thus does not imply the absence of important motions of large rotation radius. In addition, as the paleomagnetic results are obtained by an averaging process between different sites, the distinction between local block rotations and regional rotations is difficult to make, especially in Aegea where numerous local block rotations have been demonstrated to be present. However, an important point is that the rapid phase of rotation detected by paleomagnetics began ca. 15–13 Ma to the west and 16 Ma to the east, confirming that middle Miocene was an important time for the tectonics of Aegea.

The existence of this undeforming Aegea block is not integrated in recent discussions of the geodynamics of the area (e.g., Royden and Papanikolaou 2011; Vassalikis et al. 2011; Tirel et al. 2013; Pearce 2015). These recent discussions assume rapid lithosphere extension related to the subduction of the oceanic Mediterranean lithosphere since Middle Miocene. But actually, the episode of rapid extension within the present Aegea block peaked between Serravallian, ca. 12 Ma, and Messinian (7–5 Ma) and ceased to exist within this Aegea block after Messinian time (5 Ma), while it continued within the WASZ and was initiated within the GSZ between 2 and 1 Ma (Armijo et al. 1996; Sorel 2000; Flotté 2003). We attribute this cessation of extension within the present Aegea undeforming block to the shielding effect of the cold oceanic Ionian slab. The subduction of the Ionian oceanic slab started ca. 10 Ma and this shielding effect thus progressively extended over the whole southern Aegean mostly after Miocene time. Moreover, the slab now dips some 10° to 15° up to a distance of some 300 km from the Hellenic “Trench”. Despite the prodigious amounts of Messinian salt probably going down into the subduction channel, this would induce a considerable frictional stress onto the upper plate that would counteract the extension farther north in a situation not too different from the south-central Andes in Chile (see Oncken et al. 2006, figs. 16-12*a*–*f*). This would explain why the “dead” block does not extend far into the north in the Aegean Sea. Another explanation proposed by Sonder and England (1989) is that the thinning of the southern Aegean Sea that was initiated ca. 20 Ma may have reached a critical level 3–5 Ma because of the cooling of the extending lithosphere. Consequently, the strain associated with the pull toward the arc was transferred further outward, including to western Anatolia. However, their proposal does not explain why the extension continued within northern Aegea and western Anatolia, although the extension had started at about the same time there.

We now consider more carefully these two shear zones. We will show that within the West Anatolian – Aegean domain, outside of the presently undeforming Aegea block, the normal mode of shearing there, in this ductile lower crust-upper mantle environment, is through rotation of en-echelon normal faults over a 100–200 km wide shear zone (McKenzie and Jackson 1983, 1986, 1989; Jackson and McKenzie 1989). Further, the brittle distension roots in a shallow decollement above the ductile lower crust. This is because, in addition to the ductility of the lower crust and mantle below 10–15 km as in Eastern Anatolia, the thinned lithosphere is also affected by strong north–south extension due to the roll-back of the peri-Aegean subduction.

The GSZ consists of several extensional rifts oblique to the direction of motion of Aegea with respect to Eurasia, the largest of these being the Corinth and Evia grabens (see Fig. 1). These are asymmetric rifts with active decollements (Rigo et al. 1996; Jolivet et al. 2010). In this area, distributed extension is accompanied by rapid clockwise motion at ~5°/My (Le Pichon and Kreemer 2010; Floyd et al. 2010; Chousianitis et al. 2015). The width of this portion of the shear zone in a direction perpendicular to the motion of Aegea with respect to Eurasia is ~100–200 km. There is no localized strike-slip boundary there, as evidenced by the absence of strike-slip earthquakes. Yet, Durand et al. (2014) have suggested that there is a localized strike-slip boundary at depth, within the ductile portion of the lithosphere. The existence of shallow dipping decollements flattening at a depth of ~10 km suggests that the lower crust is ductile (Jolivet et al. 2010). Further, Tiberi et al (2001) have shown that the Moho topography is unrelated to the surface tectonics as the lower crust appears to have been affected by boudinage. This confirms that the lower crust is most probably ductile there. Thus, there is no reason to assume the existence of a hidden extension of the NAF at depth below the CHSZ as proposed by Durand et al. (2014). Most authors had previously recognized the absence of a localized strike-slip boundary at depth, notably Şengör (1979) and Goldsworthy et al. (2002).

The WASZ also consists of actively extending asymmetric rifts rotating counterclockwise at ~5°/My (Floyd et al. 2010). Karabulut et al. (2013) have put into evidence "small-amplitude and long-wavelength lateral variations of the Moho topography", which suggests to them that "viscous flow in a hot lower crust has smoothed out the lateral variations of crustal thickness." Aydın et al. (2005) have shown that the Curie point is at a depth of 5–10 km in this area, which confirms that the lower crust is indeed in the ductile regime. The width of the WASZ is similar to the width of the GSZ and equal to ~100–200 km. This width, of the order of the thickness of the average lithosphere, suggests that it is related to block shearing of the whole lithosphere. The deformation in the upper brittle crust is an adjustment to this underlying distributed shear. In conclusion, both the WASZ and the extensional portion of the GSZ have a similar width of ~100–200 km and have a hot and ductile lower crust. The underlying mantle is of course also hot and ductile. We can conclude that this type of shearing zone with rotating distributed extension in the upper crust is preferred in this extensional hot environment where the lower crust and upper mantle are ductile.

We then move to the two portions of the northern Aegean boundary that have not yet been discussed, on both sides of the GSZ: the Sporades Basin, at the western extremity of the NAT to the east of the GSZ, and the Kefalonia–Patras Fault system to the west. We show that these are portions of the North Aegean Boundary intermediate in character between stable pure strike-slip localized faults and highly distributed extension through rotating faults on top of a sheared lower crust and upper mantle. The Sporades Basin appears to possess a localized strike-slip fault as well as distributed extension to the north of it (the Thermaikos and Chalkidiki extensional systems). The Kefalonia–Patras Fault system has a major strike-slip fault at its northern extremity, the Kefalonia Fault, and a minor one at its southern extremity, the Patras Fault, with distributed shear in-between. Both portions of boundary appear to be sheared over a width of 100–200 km at depth in the lower crust and upper mantle.

A new insight on the behavior of these two portions of the boundary is given by the seismic sequence that followed the 6 January 2008 M_w 6.2 earthquake (37.15°N, 22.95°E). This earthquake ruptured the Ionian slab at a depth of 80 km (see Durand et al. 2014) and resulted first in roll-back of the subduction with southwestward motion of the top block toward the trench and then in dextral shear of Aegea with respect to the Eurasia plate. On 8 June 1968 an M_w 6.4 dextral strike-slip earthquake activated the Patras–Achaïa strike-slip fault over a length of 25 km, and then during the second part of 2008 the GSZ (Corinth, Sperchios, and Evia rifts) was activated in extension. This extensional activity extended northward into the NAT area within the Thermaikos and Chalkidiki extensional systems.

We now consider the velocity field across the GSZ. Floyd et al. (2010) show that both across the extensional part of the GSZ and across the Kefalonia and Patras–Achaia Fault system there is a continuous linear increase in GPS velocity with respect to Eurasia from ~5–10 mm/year north of the Aegea block to 30–35 mm/year within the block. This increase occurs over ~100–200 km, the gradient being somewhat steeper in the purely extensional area than in the Kefalonia–Patras strike-slip area (see also Shaw and Jackson 2010). The increase in velocity over more than 100 km cannot be explained only by elastic effect because this width is too large. The only reasonable explanation is that it reflects ductile shear in the underlying mantle below, as concluded by Shaw and Jackson (2010) and Floyd et al. (2010).

Considering more carefully the Kefalonia–Patras shear system, the most important fault is the Kefalonia Fault that absorbs ~15 mm/year of dextral slip (Vassilakis et al. 2011) or up to 23 mm/year (Pérouse et al. 2012). It links the northern extremity of the Aegean subduction to the Aegean northern boundary. As a consequence, the whole Kefalonia–Patras shear area lies on top of the shallow African slab that is subducted at a velocity of ~34 mm/year, much faster than the 4 mm/year convergence velocity of the Adriatic crust with the northern Greece crust, north of the Kefalonia Fault (Pérouse et al. 2012). The lithosphere being sheared is everywhere thinner than ~50–40 km (Pearce 2015). This is a very peculiar situation. Cocard et al. (1999) had shown that this domain had an important clockwise rotation rate centered on the islands of Kefalonia and Zakintos. The rate of rotation is estimated at 6°–8°/My by Chousianitis et al. (2015) and 8°/My by Vernant et al. (2014). This Patras–Achaïa area is limited to the northeast by a zone of left-lateral shear between the Gulf of Amavrakikos and the eastern tip of the Gulf of Corinth. The rate of motion along this zone of shear is estimated to be ~10 mm/year (Vassilakis et al. 2011; Vernant et al. 2014).

The 8 June 2008 earthquake activated the Patras–Achaïa Fault at the southern extremity of the Kefalonia–Patras shear system as Durand et al. (2014) have demonstrated. This fault is identified by Shaw and Jackson (2010) through its seismicity, but it only appears on GPS as a change from a gradient in velocity to the north versus a uniform velocity to the south. Vassilakis et al. (2011) tried to evaluate its motion by identifying small more or less rigid "fragments" and conclude that the motion is 7 mm/year with ~5 mm/year in extension and 5 mm/year in strike-slip. This is not in agreement with the pure strike-slip motion revealed by the 8 June 2008 earthquake. In any case, their method maximizes the motion on the boundaries between blocks as it ignores any internal deformation. Thus one can only state with certainty that the motion along this fault is too small to be properly characterized by GPS. Indeed, the fault cannot be identified on the field (Shaw and Jackson 2010). Cases of faults with strong seismogenic potential but too small a slip rate to be detected by geodetic methods have indeed been described elsewhere (e.g., Friedrich et al. 2004). Thus the Kefalonia–Patras shear area is a zone of continuous shear deformation over a width of at least 100 km bounded by two localized strike-slip faults. The most important is the Kefalonia Fault that absorbs ~20 mm/year of dextral slip (Vassilakis et al. 2011, 15 mm/year; Vernant et al. 2014, 20 mm/year; Pérouse et al. 2012, 23 mm/year). The Patras–Achaïa Fault absorbs a maximum of ~5 mm/year. The June 2008 earthquake activated it, as Durand et al. (2014) have demonstrated.

Although Reilinger et al. (2006), Le Pichon and Kreemer (2010), Pérouse et al. (2012), and Müller et al. (2013) all agree that dextral strike-slip at a rate of 22–26 mm/year occurs along the NAT, the presence of simultaneous active extension immediately to the north of the Sporades Basin in the Thermaikos and Chalkidiki extensional systems indicates that the western NAT does not correspond to pure strike-slip localized on a single fault. Pérouse et al. (2012) and Müller et al. (2013) emphasized this point. The activation of the Sporades and Chalkidiki extension, but not of the Sporades dextral strike-slip, during the 2008 seismic sequence confirms that this is an intermediate type of boundary, where a localized strike-slip fault coexists with remnants of an extensional system, on top of a broad zone of shear affecting the ductile lower crust and upper mantle. We have seen above that this intermediate type of environment also characterizes the central and western Marmara Sea with simultaneous presence both of a localized strike-slip fault, the MMF, and of active remnants of the previous extensional system.

To conclude, west of the Saros Basin, the northern boundary of the Aegean block absorbs 22–24 mm/year of dextral strike-slip over a broad 100–200 km wide zone of shear of the lithospheric mantle, with various expressions within the upper crust. From east to west, there are first both localized strike-slip along the Sporades Basin and simultaneous extension to the north in the Thermaikos and Chalkidiki area. Then there is distributed clockwise rotating extension within the GSZ. Finally, there is distributed shear between two strike-slip faults, the Kefalonia and Patras–Achaïa faults in the westernmost portion. This last portion joins the northern boundary of the Anatolia–Aegea plate to the Aegean subduction plate boundary. It crosses an area of relatively thin crust with no well-identified Moho, on top of the shallow subducting slab (Pearce 2015). The crust there probably consists of geologically recent stacks of cold nappes cut from the asthenosphere by the underlying slab as discussed by Pearce (2015). This relatively cold environment accounts for the presence of localized strike-slip faults.

It is important to note that the effect of the deformation in the GSZ and WASZ is to allow the relatively undeforming Aegea block to rotate clockwise away from Anatolia around a pivot situated near the northern extremity of the subduction zone (e.g., Le Pichon and Kreemer (2010, fig. 8) in which the GPS vectors are with respect to Anatolia). This rotation has two effects on the subduction zone. First, it increases the subduction rate to a value of ~35 mm/year along the whole northwest–southeast segment of the Hellenic subduction zone as this rotation compensates for the southeastward decrease of motion of the Anatolia–Eurasia rotation. Second, it maintains the subduction direction strictly perpendicular to the subduction zone (Le Pichon and Angelier 1979). This rotation thus appears to be governed by the roll-back of the subduction zone.

Consequences of the subduction of the Ionian slab

In respect to the drastic consequences of the subduction of the cold and heavy oceanic Ionian slab, we argue that the presence of a low dip cold slab in rapid subduction has drastic consequences for the overlying mantle and crust. This is because it cuts the overlying lithosphere from asthenospheric sources and induces a shortening environment over it. This, in our opinion, explains why major extension is absent within the present Aegea block while it was very active between 13 and 5 Ma.

The cold 200 Ma oceanic Ionian slab (Truffert et al. 1993) is presently subducted below Aegea at a velocity of ~34 mm/year, much faster than the 4 mm/year convergence velocity of the continental Adriatic crust north of the Kefalonia Fault with the northern Greece crust (Pérouse et al. 2012). The length of the seismically active slab is ~350 km below Peloponnesus (e.g., Gudmundsson and Sambridge 1998), which indicates that this rapid subduction is 10 My old or somewhat older if the average rate of subduction since the initiation of subduction was equal or somewhat smaller than the present one. The volcanic arc related to this subduction was initiated near 2.5 Ma (Le Pichon and Angelier 1979). The slab below the volcanic arc is ~150 km deep, and the length of slab from the volcanic arc to the subduction zone is ~300 km. Thus the age indicated for the initiation of subduction is also 10 Ma or somewhat older.

This age is in fair agreement with the age of formation of the accretionary wedge, which occurred after 15 Ma as established by deep sea drilling (Kastens 1991). Located within a trough near the backstop leading edge, DSDP 377 borehole penetrated early to middle Miocene (between 19 and 15 Ma) turbidites of probable African origin. At the time the turbidites were deposited, the present accretionary wedge could not have existed if the turbidites indeed came from Africa. These turbidites were covered with 15–14 Ma pelagic marls, whereas turbidites continued to be deposited to the south. Thus the change of sedimentation to pelagic marls at 15 Ma is compatible with an initiation of the present accretionary wedge at about this time. The probable limestone backstop is covered by late Miocene basins confirming that it reached its present configuration also in the late Middle Miocene, near 15 Ma (Le Pichon et al. 2002). Thus this margin was formed ca. 15 Ma. Le Pichon et al. (2002) proposed that this was a time of reinitialization of the subduction system after slab break. We adopt their proposal. This late initiation of the Ionian oceanic plate would also explain why the Kefalonia transform is geologically quite recent (post-Messinian, 5–7 Ma according to Royden and Papanikolaou 2011). We have noted above that the finite clockwise and counterclockwise rotations detected by paleomagnetics within Aegea were initiated 16–15 Ma.

The alternative is that the slab stops being seismically active 10 My after being subducted but continues at greater depth as an aseismic slab. This alternative is proposed by authors who postulate continuity of the slab to great depth on the basis of tomographic studies (Bijwaard et al. 1998; Piromallo and Morelli 2003). In this line of thought, Royden and Papanikolaou (2011) and Tirel et al. (2013) agree that rapid subduction of the cold Ionian lithosphere would only have started at 6–8 Ma, following a slower subduction episode of external carbonate platform on transitional lithosphere. However, in their hypothesis, it is hard to understand how the slab was able to maintain its continuity as it went from oceanic, in Eocene time, to semi-continental, in Oligocene and lower to middle Miocene, then back to oceanic again, in upper Miocene to recent time. Models that have been proposed to investigate the change due to the subduction of a continent (Martinod et al. 2000; Royden and Husson 2006) suggest that continental subduction induces an increase in the slab dip angle and a decrease in the subduction velocity due to a change in slab buoyancy. They also predict that the slab should break at the former location of the continental block. These models then are difficult to reconcile with the interpretations, which assume continuity of the slab and no break, such as those proposed by Tirel et al. (2013) and Pearce (2015).

The relationship between simple idealized 2-D models of subduction and actual 3-D complex Aegean subduction is not obvious. For example, the continental subduction north of the Kefalonia transform dips at the same 17° shallow angle as the oceanic subduction to the south (Pearce 2015). However, the assumption of a 200–300 km narrow Ionian slab extending uninterrupted over more than 1000 km in spite of these drastic changes in subduction type and subduction direction is based on tomography. But is the assumption justified? The presumed continuous slab depicted by tomography shows significant heterogeneity (Bijwaard et al. 1998, fig. 7*c*; Piromallo and Morelli 2003, section Ff of fig. 9). More importantly, the continuity is undermined by the proven existence of slab breaks in its upper portion. A major slab break, long suspected on the basis of tomographic studies, has been demonstrated to exist between Aegea and Anatolia (Paul et al. 2014). Pearce (2015) concludes his extensive investigation of seismic imaging of the western Hellenic subduction by stating that "there may be two overlapping slabs beneath northern Greece, one dipping at 17° toward N60°E from 30 to 70 km depth and the other sitting horizontally at 200 km depth", as shown by Soboudi et al. (2006). He also indicates that he cannot exclude a tear of the slab between northern and southern Greece as proposed by Spakman et al. (1993) and concludes that the slab may be locally segmented in some way at least near its top. The existence of these ruptures supports the conclusion of Le Pichon and Kreemer (2010) who pointed out that the continuity of the conical seismic slab with a deeper slab could not be maintained without significant rupture.

Furthermore, the extent of the Ionian slab below Aegea, as defined by the intermediate seismicity distribution (Gudmundsson and Sambridge 1998; Shaw and Jackson 2010), is broadly confirmed by the high-resolution surface tomography of Salaün et al. (2012), which shows that the low-velocity anomaly in the upper mantle, between 80 and 160 km depth, present in Anatolia and north central Aegea is limited to the south by the seismically active Ionian slab. Paul et al. (2014) show that the zone of low velocity anomaly, in Anatolia and north central Aegea, has northeast–southwest fast-wave polarization axes of shear-wave anisotropy, whereas in southern Aegea, where the seismically active slab is present, the orientation is quite different and significantly smaller.

The mapping of intermediate seismicity depth in the slab by Gudmundsson and Sambridge (1998) and Shaw and Jackson (2010) confirms that the slab is not present below the Corinth and Evia grabens, although Suckale et al. (2009) assume that the slab extends below the eastern extremity of the Corinth Gulf beyond a depth of 100 km. However, this assumption of Suckale et al. (2009) does not appear to be substantiated. This is because their composite images of the slab show that the well-defined image of the slab disappears at a depth of 100 km before reaching the area below the eastern Gulf of Corinth. The mapping of Gudmundsson and Sambridge (1998) also indicates that the slab is present below the Kefalonia–Patras Shear Zone, as discussed above. And the detailed seismic imaging of the western Hellenic subduction by Pearce (2015) confirms the presence of the slab below the Kefalonia–Patras Shear Zone, as noted above. We can conclude that the slab is absent below the GSZ and present below the Kefalonia–Patras zone, which would explain the tectonic difference below the two zones.

Note that the continuity-of-slab hypothesis also leads to another difficulty as it does not explain why the extensional collapse of the Aegean landmass, which resulted in the formation of the Sea of Crete, could have occurred above a shallow subducting slab that should have created a compressional environment. Drooger and Meulenkamp (1973) have shown that the Southern Aegean landmass fragmented and most of it came below sea level at the end of Serravallian (ca.13 Ma, see also Angelier 1979) while it is now part of the undeforming Aegean block since Messinian, at ca. 5 Ma (Angelier et al. 1982). We submit that the apparent heterogeneity of the tomographic slab may be due to the coalescence of pieces of slab following various tear episodes in Late Eocene and Middle Miocene.

If this tear of the slab did indeed occur prior to the initiation of subduction of the oceanic Ionian slab between 15 and 10 Ma, one can then distinguish between the presently subducting Ionian slab at a rate of 34 mm/year and with a dip of 17° toward north of 35°E reaching a maximum depth of 170 km and the older coalesced slabs now dipping at ~45° toward the north between 170 and ~1200 km (Bijwaard et al. 1998). This older system, which extends over 1000 km and penetrates into the lower mantle, is most probably anchored within the mantle. Consequently, its kinematics are independent of what happens at the surface. Its vertical velocity must be approximately equal to the vertical component of velocity of the subducted Ionian slab, so that contact is maintained between the two subducted pieces. Thus the vertical velocity of the Ionian slab is ~10 mm/year. This vertical velocity implies an age of the order of 100 Ma for the initiation of subduction of this older slab, which is quite reasonable.

We consequently conclude that the subducted Ionian slab now prevents the asthenosphere from reaching the base of the lithosphere and produces above it a tectonic environment that is cooler and affected by shortening, or at least much less extension. We argue that this is the reason why the essentially undeforming Aegea block coincides with the part of Aegea that is presently underlain by the Ionian slab. This then explains why the Sea of Crete that resulted from the extensional collapse of the Aegean landmass during Mid to Late Miocene, when a slab was absent below it, following the post-Oligocene break, has been part of the undeforming Aegean block since Messinian, ca. 5 Ma (Angelier et al. 1982). At this time, the Ionian slab began to propagate northeastward below the Sea of Crete and consequently cut off the asthenospheric source on which this extension thrived.

The penetration of the NAF within the western Anatolian – Aegean landmass 4 Ma

Figure 2 shows our proposed reconstruction of the NAF 4 Ma. Le Pichon et al. (2014) have shown that at this time the NAF had not yet entered the area of what is now the Sea of Marmara but had just reached its eastern extremity, near the Gulf of İzmit. We will show that this is the time at which asymmetric extensional rifts similar to those of the present Gulf of Corinth were formed in the southern part of what is now the Sea of Marmara. These rifts were oblique to the direction of motion of Anatolia with respect to Eurasia, with active decollements to the south of a large anticline on the present southern shelf of the Sea of Marmara. This distributed extension, which we consider to have been accompanied by rapid clockwise motion, accommodated the deformation on the western tip of the 4 Ma NAF (Figs. 2, 3*a*, and 3*b*).

Let us first briefly discuss the geodynamics of the western Anatolian – Aegean landmass 4 Ma. We have seen that the present geodynamics of Aegea and the prolongation of the NAF along its northern boundary are now greatly influenced by the presence of the rapidly subducting Ionian slab. This is because the subduction of the slab resulted in the formation of an undeforming Aegean block on top of the advancing slab. This subduction was initiated ca. 15 Ma, 3–4 My before the NAF initiated its westward propagation (12–11 Ma according to Şengör et al. 2005). The fact that subduction of the oceanic Ionian plate immediately preceded the formation of the NAF suggests that slab pull was essential to trigger the extrusion of Anatolia. Before the slab had sufficiently advanced to result in the formation of the relatively undeforming Aegean block, between 15 and 4 Ma, the western Anatolia – Aegea environment was dominated by ductile lower crust and upper mantle and was affected by strong north–south extension due to the roll-back of the peri-Aegean subduction distributed over the whole Aegean. In this tectonic environment, the shear between the westward motion of Anatolia and Eurasia was distributed over the whole width of Aegea. As a consequence, there was no localized northern boundary fault north of Aegea (Fig. 2).

This does not mean that extension was not present in the northern Aegean. For example, the NAT has deposits of Messinian (7–5 Ma) evaporites (Mascle and Martin 1990) and Messinian carbonates and marls are present along the coasts of Saros Gulf and Çanakkale close to NAT (Çağatay et al. 1998, 2006; Melinte-Dobrinescu et al. 2009). But there was no localized zone of shear along it. However as the Ionian slab progressed northeastward below Aegea, distension ceased within the overlying lithosphere and a relatively undeforming Aegean block progressively increased its size. Consequently, the shear could not be distributed over the whole of Aegea. Accordingly, the kinematics had to adjust and a localized zone of shear began to form along the northern boundary of Aegea. This is confirmed by the fact that the age of the GSZ is quite young, less than 2 Ma. Armijo et al. (1996) have shown that the phase of rapid extension in the Gulf of Corinth corresponds to the last million years, and Sorel (2000) and Flotté (2003) have dated the initiation of the Gulf of Corinth between 1.7 and 1.1 Ma. Flotté (2003) estimated the total extension to be 15 km. This finite extension should be compared to the present rate of extension of 15 mm/year. It is equivalent to 1 My of extension at the present rate. Nielsen (2003) estimated the dextral offset along the Kefalonia Fault at 37 km using the offset of two portions of a seamount that appeared to have been cut in two pieces. This offset would have been produced in 1.6 My using the strike-slip rate of 23 mm/year given by Pérouse et al. (2012). Similarly, Tüysüz et al. (1998) estimated the age of the initiation of dextral motion in the Gulf of Saros as between 2 and 1 Ma, Kurt et al. (2000) as Plio-Quaternary and Ustaömer et al. (2008) as Quaternary. This strike-slip phase followed a compressional phase in the Saros Gulf region (4–3 Ma) based on the age of the Conkbayırı Formation, an alluvial fan formed on the uplifted southern shoulder of Saros Gulf (northern Gelibolu Peninsula) (see e.g., Sümengen et al. 1987; Çağatay et al. 1998). Thus the present northern plate boundary of Aegea is less than ca. 2 Ma from the Gulf of Saros to the Kefalonia Fault.

We should remember, however, that the 200 km WASZ had been a zone of active extension since Late Miocene and remained

Fig. 3. (*a*) Map of the southern shelf anticlinal system. Faults on the shelf after Le Pichon et al. (2014). Contours every 100 m (light lines) and 500 m (dark lines) are estimates of amount of eroded material based on the seismic profiles. See Le Pichon et al. (2014) for network of seismic profiles used. The 3.5 Ma South Marmara Fault (SMF) is shown in red. Possible X shears related to the clockwise rotation of the blocks between 4 and 3.5 Ma are shown as dotted lines, in purple. Red barbed lines are the direction of propagation of clastics. Contours between the sea floor and 13 km depth of detachments north of the Marmara anticline after Bécel et al. (2009). Black lines with tick marks show crests of tilted blocks on top of these detachments after Bécel et al. (2009). The detachment north of the İmralı anticline is drawn on the basis of the SEISMARARA seismic profile in the İmralı Basin, as shown in Laigle et al. (2008, fig. 2*b*). The location of this profile is shown by the red line. M1 is the Marmara 1 industrial well. (*b*) Enlargement of Fig. 3*a*. (*c*) Stacked profiles from east to west with erosional contours.

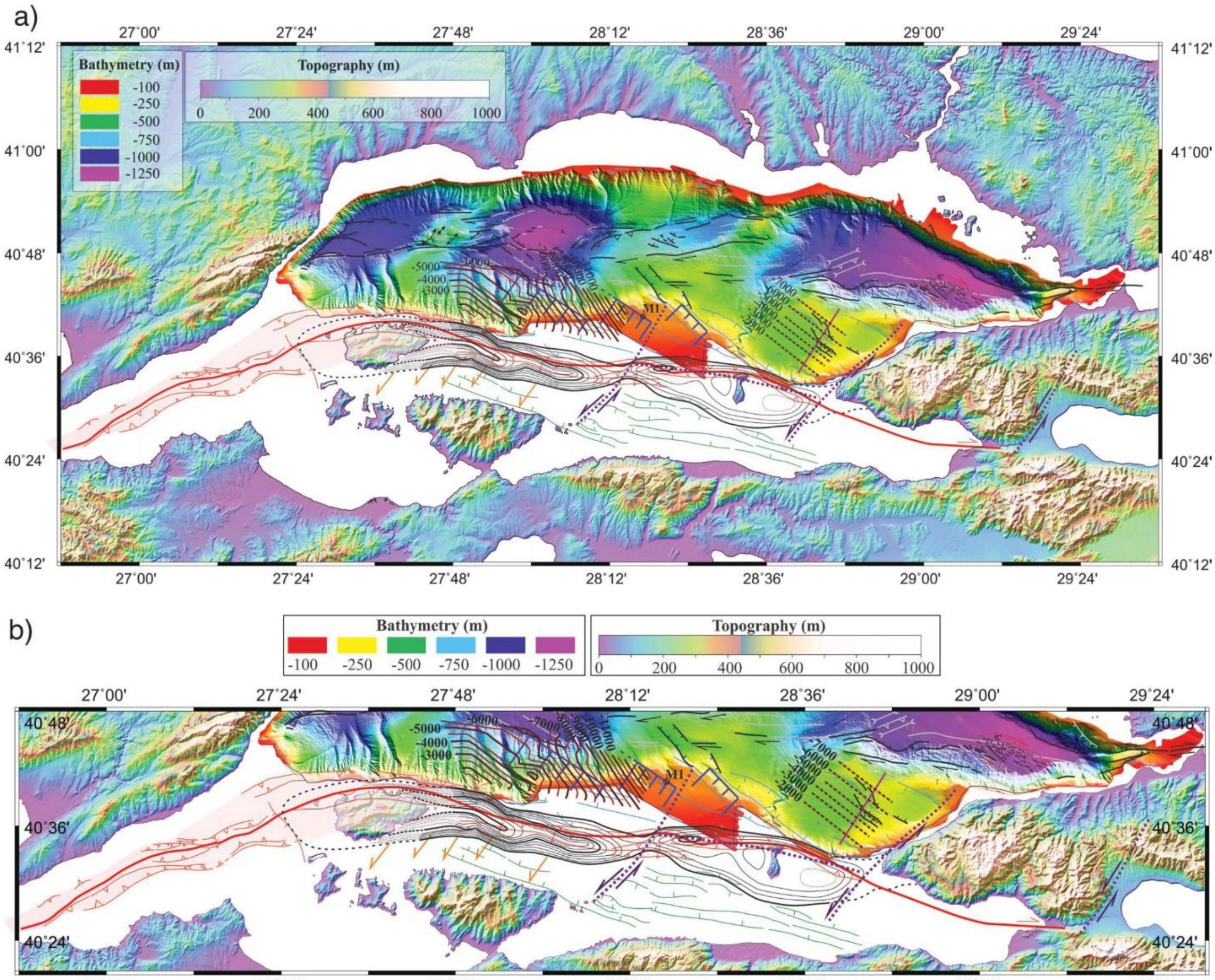

in this situation to this day. Consequently, the prolongation of the NAF within the Sea of Marmara, which is situated exactly to the north of the WASZ, can be considered to be a leaky transform. The Sea of Marmara thus marks a major transition in the propagation of the NAF toward the Aegean subduction zone.

The Pliocene Sea of Marmara

We now return to the area that will become the Sea of Marmara ca. 4 Ma. Le Pichon et al. (2014) described a continuous gently curvilinear, south-concave zone of deformation ~10 km wide that extended over the whole southern shelf of the Sea of Marmara, from the Gulf of Gemlik to the Dardanelles Strait, in Lower Pliocene time, ca. 4 Ma (Figs. 3*a* and 3*b*). They called this zone of deformation the SMF system and proposed that the SMF was then a branch of the dextral NAF. They noted that this zone of deformation was associated with a large anticline within the central part of the section, between Marmara and İmralı islands (Figs. 3*a*, 3*b*, and 3*c*). However, the anticline was not found west of Marmara Island nor east of İmralı Island, and the reason for the association of the anticline with the central part of the SMF was not elucidated in their paper.

The basement in the anticline area has been uplifted by more than 1 km, forming a 6–10 km wide anticlinal fold. The consequent uplift led to the erosion of the upper sedimentary units near the summit of the anticline. This folding occurred as the uppermost southeast-dipping foreset beds of the Alçıtepe formation (uppermost Miocene – Lower Pliocene, from 5.3 to 3.7–3.4 Ma, Melinte-Dobrinescu et al. 2009) were still being deposited to the south of the present southern shelf of the Sea of Marmara. The source of the sediments during their deposition was to the northwest and not to the south, which indicates that the Sea of Mar-

Fig. 3 (*concluded*).

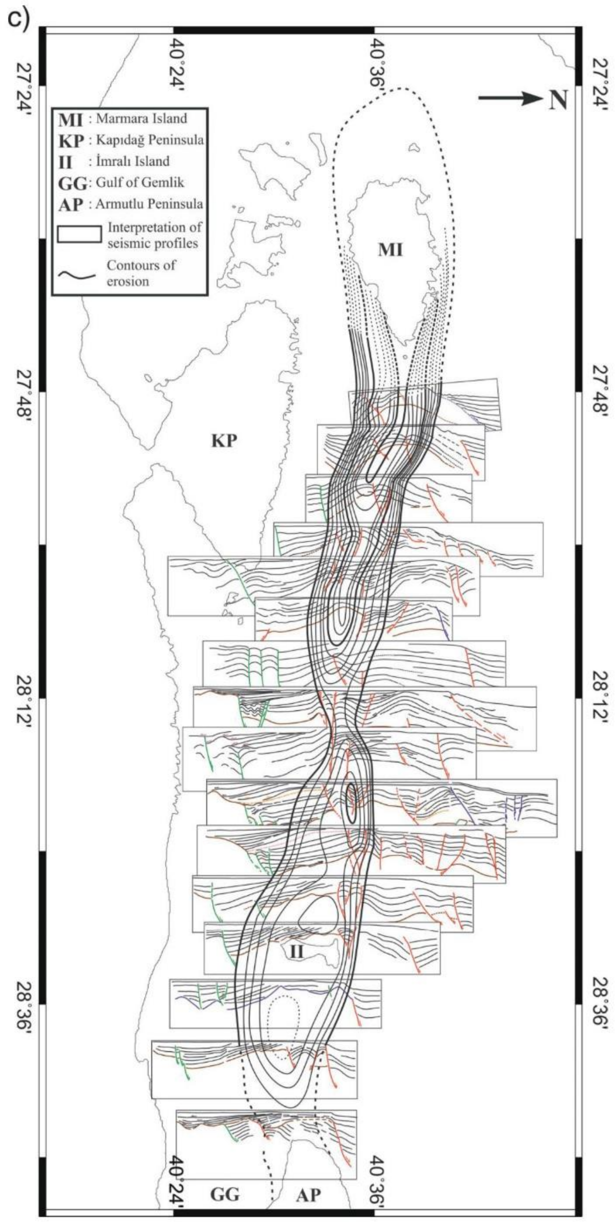

mara deep basins did not exist then. Both the upper Miocene (Kirazlı, from 11–10 to 5.3 Ma) and Uppermost Miocene – Lower Pliocene (Alçıtepe) sedimentary sequences were conformably deposited, then folded and strongly eroded (Figs. 3*c* and 4). Le Pichon et al. (2014) concluded that the uplift occurred near the end of Lower Pliocene, between approximately 4.5 and 3.5 Ma. The uplift of the basement increases westward toward Marmara Island and the maximum uplift is ~1.5–2 km over Marmara Island that was uplifted and broadly warped at this time (see Le Pichon et al. 2014 for a short discussion of the tectonics of the island). An examination of the topography of the island confirms the broad EW anticlinal upwarp of the island. We re-examined the termination of the anticline west of the island of Marmara for this paper (Fig. 4). The anticline and the uplift terminate abruptly along a north-northwest–south-southeast normal fault west of the island of Marmara.

Le Pichon et al. (2014) noted that the SMF occupies the apex of the anticline. But the SMF continues westward of Marmara island to the Biga Peninsula, just east of the Dardanelles Straits, whereas the anticline does not. If the anticline and the SMF were cogenetic, the disappearance of the anticline west of Marmara Island would be puzzling as one would expect the shortening component to increase as the SMF bends its direction southwestward west of Marmara. Indeed, the SMF is clearly compressional west of the island of Marmara and, during the Pliocene, a compressional regime prevailed in the north of the Gelibolu Peninsula, with the formation of the Anafartalar thrust and the deposition of the Conkbayırı alluvial fan related to it (e.g., Çağatay et al. 1998). However, the anticline along the SMF disappears west of the Island of Marmara, and thus this folding appears to be not contractional. This suggests that the formation of the anticline is not related to the SMF. We can conclude further that the SMF occupied the apex of the anticline immediately after the anticline was deactivated, probably because the apex was the weakest portion of the crust as Steckler and ten Brink (1986) predicted that, within a zone of continental thinning, a strength minimum exists just seaward of the hinge zone. But the activity of the SMF was geologically brief as it was terminated when Lower Pliocene fresh water calcareous mudstones were deposited, probably corresponding with the Conkbayırı Formation.

We propose that the anticline is related to a phase of extension comparable with the one now occurring within the GSZ in the Gulf of Corinth and we relate it to the detachments mapped by Bécel et al. (2009) in the southern Sea of Marmara between the sea floor and 13 km depth (see Figs. 3*a*, 3*b*, and 3*c*). We also show in Figs. 3*a* and 3*b* the crests of tilted blocks on top of these detachments as mapped by Bécel et al. (2009). To illustrate the similarity between this system and the Gulf of Corinth extensional system, we show in Fig. 5 an interpreted lithospheric southwest–northeast profile (see location in Fig. 6). The fault locations are from Le Pichon et al. (2014) and Laigle et al. (2008) and the supra-crustal model is based on Bayrakci et al. (2013) while the detachment geometry comes from Bécel et al. (2010). The Moho depth is the J. Kende et al. (in review) model and will be discussed below when presenting Fig. 6. Interpretation of seismic profiles of Turkish Petroleum was also consulted to constrain the fault and sediment deposition geometries on the southern shelf. The locations of microearthquakes are from Kandilli Observatory data. We have added in Fig. 5, below the profile, the sketch of Jolivet et al. (2010) that illustrates the possible future evolution of the Gulf of Corinth to illustrate the similarity between this structure and the Gulf of Corinth one. The possible evolution of the Gulf of Corinth described by Jolivet et al. (2010) is that of a typical Cordilleran-style metamorphic core complex. The origin of the antiform has been attributed to the footwall isostatic rebound by many authors since Spencer (1984) and Wernicke et al. (1985). We consider that Fig. 5 demonstrates that the Southern Shelf anticline and the decollement of Bécel et al. (2009) are cogenetic. Because we know the age of formation of the anticline, ca. 4 Ma, we conclude that the area corresponding to the southern portion of the present Sea of Marmara was similar to the present Gulf of Corinth ca. 4 Ma.

In Figs. 3*a*, 3*b*, and 3*c*, the anticline has two distinct portions, a Marmara portion to the west and an İmralı one to the east. They both have the same orientation and the same width. But they appear to be left-laterally offset. We have sketched in dotted line along the direction of this offset a possible shear. A similar shear with the same direction might limit the İmralı anticline portion and separate it from the Armutlu uplift. Finally, another shear might limit the western extremity of the İznik Basin. In the tectonic context of the time, these shears might correspond to left-lateral X shears and be related to the clockwise rotation that must have affected the whole area in front of the western tip of the NAF,

Fig. 4. Detail of contours of anticline around Marmara Island. Red line indicates the South Marmara Fault (SMF). Yellow barbed lines indicate the direction of propagation of clastics. The top of the Upper Miocene Kirazlı formation rises abruptly across the normal fault to less than 250 m near the island. The log of the Marmara 1 drill hole situated to the east of Marmara Island is given for reference. See Fig. 3a and Le Pichon et al. (2014).

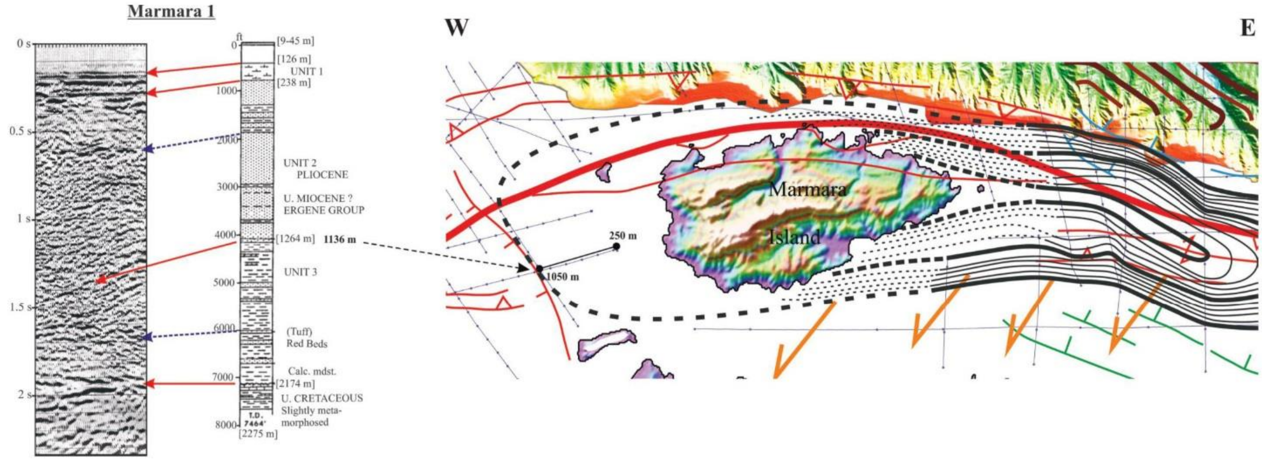

Fig. 5. Interpreted lithospheric southwest–northeast profile (see location in Fig. 7). Fault locations from Le Pichon et al. (2014) and Laigle et al. (2008), supra-crustal model based on Bayrakci et al. (2013), detachment geometry based on Bécel et al. (2010), and Moho depth from the J. Kende et al. (in review) model. Turkish Petroleum line interpretations were also consulted to constrain the fault and sediment deposition geometries on the Southern shelf. Violet faults represent the Main Marmara Fault system in the Central Basin. Black dots are microseismicity localizations from Kandilli Observatory data. For comparison, we have shown at the same scale below the profile the sketch of Jolivet et al. (2010) that illustrates the possible future evolution of the Gulf of Corinth. Green indicates phylite, quartzite. Grey indicates the ductile domain.

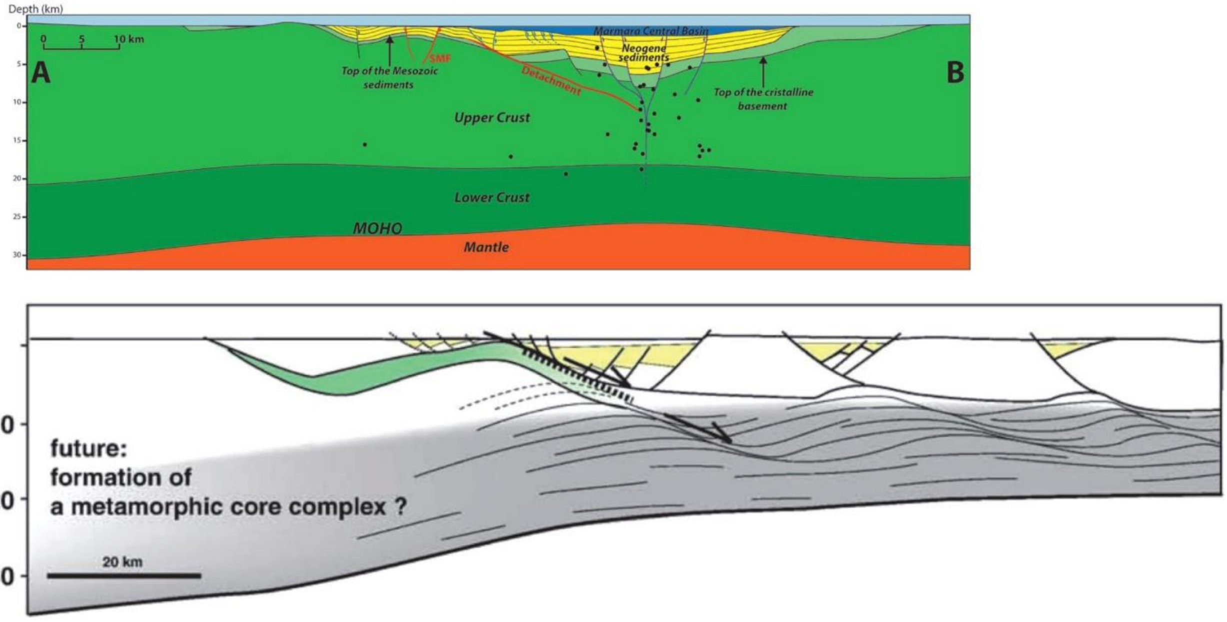

rotation which is attested by the clockwise rotation of 16° detected paleomagnetically by Avşar and İşseven (2009) on volcanic Eocene rocks of the Armutlu Peninsula. It is interesting to note in this context that the orientation of the large İmralı canyon is compatible with the direction of these probable X shears. But we do not have enough structural data to identify this other possible İmralı canyon X shear. Note, however, that, as noted above, the fault along the western end of Armutlu Peninsula has been interpreted by Armijo et al. (2002) as being presently an active dextral fault limiting the presently extending İmralı Basin.

The presence of the İmralı portion of the anticline led us to investigate whether it could also be associated with a detachment, similar to the Marmara one, to the west of the Armutlu Peninsula. We noted on the SEISMARMARA seismic profile in the İmralı Basin (Laigle et al. 2008, fig. 2b; see location of the profile in Figs. 3a and 3b) that the basement dipping northward could be interpreted as a detachment and the basement between İmralı

Fig. 6. Distribution of the marine Alçıtepe Formation (uppermost Miocene – lower Pliocene, from 5.3–3.7 to 3.4 Ma) in blue and the Pliocene undifferentiated continental deposits in yellow after the 1/500 000 map of the General Directorate of Mineral Research and Exploration (2002), Görür et al. (1997), and Sakınç et al. (1999). Map of decollements and anticlines from Fig. 3*a*. The red pattern represents the deformation zone along the South Marmara Fault (SMF).

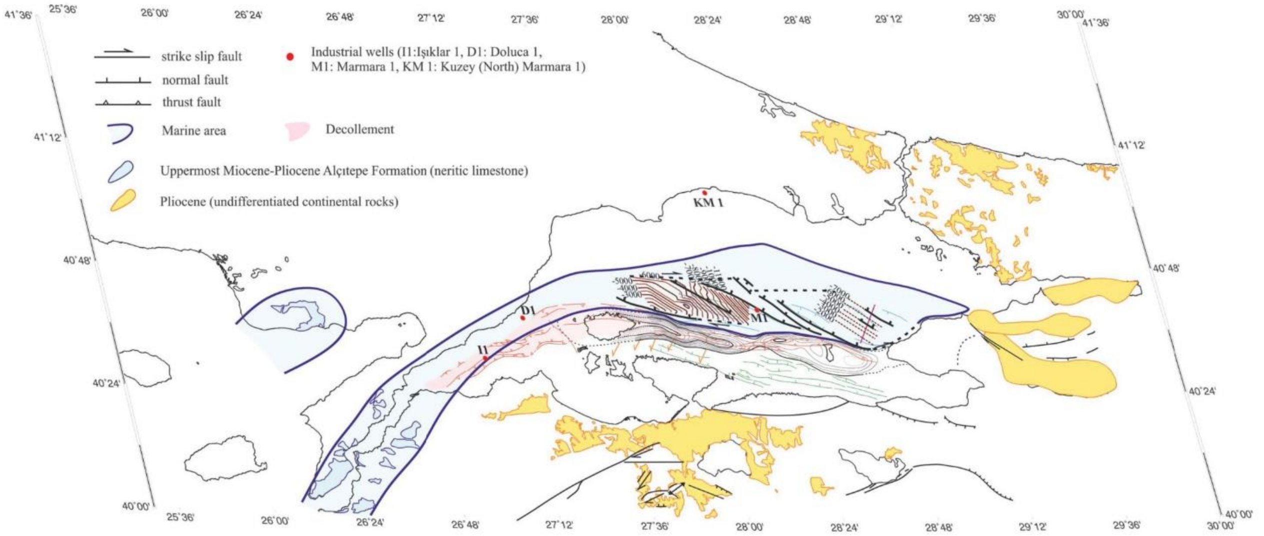

and Çınarcık as a huge tilted block. As we had no other information, we gave to this detachment the same orientation as the Bécel et al. (2009) detachment. We converted it into depth following the conversion used by Bécel et al. (2009). This double basin interpretation, i.e., a western one (paleo-Central Basin) and an eastern one (paleo-İmralı Basin), leads us to propose that the whole area corresponding to the present Sea of Marmara was occupied ca. 3.5–4.5 Ma by two asymmetric extensional basins, with detachments dipping north-northeast, within a broad zone that rotated clockwise in front of the tip of the advancing NAF, as depicted schematically in Fig. 2. This area then should correspond to the oldest portion of the Sea of Marmara and should have a purely extensional origin.

An intriguing point is that the western anticline segment increases in amplitude westward toward Marmara Island, whereas the eastern one increases in amplitude eastward toward İmralı Island. This opposite polarity would be expected if these basins formed a relay between the Eastern NAF and a just initiated paleo-Ganos – Gulf of Saros Fault. This situation then would be similar to the present situation of the GSZ as a relay between the NAT and the Kefalonia–Patras Fault system (Shaw and Jackson 2010, fig. 16).

Figure 6 shows the present distribution of the marine Alçıtepe Formation and of the continental Pliocene after the map of the General Directorate of Mineral Research and Exploration (2002), Görür et al. (1997), and Sakınç et al. (1999). This is the first time when marine Mediterranean and the Marine Paratethyan sequences began mixing in the later history of the Marmara Sea and the well-controlled shape of the marine ingression indicates that it was the southern fault systems that were governing the route of the invading seas (Sakınç et al. 1999, figs. 9 and 10). The distribution of the Alçıtepe neritic formation in the west corroborates that the basins, formed between approximately 4.5 and 3.5 Ma, were situated in the southern portion of the present Sea of Marmara. The distribution of the formations to the west of the present Sea of Marmara appears to be compatible with the initiation of a paleo-Ganos – Gulf of Saros Fault during Uppermost Miocene – Lower Pliocene.

We conclude that sometime between 4.5 and 3.5 Ma, two left-laterally offset basins were formed in a purely extensional context and now correspond to the oldest part of the present Sea of Marmara. At the end of this tectonic episode, the NAF entered for the first time in the Marmara area, through the present Gemlik Bay, within what would later become the shelf of the Sea of Marmara, following the axis of the İmralı and Marmara anticlines. It then presumably joined a paleo-Ganos – Gulf of Saros Fault. Le Pichon et al. (2014) named this branch of the NAF the SMF. Note that, in our interpretation, the present Gemlik Fault was part of the early SMF. Thus, we propose that the SMF was the primary structure in Pliocene and that prior to Pliocene, the shear was distributed over the whole western Anatolia. There was no primary structure then.

The formation of the SMF marked the end of the initial extensional phase and the beginning of the second strike-slip phase, although the transition between the two stages was most probably gradual because extension is still present today in the southern part of the Sea of Marmara. During this second phase, the strike-slip motion migrated northward and established itself along the present MMF. It was responsible for the architecture of the northern part of the Sea of Marmara, which was submitted to a strikingly different strike-slip context than the one prevailing during the first purely extensional phase.

Crustal thinning below the Sea of Marmara

Before getting into the discussion of this second mostly strike-slip phase of formation of the Sea of Marmara, we need to examine crustal thinning there in the context of the overall thinning prevalent in Aegea and western Anatolia since Middle Miocene. Crustal thinning has been investigated by different means with consistent results over the whole Aegean – western Anatolian area (e.g., Tiberi et al. 2001; Tirel et al. 2004; Karabulut et al. 2013; Pearce 2015). The crust has been systematically thinned by more than 10 km below the Aegean Sea (Tirel et al. 2004; Pearce 2015) as well as below the Sea of Marmara (Bécel et al. 2009; Karabulut et al. 2013), the GSZ (Tiberi et al. 2001), and the WASZ (Karabulut et al. 2013). The shallowest Moho is found at a depth of 24 km below the NAT, 23–24 km beneath the Sea of Crete (Tirel et al. 2004), and 23–24 km below the GSZ (Tiberi et al. 2001). In the latter case, Tiberi et al. (2001) pointed out that the highest Moho point is offset with respect to the Gulf of Corinth. This offset suggested to them that the lower crust is affected by boudinage. Below the WASZ, Karabulut et al. (2013) observed long-wavelength variations

Fig. 7. Moho topography in metres after J. Kende et al. (in review). See text. The thick black line represents the Main Marmara Fault (MMF). Blue line represents to location of Fig. 5. Detachments contours and block crests are as in Fig. 3*a*.

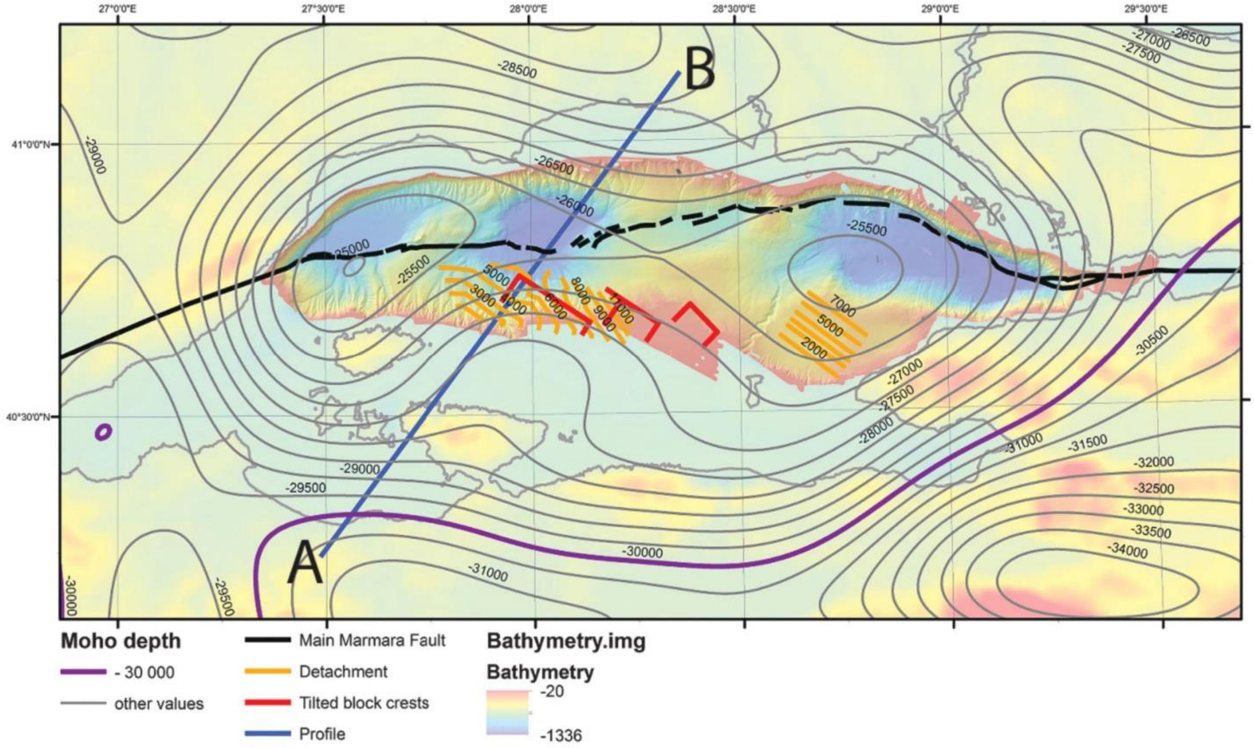

of Moho depth, from ~25 km below the Sea of Marmara (in agreement with Bécel et al. 2009) to ~32 km beneath the İzmir–Ankara suture and to ~25 km beneath the Menderes Massif. This long-wavelength variation suggested to these authors that viscous flow in a hot lower crust has smoothed out the lateral variations of crustal thickness, as mentioned above.

This brief review indicates that the overall crustal thinning in Aegea – western Anatolia has proceeded locally to maxima that lifts the Moho to a depth of ~25 km, below the Gulf of Corinth, northern Aegea, the Sea of Crete, the Sea of Marmara, and the WASZ . This value of 25 km is too prevalent to be purely coincidental. It affects regions where thinning started at widely diverse ages between 20 and 2 Ma. We suggest that this depth of ~25 km of Moho corresponds to the stage of thinning at which the gravitational potential energy of the Aegean continental lithosphere, with respect of the potential energy of the adjacent Ionian oceanic lithosphere, reaches its minimum value (see discussion for example in Le Pichon 1982). Thus, from that stage on, the thinning can only propagate laterally outward. These results suggest furthermore that the lower crust has a long-term viscous mechanical behavior, with boudinage deformation, during the thinning process, as mentioned above.

These important remarks will guide us in the following discussion of the thinning process below the Sea of Marmara in which we will use a new Moho model developed by J. Kende et al. (in review, see Appendix). J. Kende et al. (in review) selected 30 km for the depth of Moho corresponding to an absence of thinning. This value of 30 km is the one given by Karabulut et al. (2013). We preferred it to the 35 km given by Bécel et al. (2009) as they have few constraints away from the offshore domain and as their 35 km value does not seem compatible with the model of Karabulut et al. (2013) although we note that their north–south 2-D model spreads the thinning on a larger area than in our model. Our resulting Moho depth model shown in Fig. 7 maps the Moho depth below the whole Sea of Marmara. The Moho is shallowest at two locations, one north of Marmara Island and the other southwest of the Çınarcık Basin, with a smooth variation in between. The largest amount of crustal thinning is ~10 km. The western zone of highest thinning is narrower and impinges on the southern shelf, whereas the eastern zone is wider and occupies the whole width of the Çınarcık Basin. We note further that the thinning under the Sea of Marmara is asymmetric, steeper to the north and more gradual to the south. Below the MMF, the Moho depth is remarkably constant near 26 km (as discussed below). It deepens abruptly to more than 29 km as the fault leaves the Sea of Marmara, both to the east and the west. The maximum thinning is situated ~10 km to the south of the MMF in the western Marmara Moho high and ~15 km to the south of the MMF in the eastern Çınarcık Moho high. In between, near the profile shown in Fig. 5, the maximum thinning coincides with the MMF. The asymmetry is clearly seen on the profile of Fig. 5 and appears to reflect the asymmetry of the decollement mapped by Bécel et al. (2009). This suggests that the development of the deep crustal structure of the Sea of Marmara has been controlled by the two initial Alçıtepe southern rifts. This control can also be seen in the dual nature of the zone of maximum thinning, which reflects the emplacements of the two Alçıtepe rifts. The eastern Çınarcık Moho high corresponds to the paleo-İmralı Basin, whereas the western Marmara Moho high corresponds to the paleo-Central Basin.

However, it is also striking that there is no one to one correlation between the upper crust structure and the lower crust and mantle one. For example, the zone of maximum thinning to the west extends below the island of Marmara. In addition, although one should be aware of the imperfect resolution of the Moho mapping that was used, the Moho topography is quite smooth, which suggests that the lower crust is indeed governed by a ductile

Fig. 8. "Basement" topography after Bayrakci et al. (2013) superposed to Moho depth contours of Fig. 7 in metres. Basement is defined as having a seismic velocity larger than 4.2 km/s and does not coincide everywhere with crystalline basement. Thick black line represents the Main Marmara Fault (MMF). Yellow lines represent the contours of detachments as in Fig. 7. Submarine fault scarps after Armijo et al. 2002 are represented in white. Black crosses are inverted nodes and red crosses are fixed nodes in the inversion of Bayrakci et al. (2013).

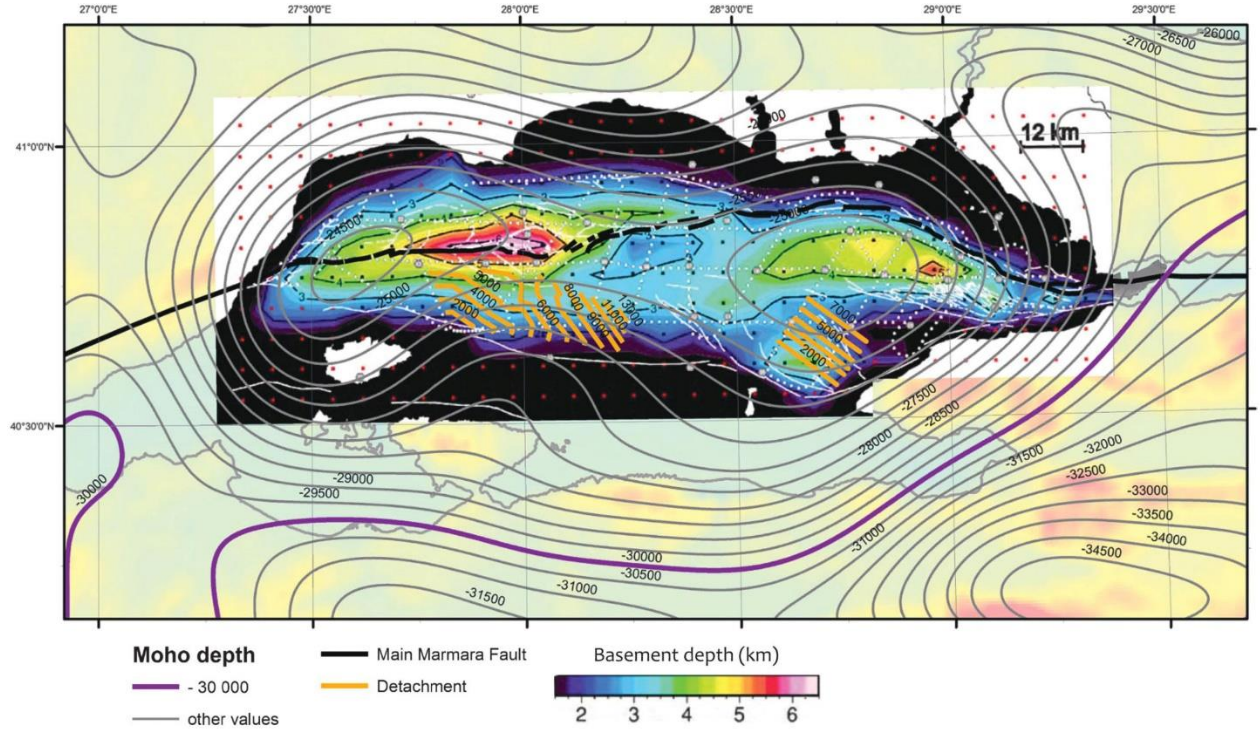

rheology that allows it to flow on a geological time scale. We noted above that Karabulut et al. (2013) had used the smoothness of the Moho topography in western Anatolia as an argument in favor of the flow of the lower crust. This change of rheology between upper and lower crust is also suggested in Fig. 5 by the confinement of the seismicity of the MMF to the upper crust. Thus the upper crust there appears to coincide with the brittle crust. We conclude that our investigation agrees with our previous discussion on the ductile nature of the lower crust and upper mantle over the Aegean – western Anatolian area. Although the structure of the Moho topography below the Sea of Marmara appears to have been in great part controlled by the formation of the two Alçıtepe extensional grabens, its evolution appears to be partly decoupled from the evolution of the upper crust. In addition, it must have been influenced by the later geological strike-slip phase, with the migration of the strike-slip fault northward to the present emplacement of the MMF and the formation of the more recent Tekirdağ and Çınarcık basins.

In Fig. 8 we compare the "basement" topography after Bayrakci et al. (2013) to the topography of the Moho shown in Fig. 7. The basement of Bayrakci et al. (2013) does not coincide everywhere with the crystalline basement. Basement in Fig. 8 is assumed to have a seismic velocity larger than 4.2 km/s. This is because they find a velocity step between 3.9 and 4.5 km/s. It can be considered to be the layer on which occurred the onset of sedimentation in the newly formed North Marmara Trough. The difference between the topography of the basement and the topography of the Moho is striking. Actually, at first sight, one does not see any significant correlation between the two topographies. However, a closer examination shows that the two east–west elongated deep basement troughs that are the main characteristic of the topography of the basement appear to be controlled by the two Alçıtepe grabens. The eastern Çınarcık basement trough corresponds to the paleo-İmralı Basin whereas the western Tekirdağ – Central Basin basement trough is closely correlated to the paleo-Central Basin. But at the difference of the two Moho highs, the linear structure of the troughs follows the direction of the present MMF. The MMF lies at the axis of the western trough; whereas the MMF, which follows the base of the continental slope in the Çınarcık Basin, is parallel but offset 10 km to the north of the eastern trough.

It is remarkable that it would be impossible to predict the present topography characterized by three main basins, Çınarcık, Central, and Tekirdağ, separated by two highs, Central and Western, on the basis of the topography of the basement! That one cannot predict the topography in such an area from the topography of the Moho is not surprising, in view of the decoupling effect of the ductile lower crust. But nobody, to our knowledge, expected the absence of correlation between the topography of the basement and the sea floor topography. This indicates that the two highs are structures that have no roots in the basement. Both highs thus are the products of sedimentary cover tectonics decoupled from the basement, most probably triggered by the strike-slip motion along the MMF. However, this remark needs to be qualified by the fact that the Central High is a zone where the crust is somewhat thicker than either east and west.

The evolution of the NAF in the Sea of Marmara from Lower Pliocene to present

Age of onset of sedimentation in the newly formed North Marmara Trough

To better understand the propagation of the NAF in the Sea of Marmara after the formation the Alçıtepe dual-basins structure,

Fig. 9. Synthesis of information on age of onset of sedimentation in the newly formed North Marmara Trough.

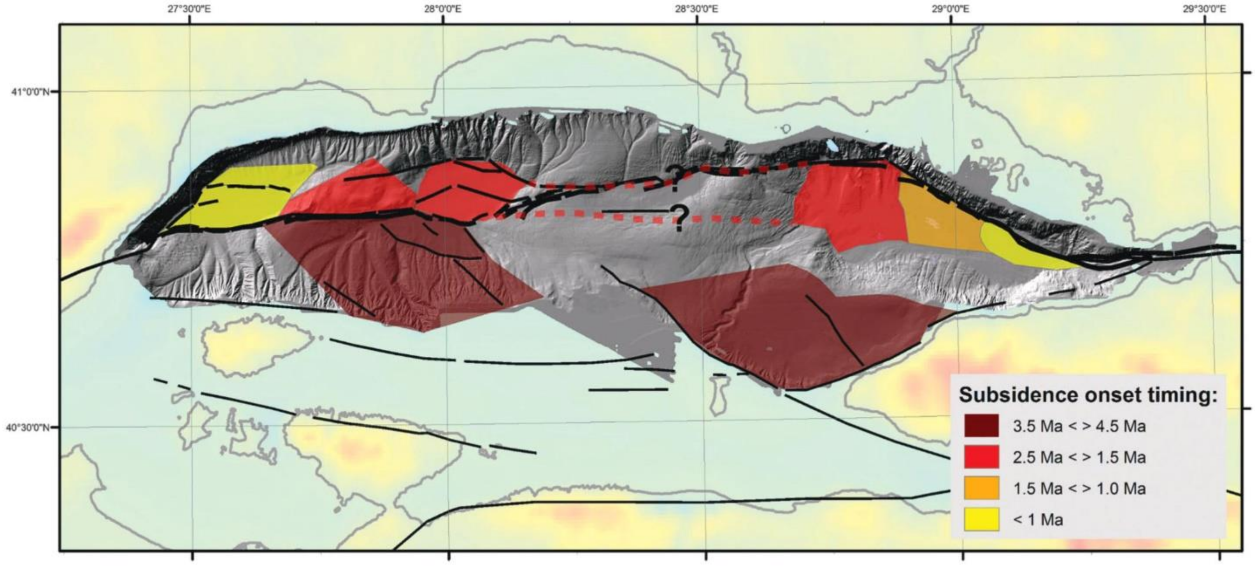

we now try to evaluate our present knowledge of the age of the onset of sedimentation within the different parts of the Sea of Marmara. A synthetic map is presented in Fig. 9. This map reflects our still considerable uncertainties. We have chosen to classify the ages in four categories.

The oldest basins, between 4.5 and 3.5 Ma, are those that were formed during the Alçıtepe extensional stage discussed above. To the west, an onset age of 5–3.5 Ma in the South Central area was proposed on the basis of a heat flow model by Grall et al. (2012). Although this evaluation is fragile, it agrees with the 4.5–3.5 Ma that we proposed above for the basin produced during Alçıtepe by extension along the Marmara decollement mapped by Bécel et al. (2009). We thus adopt an age of 4.5–3.5 Ma. This zone most probably extends further west to the western extremity of the Marmara anticline in the southern Tekirdağ Basin. To the east, in the North İmralı Basin, Sorlien et al. (2012, fig. 13) show a profile along a line north of the present depocenter. If one applies a constant rate of sedimentation and takes into account the effect of compaction, the basin in this zone should be at least 2 Ma. It is definitely older that the Çınarcık Basin to the north or the Tekirdağ Basin to the west. Having no stratigraphic constraints on the deeper horizons, we consider reasonable to assume that the age is the one predicted by the formation of the İmralı decollement and anticline between 4.5 and 3.5 Ma.

The intermediate 2.5–1.5 Ma basins might correspond to the initiation of shearing along the MMF. A maximum age of 1.5–2.5 Ma has been proposed by Grall et al. (2012) for the Central Basin. They show that if one assumes that the subsidence rates have been constant since the beginning of the formation of this basin, the age cannot exceed 2.5 Ma. But although the rate of subsidence has been constant since 250–300 ka, a more rapid subsidence may have been present earlier, which would lead to a younger age. The heat flow model of Grall et al. (2012) confirms that this basin is younger than the basin in the South Central area. We assume for the Western High a similar age in view of the great thickness of sediment (Şengör et al. 2014; Bayrakci et al. 2013). This zone might extend all the way to westernmost Çınarcık (see discussion below).

The youngest 1.5–1 Ma basins correspond to the Tekirdağ and Çınarcık basins, respectively. Seeber et al. (2004) proposed that the Tekirdağ Basin was created by oblique slip. They obtain a maximum age of 1.4 Ma with the parameters used in their model. We believe that if one takes into account the compaction, the maximum age may not exceed 1 Ma. Sorlien et al. (2012) and Kurt et al. (2013) used the same model to predict an age increasing from east to west in the Çınarcık Basin with less than 1 Ma for the easternmost Çınarcık and up to 1.4 in the central portion. We extrapolate an age of 1.5–2.5 Ma for the westernmost part of Çınarcık. Note that the young age of the Çınarcık Basin suggests that the İzmit–Sakarya segment of the NAF that now enters the İzmit Bay is definitely younger than the İznik Fault that enters the Gemlik Bay to the south.

Figure 9 then is compatible with the existence of a southern Marmara Basin formed between 4.5 and 3.5 Ma and a more complex composite younger northern Marmara Basin that propagated outward to the east and to the west sometime after 2.5 Ma along the newly formed SMF.

Subsidence along the MMF since 2.5 Ma

In the following, we explore the possibility that since 2.5 Ma the northern Marmara basins along the present MMF developed through extension accommodated mostly by oblique slip on the transform fault itself (Seeber et al. 2004, 2006; Sorlien et al. 2012; Kurt et al. 2013). Such a model was originally proposed by Seeber et al. (2004) to explain the asymmetry and time-transgressive behavior characteristic of basins, such as the Tekirdağ Basin, that form on the releasing sides of bends on strike-slip faults. The authors cited above have shown that this type of model is quite successful to account for the formation of the basins of the Sea of Marmara that are directly linked to the MMF, in particular the Tekirdağ at its western extremity and the Çınarcık at its eastern extremity. We apply the model through its simplest form. We assume that the side of the fault that is not subsiding is fixed and that the basement dip is parallel to the slip vector. Then the plunge (angle of slip motion with respect to the horizontal) of the slip vector along the main fault is the arc tangent of the subsidence velocity divided by the horizontal velocity. It is thus directly related to the subsidence rate through the rate of horizontal slip. This rather crude model is only used to test the general viability of a process of formation of the basins through extension mostly accommodated by oblique slip as discussed above.

To derive the plunge values presented in Fig. 10*c* we assumed a horizontal slip along the MMF of 18 ± 2 mm/year (Kurt et al. 2013; Grall et al. 2013), which is in agreement with the general discussion

Fig. 10. Compilation of different data along a transect following the Main Marmara Fault (MMF). (*a*) Map of the Sea of Marmara. MMF in red based on Şengör et al. (2014) and contour lines of the Moho depth from Fig. 7. (*b*) Subsidence rate along the MMF retrieved from various studies (see details in text). Dotted line indicates a lack of information to determine the uncertainty. (*c*) Fault plunge along the fault (see details in text). (*d–f*) Crustal thickness, sediment thickness, and Moho depth from Bayrakci et al. (2013) basement model and J. Kende et al. (in review) Moho model presented in Fig. 7.

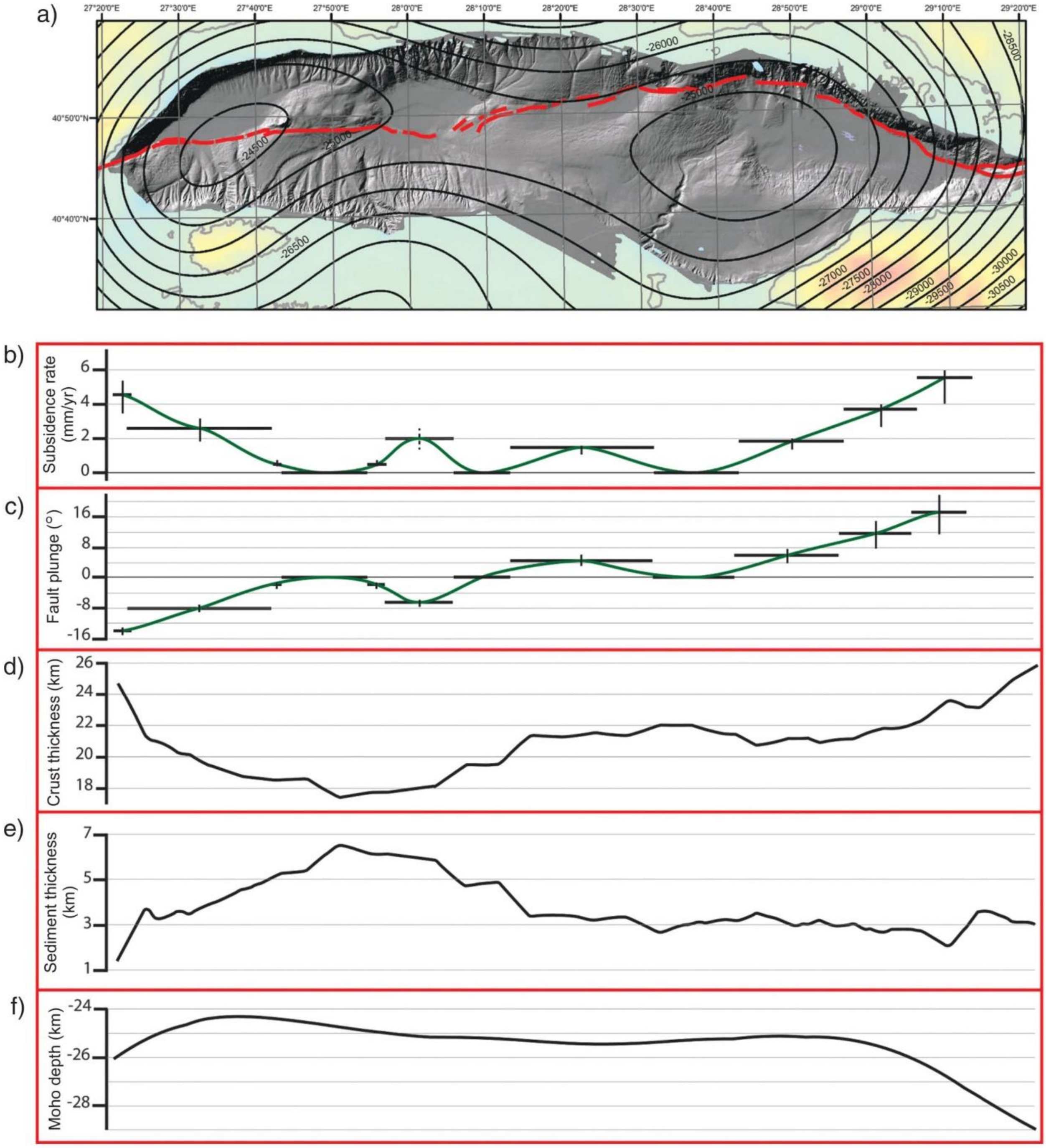

we had above on the geological slip rates along the NAF. The subsidence rates (Fig. 10*b*) were derived from various data as discussed below.

Çınarcık: Kurt et al. (2013) presented a stratigraphic interpretation of the TAMAM dense grid of multichannel seismic profiles. The subsidence rates were derived from the difference between the depths of the green-H5 horizon, a seismic reflector described by Sorlien et al (2012) whose age is estimated to be 540–630 ka (Sorlien et al. 2012; Grall et al. 2013), on each side of the fault. From the east, the subsidence rate decreases, starting at 5.5–4.7 mm/year

(Kurt et al. 2013, figs. 3 and 4) to ~3.7–3.2 mm/year in the middle part of the basin and 1.8–1.5 mm/year to the west (Kurt et al. 2013, fig. 3), giving the corresponding plunge values of 17.1°, 11.6°, and 5.9°. The 17.1° plunge value also corresponds to the dip of the basement along the fault at the eastern corner of the basin.

Kumburgaz: From the same TAMAM survey, Sorlien et al. (2012) presents a profile cutting the Kumburgaz Basin on its western part. Following the same method, a subsidence rate of 1.5–1.3 mm/year and a 4.7° plunge is derived from the green-6 (another seismic reflector described by Sorlien et al. (2012)) depth variation of 0.8 km across the fault (Sorlien et al. 2012, fig. 11).

Central Basin: Grall et al. (2012) presented two models of a profile cutting the basin: a steady-state model based on subsidence rate extrapolation and a model based on seismic line interpretation. We used the depth variation across the fault of the 2 My level in the first model and of the 1.5 My level on the second model as they are presented in their supplementary material (Grall et al. 2012). Both models yield the same subsidence rate of 2 mm/year and a plunge of 6.3°.

Western High: Grall et al. (2013) indicate a sedimentation rate over the last 39 ky that reaches a maximum of 1.5 mm/year in the eastern and western small basins pinching in the Western High (Grall et al. 2013, fig. 6). Correcting for the compaction of shallow sediment of 65%–70% porosity, subsidence at crustal level at these sites should account for about one third of the seafloor subsidence rate. This gives a subsidence rate of 0.5 mm/year corresponding to a plunge of less than 2° over the Western High.

Tekirdağ: The plunge values of 8° and 14° for, respectively, the Tekirdağ Basin and the Ganos small basin off Ganos are inferred by Seeber et al. (2004) assuming that the Tekirdağ Basin geometry is due to a stationary onset point, relatively to the south side of the fault. Thus, the 8° plunge of the basin floor along the fault must correspond to the fault plunge. For the Ganos small basin, Seeber et al. (2004) observed that the absence of horizontal offset where the fault enters the basin could be explained by a displacement plunge equal to the basin rim slope of 14°. Note that because the Tekirdağ Basin is forming northward of the fault, the plunge values are considered as negative, as for the Central Basin.

Moreover, we considered a relative subsidence equal to zero on average across the Western High and on the Central High on either side of the Kumburgaz Basin. The uncertainties were derived from values given in the cited studies, when available. Consequently, most of them were calculated based on uncertainties on age models and on horizontal slip rate (15–20 mm/year) but do not take into account the uncertainty in the relative vertical displacement.

The main interest of Figs. 10*a* and 10*b* is to illustrate the clearly anomalous nature of the western Tekirdağ Basin and of the eastern Çınarcık Basin with their fast outward propagation rate. There, the model proposed by Seeber et al. (2004) appears to account in an elegant way for the evolution of these basins in a pure strike-slip mode. In-between the rates are relatively modest and probably can be accounted for by simple additional north–south distension that is known to be present because of its seismic signature, especially to the south of the western and central part of the Sea of Marmara (Altınok and Alpar 2006; H. Karabulut, personal communication, 2015). We proposed above that in the western and central Sea of Marmara, the MMF coexists with remnants of an extensional system. Finally, as noted above, to the east, the active faulting and subsidence in the İmralı Basin area may also involve continued activity on early structures formed under extension.

Figure 10*e* shows the sediment thickness along the MMF after Bayrakci et al. (2013) and confirms the very large thickness of sediment below the Western High, up to more than 6 km. We discussed this point above. Figure 10*f* gives the depth of the Moho from the inversion of J. Kende et al. (in review) shown in Fig. 7. In Fig. 10*d*, the crustal thickness is obtained by subtraction of the bathymetry and sediment thickness from the Moho depth. The constancy of the Moho depth along the MMF at ~26.5 km is in contrast with the relatively large variation in the crustal thickness. This contrast again testifies that the lower crust acts as a decoupling level in the structuration of the Marmara area. We can also note that the overall thinning of the crust is relatively modest.

To conclude, the evidence we have discussed is compatible with a two-stage formation of the Sea of Marmara. First, two left-laterally offset basins, a paleo-Central Basin to the west and a paleo-İmralı Basin to the east, were formed between 4.5 and 3.5 Ma, in a purely extensional context, in front of the advancing NAF. They now correspond to the oldest part of the present Sea of Marmara. The formation of the SMF on the southern shelf marked the end of the initial extensional phase and the beginning of the second strike-slip phase. During this second phase, the strike-slip motion migrated northward and established itself along the present SMF. Sometime after 2.5 Ma, the northern basins were formed along the present MMF through extension accommodated mostly by oblique slip on the transform fault itself (Seeber et al. 2004, 2006; Sorlien et al. 2012; Kurt et al. 2013). However, the transition between the two stages has most probably been gradual because extension is still present today, especially in the southern part of the western and central Sea of Marmara as well as within the İmralı Basin.

From extension to strike-slip

The evidence we have presented demonstrates, in our opinion, that the formation of the Marmara deep basin began ca. 4.5 Ma during a 1 My purely extensional phase, similar to the one producing today the Corinth Rift. Furthermore, the evidence we discussed above indicates that the proposition made by Le Pichon et al. (1999) that the present MMF is a continuous dextral strike-slip fault that transfers the slip of the eastern NAF from the Gulf of İzmit to the Ganos Fault with a geological slip rate of 18 mm/year is correct. The question then is when did the tectonic change from extension to strike-slip occur and how much finite motion corresponded to each of these tectonic phases. This question does not have simple definitive answers today.

To approach this problem we may start from the total slip on the eastern branch of the NAF, which is estimated today at ~75 ± 10 km (Şengör et al. 2005). This is equivalent to 4.1 My of slip at the present geological slip rate of 18 mm/year, much smaller than the age of initiation of ca. 11 Ma. This led Şengör et al. (2005) to assume a slip rate progressively increasing from 0 at 11 Ma to the present rate during the last million years. With their model, the total finite offset at the beginning of the purely extensional phase in the Marmara area between 4.5 and 3.5 Ma is slightly more than 20 km and the geological rate of slip at that time ~12 mm/year. The modelization of Provost et al. (2003) has demonstrated that the present NAF implies an extremely low friction coefficient of less than 0.05 on the fault plane, 15 times smaller than normal. Such a low friction coefficient indicates that the principal displacement zone is well developed and has reached its maturity through the effect of regularization by many successive earthquakes, which would have produced a total offset of at least 20 km (e.g., Chester et al. 1993). Twenty kilometres is probably the minimum amount of offset one may expect at this time for the NAF to produce on its tip a well-developed extensional shear zone. We accept this 20 km estimate of Şengör et al. (2005) for the offset at 4 Ma and the corresponding probable rate of slip of 12 mm/year at this time.

Note that this conclusion has an important consequence for the tectonics of Aegea from Upper Miocene to Lower Pliocene. This is because, as a consequence, during this period, the subduction rate must have been significantly less than today, probably not more than 20 mm/year as an average, with a progressive increase between 15–12 and 4 Ma, compared to the present subduction rate of 34 mm/year.

We now move to the recent period of strike-slip. The formation of the Tekirdağ and Çınarcık basins by the present MMF occurred at approximately the present 18 mm/year geological slip rate since ca. 1.5 Ma. This indicates that ~27 km of total slip occurred since 1.5 Ma on the MMF. We are left with approximately 30 km of total slip for the period between 3.5 and 1.5 Ma. This gives an average rate of ~15 mm/year, which appears reasonable in view of the many uncertainties. The question then is how this approximate amount of 30 km of total slip was distributed? What was the part of the emerging MMF between 2.5 and 1.5 Ma, the part of possible intermediate systems of strike-slip between the SMF and the MMF, and the part absorbed in the still existing extensional system? We do not have the information necessary to answer this. We can only state with certainty that the present strike-slip system along the MMF was fully functional at the present rate since 1.5 Ma.

Le Pichon et al. (2001) and Le Pichon et al. (2003) had been impressed by the observation that the MMF cuts across older existing structures in the Sea of Marmara. They concluded that the MMF appeared in a late stage of evolution of the Sea of Marmara. Noting that back-slipping the MMF by 4 km appears to restore the Central Bassinette to a symmetric shape, Le Pichon et al. (2001) concluded the MMF appeared only ca. 200 ka. This estimate appeared to be reinforced by the discovery by Armijo et al. (2002) of an offset of 3.5 km of a north–south fold on the Central High. This conclusion was further elaborated by Rangin et al. (2004) and Şengör et al. (2005). It is clear now that this interpretation was not correct and that the event that affected the MMF ca. 200 ka was probably a re-adjustment of the MMF (Grall et al. 2012). But this does not change the observation that the MMF cut across the Marmara Basin more than 2 Ma after its initial extensional formation and that the structures related to it, such as the two elongated basement troughs mapped by Bayrakci et al. (2013), are superimposed on an older principally extensional framework.

Additional discussion of the geodynamics

We pointed out throughout this paper that the lithospheric mantle of the Aegea–Anatolia plate appears to be very thin or even absent and thus that the plate corresponds to a huge ductile mass. This is because the Curie point isotherm (580 °C) south of the NAF is nearly everywhere at a depth of less than 20 km (Aydın et al. 2005), which puts the temperature at more than 900 °C at the Moho. This Curie point isotherm rises to less than 10 km in southwestern Anatolia! McKenzie et al. (2005) have shown that, in continental as well as oceanic lithosphere, the brittle seismogenic zone is limited at its base by the 600 °C isotherm. And numerous studies have confirmed that the part of the mantle that is above 600 °C does not contribute significantly to the elasticity of the plate. As a consequence, the mantle in most of Anatolia and Aegea, south of the NAF, has negligible mechanical resistance. Further, because the temperature within the lower crust exceeds 750 °C, many models predict that channel flow is possible if the composition of the crust is not granulitic (e.g., Beaumont et al. 2004). In addition, because partial fusion is prevalent in many places within the lower crust, transient channel flow would appear as soon as the rate of partial fusion is sufficiently high (McKenzie and Jackson 2002). We can conclude that the mechanical resistance of the Aegean–Anatolian lithosphere lies essentially within its upper brittle crust and that everything happens as if the lower crust acts as a decoupling level. The existence of a decoupling level, somewhere within the lower crust or at the Moho, has been an important acquisition of modern tectonics (e.g., Wernicke et al. 2008). The presence of a decoupling level below the upper crust explains the observation we made above that the NAF appears not to be able to stabilize unless the whole crust is in the brittle domain. If there is possible flow in the lower crust, the upper part of the fault is disconnected from its roots and rapidly looses its “memory”.

If the Aegean–Anatolian lithosphere is mechanically so weak, then how is it possible that traction at its southwestern extremity can be transmitted over 1500 km to its eastern extremity? The answer lies in the role played by the surface relief. The sometime exclusive interest given to the role of the detachments of the slabs in the last few years has led to a neglect of the very important role played by the evolution of topography, with the notable exception of Floyd et al. (2010), for the Aegean – West Anatolian area.

McKenzie (1972) and Le Pichon (1982) had both proposed that the westward movement of the Anatolian lithosphere responded to a gradient in gravitational energy. Currently, the elevation of this plateau is ~2 km and the elevation regularly decreases westward to below sea level within the Aegean Sea (see Fig. 11). The existence of this westward slope of 1.5/1000 results in a gradient of potential gravitational energy that enables the transmission of boundary forces to occur smoothly over the whole length of the Anatolia–Aegea plate (see Le Pichon and Kreemer (2010) for a more complete discussion of these dynamics). And this gradient explains how the southwestward trench pull upon the Aegean lithosphere can lead to a westward traction of Anatolia. But when and how was this gradient established?

Let us first consider when this gradient was established? There is a paradox there. The last marine sediments deposited above the present East Anatolian Plateau date from Serravallian, 13–11 Ma (Şengör et al. 2003). Thus the uplift started at this time, as indicated by the volcanic activity, that was initiated 11 Ma and became plateau-wide at 8 Ma. Şengör et al. (2003) reasonably attributed part of the uplift of the East Anatolian Plateau to slab break-off, arguing that the asthenosphere appeared to lie immediately below the crust, as evidenced by its anomalously low seismic velocity. The existence of a slab break-off was also proposed by Faccenna et al. (2006) and by many others since, as tomographic studies have demonstrated that the plunging African slab below Turkey is detached from the African plate. But, during the same Serravallian time, most of what now forms the central and southern Aegean Sea was rapidly subsiding. Drooger and Meulenkamp (1973) have described the spectacular fragmentation of the southern Aegean landmass that passed below sea level ca. 13 Ma. Yet, the Aegean Sea crust is also underlain by hot asthenosphere (Salaün et al. 2012; Paul et al. 2014), as below the East Anatolian Plateau. As discussed above, the subsidence there, in spite of the presence of hot mantle, results from the fact that, during middle to late Miocene, the crust of the Aegean Sea was thinned by more than 10 km.

Since the work of Aubouin et al. (1976), it has been demonstrated that after the Paleogene phase of nappe stacking, the central Aegean had been the site of intense crustal extension since the beginning of Miocene. This extension had formed core complexes through uplift of the lower middle continental crust to the surface during the middle to late Miocene (Lister et al. 1984). It seems reasonable to assume that the present location of the core complexes were in late Oligocene to early Miocene, the sites of maximum crustal thickness and highest topography, and that they became the sites of maximum crustal extension (Le Pichon et al. 2002). We have argued above that this occurred because the Aegean portion of the slab broke, sometime in late Oligocene, ~10 My earlier than below the East Anatolia Plateau. Consequently, at this time, the asthenosphere rose to come in contact with the lower crust at the Moho. As its southern boundary was a free boundary, able to migrate southward, the crust reacted by southward extension, whereas, 10 My later, below the East Anatolia Plateau no extension was possible because of the collision to the south at the Bitlis suture: the only possibility was uplift. We thus had a situation in early Miocene in which the Aegean and westernmost Anatolia were relatively high, whereas the East

Fig. 11. Topography of the Anatolia–Aegea area. Note the 2 000 m altitude of the East Anatolia Plateau, opposite the Arabian indenter, and the progressive decrease of the elevation westward to less than sea level below the Aegean Sea. The depth contours of the Aegean slab are shown by dashed black lines. The fast-wave polarization axes of shear waves detected by Paul et al. (2014) are also shown (red their measurements, blue previous measurements). Note the progressive counterclockwise rotation of the axes as one gets closer to the Aegean slab. The east–west profiles along 39.5°N show the smoothed topography in blue and the crustal thickness in red after Karabulut et al. (2015).

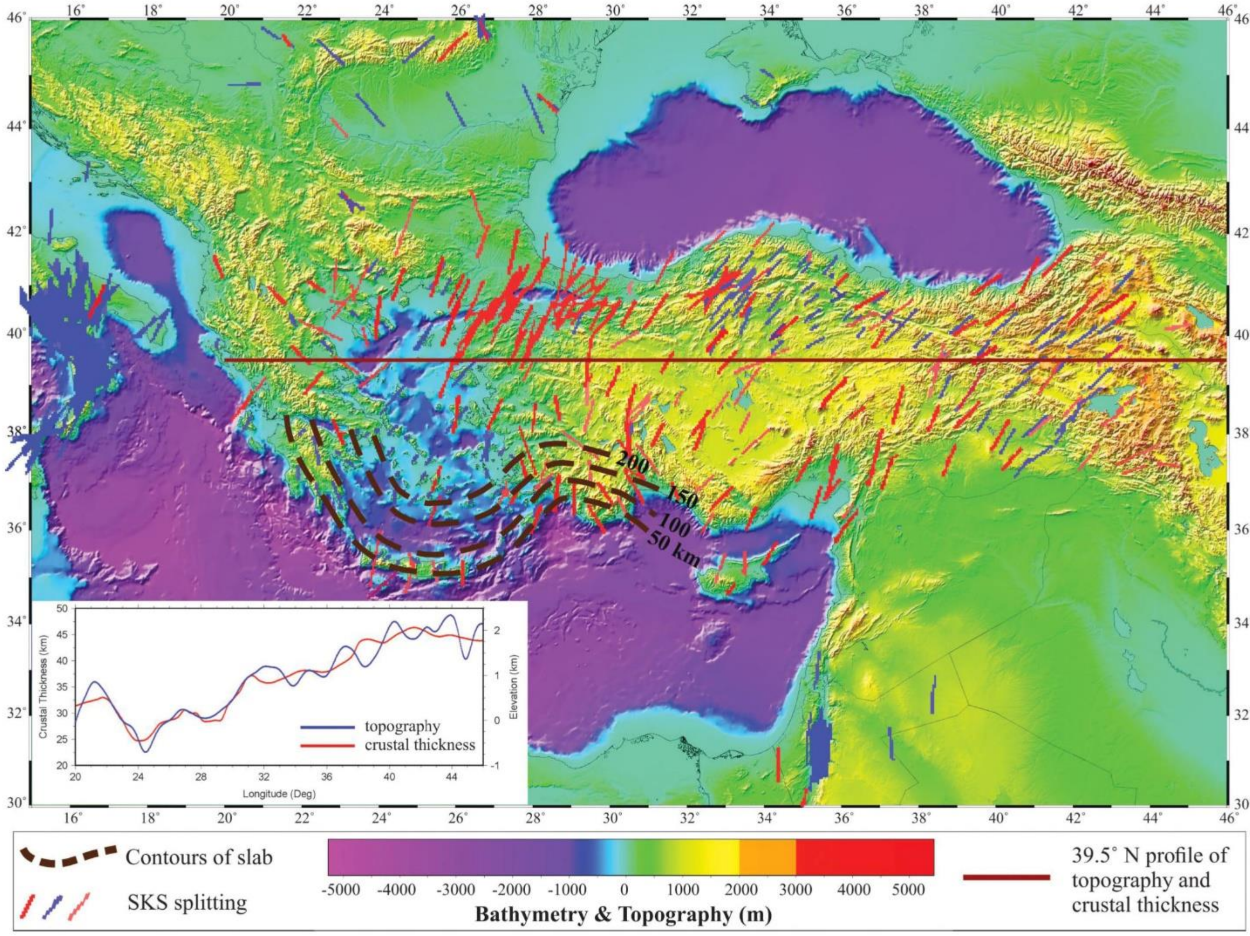

Anatolia Plateau was close to sea level, the exact reverse of what it is now.

We now try to consider how the gradient was established. The topographic and crustal thickness profiles in Fig. 11 indicate that there is a linear relationship between topographic elevation h and crustal thickness T:$h = (T - 27)/9.5$ in kilometres. The crustal thickness for sea level is 27 km and for an altitude of 2 km, on the plateau, 46 km. This is to be compared to the relationship for Tibet, $h = (T - 35)/7$ (Le Pichon et al. 1992). The linear relationship demonstrates that a simple Airy type isostasy prevails there. The fact that, to produce 1 km of additional elevation, one has 9.5 km of additional crustal thickness in Anatolia–Aegea instead of 7 km in Tibet indicates a lower density contrast at the Moho for Anatolia–Aegea than for Tibet. For example, using the values of upper crust density of 2.67 and of lower crust density of 2.95, as adopted by J. Kende et al. (in review), the density of the mantle would be 3.26 for Anatolia–Aegea and 3.39 for Tibet. Of course, this model is very crude but it does confirm that the mantle below the Moho is unusually light, and consequently hot, below Anatolia–Aegea.

If the thickening to 45 km of the crust below the East Anatolia Plateau can be explained by crustal thickening north of the Arabian indenter, no such effect can be invoked to explain the variation in thickness of the crust in central and western Anatolia. The only process that we are able to invoke is lower crust flow from the East Anatolia Plateau toward the west. Such a flow should actually be expected in view of the large amount of magmatism since 8 Ma. This magmatism would have greatly decreased the viscosity of the middle-lower crust (McKenzie and Jackson 2002). Actually, this tectonic situation can be compared with what is now happening on the eastern border of the Tibetan Plateau. This eastern border has been uplifted, without substantial shortening of the upper crust, since 8 Ma, because of the occurrence of east–southeastward flow of the middle-lower crust (e.g., Royden et al. 2008). We conclude that an eastward flow of the lower crust of the East Anatolia Plateau has led to the progressive uplift of Anatolia from east to west.

But was the mantle involved in this westward flow? We have argued that a level of decoupling exists in Anatolia–Aegea within the lower crust. Consequently, the mantle may not necessarily take part in this flow. However, the asthenosphere that had risen up below the East Anatolia Plateau had to escape outward, being pushed by the advancing Arabian indenter and the only possibility of escape for the asthenosphere was to the southwest, toward the Mediterranean, between the Arabian indenter to the east and the Aegean slab to the west. Do we have any indication that such a flow has existed? We can again consider the Tibetan area where the orientation of the fast-wave polarization axes of shear waves aligns itself with directions of principal shear indicating a flow in the mantle, in the same direction as the surface one, with deformation rates exceeding 75% (Holt 2000). On the southeastern border of the Tibetan Plateau, however, Flesch et al. (2005) conclude that the mantle flow, as indicated by these polarization axes, is probably decoupled from the crust. The eastward flow is actually close to the extensional direction, at an angle with the southeastward surface flow, suggesting that deformation rates are smaller there.

In Fig. 11, we show the northeast–southwest orientations of the fast-wave polarization axes of shear waves detected by Paul et al. (2014) over most of Anatolia and the northern Aegean Sea. These are remarkably similar to the extensional directions from GPS (e.g., Le Pichon and Kreemer 2010, fig. 7) or from earthquake fault plane solutions (e.g., Floyd et al. 2010), including the same counterclockwise rotation from eastern Anatolia to the northern Aegean Sea noted by Paul et al. (2014). Thus the upper mantle appears to be decoupled from the crust, flowing along the lithospheric extensional direction, toward the easternmost Mediterranean. This direction of flow is not surprising, as the new Aegean slab has blocked the possible outflow of the asthenosphere in the Aegean – West Anatolian area in the last few million years. Finally, this discussion helps us to understand why, although the westward extrusion of the Anatolia–Aegea plate was initiated 11 Ma, the formation and westward propagation of the NAF took a few million more years to develop, as the westward gravitational gradient was being established.

Conclusions

The Sea of Marmara appears to be a key point in the history of the propagation of the NAF toward the northern extremity of the Aegean subduction during the last 10 My. There is no indication that a localized plate boundary existed north of the Aegean portion of the Anatolia plate before 2 Ma. Prior to this age, the shear produced by the motion of Anatolia with respect to Eurasia was distributed over the whole width of the Aegean – West Anatolian western portion. This was most probably related to the presence there of a north–south component of extension produced by the southward migration of the Aegean subduction. It is no coincidence that fast subduction of the oceanic Ionian lithosphere was initiated a few million years before the Anatolia westward motion. These two processes are obviously tightly linked.

The beginning of the formation of a localized plate boundary occurred between 4.5 and 3.5 Ma at the location of the present Sea of Marmara by the initiation of a shear zone comparable to the present GSZ in central Greece. Thus, the first part of the formation of the Sea of Marmara was purely extensional. The present strike-slip system that today cuts across the whole Sea of Marmara, and that is called MMF, began to develop after 2.5 Ma. Shortly after, the plate boundary migrated westward along the northern border of Aegea from the NAT to the GSZ and to the Kefalonia Fault. There, it finally linked with the northern tip of the Aegean subduction zone, completing the system of plate boundaries delimiting the Anatolia–Aegea plate. We have related the remarkable change in the distribution of shear over Aegea from Miocene to Pliocene to the formation of a relatively undeforming block in Pliocene that forced the shear to be distributed over a narrow plate boundary to the north of it. We attribute the formation of this relatively undeforming Aegean block to the northeastward progression of the cold oceanic Ionian slab. This is because the slab cuts the overlying lithosphere from asthenospheric sources and induces a shortening environment over it. We noted, however, that another possible contribution was the lower subduction rate during the Miocene.

Finally, we wish to make three remarks that may have significant implications for the evaluation of the seismic risk in the Sea of Marmara.

(1) The present structure of the Sea of Marmara results from the superposition of a purely strike-slip system on top of an initial purely en-echelon extensional system. This superposition explains the occurrence of large strike-slip earthquakes together with significant extensional earthquakes that reactivate earlier extensional structures.
(2) The MMF is a continuous dextral strike-slip fault through the whole basin with a present seismic activity strikingly different from the portions of land fault broken by the 1999 Kocaeli and the 1912 Ganos earthquakes. Its continuity and relative homogeneity suggests that one cannot discard the possibility that the whole MMF will break in a single earthquake as proposed by Le Pichon et al. (1999).
(3) The MMF closely follows the base of the northern Marmara margin east of 28°E. As a result there is a 4–6 km offset between the basement on both sides of the fault. Jim Rice (personal communication to X.L.P. 2002) pointed out that this would induce a significant asymmetry of elastic deformation. This asymmetry has very important implications that have essentially been ignored up to this day.

Acknowledgements

X.L.P. thanks the editors for their invitation to write a paper in this special issue of the *Canadian Journal of Earth Sciences* honouring Kevin C. Burke and John F. Dewey. This presentation is one of the outcomes of 15 years of cooperative work with many French and Turkish colleagues. We wish to thank Michel Bouchon for communicating important papers and theses and for discussions on the seismicity of Aegea. We thank the reviewers Michel Bouchon, Namık Çağatay, and Brian Wernicke and the editor Ali Polat for careful and very useful comments. We especially wish to thank Brian Wernicke for many insightful suggestions.

References

Aitken, A.R.A., Salmon, M.L., and Kennett, B.L.N. 2013. Australia's Moho: a test of the usefulness of gravity modelling for the determination of Moho depth. Tectonophysics, **609**: 468–479. doi:10.1016/j.tecto.2012.06.049.

Aksoy, M.E. 2009. Active tectonics and paleoseismology of the Ganos fault segment and seismic characteristics of the 9 August 1912 Mürefte earthquake of the North Anatolian fault (western Turkey). PhD Thesis, Eurasia Institute of Earth Sciences, İstanbul Technical University, Institute de Physique du Globe de Strasbourg, University of Strasbourg.

Allen, C. 1975. Geological criteria for evaluating seismicity—Address as Retiring President of The Geological Society of America, Miami Beach, Florida, November 1974. Geological Society of America Bulletin, **86**: 1041–1057. doi:10.1130/0016-7606(1975)86<1041:GCFES>2.0.CO;2.

Altınok, Y., and Alpar, B. 2006. Marmara Island earthquakes, of 1265 and 1935; Turkey. Natural Hazards and Earth System Science, **6**: 999–1006. doi:10.5194/nhess-6-999-2006.

Angelier, J. 1979. Néotectonique de l'Arc Egéen. Société Géologique du Nord.

Angelier, J., Lybéris, N., Le Pichon, X., Barrier, E., and Huchon, P. 1982. The tectonic development of the Hellenic arc and the Sea of Crete: a synthesis. Tectonophysics, **86**: 159–196. doi:10.1016/0040-1951(82)90066-X.

Armijo, R., Meyer, B., King, G.C.P., Rigo, A., and Papanastassiou, D. 1996. Quaternary evolution of the Corinth Rift and its implications for the Late Cenozoic evolution of the Aegean. Geophysical Journal International, **126**: 11–53. doi:10.1111/j.1365-246X.1996.tb05264.x.

Armijo, R., Meyer, B., Navarro, S., King, G., and Barka, A. 2002. Asymmetric slip partitioning in the Sea of Marmara pull-apart: a clue to propagation processes of the North Anatolian Fault? Terra Nova, **14**: 80–86. doi:10.1046/j.1365-3121.2002.00397.x.

Aubouin, J., Bonneau, M., Davidson, J., Leboulenger, P., Matesco, S., and Zambetakis, A. 1976. Esquisse structurale de l'arc Egéen externe: des Dinarides aux Taurides. Bulletin de la Société Geologique de France, **18**: 327–336. doi:10.2113/gssgfbull.S7-XVIII.2.327.

Avşar, Ü., and İşseven, T. 2009. Regional clockwise rotation of the Armutlu Peninsula, western Turkey, resolved from paleomagnetic study of Eocene volcanics. Tectonophysics, **475**: 415–422. doi:10.1016/j.tecto.2009.05.021.

Aydın, İ., Karat, H.İ., and Koçak, A. 2005. Curie-point depth map of Turkey. Geophysical Journal International, **162**: 633–640. doi:10.1111/j.1365-246X.2005.02617.x.

Bayrakci, G., Laigle, M., Bécel, A., Hirn, A., Taymaz, T., Yolsal-Çevikbilen, S., and SEISMARMARA team. 2013. 3-D sediment-basement tomography of the Northern Marmara trough by a dense OBS network at the nodes of a grid of controlled source profiles along the North Anatolian fault. Geophysical Journal International, **194**: 1335–1357. doi:10.1093/gji/ggt211.

Beaumont, C., Jamieson, R.A., Nguyen, M.H., and Medvedev, S. 2004. Crustal channel flows: 1. Numerical models with applications to the tectonics of the Himalayan–Tibetan orogen. Journal of Geophysical Research: Solid Earth, **109**: B06406. doi:10.1029/2003JB002809.

Bécel, A., Laigle, M., de Voogd, B., Hirn, A., Taymaz, T., Galvé, A., Shimamura, H., et al. 2009. Moho, crustal architecture and deep deformation under the North Marmara Trough, from the SEISMARMARA Leg 1 offshore-onshore reflection-refraction survey. Tectonophysics, **467**: 1–21. doi:10.1016/j.tecto.2008.10.022.

Bécel, A., Laigle, M, de Voogd, B., Hirn, A., Taymaz, T., Yolsal-Cevikbilen, S., and Shimamura, H. 2010. North Marmara Trough architecture of basin infill, basement and faults, from PSDM reflection and OBS refraction seismics. Tectonophysics, **490**: 1–14. doi:10.1016/j.tecto.2010.04.004.

Bijwaard, H., Spakman, W., and Engdahl, E.R. 1998. Closing the gap between regional and global travel time tomography. Journal of Geophysical Research, **103**(B12): 30055–30078. doi:10.1029/98JB02467.

Bulut, F., Bohnhoff, M., Ellsworth, W.L., Aktar, M., and Dresen, G. 2009. Microseismicity at the North Anatolian Fault in the Sea of Marmara offshore Istanbul, NW Turkey. Journal of Geophysical Research: Solid Earth, **114**: B09302. doi:10.1029/2008JB006244.

Çağatay, M.N., Görür, N., Alpar, B., Saatçılar, R., Akkök, R., Sakınç, M., Yüce, H., et al. 1998. Geological evolution of the Gulf of Saros, NE Aegean Sea. Geo-Marine Letters, **18**: 1–9. doi:10.1007/s003670050045.

Çağatay, M.N., Görür, N., Flecker, R., Sakınç, M, Tünoğlu, C., Ellam, R., Krijgsman, W., et al. 2006. Paratethyan–Mediterraenan connectivity in the Sea of Marmara region (NW Turkey) during the Messinian. Sedimentary Geology, **188–189**: 171–187. doi:10.1016/j.sedgeo.2006.03.004.

Chester, F.M., Evans, J.P., and Biegel, R.L. 1993. Internal structure and weakening mechanisms of the San Andreas fault. Journal of Geophysical Research, **98**: 771–786. doi:10.1029/92JB01866.

Chousianitis, K., Ganas, A., and Evangelidis, C.P. 2015. Strain and rotation rate patterns of mainland Greece from continuous GPS data and comparison between seismic and geodetic moment relaease. Journal of Geophysical Research (Solid Earth), **120**: 3909–3931. doi:10.1002/2014JB011762.

Cocard, M., Kahle, H.-G., Peter, Y., Geiger, A., Veis, G., Felekis, S., Paradissis, D., and Billiris, H. 1999. New constraints on the rapid crustal motion of the Aegean region: recent results inferred from GPS measurements (1993–1998) across the West Hellenic arc, Greece. Earth and Planetary Science Letters, **172**: 39–47. doi:10.1016/S0012-821X(99)00185-5.

Drooger, C.W., and Meulenkamp, J.E. 1973. Stratigraphic contribution to geodynamics in the Mediterranean Area: Crete as a case history. Bulletin of the Geological Society of Greece, **10**: 193–200.

Durand, V., Bouchon, M., Floyd, M.A., Theodulidis, N., Marsan, D., Karabulut, H., and Schmittbuhl, J. 2014. Observation of the spread of slow deformation in Greece following the breakup of the slab. Geophysical Research Letters, **41**: 7129–7134. doi:10.1002/2014GL061408.

Faccenna, C., Bellier, O., Martinod, J., Piromallo, C., and Regard, V. 2006. Slab detachment beneath eastern Anatolia: a possible cause for the formation of the North Anatolian Fault. Earth and Planetary Science Letters, **242**: 85–97. doi:10.1016/j.epsl.2005.11.046.

Flesch, L.M., Haines, A.J., and Holt, W.E. 2005. Constraining the extent of crust–mantle coupling in central Asia using GPS, geologic, and shear-wave splitting data. Earth and Planetary Science Letters, **238**: 248–268. doi:10.1016/j.epsl.2005.06.023.

Flotté, N. 2003. Caractérisation Structurale et Cinématique d'un Rift sur Détachement: Le Rift de Corinthe-Patras, Grèce. Thèse de Doctorat, Orsay: Univ Paris-Sud.

Floyd, M.A., Billiris, H., Paradissis, D., Veis, G., Avallone, A., Briole, P., McClusky, S., et al. 2010. A new velocity field for Greece: implications for the kinematics and dynamics of the Aegean. Journal of Geophysical Research, **115**: B10403. doi:10.1029/2009JB007040.

Friedrich, A.M., Lee, J., Wernicke, B.P., and Sieh, K. 2004. Geologic context of geodetic data across a Basin and Range normal fault, Crescent Valley, Nevada. Tectonics, **23**: TC2015. doi:10.1029/2003TC001528.

Gasperini, L., Polonia, A., Çağatay, M.N., Bortoluzzi, G., and Ferrante, V. 2011. Geological slip rate along the North Anatolian Fault in the Marmara region. Tectonics, **30**: TC6001. doi:10.1029/2011TC002906.

General Directorate of Mineral Research and Exploration. 2002. 1/500 000 Geological Map of Turkey.

Goldsworthy, M., Jackson, J., and Haines, J. 2002. The continuity of active fault systems in Greece. Geophysical Journal International, **148**(3): 596–618. doi:10.1046/j.1365-246X. 2002.01609.x.

Görgün, E., and Görgün, B. 2015. Seismicity of the 24 May 2014 M_w 7.0 Aegean Sea earthquake sequence along the North Aegean Trough. Journal of Asian Earth Sciences, **111**: 459–469. doi:10.1016/j.jseaes.2015.06.018.

Görür, N., Çağatay, M.N., Sakınç, M., Sümengen, M., Şentürk, K., Yaltırak, C., and Tchapalyga, A. 1997. Origin of the Sea of Marmara as deduced from Neogene to Quaternary paleogeographic exposition of its framework. International Geology Review, **39**: 342–352. doi:10.1080/00206819709465276.

Grall, C., Henry, P., Tezcan, D., de Lepinay, B.M., Bécel, A., Geli, L., Rudkiewicz, J.-L., et al. 2012. Heat flow in the Sea of Marmara Central Basin: possible implications for the tectonic evolution of the North Anatolian fault. Geology, **40**(1): 3–6. doi:10.1130/G32192.1.

Grall, C., Henry, P., Thomas, Y., Westbrook, G.K., Çağatay, M.N., Marsset, B., Saritas, H., et al. 2013. Slip rate estimation along the western segment of the Main Marmara Fault over the last 405–490 ka by correlating Mass Transport Deposits. Tectonics, **32**(6): 1587–1601. doi:10.1002/2012TC003255.

Gudmundsson, O., and Sambridge, M. 1998. A regionalized upper mantle (RUM) seismic model. Journal of Geophysical Research, **103**(B4): 7121–7136. doi:10.1029/97JB02488.

Holt, W.E. 2000. Correlated crust and mantle strain fields in Tibet. Geology, **28**: 67–70. doi:10.1130/0091-7613(2000)28<67:CCAMSF>2.0.CO;2.

Hubert-Ferrari, A., Armijo, R., King, G., Meyer, B., and Barka, A. 2002. Morphology, displacement, and slip rates along the North Anatolian fault, Turkey. Journal of Geophysical Research: Solid Earth, **107**(B10): ETG 9-1–ETG 9-33. doi:10.1029/2001JB000393.

Jackson, J., and McKenzie. D. 1989. Relation between seismicity and paleomagnetic rotation in zones of distributed continental deformation. *In* Paleomagnetic Rotations and Continental Deformation. *Edited by* C. Kissel and C. Laj. Kluwer Academic Publishers, The Hague. pp. 33–49.

Jolivet, L., Labrousse, L., Agard, P., Lacombe, O., Bailly, V., Lecomte, E., Mouthereau, F., and Mehl, C. 2010. Rifting and shallow-dipping detachments, clues from the Corinth Rift and the Aegean. Tectonophysics, **483**: 287–304. doi:10.1016/j.tecto.2009.11.001.

Karabulut, H., Bouin, M.P., Bouchon, M., Dietrich, M., Cornou, C., and Aktar, M. 2002. The seismicity in the eastern Marmara Sea after the 17 August 1999 İzmit earthquake. Bulletin of the Seismological Society of America, **92**(1): 387–393. doi:10.1785/0120000820.

Karabulut, H., Roumelioti, Z., Benetatos, C., Kömec-Mutlu, A., Özalaybey, S., Aktar, M., and Kiratzi, A. 2006. A source study of the 6 July 2003 (M_w 5.7) earthquake sequence in the Gulf of Saros (Northern Aegean Sea): seismological evidence for the western continuation of the Ganos fault. Tectonophysics, **412**: 195–216. doi:10.1016/j.tecto.2005.09.009.

Karabulut, H., Schmittbuhl, J., Özalaybey, S., Lengliné, O., Kömeç-Mutlu, A., Durand, V., Bouchon, M., et al. 2011. Evolution of the seismicity in the eastern Marmara Sea a decade before and after the 17 August 1999 İzmit earthquake. Tectonophysics, **510**: 17–27. doi:10.1016/j.tecto.2011.07.009.

Karabulut, H., Paul, A., Ergün, T.A., Hatzfeld, D., Childs, D.M., and Aktar, M. 2013. Long-wavelength undulations of the seismic Moho beneath the strongly stretched western Anatolia. Geophysical Journal International, **194**(1): 450–464. doi:10.1093/gji/ggt100.

Karabulut, H., Paul, A., Cambaz, D., Kömeç Mutlu, A., Aksarı, D., and Ergün, T.A. 2015. The images of Anatolia. EGU General Assembly, 12–17 April, 2015, Vienna, Austria. id.8921.

Kastens, K.A. 1991. Rate of outward growth of the Mediterranean Ridge accretionary complex. Tectonophysics, **199**: 25–50. doi:10.1016/0040-1951(91)90117-B.

Kissel, C., Laj, C., Poisson, A., and Görür, N. 2003. Paleomagnetic reconstruction of the Cenozoic evolution of the eastern Mediterranean. Tectonophysics, **362**: 199–217. doi:10.1016/S0040-1951(02)00638-8.

Kozacı, Ö., Dolan, J.F., and Finkel, R.C. 2009. A late Holocene slip rate for the central North Anatolian fault, at Tahtaköprü, Turkey, from cosmogenic ^{10}Be geochronology: implications for fault loading and strain release rates. Journal of Geophysical Research: Solid Earth, **114**: B01405. doi:10.1029/2008JB005760.

Kurt, H., Demirbağ, E., and Kuşçu, İ. 2000. Active submarine tectonism and formation of the Gulf of Saros, northeast Aegean Sea, inferred from multichannel seismic reflection data. Marine Geology, **165**: 13–26. doi:10.1016/S0025-3227(00)00005-0.

Kurt, H., Sorlien, C.C., Seeber, L., Steckler, M.S., Shillington, D.J., Cifci, G., Cormier, M.H., et al. 2013. Steady late quaternary slip rate on the Cinarcik section of the North Anatolian fault near Istanbul, Turkey. Geophysical Research Letters, **40**: 4555–4559. doi:10.1002/grl.50882.

Laigle, M., Bécel, A., de Voogd, B., Hirn, A., Taymaz, T., Ozalaybey, S., and members of SEISMARMARA Leg1 Team. 2008. A first deep seismic survey in the Sea of Marmara: deep basins and whole crust architecture and evolution. Earth and Planetary Science Letters, **270**: 168–179. doi:10.1016/j.epsl.2008.02.031.

Le Pichon, X. 1982. Land-locked oceanic basins and continental collision: the eastern Mediterranean as a case example. *In* Mountain Building Processes. *Edited by* K.J. Hsü. Academic Press, London. pp. 201–211.

Le Pichon, X., and Angelier, J. 1979. The Hellenic arc and trench system: a key to the neotectonic evolution of the eastern Mediterranean area. Tectonophysics, **60**: 1–42. doi:10.1016/0040-1951(79)90131-8.

Le Pichon, X., and Angelier, J. 1981. The Aegean Sea. Philosophical Transactions of the Royal Society of London, **A300**: 357–372.

Le Pichon, X., and Kreemer, C. 2010. The Miocene-to-present kinematic evolution of the eastern Mediterranean and Middle East and its implications for dynamics. Annual Review of Earth and Planetary Sciences, **38**: 323–351. doi:10.1146/annurev-earth-040809-152419.

Le Pichon, X., Fournier, M., and Jolivet, L. 1992. Kinematics, topography, shortening, and extrusion in the India–Eurasia collision. Tectonics, **11**(6): 1085–1098. doi:10.1029/92TC01566.

Le Pichon, X., Chamot-Rooke, N., Huchon, P., and Luxey, P. 1993. Implication des nouvelles mesures de géodésie spatiale en Grèce et Turquie sur l'extrusion latérale de l'Anatolie et de l'Egée. C. R. Académies des Sciences, Paris II, **316**: 983–990.

Le Pichon, X., Chamot-Rooke, N., Lallemant, S., Noomen, R., and Veis, G. 1995. Geodetic determination of the kinematics of central Greece with respect to Europe: implications for eastern Mediterranean tectonics. Journal of Geophysical Research, **100**: 12675–12690. doi:10.1029/95JB00317.

Le Pichon, X., Taymaz, T., and Şengör, A.M.C. 1999. The Marmara fault and the future Istanbul earthquake. *In* ITU-IAHS International Conference on the Kocaeli earthquake 17 August 1999. *Edited by* M. Karaca and D.N. Ural. Istanbul Technical University, Turkey. pp. 41–54.

Le Pichon, X., Şengör, A.M.C., Demirbağ, E., Rangin, C., İmren, C., Armijo, R., Görür, N., et al. 2001. The active main Marmara fault. Earth and Planetary Science Letters, **192**: 595–616. doi:10.1016/S0012-821X(01)00449-6.

Le Pichon, X., Lallemant, S.J., Chamot-Rooke, N., Lemeur, D., and Pascal, G. 2002. The Mediterranean Ridge backstop and the Hellenic nappes. Marine Geology, **186**: 111–125. doi:10.1016/S0025-3227(02)00175-5.

Le Pichon, X., Chamot-Rooke, N., Rangin, C., and Şengör, A.M.C. 2003. The North Anatolian fault in the Sea of Marmara. Journal of Geophysical Research, **108**(B4): 2179. doi:10.1029/2002JB001862.

Le Pichon, X., İmren, C., Rangin, C., Şengör, A.M.C., and Siyako, M. 2014. The South Marmara Fault. International Journal of Earth Sciences (Geol Rundsch), **103**: 219–231. doi 10.1007/s00531-013-0950-0.

Lister, C.S., Banga, G., and Feenstra, A. 1984. Metamorphic core complexes of Cordilleran type in the Cyclades, Aegean Sea, Greece. Geology, **12**: 221–225. doi:10.1130/0091-7613(1984)12<221:MCCOCT>2.0.CO;2.

Martinod, J., Hatzfeld, D., Brun, J.P., Davy, P., and Gautier, P. 2000. Continental collision, gravity spreading, and kinematics of Aegea and Anatolia. Tectonics, **19**(2): 290–299. doi:10.1029/1999TC900061.

Mascle, J., and Martin, L. 1990. Shallow structure and recent evolution of the Aegean Sea: a synthesis based on continuous reflection profiles. Marine Geology, **94**(4): 271–299. doi:10.1016/0025-3227(90)90060-W.

McClusky, S., Balassanian, S., Barka, A., Demir, C., Ergintav, S., Georgiev, I., Gurkan, O., et al. 2000. Global positioning system constraints on plate kinematics and dynamics in the eastern Mediterranean and Caucasus. Journal of Geophysical Research, **105**(B3): 5695–5719. doi:10.1029/1999JB900351.

McClusky, S., Reilinger, R., Mahmoud, S., Sari, D.B., and Tealeb, A. 2003. GPS constraints on Africa (Nubia) and Arabia plate motions. Geophysical Journal International, **155**: 126–138. doi:10.1046/j.1365-246X.2003.02023.x.

McKenzie, D.P. 1970. Plate tectonics of the Mediterranean region. Nature, **226**(5242): 239–243. doi:10.1038/226239a0. PMID:16057188.

McKenzie, D.P. 1972. Active tectonics of the Mediterranean region. Geophysical Journal International, **30**: 109–185. doi:10.1111/j.1365-246X.1972.tb02351.x.

McKenzie, D., and Jackson, J. 1983. The relationship between strain rates, crustal thickening, palaeomagnetism, finite strain and fault movements within a deforming zone. Earth and Planetary Science Letters, **65**(1): 182–202. doi:10.1016/0012-821X(83)90198-X.

McKenzie, D., and Jackson, J. 1986. A block model of distributed deformation by faulting. Journal of the Geological Society, **143**(2): 349–353. doi:10.1144/gsjgs.143.2.0349.

McKenzie, D., and Jackson, J. 1989. The kinematics and dynamics of distributed deformation. *In* Paleomagnetic rotations and continental deformation. *Edited by* C. Kissel and C. Laj. Kluwer Academic Publishers, The Hague. pp. 33–49.

McKenzie, D., and Jackson, J. 2002. Conditions for flow in the continental crust. Tectonics, **21**(6): 5-1–5-7. doi:10.1029/2002TC001394.

McKenzie, D., Jackson, J., and Priestley, K. 2005. Thermal structure of oceanic and continental lithosphere. Earth and Planetary Science Letters, **233**: 337–349. doi:10.1016/j.epsl.2005.02.005.

Meade, B.J., Hager, B.H., McClusky, S.C., Reilinger, R.E., Ergintav, S., Lenk, O., Barka, A., and Özener, H. 2002. Estimates of seismic potential in the Marmara Sea region from block models of secular deformation constrained by global positioning system measurements. Bulletin of the Seismological Society of America, **92**(1): 208–215. doi:10.1785/0120000837.

Meghraoui, M., Aksoy, M.E., Aksyüz, H.S., Ferry, M., Dikbaş, A., and Altunel, E. 2012. Paleoseismology of the North Anatolian Fault at Güzelköy (Ganos segment, Turkey): size and recurrence time of earthquake ruptures west of the Sea of Marmara. Geochemisty, Geophysics, Geosystems, **13**(4): Q04005. doi:10.1029/2011GC003960.

Melinte-Dobrinescu, M.C., Suc, J.-P., Clauzon, G., Popescu, S.-M., Armijo, R., Meyer, B., Biltekin, D., et al. 2009. The Messinian salinity crisis in the Dardanelles region: chronostratigraphic constraints. Paleogeography, Paleoclimatology, Palaeoecology, **278**: 24–39. doi:10.1016/j.palaeo.2009.04.009.

Müller, M.D., Geiger, A., Kahle, H.G., Veis, G., Billiris, H., Paradissis, D., and Felekis, S. 2013. Velocity and deformation fields in the North Aegean domain, Greece, and implications for fault kinematics, derived from GPS data 1993–2009. Tectonophysics, **597–598**: 34–49. doi:10.1016/j.tecto.2012.08.003.

Nielsen, C. 2003. Etude des zones de subduction en convergence hyper-oblique: ride méditerranéenne, marge indo-birmane. Thèse de doctorat, Université Paris XI, Orsay.

Oldenburg, D.W. 1974. The inversion and interpretation of gravity anomalies. Geophysics, **39**(4): 526–536. doi:10.1190/1.1440444.

Oncken, O., Chong, G., Franz, G., Giese, P., Götze, H.-J., Ramos, V.A., Strecker, M.R., and Wigger, P. 2006. An Andes: Active Subduction Orogeny (Frontiers in the Earth Sciences Series). Springer, Berlin.

Örgülü, G. 2011. Seismicity and source parameters for small-scale earthquakes along the splays of the North Anatolian Fault (NAF) in the Marmara Sea. Geophysical Journal International, **184**(1): 385–404. doi:10.1111/j.1365-246X.2010.04844.x.

Parker, R.L. 1973. The Rapid Calculation of Potential Anomalies. Geophysical Journal International, **31**(4): 447–455. doi:10.1111/j.1365-246X.1973.tb06513.x.

Paul, A., Karabulut, H., Kömec-Mutlu, A., and Salaün, G. 2014. A comprehensive and densely sampled map of shear-wave azimuthal anisotropy in the Aegean–Anatolia region. Earth and Planetary Science Letters, **389**: 14–22. doi:10.1016/j.epsl.2013.12.019.

Pearce, F.D. 2015. Seismic imaging of the western Hellenic subduction zone: the relationship between slab composition, retreat rate, and overriding lithosphere genesis. PhD thesis, Department of Earth, Atmospheric, and Planetary Sciences, Massachussetts Institute of Technology, Cambridge, MA, USA.

Pérouse, E., Chamot-Rooke, N., Rabaute, A., Briole, P., Jouanne, F., Georgiev, I., and Dimitrov, D. 2012. Bridging onshore and offshore present-day kinematics of central and estern Mediterranean: implications for crustal dynamics and mantle flow. Geochemistry, Geophysics, Geosystems, **13**(9): Q09013. doi:10.1029/2012GC004289.

Piromallo, C., and Morelli, A. 2003. *P* wave tomography of the mantle under the Alpine–Mediterranean area. Journal of Geophysical Research, **108**(B2): 2065. doi:10.1029/2002JB001757.

Provost, A.S., Chéry, J., and Hassani, R. 2003. 3-D mechanical modeling of the GPS velocity field along the North Anatolian Fault. Earth and Planetary Science Letters, **209**: 361–377. doi:10.1016/S0012-821X(03)00099-2.

Rangin, C., Le Pichon, X., Demirbag, E., and Imren, C. 2004. Strain localization in the Sea of Marmara: propagation of the North Anatolian Fault in a now inactive pull-apart. Tectonics, **23**: TC2014. doi:10.1029/2002TC001437.

Reilinger, R.E., McClusky, S.C., Oral, M.B., King, R.W., Toksoz, M.N., Barka, A.A., Kinik, I., et al. 1997. Global positioning system measurements of present-day crustal movements in the Arabia–Africa–Eurasia plate collision zone. Journal of Geophysical Research, **102**(B5): 9983–9999. doi:10.1029/96JB03736.

Reilinger, R., McClusky, S., Vernant, P., Lawrence, S., Ergintav, S., Cakmak, R., Ozener, H., et al. 2006. GPS constraints on continental deformation in the Africa–Arabia–Eurasia continental collision zone and implications for the dynamics of plate interactions. Journal of Geophysical Research: Solid earth, **111**(B5). doi:10.1029/2005JB004051.

Rigo, A., Lyon-Caen, H., Armijo, R., Deschamps, A., Hatzfeld, D., Makropoulos, K., Papadimitriou, P., and Kassaras, I. 1996. A microseismic study in the western part of the Gulf of Corinth (Greece): implications for large-scale normal faulting mechanisms. Geophysical Journal International, **126**(3): 663–688. doi:10.1111/j.1365-246X.1996.tb04697.x.

Royden, L.H., and Husson, L. 2006. Trench motion, slab geometry and viscous stresses in subduction systems. Geophysical Journal International, **167**(2): 881–905. doi:10.1111/j.1365-246X.2006.03079.x.

Royden, L.H., and Papanikolaou, D.J. 2011. Slab segmentation and late Cenozoic disruption of the Hellenic arc. Geochemistry, Geophysics, Geosystems, **12**(3): Q03010. doi:10.1029/2010GC003280.

Royden, L.H., Burchfiel, B.C., and van der Hilst, R.D. 2008. The geological evolution of the Tibetan Plateau. Science, **321**: 1054–1058. doi:10.1126/science.1155371. PMID:18719275.

Sakınç, M., Yaltırak, C., and Oktay, F.Y. 1999. Palaeogeographical evolution of the Thrace Neogene Basin and the Tethys–Paratethys relations at northwestern Turkey (Thrace). Palaeogeography, Palaeoclimatology, Palaeoecology, **153**: 17–40. doi:10.1016/S0031-0182(99)00071-1.

Salaün, G., Pedersen, H.A., Paul, A., Farra, V., Karabulut, H., Hatzfeld, D., Papazachos, C., et al. 2012. High resolution surface wave tomography beneath the Aegean–Anatolia region: constraints on upper-mantle structure. Geophysical Journal International, **190**(1): 406–420. doi:10.1111/j.1365-246X.2012.05483.x.

Seeber, L., Emre, O., Cormier, M.-H., Sorlien, C.C., McHugh, C., Polonia, A., Ozer, N., et al. 2004. Uplift and subsidence from oblique slip: the Ganos–Marmara bend of the North Anatolian Transform, western Turkey. Tectonophysics, **391**(1–4): 239–258. doi:10.1016/j.tecto.2004.07.015.

Seeber, L., Cormier, M.H., McHugh, C., Emre, O., Polonia, A., and Sorlien, C. 2006. Rapid subsidence and sedimentation from oblique slip near a bend on the North Anatolian transform fault in the Marmara Sea, Turkey. Geology, **34**(11): 933–936. doi:10.1130/G22520A.1.

Şengör, A.M.C. 1979. The North Anatolian Transform Fault: its age, offset and tectonic significance. Journal of the Geological Society, **136**: 269–282. doi:10.1144/gsjgs.136.3.0269.

Şengör, A.M.C. 1982. Ege'nin neotektonik evrimini yöneten etkenler [Factors controlling the neotectonics of the Aegean]. *In* Batı Anadolu'nun Genç Tektoniği ve Volkanizması. *Edited by* O. Erol and V. Oygür. Türkiye Jeoloji Kurumu, Ankara, pp. 59–71.

Şengör, A.M.C., and Zabcı, C. 2016 The North Anatolian Fault and the North Anatolian Shear Zone. *In* Landscapes of Turkey. *Edited by* C. Kuzucuoğlu and A. Ciner. Springer, Berlin. [In press].

Şengör, A.M.C., Burke, K., and Dewey, J.F. 1982. Tectonics of the North Anatolian transform fault. *In* Multidisciplinary approach to earthquake prediction. *Edited by* A.M. Işıkara and A. Vogel. Friedr. Vieweg Sohn, Braunschweig/Wiesbaden, pp. 3–22.

Şengör, A.M.C., Özeren, S., Genç, T., and Zor, E. 2003. East Anatolian high plateau as mantle-suppoted, north–south shortened domal structure? Geophysical Research Letters, **30**(24): doi:10.1029/2003GL017858.

Şengör, A.M.C., Tüysüz, O., İmren, C., Sakınç, M., Eyidoğan, H., Görür, N., Le Pichon, X., and Rangin, C. 2005. The North Anatolian Fault: a new look. Annual Review of Earth and Planetary Sciences, **33**: 37–112. doi:10.1146/annurev.earth.32.101802.120415.

Şengör, A.M.C., Grall, C., İmren, C., Le Pichon, X., Görür, N., Henry, P., Karabulut, H., and Siyako, M. 2014. The geometry of the North Anatolian transform fault in the Sea of Marmara and its temporal evolution: implications for the development of intracontinental transform faults. Canadian Journal of Earth Sciences, **51**: 222–242. doi:10.1139/cjes-2013-0160.

Shaw, B., and Jackson, J. 2010. Earthquake mechanisms and active tectonics of the Hellenic subduction zone. Geophysics Journal International, **181**(2): 966–984. doi:10.1111/j.1365-246X.2010.04551.x.

Smith, W.H.F., and Sandwell, D.T. 1997. Global sea floor topography from satellite altimetry and ship depth soundings. Science, **277**: 1956–1962. doi:10.1126/science.277.5334.1956.

Sodoudi, F., Kind, R., Hatzfeld, D., Priestley, K., Hanka, W., Wylegalla, K., Stavrakakis, G., Vafidis, A., Harjes, H.P., and Bohnhoff, M. 2006. Lithospheric structure of the Aegean obtained from P and S receiver functions. Journal of Geophysical Research, **111**(B12): B12307. doi:10.1029/2005JB003932.

Sonder, L.J., and England, P.C. 1989. Effects of a temperature-dependent rheology on large-scale continental extension. Journal of Geophysical Research, **94**(B6): 7603–7619. doi:10.1029/JB094iB06p07603.

Sorel, D. 2000. A Pleistocene and still-active detachment fault and the origin of the Corinth–Patras rift, Greece. Geology, **28**(1): 83–86. doi:10.1130/0091-7613(2000)28%3C83:APASDF%3E2.0.CO;2.

Sorlien, C.C., Akhun, S.D., Seeber, L., Steckler, M.S., Shillington, D.J., Kurt, H., Çifçi, G., et al. 2012. Uniform basin growth over the last 500 ka, North Anatolian Fault, Marmara Sea, Turkey. Tectonophysics, **518–521**: 1–16. doi:10.1016/j.tecto.2011.10.006.

Spakman, W., van der Lee, S., and van der Hilst, R. 1993. Travel time tomography of the European–Mediterranean mantle down to 1400 km. Physics of Earth and Planetary Interiors, **79**(1–2): 3–74. doi:10.1016/0031-9201(93)90142-V.

Spencer, J.E. 1984. Role of tectonic denudation in the warping and uplift of low-angle normal faults. Geology, **12**: 95–98. doi:10.1130/0091-7613(1984)12<95:ROTDIW>2.0.CO;2.

Steckler, M.S., and ten Brink, U.S. 1986. Lithospheric strength variations as a control on new plate boundaries: examples from the northern Red Sea region. Earth and Planetary Science Letters, **79**(1–2): 120–132. doi:10.1016/0012-821X(86)90045-2.

Suckale, J., Rondenay, S., Sachpazi, M., Charalampakis, M., Hosa, A., and Royden, L.H. 2009. High-resolution seismic imaging of the western Hellenic subduction zone using teleseismic scattered waves. Geophysical Journal International, **178**(2): 775–791. doi:10.1111/j.1365-246X.2009.04170.x.

Sümengen, M., Terlemez, İ., Şentürk K, Karaköse, C., Erkan, E., Ünay, E., Gürbüz, M. and Atalay, Z. 1987. Stratigraphy, sedimentology, and tectonics of the Tertiary sequences in Gelibolu Peninsula and southwestern Thrace. Mineral Research and Exploration of Turkey. Technical Report 8128. [In Turkish.]

Tarantola, A. 2005. Inverse problem theory and methods for model parameter estimation. Society for Industrial and Applied Matematics.

Tiberi, C., Diament, M., Lyon-Caen, H., and King, T. 2001. Moho topography beneath the Corinth Rift area (Greece) from inversion of gravity data. Geophysical Journal International, **145**(3): 797–808. doi:10.1046/j.1365-246x.2001.01441.x.

Tirel, C., Gueydan, F., Tiberi, C., and Brun, J.P. 2004. Aegean crustal thickness inferred from gravity inversion. Geodynmaical Implications. Earth and Planetary Science Letters, **228**: 267–280. doi:10.1016/j.epsl.2004.10.023.

Tirel, C., Brun, J.P., Burov, E., Wortel, M.J.R., and Lebedev, S. 2013. A plate tectonics oddity: caterpillar-walk exhumation of subducted continental crust. Geology, **41**(5): 555–558. doi:10.1130/G33862.1.

Truffert, C., Chamot-Rooke, N., Lallemant, S., de Voogd, B., Huchon, P., and Le Pichon, X. 1993. The crust of the Western Mediterranean Ridge from deep seismic data and gravity modelling. Geophysical Journal International, **114**(2): 360–372. doi:10.1111/j.1365-246X.1993.tb03924.x.

Tüysüz, O., Barka, A., and Yiğitbaş, E. 1998. Geology of the Saros graben and its implications for the evolution of the North Anatolian fault in the Ganos–Saros region, northwestern Turkey. Tectonophysics, **293**(1–2): 105–126. doi:10.1016/S0040-1951(98)00085-7.

Ustaömer, T., Gökaşan, E., Tur, H., Görüm, T., Batuk, F.G., Kalafat, D., Alp, H., et al. 2008. Faulting, mass-wasting and deposition in an active dextral shear zone, the Gulf of Saros and the NE Aegean Sea, NW Turkey. Geo-Marine Letters, **28**(3): 171–193. doi:10.1007/s00367-007-0099-6.

Van Hinsbergen, D.J.J., Langereis, C.G., and Meulenkamp, J.E. 2005. Revision of the timing, magnitude and distribution of Neogene rotations in the western Aegean region. Tectonophysics, **396**(1–2): 1–34. doi:10.1016/j.tecto.2004.10.001.

Van Hinsbergen, D.J.J., Dekkers, M.J., Bozkurt, E., and Koopman, M. 2010. Exhumation with a twist: paleomagnetic constraints on the evolution of the Menderes metamorphic core complex, western Turkey. Tectonics, **29**(3): TC3009. doi:10.1029/2009TC002596.

Vassalikis, E., Royden, L., and Papanikolaou, D. 2011. Kinematic links between subduction along the Hellenic trench and extension in the Gulf of Corinth, Greece: a multidisciplinary analysis. Earth and Planetary Science Letters, **303**(1–2): 108–120. doi:10.1016/j.epsl.2010.12.054.

Vernant, P., Reilinger, R., and McClusky, S. 2014. Geodetic evidence for low coupling on the Hellenic subduction plate interface. Earth and Planetary Science Letters, **385**: 122–129. doi:10.1016/j.epsl.2013.10.018.

Wernicke, B., Walker, J.D., and Beaufait, M.S. 1985. Structural discordance between neogene detachments and frontal sevier thrusts, central Mormon mountains, southern Nevada. Tectonics, **4**(2): 213–246. doi:10.1029/TC004i002p00213.

Wernicke, B., Davis, J.L., Niemi, N.A., Luffi, P., and Bisnath, S. 2008. Active megadetachment beneath the western United States. Journal of Geophysical Research, **113**: B11409. doi:10.1029/2007JB005375.

Appendix A

Moho model

The model of J. Kende et al. (in review) was obtained through a gravity inversion in the Fourier domain of the measured gravity corrected from the upper crust geology. The gravity and topography data used are satellite data (Smith and Sandwell 1997) retrieved from the Scripps Institution of Oceanography website. Gravity data were refined, when possible, with the records from the Bodenseewerk KSS 31 gravimeter during the Marsite Cruise on board the NO "Pourquoi Pas?" in October and November 2014. To avoid superficial crustal effects, the topography was filtered with a 20 km window Gaussian filter before being used to apply a Bouguer correction onshore. Then, the offshore gravity was corrected from the known basin geology. The two sediment layers basin model from Bayrakci et al. (2013) was used, completed on the southern shelf with Turkish Petroleum multichannel seismic line interpretations. The correction was made in the Fourier domain using the Parker method (Parker 1973). A first Moho depth variation was computed by inverting the residual gravity anomaly and a lower crust/upper crust boundary (LC/UC) was defined 9 km above this depth model. An iterative process was then launched. It used the sediment basin model and the newly defined LC/UC to correct the measured gravity with the Parker method, obtaining a new gravity residual. The inversion of this new gravity residual led to a new Moho depth model. This process, repeated twice, enhanced the overall model significantly as it lowered the final residual anomaly.

The method developed for the study of J. Kende et al. (in review) is close to the Parker-Oldenburg method (Oldenburg 1974) and is based on a least-square linear inversion with preconditioning (Tarantola 2005). This method proved to be fast and effective for large-scale 2-D models. It also avoided part of the human bias associated with forward modeling (Aitken et al. 2013). However, because this model relies on a simplified basin structure, the choice of the densities of the two sedimentary layers has a strong impact on the Moho depth variation amplitude. Data well constrain the Moho geometry only at spatial wavelengths longer than crustal thickness. To damp Moho oscillations at shorter wavelengths, Moho deviation from the mean regional value is preconditioned to zero and a third parameter (Moho variance scaling) entered by the user defines the weight of this preconditioning. After defining a range of possible mean densities for each of these parameters, the final values used for the results presented here were those that best agreed with Bécel et al. (2009) and Karabulut et al. (2013) Moho depth models.

Bécel et al. (2009) presented a Moho model based on a dense grid of multi-channel marine seismic profiles with a high penetration depth retrieved during the SEISMARMARA Leg 1, completed with the data from on-land temporary seismometers and ocean bottom seismometers (OBSs). Their study was designed so that the profiles crossed each other at OBS positions and had land stations in their continuity. Crossing profiles permitted, for instance, to identify side echoes that could appear as flat interface events on some profiles, while OBSs first arrival time of refracted waves on the basement were used to build a basement velocity and geometry model. Finally, on land, station records of refraction on the upper mantle (Pn waves) were integrated, which was critical for the 2-D model under the Northern Marmara Trough as only two OBSs clearly recorded refraction on the Moho. Bécel et al. (2009) concluded that there had been a 5 km crustal thinning below the Northern Marmara Trough and under the İmralı Basin as the Moho height was essentially constant at a depth of 26 km. Their study, however, put no constraint on the possible existence of small-scale thinning variations. Because the north–south Moho depth variation obtained was close to the data resolution, they could not resolve conclusively the existence of possible north–south variations.

Karabulut et al. (2013) on the other hand published a north–south 650 km long profile of lithospheric structures. This profile crosses the Sea of Marmara in the eastern part of the Tekirdağ Basin. They relied on a set of 17 permanent broadband seismic stations and 23 temporary stations installed as part of the SIMBAD project to fill the gaps and create a spacing between stations of ~15 km along the transect. After a year of recording, they selected 60 events with a magnitude superior or equal to 5.5 and a tolerable noise level. They then performed a depth migration of the P-to-S converted phases and interpreted the Moho as the level of sharp increase of amplitude undulating between 25 and 32 km. Their station coverage is not tight enough at the level of the Marmara Sea to determine the detailed Moho depth variation but Karabulut et al. (2013) showed an uplift of 6–7 km centered under the sea with a width of less than 250 km. The highest Moho under the Sea of Marmara obtained in the two studies is the same, ~25 km.

Résumé

La mer de Marmara, reliée à la Méditerranée par le détroit des Dardanelles et à la mer Noire par le Bosphore, est la clef de voute d'un système hydrique complexe où l'eau douce transite vers l'Ouest tandis que de l'eau salée circule en profondeur vers l'Est. Toutefois cet équilibre a régulièrement été rompu, lorsque la baisse du niveau global des océans provoquait l'isolement de la Mer de Marmara. L'alternance de dépôts sédimentaires lacustres et marins témoigne de ces variations. Mais la mer de Marmara est aussi une structure tectonique active dont la morphologie est lentement modifiée par la branche nord de la faille Nord-Anatolienne. Cette faille décrochante continentale, l'une des plus longues du monde, est régulièrement à l'origine de forts tremblements de terre et menace Istanbul et ses 15 millions d'habitants. Les études scientifiques sont nombreuses à vouloir caractériser le fonctionnement actuel et passé de la faille pour préciser l'aléa sismique auquel Istanbul est exposé. Cette thèse est constituée de deux études qui s'attaquent à cette question.

La première propose une interprétation des liens entre la structure crustale et la géométrie des failles, ainsi qu'une quantification de l'extension totale accommodée dans la région depuis l'ouverture des premiers bassins. Elle se base sur l'analyse d'un modèle 3D de la croûte construit par inversion de données gravimétriques corrigées de l'influence des bassins sédimentaires. La différence entre la surface actuelle du domaine d'étude et la surface accommodable avant déformation avec le volume modélisé donne une estimation de l'extension dans la région. Comparé aux vitesses actuelles mesurées par GPS, notre estimation indique que les taux de déformation par extension ont peu varié depuis un premier stade probablement purement extensif antérieur à l'incursion de la faille. La comparaison de la géométrie du volume représenté par la croûte et de la localisation des failles permet aussi de proposer des mécanismes différents de propagation de la faille entre deux blocs Est et Ouest. Enfin, l'amincissement de la croûte inférieure, étalé au-delà des limites des bassins profonds de la mer de Marmara, révèle le rôle de flux ductiles modérés dans la répartition de la déformation. La deuxième étude visait à confirmer les modèles d'âges des sédiments proposés actuellement en mer de Marmara. Ces modèles reposent sur l'interprétation d'horizons sismiques constituant des figure sédimentaires répétitives, reliées aux cycles glacio-eustatiques, et sur l'extrapolation de taux de sédimentation récents. Or, les seules estimations de vitesse de la faille à moyen terme (~500 000 ans) reposent sur ces modèles. En choisissant des points de carottage précis, nous avons cherché à atteindre directement les sédiments à l'origine des premiers réflecteurs sismiques interprétés afin de vérifier les âges proposés pour, ensuite, valider ou non les estimations de vitesses de la faille. Les méthodes appliquées lors de ce travail vont de la géophysique, pour la corrélation précise des carottes de sédiment et des signaux sismiques, à la caractérisation paléo-environnementale des dépôts, pour la construction d'un modèle d'âge au sein de la carotte, en passant par l'application de méthodes de datation indirectes telles que le paléomagnétisme et la téphrochronologie. Les résultats ont permis de dater précisément le premier réflecteur ainsi que d'en comprendre l'origine. L'âge que nous proposons est plus jeune que ceux déterminés jusqu'alors. S'il n'invalide pas les modèles d'âges antérieurs, il suggère que les âges proposés sont sans doute décalés au sein des cycles glacio-eustatiques. A travers ce travail, nous proposons également une reconstitution détaillée de l'évolution paléo-environnementale et paléo-hydrologique de la mer de Marmara depuis le dernier interglaciaire retraçant notamment la désalinisation graduelle de la colonne d'eau et sa stratification pendant la période de transition vers la glaciation.

Abstract

The Marmara Sea, connected to the Mediterranean Sea through the Dardanelles Strait and to the Black Sea through the Bosphorus, is the keystone of a complex hydrological system. Through the Marmara Sea, freshwater flows westward while heavier marine water flows eastward below. However, the balance between inputs and outputs has been disturbed during glacial periods when the global ocean level dropped below the sill depths, isolating the Marmara Sea. The Sea of Marmara is also an active tectonic structure and its morphology is still slowly being modified by the movements of the North-Anatolian fault northern branch. The ruptures of this continental dextral transform fault, one of the longest fault in the world, are regularly causing massive earthquakes and are a threat to Istanbul and its 15 million inhabitants. Since the Ganos and the Koaceli earthquakes that occurred east and west of the Marmara Sea during the 20th century, many scientific studies are aiming at characterizing the fault structure and its functioning in the hope of being able to foresee the next earthquake close to Istanbul. This thesis presents two studies tackling this subject from two different time and space-scale.

The first study presents an interpretation of the relations between the crustal structure and the fault geometry that led to a quantification of the total extension taken by the area since the opening of the first basins. Calculations are based on the analysis of a 3D crustal model built from the inversion of gravity data corrected from the influence of sedimentary basins. We then compared the surface that can be covered by the resulting crust volume before deformation with the surface of our studied area. The difference corresponds to an estimation of the total extension. When compared with GPS extension rate, it indicates that the extension rate has been close to stable since a first purely extensional stage before the North Anatolian Fault incursion. Moreover, based on the comparison of the crust model geometry with the faults location, we propose that the mechanisms of the fault propagation were not the same in the whole Marmara Sea. Finally, the lower crust thinning away from the basins reveals the role of ductile flows in the deformation distribution. The second study purpose was to confirm or reverse, the sedimentary age models available in the Marmara Sea. These models are primarily based on the interpretation of seismic horizons showing repetitive sedimentary figures, related to climatic cycles, and on the extrapolation of recent sedimentation rate. The only estimations of medium term fault slip rates (~500 000 years) are based on these models. By targeting precise coring locations on the sea floor, we tried to reach directly the sediments constituting the first main reflectors in order to verify the proposed ages and, ultimately, to verify the age models and the fault slip rate estimations. We used a broad range of methods to build a new age model for one core such as geophysics, for correlating precisely seismic synthetics and seismic signals, or indirect dating methods such as paleo-magnetism, and tephrochronology. A paleo-environmental characterization of the sediments from fossil, mineral and chemical contents completed this work. The results give a date for the first main reflector that is younger than the one assessed by previous studies. If it does not reverse entirely the models, it suggests that the proposed ages may be shifted inside one 100 ky glacio-eustatic cycle. From our various results, we also propose a detailed reconstitution of the paleo-environment and paleo-hydrology evolution in the Marmara Sea since the last interglacial stage. In particular, we give evidence for the gradual salinity decrease and for the establishment of a stratified water column at the beginning of the glacial stage.